

The Late Light Show with Long-Lived Particles:
A Search for Displaced and Delayed Diphoton and Dielectron Vertices at the LHC

Kiley Elizabeth Kennedy

Submitted in partial fulfillment of the
requirements for the degree of
Doctor of Philosophy
under the Executive Committee
of the Graduate School of Arts and Sciences

COLUMBIA UNIVERSITY

2022



© 2022

Kiley Elizabeth Kennedy

All Rights Reserved

ABSTRACT

The Late Light Show with Long-Lived Particles:
A Search for Displaced and Delayed Diphoton and Dielectron Vertices at the LHC

Kiley Elizabeth Kennedy

The Standard Model of particle physics constitutes the most accurate and comprehensive known description of the fundamental building blocks of the universe. However, overwhelming evidence suggests that the theory is incomplete and that new physics may be hiding at the TeV-scale. The Large Hadron Collider (LHC) at CERN probes these high-energy scales, opening a potential gateway to access physics beyond the Standard Model (BSM). Long-lived particles (LLPs) arise in many promising BSM theories, but they remain weakly constrained at the LHC. This thesis presents a novel search for displaced and delayed diphoton and dielectron vertices originating from the decay of a neutral LLP. The analysis uses the full LHC Run 2 dataset of pp collisions at a center-of-mass energy of $\sqrt{s} = 13$ TeV recorded by the ATLAS detector, corresponding to an integrated luminosity of 139 fb^{-1} . The search harnesses the capabilities of the ATLAS Liquid Argon calorimeter to precisely measure the displacement and delay of the final state electromagnetic objects. The results are interpreted in a gauge-mediated supersymmetry breaking model that features the pair-production of LLPs, with each LLP subsequently decaying into either a Higgs boson or a Z boson. Since no significant excess is observed above the background expectation, the results are used to set upper limits on the cross section of LLP pair-production for signal models with an LLP mass between 100 and 725 GeV and lifetime between 0.25 ns and $1 \mu\text{s}$. A model-independent limit is also set on the production of pairs of photons or electrons with a significantly delayed arrival at the calorimeter.

TABLE OF CONTENTS

| | |
|--|-------|
| ACKNOWLEDGMENTS | xiii |
| DEDICATION | xvi |
| PREFACE | xvii |
| INTRODUCTION | 1 |
| I THEOREY | 4 |
| 1 THE STANDARD MODEL | 5 |
| 1.1 Symmetries and Forces | 6 |
| 1.2 Spontaneous Symmetry Breaking and the Higgs Mechanism | 8 |
| 1.3 Fermions and Phenomenology | 9 |
| 1.4 Empirical Validation of the Standard Model | 11 |
| 1.5 Limitations of the Standard Model | 12 |
| 2 SUPERSYMMETRY | 15 |
| 2.1 Motivation for Supersymmetry: Two Perspectives | 16 |
| 2.1.1 Supersymmetry as a Spacetime Symmetry | 16 |
| 2.1.2 Supersymmetry as a Solution to the Hierarchy Problem | 17 |
| 2.2 The Minimal Supersymmetric Standard Model | 18 |
| 2.3 Supersymmetry Breaking | 21 |

| | | |
|-----------|---|-----------|
| 2.3.1 | Soft Supersymmetry Breaking in the MSSM | 21 |
| 2.3.2 | Gauge-Mediated Supersymmetry Breaking | 24 |
| 2.4 | Long-Lived Particles | 25 |
| 2.4.1 | Experimental Landscape at the LHC | 26 |
| 2.4.2 | Long-Lived Higgsinos | 27 |
| II | EXPERIMENT | 30 |
| 3 | THE LARGE HADRON COLLIDER | 31 |
| 3.1 | Accelerator Physics | 32 |
| 3.2 | LHC Design | 32 |
| 3.3 | Run 2 Beam Conditions | 34 |
| 4 | THE ATLAS DETECTOR | 37 |
| 4.1 | Coordinate System and Geometry | 39 |
| 4.2 | Inner Detector | 41 |
| 4.3 | Liquid Argon Calorimeter | 43 |
| 4.3.1 | Electromagnetic Calorimeter | 44 |
| 4.3.2 | Hadronic End-Cap Calorimeter | 46 |
| 4.3.3 | Forward Calorimeter | 47 |
| 4.4 | Tile Calorimeter | 47 |
| 4.5 | Muon Spectrometer | 49 |
| 4.6 | Magnet System | 51 |
| 4.7 | Forward Detectors and Luminosity Calculation | 52 |
| 4.8 | Trigger and Data Acquisition System | 53 |
| 5 | OBJECT RECONSTRUCTION AND IDENTIFICATION | 56 |
| 5.1 | Inner Detector Tracks and Vertices | 57 |
| 5.2 | Topological Calorimeter Clusters | 58 |

| | | |
|-------|--|----|
| 5.3 | Photons and Electrons | 59 |
| 5.3.1 | Electromagnetic Superclusters | 60 |
| 5.3.2 | Photon and Electron Identification | 61 |
| 5.3.3 | Isolation Requirements | 64 |
| 5.4 | Jets | 64 |
| 5.5 | Muons | 65 |
| 5.6 | Overlap Removal | 66 |
| 5.7 | Missing Transverse Energy | 67 |
| 6 | VERTEXING AND TIMING MEASUREMENTS | 69 |
| 6.1 | Trackless Calo-Vertexing | 70 |
| 6.1.1 | Calorimeter Pointing | 70 |
| 6.1.2 | Vertexing Strategy | 73 |
| 6.1.3 | Vertexing Performance | 74 |
| 6.2 | Timing | 77 |
| 6.2.1 | Electronic Readout | 77 |
| 6.2.2 | Measurement | 79 |
| 6.2.3 | Calibration | 80 |
| 6.2.4 | Satellite Collisions | 83 |
| 6.2.5 | Monte Carlo Smearing | 84 |
| III | SEARCH | 86 |
| 7 | DATA AND SIMULATED SAMPLES | 87 |
| 7.1 | Data | 88 |
| 7.2 | Monte Carlo Simulation | 89 |
| 7.3 | Simulated Signal Samples | 89 |

| | | |
|-------|---|-----|
| 8 | ANALYSIS STRATEGY | 93 |
| 8.1 | Event Selection | 94 |
| 8.1.1 | Photon Object Selection | 94 |
| 8.1.2 | Event-Level Requirements | 99 |
| 8.2 | Analysis Region Definitions | 100 |
| 8.2.1 | Timing | 101 |
| 8.2.2 | Missing Transverse Energy | 102 |
| 8.2.3 | Diphoton Mass, Momentum, and Angular Separation | 102 |
| 8.2.4 | Summary of Analysis Regions | 104 |
| 8.3 | Sensitive Variable Selection | 106 |
| 8.4 | Analysis Optimization And Binning | 110 |
| 8.5 | Background Estimation | 114 |
| 8.5.1 | Purity Scaling | 115 |
| 8.5.2 | $E_{\text{cell}}^{\text{max}}$ Reweighting | 116 |
| 8.5.3 | Residual Time-Shifting | 116 |
| 8.5.4 | Treatment of the Control Region | 116 |
| 9 | SYSTEMATIC UNCERTAINTIES | 118 |
| 9.1 | Background Uncertainties | 119 |
| 9.1.1 | Photon Purity Fraction | 119 |
| 9.1.2 | $E_{\text{cell}}^{\text{max}}$ Reweighting | 120 |
| 9.1.3 | Pileup Distribution | 120 |
| 9.2 | Signal Uncertainties | 123 |
| 9.2.1 | Integrated Luminosity Uncertainty | 123 |
| 9.2.2 | Theory Uncertainties | 125 |
| 9.2.3 | Instrumental Uncertainties | 125 |
| 9.2.4 | Timing Resolution Uncertainty | 127 |

| | | |
|-----------|--|------------|
| 10 | STATISTICAL ANALYSIS AND FIT VALIDATION | 129 |
| 10.1 | Hypothesis Testing and Interpretation | 130 |
| 10.2 | Fit Implementation and Validation | 132 |
| 10.2.1 | Validation of Fit Procedure | 132 |
| 10.2.2 | Validation of Background Modeling | 134 |
| 10.2.3 | Validation of Discovery Region | 137 |
| 11 | RESULTS AND INTERPRETATION | 138 |
| 11.1 | Unblinded Signal Region Results | 138 |
| 11.2 | Limits and Exclusions on Supersymmetric Models | 142 |
| 11.3 | Model-Independent Limits | 145 |
| 12 | CONCLUSIONS AND OUTLOOK | 147 |
| | REFERENCES | 150 |
| | APPENDICES | 158 |
| A | TRACKLESS CALO-VERTEXING PERFORMANCE | 159 |
| B | SATELLITE COLLISION STUDIES | 163 |
| B.1 | Satellite Collisions Across Analysis Regions | 163 |
| B.2 | Satellite Collision Event in the Signal Region | 168 |
| C | TIMING STUDIES | 170 |
| C.1 | Lifetime Reweighting | 170 |
| C.2 | Timing Shapes Across Quadrants | 171 |
| C.3 | Timing Resolutions Across Critical Variables | 173 |
| C.4 | Comparison of Timing Variable Candidates | 175 |

| | | |
|-----|---|-----|
| D | ANALYSIS DEVELOPMENT: ADDITIONAL MATERIAL | 177 |
| D.1 | Trigger Studies | 177 |
| D.2 | Signal Contamination | 180 |
| D.3 | Signal and Background Topology | 182 |
| E | FIT STUDIES | 185 |
| E.1 | Fit Validation | 185 |
| E.2 | Signal Region Results | 188 |

LIST OF FIGURES

| | | |
|------|--|----|
| 1.1 | Diagram of the Higgs boson potential | 8 |
| 1.2 | Diagram of Standard Model particles | 10 |
| 1.3 | Standard Model cross section measurements | 13 |
| 2.1 | Loop contributions to the Higgs boson propagator | 17 |
| 2.2 | Long-lived particles in the Standard Model | 27 |
| 2.3 | Feynman diagram of pair-produced electroweakinos | 29 |
| 3.1 | The LHC accelerator complex at CERN | 33 |
| 3.2 | Pileup distributions during LHC Run 2 | 35 |
| 3.3 | Diagram of LHC proton bunch structure | 36 |
| 4.1 | Diagram of the ATLAS Detector | 38 |
| 4.2 | ATLAS coordinate system | 40 |
| 4.3 | Diagram of the Inner Detector system | 41 |
| 4.4 | Transverse slice of the LAr EM calorimeter | 44 |
| 4.5 | Diagram of a LAr calorimeter cell | 46 |
| 4.6 | Diagram of a LAr HEC module | 47 |
| 4.7 | Diagram of the LAr FCal | 47 |
| 4.8 | Diagram of a TileCal module | 48 |
| 4.9 | Profile view of the muon spectrometer | 50 |
| 4.10 | Schematic of the ATLAS magnet system | 52 |

| | | |
|------|---|-----|
| 4.11 | ATLAS trigger and data acquisition system | 54 |
| 4.12 | MEDIUM photon trigger efficiencies | 55 |
| 5.1 | Interactions of physics objects in the ATLAS detector | 57 |
| 5.2 | Primary vertex reconstruction efficiency | 58 |
| 5.3 | Primary vertex resolution | 58 |
| 5.4 | Schematic of superclustering algorithm for electrons and photons | 60 |
| 5.5 | Illustration of electromagnetic showers of a photon and π^0 meson | 63 |
| 5.6 | Resolution of E_T^{miss} measurement | 68 |
| 6.1 | Illustration of calorimeter pointing approach | 71 |
| 6.2 | Pointing resolution for $Z \rightarrow ee$ data and simulation and several signal models | 72 |
| 6.3 | Illustration of the Trackless Calo-Vertexing strategy | 73 |
| 6.4 | Vertexing resolution as a function of $\Delta\eta_{ee}$ for $Z \rightarrow ee$ data and MC | 74 |
| 6.5 | Vertexing distributions and $\Delta\eta_{ee}$ requirements | 76 |
| 6.6 | LAr calorimeter pulse | 78 |
| 6.7 | Comparison of electron timing distributions before and after calibration . . | 81 |
| 6.8 | Timing resolution as a function of E_{cell}^{max} | 83 |
| 6.9 | 2D timing distribution of electrons from $Z \rightarrow ee$ events | 84 |
| 7.1 | Integrated luminosity delivered during LHC Run 2 | 88 |
| 8.1 | Photon identification efficiency as a function of displacement | 96 |
| 8.2 | Trigger and photon identification efficiency as a function of signal mass . . . | 97 |
| 8.3 | Photon isolation efficiency as a function of displacement | 98 |
| 8.4 | Distribution of $\Delta\eta_{\gamma\gamma}$ and impact of $\Delta\eta_{\gamma\gamma}$ selection | 100 |
| 8.5 | Schematic drawing of timing region quadrants | 101 |
| 8.6 | Distributions of E_T^{miss} , $m_{\gamma\gamma}$, $p_T^{\gamma\gamma}$, and $\Delta\phi_{\gamma\gamma}$ | 103 |
| 8.7 | Visualization of analysis regions | 104 |

| | | |
|------|---|-----|
| 8.8 | Distribution of timing variables in data and simulated signal | 107 |
| 8.9 | Distribution of vertexing variables in data and simulated signal | 109 |
| 8.10 | Distributions of t_{avg} and ρ in data and simulated signal | 110 |
| 8.11 | Distribution ρ vs. t_{avg} for data and simulated signal | 112 |
| 8.12 | Background and simulated signal yields in analysis binning | 113 |
| 8.13 | Photon purity distributions | 115 |
| 9.1 | Background photon purity systematic uncertainties | 121 |
| 9.2 | Background $E_{\text{cell}}^{\text{max}}$ systematic uncertainties | 122 |
| 9.3 | Background pileup systematic uncertainties | 124 |
| 9.4 | Signal timing resolution systematic uncertainties | 128 |
| 10.1 | Spurious signal test | 133 |
| 10.2 | Signal injection test | 133 |
| 10.3 | Background-only fit to VR(t) data | 135 |
| 10.4 | Pull distributions of background-only fit to VR data | 136 |
| 11.1 | Background-only fit to SR data | 140 |
| 11.2 | Pull distributions of background-only fit to SR data | 141 |
| 11.3 | Exclusion limits as a function of $\tilde{\chi}_1^0$ mass | 142 |
| 11.4 | Exclusion limits as a function of $\tilde{\chi}_1^0$ lifetime | 143 |
| 11.5 | Exclusion limits as a function of $\tilde{\chi}_1^0$ branching ratio | 144 |
| 11.6 | Exclusions on $\tilde{\chi}_1^0$ production as a function of mass and lifetime | 145 |
| 11.7 | Exclusions on $\tilde{\chi}_1^0$ production as a function of mass, lifetime, and branching ratio | 146 |
| A.1 | Vertexing distributions in $Z \rightarrow ee$ data and MC simulation | 160 |
| A.2 | Vertexing resolution as a function of electron kinematics | 161 |
| A.3 | Vertexing resolution as a function of dielectron kinematics | 162 |

| | | |
|-----|---|-----|
| B.1 | Timing distributions in data, including satellite collision candidates | 164 |
| B.2 | Prevalence of satellite collisions as a function of event-level variables | 166 |
| B.3 | Prevalence of satellite collisions as a function of photon object variables | 167 |
| B.4 | Event display of ATLAS run 359593, event 761048468 | 168 |
| C.1 | Lifetime reweighting extrapolation range and validation | 172 |
| C.2 | Average timing distribution across timing quadrants | 173 |
| C.3 | Timing resolution as a function of E_T^{miss} , $m_{\gamma\gamma}$, $\Delta\phi_{\gamma\gamma}$, and $p_T^{\gamma\gamma}$ | 174 |
| D.1 | Trigger efficiencies and event yields as a function of $\tilde{\chi}_1^0$ mass | 178 |
| D.2 | Venn diagrams of Run 2 signal yields for various trigger candidates | 179 |
| D.3 | Trigger efficiency as a function of $m_{\gamma\gamma}$ | 180 |
| D.4 | Signal contamination in various analysis regions | 181 |
| D.5 | Photon kinematics in data and simulated signal | 183 |
| D.6 | Vertexing variables in data and simulated signal | 184 |
| E.1 | Background-only fit to $\text{VR}(E_T^{miss})^{t>0}$ data | 186 |
| E.2 | Background-only fit to $\text{VR}(E_T^{miss})^{t<0}$ data | 187 |
| E.3 | Signal significances and p_0 -values in the SR | 188 |

LIST OF TABLES

| | | |
|------|---|-----|
| 2.1 | Supermultiplets of the MSSM | 20 |
| 2.2 | Gauge and mass eigenstates of the MSSM | 23 |
| 4.1 | ATLAS subsystem design resolutions and η coverage | 39 |
| 4.2 | Design specifications of the Inner Detector | 42 |
| 4.3 | LAr EM calorimeter cell granularities | 45 |
| 4.4 | Design specifications of the muon spectrometer | 50 |
| 4.5 | Forward detector position and pseudorapidity coverage | 53 |
| 5.1 | Shower shape variables used in photon and electron identification | 62 |
| 6.1 | Comparison of timing resolutions before and after calibration | 82 |
| 7.1 | Grid of long-lived higgsino signal models | 90 |
| 8.1 | Summary of event selection | 99 |
| 8.2 | Summary of analysis region selections | 105 |
| 9.1 | Summary of background systematic uncertainties | 119 |
| 9.2 | Breakdown of theory systematic uncertainties for simulated signal | 125 |
| 9.3 | Summary of signal systematic uncertainties | 126 |
| 10.1 | Fitted p_0 -values and significances for the VRs | 136 |
| 10.2 | Number of events in the highest timing bin of each VR | 137 |

| | | |
|-----|--|-----|
| B.1 | Predicted and measured number of satellite collisions across regions | 164 |
| B.2 | Key event variables for ATLAS run 359593, event 761048468 | 169 |

ACKNOWLEDGMENTS

First and foremost, I want to express my sincere gratitude to my advisor, John Parsons, for his invaluable guidance, unwavering support, and genuine compassion throughout the past several years. John – it was you who inspired me to pursue this degree, and your encouragement has driven me to stick with it. I deeply appreciate how you so earnestly care for the well-being of those around you, especially during the pandemic and some particularly difficult times. Thank you for your extraordinary mentorship.

I have also had the privilege to work with and learn from the incredibly talented (and impressively organized!) postdoc, Julia Gonski. Julia – you have been such a phenomenal role model for me in both research and outreach, and have helped shape me into the scientist I am today. Thank you for teaching me how to tackle problems in new ways, for patiently answering my offbeat questions, and for always having my back.

The search presented in this thesis is the product of tireless work by a tenacious, lively, and cohesive analysis team. Thank you to Tim Andeen, Nikiforos Nikiforou, Devanshu Panchal, Elena Busch, Andrew Smith, and Eleanor Woodward (and, of course, John and Julia) for your commitment and camaraderie. It has honestly been a blast to work with and get to know each of you. Tim – I greatly appreciate your guidance over the past several years, particularly for teaching me particle physics from scratch during my REU summer and serving on my Ph.D. advisory committee. And Nikiforos – you never fail to teach me something interesting and/or remarkably helpful, and I have been lucky to work with you on so many projects. I would also like to thank the broader ATLAS and SUSY community,

whose support and valuable feedback significantly strengthened this analysis, especially Laura Jeanty, Rosa Simoniello, Ben Hooberman, Javier Montejo Berlingen, Jeff Shahinian, Helen Hayward, Cristiano Alpigiani, and James Beacham.

When I arrived at CERN in 2018, I was welcomed by an enthusiastic and dynamic LAr Operations Team. Thank you to all the members of this fantastic team, especially Adriana Milic, Clement Camincher, Emmanuel Monnier, and Nikiforos, for getting me up to speed, creating such a collaborative environment, and introducing me to the venerable LAr-BQ.

I want to thank my fellow members of the Columbia ATLAS group for passing on so much wisdom about physics, hidden twikis, and niche Linux commands. In addition to the cohort already mentioned, thank you to Gustaaf Brooijmans, Mike Tuts, Ines Ochoa, Konie Al Khoury, Devin Mahon, Alex Emerman, and Alan Kahn. A special shout-out goes to Devin and Alex for answering (and often anticipating) so many of my LAr-related questions; and to Devin for trailblazing the Run 2 displaced photons effort, developing such an impressive and easy-to-use timing tool, and sending me countless snippets of code. Thank you to the entire Nevis Labs community, especially Amy Garwood, Grace Ho, and Bill Seligman for keeping everything up and running, and Georgia Karagiorgi for serving on my Ph.D. advisory committee. I would also like to thank James Applegate, Frederik Denef, Andy Haas, and Mike Shaevitz for reviewing this thesis and serving on my defense committee.

I am incredibly grateful for those at CERN, Columbia, and beyond who have helped me cultivate my love of science outreach and public engagement. Thank you to the dedicated members of the US LHC Users Association and the ATLAS Outreach Group, especially Steve Goldfarb, Muhammad Alhroob, and Clara Nellist. I appreciate the support from those at the Columbia Center for Teaching and Learning, and Jeremy Dodd's guidance on several teaching-related initiatives during my early years of graduate school. A big thank you to Keri Gilder for providing such valuable advice for my career and professional development.

I am indebted to the teachers and professors who inspired my fascination for physics long before I had any aspirations of pursuing a Ph.D. A very special thank you to Ben Small, Lawrence Stowe, Greg Voth, and especially Francis Starr – each of you, in no small part, has helped lead me to where I am today.

I got by with *a lot* of help from my friends and family. Shout-out to all of my life-long buddies back home, especially Grace, Beaux, Ellen, Rachel, Jess, Jake, Madeline, and Elaine, and to my incredible amiguis abroad who will forever keep me tethered to Geneva, especially Alba, Ana, Clau, Cris, Emma, and Jara. I would not have made it through the past few years without the warmth and generosity of Tom and Diana, the friendship of JP and Chiara, and the many adventures of my pandemic-winter-weekend survival crew, Linda, Elias, and Mikel. Finally, to my Mom, Dad, and brother, Teddy, thank you for putting up with me and being my most steadfast support system. I am grateful beyond words, and I love you all so much.

To my mother and father,
who gave me the universe
and the curiosity to study it.

PREFACE

When you're getting ready to launch into space, you're sitting on a big explosion waiting to happen.

— Sally Ride

The first time I laid eyes on the ATLAS detector, after scrambling through crawlspaces and up scaffolding 100 m below the Franco-Swiss border, I gazed at the thousands of Analog-to-Digital Converter (ADC) chips that I had hand-tested, one by one, being installed on the detector. I was struck by a riveting realization: my careful handiwork now connected me to this colossal detector.

At the time, I was a third-year graduate student. My work on ATLAS had started years before, during a hot New York City summer, when, as an undergraduate in Columbia's Nevis REU Program, I landed in the ATLAS group working with Professor John Parsons. My project focused on a search for vector-like quarks, offering an exciting first glimpse into the world of particle physics. Inspired by this experience and resolved to delve further into the field, I returned to Columbia University the following year, in the fall of 2016, to pursue my Ph.D. on the ATLAS experiment.

During my first few years of graduate school, much of my work focused on hardware testing and development for various upgrades to the ATLAS Liquid Argon (LAr) calorimeter. As mentioned, one such task included assessing a portion of the 12,000+ ADC application-specific integrated circuit chips [1] for the ATLAS Phase I upgrade, whose in-

stallation period spanned late 2018 to early 2022. This upgrade successfully increased the granularity of the detector's readout channels at the trigger level, thus enhancing our ability to quickly discern appealing collision events that may contain intriguing physics processes from less interesting ones.

My primary contribution to ATLAS hardware development was for the HL-LHC upgrade of the LAr calorimeter, where I evaluated the performance of two ADC candidates: one custom-designed and one commercial. This upgrade, scheduled to begin installation in 2026, endeavors to further improve the detector granularity at the trigger level (to equal that of offline analysis) and to increase the precision of the readout channels. This challenging task requires the complete replacement of most of the on-detector LAr calorimeter electronics. The ADC specifications include an effective number of bits (ENOB) > 11 , a 40 MSPS sampling rate, a 14-bit dynamic range, and a high degree of radiation hardness. In collaboration with a team of electrical engineers, who designed the chips and tweaked their test boards, I oversaw test setups, controlled data acquisition, and characterized any unusual or unexpected features in chip output signals. I assessed various "standard" ADC performance metrics, like ENOB, non-linearity, and clock jitter, as well as higher-order behavior, including gain transition effects, crosstalk between channels, and various sources of noise. My studies established the commercial ADC as a suitable upgrade backup and informed the design of future iterations of the custom chip, which is set to be installed on-detector during the next LHC shutdown. A technical paper detailing the design, characteristics, and performance of the ADC for the LAr calorimeter HL-LHC upgrade is currently in preparation.

When I relocated to CERN in 2018, I immersed myself in LAr detector operations. During the final months of LHC Run 2, I had the opportunity to serve as a control room "shifter," monitoring data-taking and machine performance, and later, as a LAr Software On-Call, troubleshooting various software issues identified by the shifters. As the LAr operations team transitioned from Run 2 data-taking to the Phase I upgrade installation,

I continued my software-related responsibilities, developing tools for the upgrade commissioning process. I also took on the rotating role of LAr Run Coordinator, where, for week-long shifts, I managed the activities of the LAr detector, responded to hardware failures, coordinated with experts of other ATLAS subsystems, and helped train incoming students and postdocs. I found tackling these problems thrilling, and the team's supportive and "can-do" environment made learning the system fun. In 2019, I was honored to represent the LAr operations team at the IEEE Nuclear Science Symposium, where I presented on LAr detector performance during LHC Run 2 [2].

In conjunction with these hardware and operations activities, I began exploring various analysis topics for this thesis. Searches for long-lived particles (LLPs) immediately captured my attention, mainly because the experimental coverage of LLP signatures remains largely unexplored. Furthermore, many theories beyond the Standard Model – including supersymmetry (SUSY), exotic Higgs models, dark matter models, and warped extra dimensions – allow for (and sometimes even predict) the presence of LLPs. So, in 2019, when the opportunity arose to get involved with an analysis searching for LLPs, I jumped at the chance.

My first LLP analysis targeted exotic decays of the Higgs boson into long-lived neutral particles that then decay into photons. This model is primarily motivated by the Higgs boson's direct coupling to mass, which offers a powerful portal to hypothetical new particles. The critical discriminants – photon pointing and timing – account for the displacement and delay of the final state photon. These quantities rely on specialized, low-level measurements of the LAr calorimeter, dovetailing elegantly with my hardware and operations expertise.

In addition to contributing to early analysis development, I focused on optimizing the photon *pointing* variable, which determines photon object displacement. My study reparameterized the LAr calorimeter shower information that went into the pointing measurement, a project that frequently saw me consulting various LAr experts and digging

through the LAr Technical Design Report from the 1990s (which to this day still lives on my computer desktop). My familiarity with the LAr detector and community made this highly technical task slightly easier and far more enjoyable. Earlier this year, this analysis established exclusion limits on the branching ratio of the Higgs boson to certain SUSY particles, with some branching ratio constraints as low as 1% [3]. A publication documenting this analysis is being submitted to *Physical Review D*.

My experience working on this non-pointing photon search laid the groundwork for the analysis described in this thesis. To prepare for this pursuit, I developed, evaluated, and validated a tool that builds upon my pointing study, using LAr calorimeter measurements to vertex two displaced photons. The product is the novel Trackless Calo-Vertexing Tool, which, together with the LAr timing measurement and calibration pioneered by the earlier analysis, form the crux of my thesis. The results of this analysis were recently made public this past July [4], with plans to submit to *Physical Review D* in the near future. Although the twelve chapters that follow focus on this particular analysis and result, my many years of preparation for this search have played just as important a role in making me the physicist I am today.

INTRODUCTION

If you wish to make an apple pie from scratch, you must first invent the universe.

— Carl Sagan

Modern experimental particle physics research explores the nature of the fundamental building blocks of the universe – fields and particles. The Standard Model of particle physics (SM) represents the most accurate and empirically verified description of elementary particles’ properties, dynamics, and interactions; however, the theory remains flawed and incomplete. The groundbreaking discovery of the Higgs boson in 2012 concluded a several-decades-long quest to detect all fundamental particles predicted by the SM. At the same time, this triumph ushered in a new era of high-energy particle physics research targeting physics *beyond* the SM (BSM).

In the ten years since the discovery of the Higgs boson, physicists at CERN’s Large Hadron Collider (LHC) have endeavored to unearth new physics that might explain or resolve some of the most troubling shortcomings of the SM. However, these searches have not yet provided definitive evidence for BSM physics. Given the many sensible BSM theories that propose new TeV-scale physics within reach of the LHC, the fundamental question becomes: *where is new physics hiding?* One class of elusive and intriguing signatures, called long-lived particles (LLPs), may hold the answer. LLPs exist in numerous theories, both within and beyond the SM. Despite their theoretical promise, LLPs remain weakly

constrained at the LHC: their experimental signatures, generally consisting of displaced decays, tend to evade the vast majority of LHC searches that assume particles decay immediately, with little to no displacement.

This thesis presents a search for an experimentally unexplored LLP signature: a displaced and delayed diphoton vertex. The analysis is also sensitive to displaced and delayed dielectron vertices. The search employs the dataset collected by the ATLAS detector during Run 2 of the LHC and harnesses the capabilities of the ATLAS Liquid Argon (LAr) calorimeter to determine both the delay and displacement of these challenging and unique signatures. Results are presented in the context of a supersymmetry (SUSY) signal model with LLPs; in addition, since displaced diphoton and dielectron vertices emerge throughout a wide swath of BSM physics models, results are generalized to a model-independent interpretation. This thesis chronicles this analysis in three parts – the theory, the experiment, and the search – as described below.

Part I introduces the theoretical context, principles, and motivation behind the search, beginning with the properties, achievements, and limitations of the SM in Chapter 1. Chapter 2 establishes SUSY as a compelling extension to the SM and characterizes the phenomenology of a popular class of SUSY models; it also details the general mechanisms for and typical properties of LLPs, which appear in many variations of SUSY models.

Part II illustrates the experimental approach used to search for an experimental signature of the theories from Part I. Chapter 3 summarizes basic principles of accelerator physics and the design of the LHC. The description of the ATLAS detector and its subsystems, used to measure the products of LHC collisions, follows in Chapter 4. Chapter 5 then delineates how various reconstruction and identification algorithms assemble and classify physics objects from raw ATLAS detector hits. Next, Chapter 6 presents the LAr calorimeter timing and vertexing variables, which measure the delay and displacement of the photons and electrons in the chosen signal model.

Part III describes the search itself, opening with an overview of the data and simulated samples utilized in Chapter 7. Chapter 8 details the analysis strategy, including the selection of collision events and physics objects, the optimization of the analysis, and the background estimation. The systematic uncertainties considered in the search are outlined in Chapter 9. Chapter 10 highlights the statistical methods and validation procedures employed by the analysis, and Chapter 11 presents the results and interpretation of the search. Finally, Chapter 12 concludes with an outlook on the context of the experimental landscape at the LHC and future efforts that might build upon this work.

PART I:

THEORY

CHAPTER 1:

THE STANDARD MODEL

All models are wrong, but some are useful.

— George Box

The SM constitutes the most complete and experimentally validated theory of particle physics, describing the behavior of all known elementary particles and their interactions via three of the four known fundamental forces. The theory, patched together in the decades leading up to its modern formulation in the 1970s, has withstood extensive experimental scrutiny, predicted a wide variety of physical phenomena, and guided the direction of particle physics research for the past half-century.

This chapter summarizes the general properties of the SM: Section 1.1 introduces its fundamental assumptions and underlying symmetries; Sections 1.1-1.3 discuss its emergent properties; Section 1.4 highlights its salient experimental achievements; and Section 1.5 reviews several of its shortcomings.

1.1 SYMMETRIES AND FORCES

The SM is a local quantum field theory, a formalism that unites the fundamental principles of quantum mechanics, special relativity, and classical field theory. The SM Lagrangian, \mathcal{L}_{SM} , encapsulates SM dynamics and describes the properties and interactions of its underlying quantum fields, excitations of which give rise to observable particles.

One can construct \mathcal{L}_{SM} by writing down the most general renormalizable Lagrangian that respects a set of given symmetries. The SM respects the complete external symmetry of special relativity, the Poincaré group (\mathcal{P}), which dictates that the laws of physics should be the same in every reference frame. The SM Lagrangian is consequently invariant under spacetime translations, rotations, and boosts. By construction, \mathcal{L}_{SM} is invariant under the local internal gauge symmetry, G_{SM} :

$$G_{SM} = SU(3)_C \times SU(2)_L \times U(1)_Y \quad (1.1)$$

where $SU(3)_C$ constitutes the symmetry group of Quantum Chromodynamics (QCD), the theory of the strong interaction, and $SU(2)_L \times U(1)_Y$ represents the symmetry group of the electroweak interaction.

Several interesting physical properties arise directly from the symmetries of the SM via the application of Noether's theorem, which stipulates that each continuous symmetry is associated with a conserved quantity [5]. The Poincaré symmetry yields conservation of energy, momentum, and angular momentum, and the local gauge symmetry G_{SM} leads to the conservation of SM charges. The SM Lagrangian is also invariant under CPT , the combination of three additional discrete symmetries: charge conjugation (C) transforms particles into anti-particles, effectively reversing their charge and other quantum numbers; parity conjugation (P) transforms left-handed particles into right-handed particles and vice-versa; and time-reversal (T), not surprisingly, reverses time.

The electroweak interaction comprises the symmetries of two distinct groups, $SU(2)_L$ and $U(1)_Y$. The $SU(2)_L$ symmetry is generated by vector bosons ($W^{1,2,3}$) and conserves weak isospin ($T_{1,2,3}$). Here, L indicates that the symmetry only applies to the left-handed components of fermions;¹ correspondingly, the $W^{1,2,3}$ bosons only interact with left-handed particles, a process that notably violates CP (the combination of charge and parity) symmetry. $U(1)_Y$ is generated by the B boson and conserves weak hypercharge (Y). The $W^{1,2,3}$ and B bosons are massless since any Lagrangian mass terms for them would break the very symmetry they generate.

At low energies, the electroweak symmetry is spontaneously broken as follows: $SU(2)_L \times U(1)_Y \rightarrow U(1)_{EM}$ (see Section 1.2). This process causes the four electroweak vector boson fields to mix and for three of them to acquire mass. The three massive electroweak bosons (W^\pm and Z^0) mediate the weak interaction, which operates on very small distance scales due to the large mediator masses. In contrast, the electromagnetic interaction has an infinite interaction range due to the fact that the photon is both massless and non-self-interacting.² The breaking of the electroweak symmetry violates the conservation of weak isospin and hypercharge, leaving only the electromagnetic charge ($Q = T_3 + \frac{Y}{2}$) of the $U(1)_{EM}$ symmetry conserved.

The strong interaction is generated by eight real spin-1 fields called gluons (g) that form a linearly independent octet [6,7]. The conserved charge associated with the $SU(3)_C$ symmetry is called color (C). Unlike the electromagnetic interaction, QCD is a non-Abelian gauge theory, giving rise to gluon self-coupling terms and a strong coupling constant (α_s), which approaches zero at high energies and infinity at low energies [8, 9]. Section 1.3 addresses several of the phenomenological implications of this feature.

¹A particle's "handedness," or chirality, is determined by whether the particle transforms in a right- or left-handed representation of the Poincaré group.

² The electromagnetic interaction is an *Abelian* gauge theory, meaning that its gauge transformations commute; this property prevents the photon from carrying electromagnetic charge and, therefore, from interacting with itself.

1.2 SPONTANEOUS SYMMETRY BREAKING AND THE HIGGS MECHANISM

Spontaneous symmetry breaking causes a Lagrangian that is invariant under a symmetry at high energies to not obey that same symmetry at low energies. In the SM, the electroweak symmetry is broken spontaneously via the Higgs mechanism [10–15], as described below.

The electroweak gauge symmetry permits the existence of a complex scalar $SU(2)$ doublet (Φ) with a Lagrangian potential given by:

$$V(\Phi) = \mu^2 \Phi^\dagger \Phi + \lambda (\Phi^\dagger \Phi)^2 \quad (1.2)$$

where Φ^\dagger is the Hermitian conjugate of Φ , and μ and λ are free, measurable parameters. Figure 1.1 illustrates two possible cases for the solution to Equation 1.2. First, if $\mu^2 > 0$, there are no degeneracies in the vacuum state solution, and the vacuum expectation value (VEV) is zero. However, if $\mu^2 < 0$, as is the case observed in nature, then there exists a degeneracy of the minimum of the potential in the complex plane, with a non-zero VEV (measured to be 246 GeV). This degeneracy of the VEV in the complex plane spontaneously breaks the $SU(2)_L \times U(1)_Y$ symmetry of \mathcal{L}_{SM} .

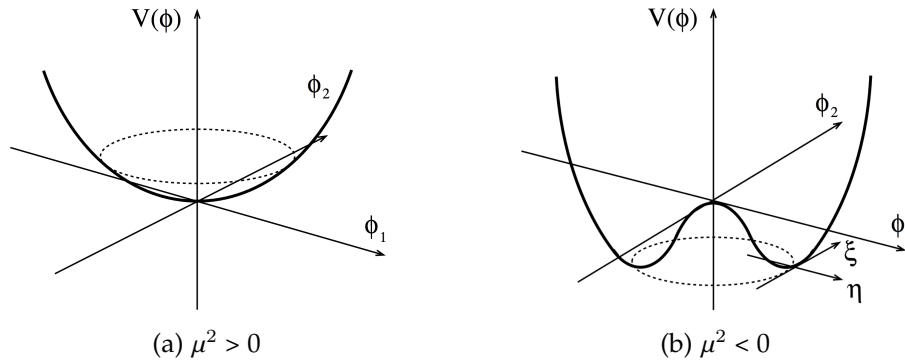


Figure 1.1: Diagram of the Higgs boson potential, $V(\Phi)$, for (a) $\mu^2 > 0$ and (b) $\mu^2 < 0$ [16].

The spontaneous breaking of any local continuous symmetry generates massless fields called Goldstone bosons [17,18]. A simplified description of this mechanism is that, in the ground state, the complex scalar field Φ splits into two real scalar fields, shown as η and ξ in Figure 1.1b. Here, η constitutes the massive Higgs field with mass $m^2 = -2\mu^2$, while ξ represents a massless field in the flat direction of the potential, corresponding to a massless Goldstone boson. Since the Higgs field is a complex doublet, it contains four degrees of freedom; after spontaneous symmetry breaking, the real scalar Higgs field assumes one degree of freedom, and three Goldstone bosons account for the remaining three.

The Higgs mechanism is the process by which the three massless Goldstone bosons mix with the massless $W^{1,2,3}$ and B bosons: three of the four mixed states absorb a Goldstone boson in their longitudinal component, endowing them with mass, and the fourth mixed state remains massless. The resulting mass eigenstates are two oppositely-charged massive vector bosons (W^\pm), one neutral massive vector boson (Z^0), and one massless vector boson (the photon, γ). The photon corresponds to the unbroken $U(1)_{EM}$ symmetry of the ground state SM Lagrangian.

1.3 FERMIONS AND PHENOMENOLOGY

The representations of the SM symmetry group are spin- $\frac{1}{2}$ fermions. The SM classifies fermions as leptons or quarks, each of which contains six different *flavors* of particles organized into three generations. Most interactions in the SM, including the electromagnetic and strong forces, conserve flavor; however, the weak force permits flavor-changing interactions via the W^\pm boson.³ Figure 1.2 outlines the organization and properties of SM particles, including their masses, electromagnetic charges, and spins. Each particle depicted in the figure has an associated *anti-particle* with the same mass but inverted quantum numbers (e.g., opposite sign electric charge).

³ There has been no experimental observation of flavor-changing neutral currents, which would occur if the Z^0 boson mediated flavor-changing processes.

Standard Model of Elementary Particles

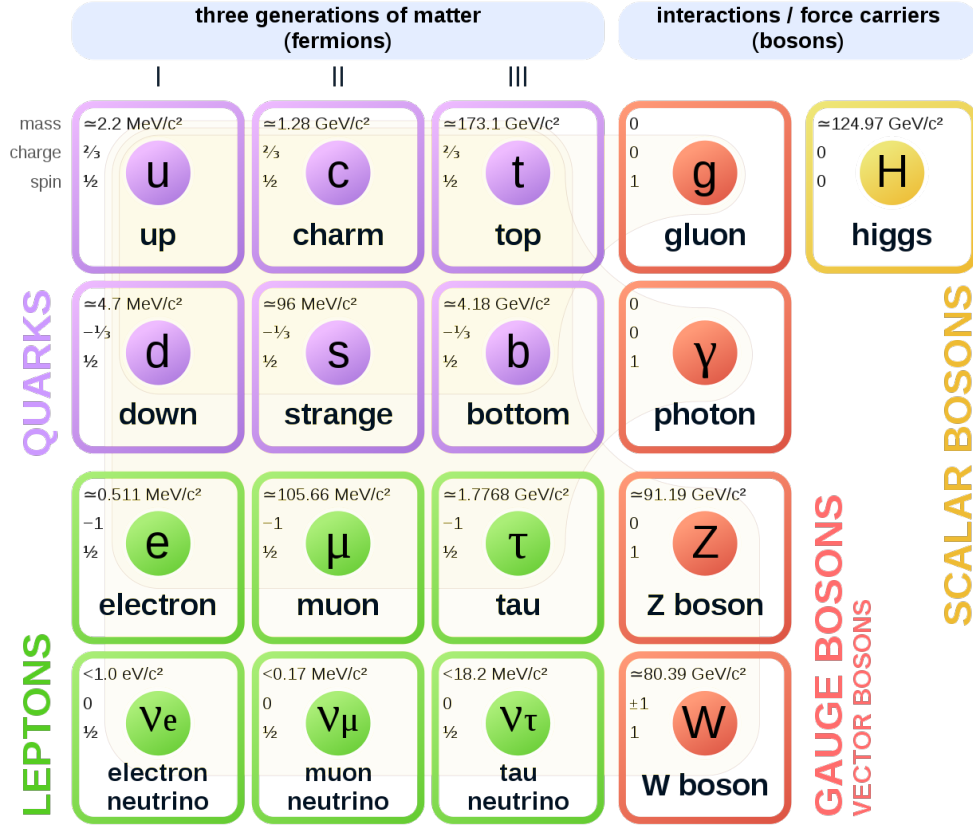


Figure 1.2: Standard Model particle content, including the fermions, gauge bosons, and the Higgs boson. Electromagnetic charges are given in units of elementary charge, e , and spins in units of the reduced Planck constant. Anti-particles are not explicitly depicted, though they are accounted for in the SM.

There are three pairs of oppositely charged leptons (e^- , μ^- , τ^- with anti-particles e^+ , μ^+ , τ^+), which interact via the electromagnetic and weak forces, and three pairs of neutral leptons, the neutrinos (ν_e , ν_μ , ν_τ with anti-particles $\bar{\nu}_e$, $\bar{\nu}_\mu$, $\bar{\nu}_\tau$), which interact via the weak force (SM neutrinos are therefore left-handed).⁴ Each generation of the left-handed negatively charged leptons and the neutrinos are arranged into doublets, while the right-handed positively charged leptons form standalone singlet states. A distinguishing feature of neutrinos, unlike the charged leptons, is that their flavor eigenstates and mass eigenstates are

⁴ The SM does not account for right-handed neutrinos. While the existence of these particles has been theorized, it is not yet experimentally verified [19].

not the same; consequently, neutrinos "oscillate" between flavor states as they propagate through the universe [20].

Quarks interact with all three forces in the SM and are organized into sets of three up-type quarks (u, s, t) and three down-type quarks (d, c, b), where each of the six quark flavors carries both electromagnetic and color charge. Like the leptons, left-handed quarks assemble into weakly interacting doublets.

The running of the strong coupling constant (α_s) compels quarks to exhibit intriguing behavior. Due to their self-coupling, the gluon fields form "flux tubes" that exert a constant force on quarks when stretched. As two quarks get pulled apart, it becomes more energetically favorable to generate a quark-antiquark pair out of the vacuum than to maintain the flux tube. *Color confinement* refers to the property that at low energies, all quarks come in bound, colorless states, called hadrons: mesons contain an even number of quarks (typically a quark-antiquark pair, $q\bar{q}$), while baryons like protons and neutrons contain an odd number. At high energies (and small distances), α_s becomes increasingly small, allowing quarks to move relatively freely – a property called *asymptotic freedom*.

The SM Lagrangian does not contain terms that explicitly endow fermions with mass, as such expressions would violate G_{SM} . Instead, quarks and charged leptons obtain mass via so-called *Yukawa couplings* to the Higgs field, where the mass of a fermion is equal to the product of its Yukawa coupling and the VEV. The SM treats neutrinos as massless, and so far, the mechanism for and magnitudes of neutrino masses are unknown (see Section 1.5).

1.4 EMPIRICAL VALIDATION OF THE STANDARD MODEL

The rise of the SM in the mid-20th century precipitated a cascade of corroborating discoveries and impressive attestations to its predictive power. The charm quark, theorized in 1970 to explain the absence of flavor-changing neutral currents [21], was later identified in 1974 [22,23]. The discovery of the τ lepton (1975) [24] and bottom quark (1977) [25] consol-

idated evidence for a third generation of matter, demystifying the observed CP violation of the weak force, which could not be explained by two generations of matter alone [26]. In 1983, the SPS collider at CERN heralded twin discoveries of the W^\pm [27] and Z^0 [28] bosons, whose masses were compatible with (and even predicted by) constraints on the weak mixing angle established a decade earlier [29]. The subsequent detections of the top quark (1995) [30,31] and tau neutrino (2000) [32] reinforced the durability of the SM. The final piece of the SM puzzle finally slid into place with the 2012 breakthrough discovery of the Higgs boson at the LHC [33,34].

Although the values of the 19 free parameters of the SM can only be determined through direct measurement, many others can be calculated, including cross sections and decay branching ratios. Figure 1.3 demonstrates the remarkable compatibility between the theoretical prediction and experimental measurement of the cross section of various SM processes. At the time of writing this thesis, no known SM parameter has been measured to differ from the theory by more than 5σ , with one notable exception: the CDF Collaboration’s recent, and as yet unconfirmed, measurement of a 7σ deviation from the theoretical W^\pm boson mass [35].

1.5 LIMITATIONS OF THE STANDARD MODEL

Despite its indisputable success, the SM remains an effective field theory, describing only an approximation of our reality (albeit an extraordinarily good one). Several shortcomings of the SM are based on experimental evidence, stemming from incompatibilities with observed phenomena:

- *Gravity* (or lack thereof). Most glaringly, the SM fails to account for the gravitational force.
- *Dark Matter*. The SM provides no particle-level candidate for this elusive form of invisible matter, whose existence is experimentally supported by astrophysical and

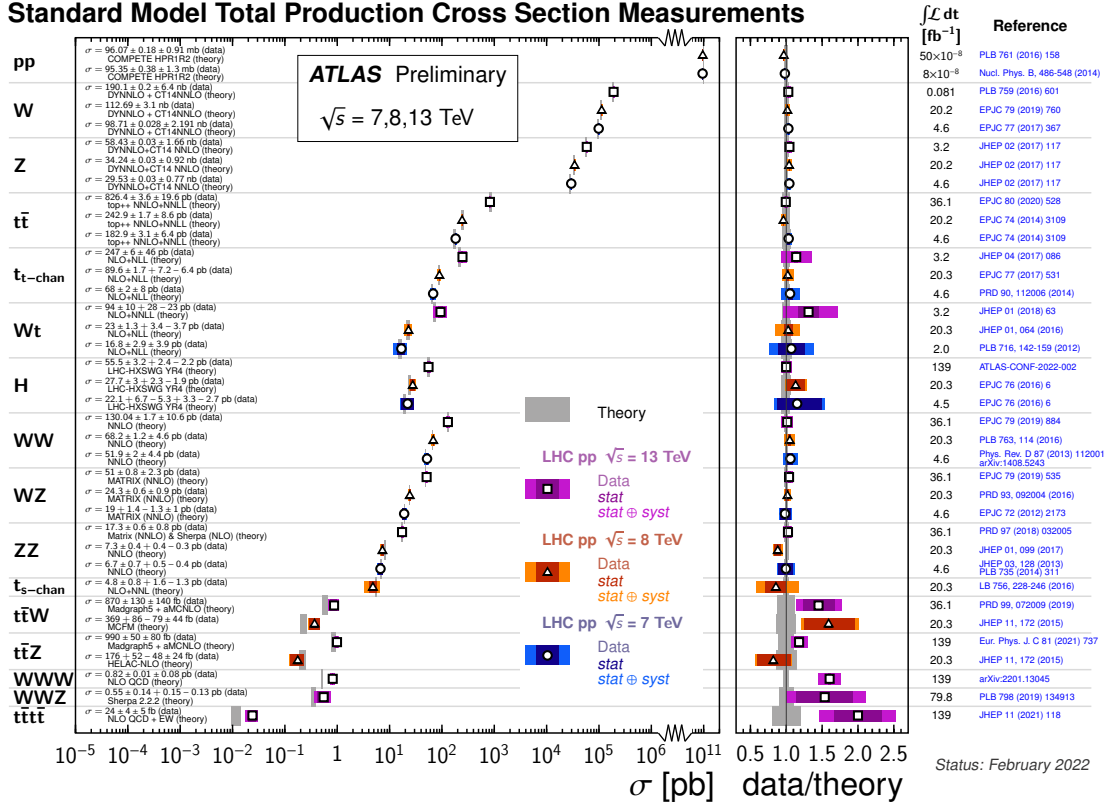


Figure 1.3: Summary of several Standard Model total production cross section measurements performed by the ATLAS Collaboration, corrected for branching fractions, compared to the corresponding theoretical expectations. The right panel shows the ratio of the experimental measurement with respect to theory [36].

cosmological observations, including those of galactic rotation curves [37] and gravitational lensing [38].

- *Matter-Antimatter Asymmetry.* The degree of CP violation in the SM does not account for the vast disparity between the relative abundance of matter and antimatter in the universe.
- *Neutrino Masses.* The SM assumes that neutrinos are massless; however, they must have some non-zero mass to generate the observed effect of neutrino oscillations [20].

The SM also leaves many theoretical – and arguably philosophical – questions unanswered. Many of these questions are rooted in the notion of *naturalness*, which dictates that nature should not be *fine-tuned*, i.e., dimensionless quantities should be roughly the same

order of magnitude. Instances where this is not the case, including some of the following examples, suggest that a more fundamental theory is needed:

- *Hierarchy Problem.* It is not yet understood why the interaction strengths of the four fundamental forces span so many orders of magnitude (the strong force is roughly 40 orders of magnitude stronger than the force of gravity). Chapter 2 discusses the related problem of why the 125 GeV Higgs boson is so light compared to the Planck scale (10^{19} GeV).
- *Grand Unification.* Extensions to the SM posit that, just as the electromagnetic and weak forces unify at high energies, so too do the electroweak and strong forces. However, there appears to be no consistent point of convergence of the strengths of the coupling constants of the three fundamental forces of the SM.
- *Strong CP Problem.* Unlike the weak force, the strong force seems to preserve CP symmetry [39], a feature that appears to emerge from the fine-tuning of a complex phase parameter.
- *Values of Free Parameters.* The 19 free parameters of the SM can only be determined through measurement – not from fundamental principles alone.

These limitations of the SM hint at where new physics may lie and what form it might take. The next chapter introduces supersymmetry, a promising extension to the SM, which has the potential to address several of these questions.

CHAPTER 2:

SUPERSYMMETRY

If I could remember the names of these particles, I would have been a botanist.

— Enrico Fermi

Supersymmetry (SUSY) encompasses a broad class of mathematically elegant theories, with the defining feature generating fermion-boson symmetry [40–46]. The appeal of SUSY extends beyond its mathematical beauty: SUSY proposes a quantum theory of gravity, possibly cures the Higgs mass hierarchy problem, and, in many cases, even introduces a dark matter candidate. Additionally, SUSY modifies the running of the SM gauge couplings such that they miraculously unify at very high energy scales [47–54].

This chapter opens with two notable theoretical motivations for SUSY (Section 2.1). Sections 2.2 and 2.3 discuss some of the distinctive phenomenological features of SUSY, focusing on scenarios that impose the fewest new assumptions while remaining compatible with experimental observation. Finally, Section 2.4 addresses the general features of LLPs, which exist in many varieties of SUSY.

2.1 MOTIVATION FOR SUPERSYMMETRY: TWO PERSPECTIVES

SUSY was not initially devised to address the limitations of the SM; instead, its origins are grounded in the emergent symmetries of a four-dimensional spacetime. Somewhat astonishingly, it was later discovered that SUSY also has the potential to resolve several of the most prominent shortcomings of the SM, including the Higgs boson mass hierarchy problem. This section reviews the historical context of SUSY as a spacetime symmetry, and paints a mathematical picture of SUSY's role in reconciling the hierarchy problem.

2.1.1 SUPERSYMMETRY AS A SPACETIME SYMMETRY

Historically, SUSY gained traction in the second half of the 1970s with the extension of the Poincaré spacetime symmetry into the *super*-Poincaré symmetry [55]. Previously, the consensus view (via the Coleman-Mandula theorem [56]) was that the symmetry group of a consistent four-dimensional QFT must be the product of the Poincaré group and an internal symmetry group (e.g., G_{SM}). However, this "no-go" theorem contains a loophole: it focuses only on *commuting* symmetry generators and fails to account for *anticommuting* symmetry generators. The latter can lead to conserved *supercharges* and a consistent *superalgebra* [55].

Therefore, the underlying foundation of SUSY revolves around the addition of a new spacetime symmetry. Together with the internal symmetry group of the SM, these symmetries come to define the properties and behavior of supersymmetric theories. In the most general case, the anticommuting SUSY generators (Q and its Hermitian conjugate, \bar{Q}) transform fermionic states into bosonic states and vice versa [40–46]. Together, fermion-boson pairs form *supermultiplets*, which are irreducible representations of superalgebra. Since Q commutes with the generators of SM gauge transformations, the fields of each supermultiplet pair have identical mass, degrees of freedom, and SM quantum numbers (except for spin, which differs by $\frac{1}{2}$) [55, 56].

2.1.2 SUPERSYMMETRY AS A SOLUTION TO THE HIERARCHY PROBLEM

The Higgs boson mass hierarchy problem represents one of the most troubling features of the SM: the appearance of extreme fine-tuning [57–60]. To appreciate the source of (and a solution to) this problem, consider the breakdown of the Higgs boson mass-squared (m_H^2) into its Feynman diagram tree ($m_{H,tree}^2$) and loop (Δm_H^2) contributions:

$$m_H^2 = m_{H,tree}^2 + \Delta m_H^2 \quad (2.1)$$

Here, $m_{H,tree}^2$ is a free parameter, and Δm_H^2 subsumes contributions from all particles that interact either directly or indirectly with the Higgs field. The loop contribution of a single SM fermion, f , visualized in Figure 2.1, is described by:

$$\Delta m_{H,f}^2 = -\frac{|\lambda_f^2|}{16\pi^2} \left[2\Lambda_{UV}^2 - \mathcal{O}\left(m_f^2 \ln \frac{\Lambda_{UV}}{m_f}\right) \right] \quad (2.2)$$

where m_f and λ_f are the mass and Yukawa coupling strength of the fermion. Assuming that no source of BSM physics exists, Λ_{UV} corresponds to the Planck scale (10^{19} GeV), and the resulting quantum corrections to m_H^2 are on the order of 10^{38} GeV².

The hierarchy problem arises from the fact that the Planck scale is tremendously greater than the Higgs boson mass, which is on the order of the weak scale ($m_H^2 \sim 10^4$ GeV²). In

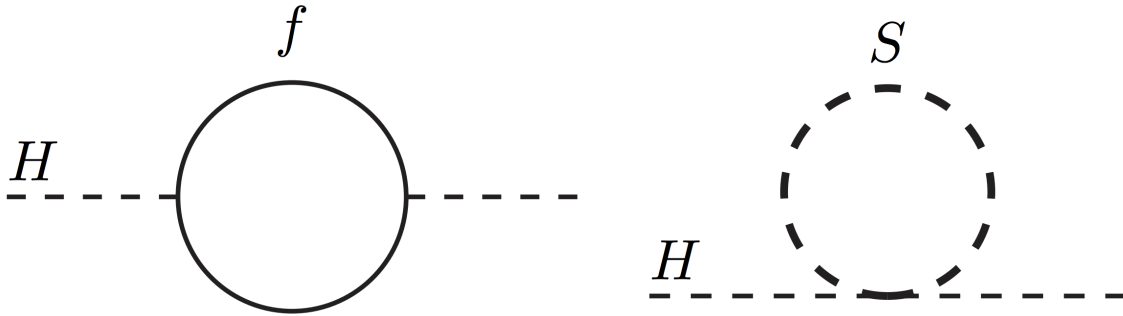


Figure 2.1: Feynman diagram showing the loop contributions from a fermion (left) and scalar (right) in the Higgs boson propagator [61].

the absence of new physics, these vastly disparate hierarchies of scale suggest that $m_{H,tree}^2$ is extremely fine-tuned, deviating from the quadratic corrections by only 1 part in 10^{34} . While the laws of physics do not explicitly prohibit such fine-tuning, the appearance of fine-tuning typically indicates that a theory is incomplete. As the *naturalness strategy* argues, a hidden or misunderstood physical mechanism may introduce terms that cancel out higher-order corrections like those in Equation 2.2.¹

Consider the loop contributions to the Higgs mass calculation provided by a scalar boson, S , shown in Figure 2.1:

$$\Delta\tilde{m}_{H,S}^2 = +\frac{|\lambda_S^2|}{16\pi^2} \left[2\Lambda_{UV}^2 - \mathcal{O}\left(m_S^2 \ln \frac{\Lambda_{UV}}{m_S}\right) \right] \quad (2.3)$$

where m_S is the scalar mass and λ_S is its coupling parameter. The expressions for $\tilde{m}_{H,S}^2$ and $\Delta m_{H,f}^2$ in Equations 2.2 and 2.3 have opposite signs; therefore, the Higgs boson mass contributions of a fermion-scalar pair would cancel each other out if $\lambda_f = \lambda_S$ and $m_f = m_S$, and the hierarchy problem would evaporate. At face value, introducing a set of particles with precisely the right parameters appears to necessitate even further fine-tuning; however, it is possible to bring about this effect very naturally – through the introduction of a new *spacetime (super)symmetry*.

2.2 THE MINIMAL SUPERSYMMETRIC STANDARD MODEL

Given the unwieldy (and possibly infinite) cornucopia of models that might satisfy SUSY, a reasonable and popular choice of model is the Minimal Supersymmetric Standard Model (MSSM). The MSSM introduces the fewest number of new particles required to accommodate SUSY [62, 63].

¹ Several hierarchy problems throughout history have been solved this way. For example, the electron mass includes a self-coupling contribution of $\gtrsim 100$ GeV (corresponding to an upper bound of the electron radius of $\lesssim 10^{-18}$ m), which is many orders of magnitude larger than its observed mass of 0.511 MeV. When accounting for the positron, the self-coupling contributions cancel out.

In the MSSM, particles and their supersymmetric partners, or *superpartners*, form three types of supermultiplets (this is true for many SUSY scenarios). The first arrangement, a *chiral supermultiplet*, consists of a spin- $\frac{1}{2}$ fermion and a complex spin-0 scalar boson. The second, a *gauge supermultiplet*, contains a spin-1 gauge boson and a spin- $\frac{1}{2}$ fermion.² A third supermultiplet incorporates the gravitational interaction: the *gravity supermultiplet* includes a spin-2 graviton and its spin- $\frac{3}{2}$ superpartner, the gravitino.

For most SM particles, the MSSM introduces a single new superpartner³ – the two exceptions are the addition of a gravity supermultiplet and the inclusion of a second Higgs boson supermultiplet (see below). Typically, bosonic superpartners assume a prefix *s-* (e.g., *quarks* \leftrightarrow *squarks*), while fermionic superpartners receive the suffix *-ino* (e.g., *Higgs* \leftrightarrow *higgsino*). The MSSM particle content and supermultiplets are summarized in Table 2.1.

As their name indicates, SM gauge bosons form a gauge supermultiplet with spin- $\frac{1}{2}$ fields. The superpartners correspond to the generators of the unbroken local gauge symmetry group, G_{SM} : the gluons, $W^{1,2,3}$ bosons, and B boson form supermultiplets with gluinos, winos, and the bino, respectively. Since SM fermions violate parity maximally, they cannot partner with a gauge boson; instead, they form chiral supermultiplets with complex scalar fields. Left-handed fermions assume $SU(2)_L$ doublets with their superpartners, while right-handed fermions constitute singlet supermultiplets.

The Higgs boson, a scalar, also forms a chiral supermultiplet with a spin- $\frac{1}{2}$ fermion. However, a single Higgs boson supermultiplet adds non-renormalizable terms to the Lagrangian, causing a gauge anomaly [61]. The MSSM addresses this issue by extending the Higgs sector to include two complex doublets with $Y = \pm\frac{1}{2}$, where the non-renormalizable terms of the two Higgs boson supermultiplets effectively cancel out. The doublet corre-

² Fermions in the gauge supermultiplet must have right- and left-handed components that transform identically under gauge transformations, while those in a chiral supermultiplet do not. This property arises because, like their superpartner gauge bosons, fermions of the gauge supermultiplet must transform under the adjoint representation of the gauge group [61].

³ There are no standalone supermultiplets in the SM.

| Chiral Supermultiplets | | | |
|--------------------------------|--------------------------------------|--------------------------------------|--|
| Content | Spin-$\frac{1}{2}$ | Spin-0 | $SU(3)_C, SU(2)_L, U(1)_Y$ |
| quarks – squarks | (u_L, d_L) | $(\tilde{u}_L, \tilde{d}_L)$ | $(3, 2, \frac{1}{6})$ |
| | \bar{u}_R | \tilde{u}_R^* | $(3, 1, -\frac{2}{3})$ |
| | \bar{d}_R | \tilde{d}_R^* | $(3, 1, \frac{1}{3})$ |
| leptons – sleptons | (ν_L, e_L) | $(\tilde{\nu}_L, \tilde{e}_L)$ | $(1, 2, -\frac{1}{2})$ |
| | \bar{e}_R | \tilde{e}_R^* | $(1, 1, 1)$ |
| Higgsinos – Higgs | $(\tilde{H}_u^+, \tilde{H}_u^0)$ | (H_u^+, H_u^0) | $(1, 2, \frac{1}{2})$ |
| | $(\tilde{H}_d^0, \tilde{H}_d^-)$ | (H_d^0, H_d^-) | $(1, 2, -\frac{1}{2})$ |
| Gauge Supermultiplets | | | |
| Content | Spin-1 | Spin-$\frac{1}{2}$ | $SU(3)_C, SU(2)_L, U(1)_Y$ |
| gluon – gluino | g | \tilde{g} | $(8, 1, 0)$ |
| W bosons – Winos | W^\pm, W^0 | $\tilde{W}^\pm, \tilde{W}^0$ | $(1, 3, 0)$ |
| B boson – Bino | B | \tilde{B} | $(1, 1, 0)$ |
| Gravity Supermultiplets | | | |
| Content | Spin-2 | Spin-$\frac{3}{2}$ | $SU(3)_C, SU(2)_L, U(1)_Y$ |
| graviton – gravitino | G | \tilde{G} | $(1, 1, 0)$ |

Table 2.1: The chiral, gauge, and gravity supermultiplets of the MSSM with their representations in $SU(3)_C \times SU(2)_L \times U(1)_Y$. Only the first generation of quarks and leptons is shown; the same configuration is assumed for the second and third generations.

sponding to $Y = +\frac{1}{2}$ (H_u^+ and H_u^0) gives mass to the up-type quarks, while the doublet corresponding to $Y = -\frac{1}{2}$ (H_d^0 and H_d^-) does so for the down-type quarks and charged leptons. The SM Higgs boson, h^0 , represents a linear combination of the H_u^0 and H_d^0 states.

The SM prohibits proton decay because no renormalizable Lagrangian terms break the conservation of baryon number (B) or lepton number (L). Indeed, there exists no experimental evidence for this process [64]. However, the MSSM allows for renormalizable B - and L -violating terms. To ensure the phenomenological consistency of the MSSM with the

observation that the proton is stable, an additional symmetry, R-parity (P_R), is introduced:

$$P_R = (-1)^{3(B-L)+2s} \quad (2.4)$$

where s is particle spin [65]. SM particles, including the scalar Higgs boson and the graviton, have $P_R = +1$, while SUSY particles have $P_R = -1$.

By definition, the MSSM conserves R-parity, sparking several consequences. First, SM and SUSY particle states cannot mix; therefore, the lightest SUSY particle (LSP) is stable and is generally considered a promising dark matter candidate. Additionally, in collisions, SUSY particles must be produced in even numbers, usually in pairs; a SUSY particle then cascade decays into lighter states, culminating in a final state with an odd number of LSPs, typically one. While R-parity violating (RPV) models exist, they require additional Lagrangian terms and are not part of the MSSM. The model investigated in this thesis assumes R-parity conservation (RPC).

2.3 SUPERSYMMETRY BREAKING

The preceding discussion introduced SUSY as an unbroken symmetry, stipulating that the masses of particles and their superpartners are identical. However, experimental evidence excludes this possibility since a theory with an identical mass spectrum to that of the SM would have already been discovered. Therefore, if SUSY is a genuine symmetry in nature, it must be a broken symmetry.

2.3.1 SOFT SUPERSYMMETRY BREAKING IN THE MSSM

A consequence of SUSY breaking is that particle and superpartner masses no longer agree, preventing the perfect cancellation of the fermion and scalar loop contributions to the Higgs mass. In order to preserve SUSY's ability to solve the hierarchy problem, SUSY breaking must therefore be *soft* [66]. Soft SUSY breaking entails dividing the MSSM La-

grangian into two components. The first subsumes all gauge and Yukawa interactions that preserve SUSY, while the second contains the terms that violate SUSY. In this realization, the divergent $O(\Lambda_{UV}^2)$ corrections to the Higgs boson mass successfully cancel out, leaving a residual mass correction of:

$$\Delta m_H^2 = O\left(\frac{|\lambda|^2 m_{soft}^2}{16\pi^2} \ln \frac{\Lambda_{UV}}{m_{soft}}\right) \quad (2.5)$$

where m_{soft} is the largest mass scale in the SUSY-violating part of the Lagrangian, and λ is its respective Yukawa coupling. Equation 2.5 demonstrates that a softly broken SUSY can still resolve the Higgs mass hierarchy problem, provided that m_{soft} is comparable to the weak scale. Therefore, if SUSY is a valid theory, it should produce particles comparable to or lighter than the SUSY breaking scale, which is generally assumed to be on the TeV scale. Such particles could be within the reach of the LHC.

As a result of SUSY breaking and electroweak symmetry breaking, MSSM superpartners occupy different flavor and mass eigenstates, summarized in Table 2.2. In the case of the Higgs sector, the MSSM's introduction of a second Higgs doublet doubles the number of degrees of freedom from four to eight. Three of these degrees of freedom are associated with the three massless Goldstone bosons produced from the non-zero VEV and absorbed into the longitudinal components of the W^\pm and Z^0 bosons, as described in Section 1.2. The remaining five degrees of freedom mix to form two CP-even neutral scalars (h^0 and H^0), one CP-odd neutral scalar (A^0), and two charged scalars (H^\pm).

The flavor eigenstates of higgsinos, the superpartners of the Higgs bosons, and gauginos, the superpartners of the vector gauge bosons, also mix. The neutral higgsinos ($\tilde{H}_u^0, \tilde{H}_d^0$) and neutral gauginos (\tilde{W}^0, \tilde{B}^0) mix to produce four neutral mass eigenstates called neutralinos ($\tilde{\chi}_{1,2,3,4}^0$). The charged higgsinos ($\tilde{H}_u^\pm, \tilde{H}_d^\pm$) and charged winos (\tilde{W}^\pm) mix to form oppositely charged mass eigenstates called charginos ($\tilde{\chi}_{1,2}^\pm$).

| Names | Spin | P_R | Gauge Eigenstates | Mass Eigenstates |
|--------------|---------------|-------|---|---|
| Higgs bosons | 0 | +1 | $H_u^0 H_d^0 H_u^+ H_d^-$ | $h^0 H^0 A^0 H^\pm$ |
| squarks | 0 | -1 | $\tilde{u}_L \tilde{u}_R \tilde{d}_L \tilde{d}_R$ | same |
| | | | $\tilde{s}_L \tilde{s}_R \tilde{c}_L \tilde{c}_R$ | same |
| | | | $\tilde{t}_L \tilde{t}_R \tilde{b}_L \tilde{b}_R$ | $\tilde{t}_1 \tilde{t}_2 \tilde{b}_1 \tilde{b}_2$ |
| sleptons | 0 | -1 | $\tilde{e}_L \tilde{e}_R \tilde{\nu}_e$ | same |
| | | | $\tilde{\mu}_L \tilde{\mu}_R \tilde{\nu}_\mu$ | same |
| | | | $\tilde{\tau}_L \tilde{\tau}_R \tilde{\nu}_\tau$ | $\tilde{\tau}_1 \tilde{\tau}_2 \tilde{\nu}_\tau$ |
| neutralinos | $\frac{1}{2}$ | -1 | $\tilde{B}^0 \tilde{W}^0 \tilde{H}_u^0 \tilde{H}_d^0$ | $\tilde{\chi}_1^0 \tilde{\chi}_2^0 \tilde{\chi}_3^0 \tilde{\chi}_4^0$ |
| charginos | $\frac{1}{2}$ | -1 | $\tilde{W}^\pm \tilde{H}_u^\pm \tilde{H}_d^\pm$ | $\tilde{\chi}_1^\pm \tilde{\chi}_2^\pm$ |
| gluino | $\frac{1}{2}$ | -1 | \tilde{g} | same |
| gravitino | $\frac{3}{2}$ | -1 | \tilde{G} | same |

Table 2.2: Particle content of new particles introduced by the MSSM, organized by gauge and mass eigenstates. The SM Higgs boson is also included.

Since gluinos carry color charge, they do not mix with the neutralinos and charginos (collectively called electroweakinos). Instead, gluinos form a linearly independent octet, analogous to that of gluons in the SM. Mixing between sfermionic states is allowed but only occurs significantly between third-generation squarks and charged sleptons in the MSSM. Therefore, the model prescribes negligible mixing between the first two generations of sfermions to preserve consistency with the observed lack of flavor-changing neutral currents (FCNCs) in the SM [61].

To properly account for the gravitational interaction, SUSY must be promoted from a global symmetry to a local symmetry. The local theory of SUSY is called *supergravity* [67]. In the absence of SUSY breaking, both the graviton and the gravitino are massless. However, the spontaneous symmetry breaking of SUSY produces a *goldstino*, a particle analogous to the Goldstone bosons produced via electroweak symmetry breaking. The gravitino absorbs the goldstino into its longitudinal component, acquiring mass [68].

2.3.2 GAUGE-MEDIATED SUPERSYMMETRY BREAKING

One of the many open questions surrounding SUSY is the mechanism that causes its breaking. A key constraint on this mechanism is that SUSY breaking cannot be communicated at the tree-level, which would lead to phenomenological inconsistencies like SM particles being heavier than their superpartners [69,70]. Instead, many proposals of soft SUSY breaking mechanisms introduce a "hidden sector" where SUSY breaking occurs; then, "messenger" fields communicate the breaking of SUSY to the "visible sector" of the MSSM via 1- and 2- loop interactions. In Gauge-Mediated SUSY Breaking (GMSB) models [68,71–75], the messenger fields form chiral supermultiplets that couple to both the hidden and visible sectors via the traditional gauge interactions. An attractive feature of GMSB models is that, unlike other SUSY-breaking scenarios, they guarantee minimal flavor violation of sfermions in a way that is consistent with the observed lack of FCNCs in the SM [70].

One of the most distinctive features of GMSB models is that the masses of SUSY particles are related to the scale of their gauge couplings, leading to very heavy squarks (which interact via the strong force) and a very light gravitino (which interacts only gravitationally). In all reasonable SUSY GMSB scenarios, the gravitino is the LSP, with a mass given by:

$$m_{\tilde{G}} = \frac{F}{\sqrt{3}M_P} \quad (2.6)$$

where \sqrt{F} represents the SUSY-breaking scale of the hidden sector and M_P is the Planck mass. Under the standard assumption that $\sqrt{F} \ll M_P$, the gravitino is very light.

In many GMSB models, the next-to-lightest SUSY particle (NLSP) is the lightest neutralino, $\tilde{\chi}_1^0$ [70]. The only permitted RPC decay modes of the NLSP are decays into the gravitino LSP plus an SM particle. The NLSP lifetime, τ_{NLSP} , relates to other parameters of the theory via:

$$\tau_{\text{NLSP}} \propto \frac{F^2}{\kappa_i m_{\text{NLSP}}^5} \quad (2.7)$$

where m_{NLSP} is the NLSP mass, and κ_i is a parameter determined by neutralino mixing. Neutralino NLSPs and their lifetimes are discussed further in Section 2.4.2.

2.4 LONG-LIVED PARTICLES

LLPs are ubiquitous throughout physics theories, including the SM, a variety of SUSY scenarios, and other BSM physics models. For a particle to have a relatively long lifetime, its decay matrix element (\mathcal{M}) must be small, or there must be limited phase space for the decay. This section first discusses how these properties can (and do) emerge in both the SM and SUSY. Next, Section 2.4.1 outlines the experimental landscape of LLP searches at the LHC, and Section 2.4.2 describes the specific SUSY model considered in this thesis.

One mechanism that naturally suppresses \mathcal{M} is the presence of highly virtual intermediate states, which arise when the energy scale of an interaction is much larger than the mass of the decaying particle. For example, in the SM, the weak interaction mediates the decay of the charged pion, π^\pm ($m_{\pi^\pm} = 140$ MeV), which occurs via the exchange of a virtual W^\pm boson ($m_W = 81$ GeV). The lifetime of π^\pm , which is proportional to $m_W^4/m_{\pi^\pm}^5$, is measured to be 26 ns – nine orders of magnitude larger than that of the neutral pion, π^0 , which is permitted to decay via the electromagnetic interaction ($m_\gamma = 0$) [64]. Through a similar mechanism, SUSY GMSB models can feature long-lived NLSPs when $\sqrt{F} \gg m_{\text{NLSP}}$ [76] (see Equation 2.7).

Small couplings also contribute to a small decay matrix element. The measured coupling of the bottom quark (b) to the top quark (t) is very large, leaving very small coupling strengths between the bottom and lighter quarks. However, the bottom quark is only allowed to decay to lighter quarks since a decay to the top quark is kinematically forbidden ($m_b \ll m_t$). The small couplings of permitted decays contribute to the relatively long lifetime of the bottom quark ($\tau_b \sim 10^{-12}$ s) when compared to other heavy quarks ($\tau_t \sim 10^{-24}$ s).

In RPV SUSY, any RPV coupling must be small to preserve the theory's compatibility with the lack of observed proton decay; such a minuscule coupling often engenders LLPs [77].

Limited phase space for a decay typically arises from the existence of an approximate symmetry, where the decay would be forbidden if the symmetry were exact. This phenomenon is usually associated with small mass splittings between particles. In the SM, the weak isospin symmetry between the proton and the neutron, and the particles' corresponding near mass degeneracy, dominates the contribution to the neutron lifetime, which is nearly 10^3 s [64]. Small mass splittings also appear in anomaly-mediated SUSY breaking models, where the lifetime of a particle is inversely related to the difference between near-degenerate particle masses [77].

The mechanisms that give rise to long particle lifetimes, including hierarchies of scale, small couplings, and approximate symmetries, are both fundamental and far-reaching. The pervasiveness of LLPs in the SM, as illustrated in Figure 2.2, suggests that LLPs may also abound in SUSY and other BSM physics models and that dedicated LLP searches play an indispensable role in the search for new physics.

2.4.1 EXPERIMENTAL LANDSCAPE AT THE LHC

LLP searches have risen in prominence over the past several years in response to their theoretical promise, limited experimental coverage, and the lack of direct evidence of (largely prompt) BSM physics. Since LLPs typically produce displaced signatures, they often evade standard prompt-based reconstruction algorithms. Therefore, dedicated collider searches that expand phase space coverage in the long-lived regime are paramount.

A given long-lived signature can arise from many BSM physics models, leading the LLP community at the LHC to adopt a systematic, signature-driven approach to extending the experimental coverage of LLPs. LLP searches typically uphold this model-agnostic philosophy in conjunction with targeting one (or a few) "benchmark" signal models. So

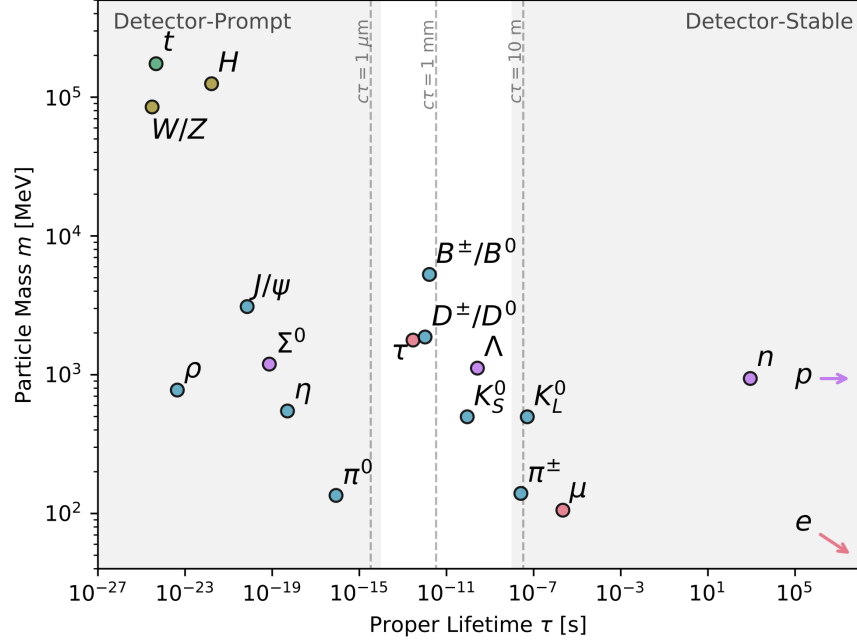


Figure 2.2: Distribution of the masses and proper lifetimes of a variety of SM particles. Shaded regions roughly represent detector-prompt and detector-stable regions of the lifetime space for a particle moving close to the speed of light [77].

far, an extensive list of detector signatures, or *final states*, has been studied. However, an LLP signature that produces displaced diphoton vertices remains unexplored – until now.

Several BSM physics models allow for – and even predict – the presence of LLPs or their children decaying resonantly into two photons, including several varieties of SUSY [76, 78–80] and other exotic BSM models [81–84]. The analysis explored in this thesis targets this signature, implementing a SUSY GMSB simplified model with a long-lived neutralino NLSP as a benchmark signal model.

2.4.2 LONG-LIVED HIGGSINOS

In GMSB SUSY models, the lifetime of a neutralino NLSP ($\tilde{\chi}_1^0$) depends on the SUSY-breaking scale, which is a free parameter (see Equation 2.7). For \sqrt{F} in the $10^2 - 10^3$ TeV range, this signature would likely elude the reach of prompt searches but still mainly produce decays within the volume of an LHC detector like ATLAS.

As discussed in Section 2.3.1, the lightest neutralino, $\tilde{\chi}_1^0$, comprises a mixture of the neutral higgsino, bino, and wino flavor eigenstates; if it carries a dominant component of any of these flavor eigenstates, it is referred to as "higgsino-like," "bino-like," or "wino-like," respectively. A higgsino-like $\tilde{\chi}_1^0$ scenario is highly favored by "natural" SUSY arguments, i.e., as a solution to the Higgs boson mass hierarchy problem. Such a flavor-mixing scheme would engender a nearly-degenerate mass triplet of the lightest three electroweakinos ($\tilde{\chi}_1^\pm$, $\tilde{\chi}_2^0$, and $\tilde{\chi}_1^0$), with the $\tilde{\chi}_1^0$ (with GMSB) having high branching fractions to the Higgs boson or Z boson plus a gravitino LSP.⁴ [76, 85–87].

This thesis targets the direct pair-production of electroweakinos ($\tilde{\chi}_2^0$ and $\tilde{\chi}_1^\pm$) that decay into a long-lived higgsino-like $\tilde{\chi}_1^0$ NLSP, which subsequently decays into the SM Higgs boson or Z boson plus a gravitino. Figure 2.3 illustrates this process, together with the final state of interest: displaced diphoton vertices, via $H \rightarrow \gamma\gamma$ (for the remainder of this thesis, a capital " H " denotes the SM Higgs boson). Interestingly, displaced diphoton and dielectron vertices produce similar detector signatures (see Chapters 5 and 6); therefore, this thesis also targets displaced dielectron final states via $Z \rightarrow ee$. Details of the simulation of this model are described in Chapter 7.

⁴ A wino-like NLSP would also have high branching fractions to the Higgs or Z boson plus a gravitino.

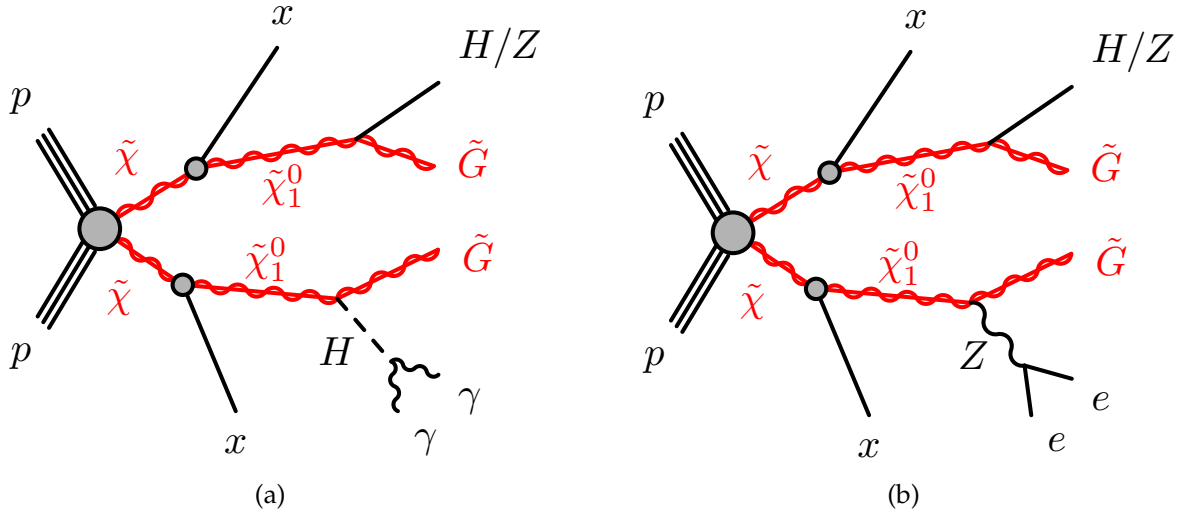


Figure 2.3: Feynman diagram of pair-produced electroweakinos, where $\tilde{\chi} \in (\tilde{\chi}_2^0, \tilde{\chi}_1^\pm)$, and $\tilde{\chi}_1^0$ decays to either $H+\tilde{G}$ or $Z+\tilde{G}$. The analysis targets the displaced $H \rightarrow \gamma\gamma$ (left) and $Z \rightarrow ee$ (right) final states. Decay legs marked with an "x" correspond to soft, light SM fermions (all leptons and quarks except t and b).

PART II:

EXPERIMENT

CHAPTER 3:

THE LARGE HADRON COLLIDER

If I have seen further it is by standing on the shoulders of giants.

— Sir Isaac Newton

The LHC [88] is a circular particle accelerator located at CERN (European Organization for Nuclear Research) in Geneva, Switzerland. Designed to collide counter-circulating proton¹ beams at center-of-mass energies of up to 14 TeV, the 27 km synchrotron has spearheaded the energy frontier of particle physics since operations began in 2010. The LHC employs the infrastructure of several of its predecessors as part of its beam injection chain and occupies the subterranean tunnel, up to 170 m underground, that previously housed the Large-Electron-Positron Collider (LEP).

This chapter discusses principles of accelerator physics (Section 3.1), describes the design of the LHC machine (Section 3.2), and details the key properties and conditions of the proton beams during LHC Run 2, collected from 2015-18, which constitutes the data-taking period for this thesis (Section 3.3).

¹ The LHC is also capable of colliding heavy ions, including lead.

3.1 ACCELERATOR PHYSICS

The LHC seeks to maximize the center-of-mass energy and number of pp collision events to access potential new physics at high energy scales and facilitate the study of extremely rare processes. The number of events of a process α produced in a series of collisions is given by:

$$N_\alpha = \sigma_\alpha \times \mathcal{L} = \sigma_\alpha \int L(t) dt \quad (3.1)$$

where the cross section, σ_α , corresponds to the probability of process α to occur; the integrated luminosity, \mathcal{L} , is proportional to the total number of collisions; and the instantaneous luminosity, L , represents the intensity of the beam collisions. At the LHC, the unit of cross section is given in barns (b), equal to 10^{-28}m^2 , and that of integrated luminosity in inverse barns (b^{-1}) (note that their product is dimensionless). Therefore, maximizing N_α involves maximizing both the data-taking time period and the instantaneous luminosity.

The instantaneous luminosity can be broken down as follows:

$$L = \frac{n_b n_1 n_2 f_{rev}}{2\pi \sigma_x \sigma_y} \quad (3.2)$$

where n_b is the total number of bunches per beam, n_1 and n_2 are the number of particles per bunch for each beam, f_{rev} is the revolution frequency, and σ_x and σ_y characterize the horizontal and vertical components of the beam width. Equation 3.2 demonstrates the importance of engineering densely packed and highly-focused proton beams.

3.2 LHC DESIGN

The LHC proton beams begin as hydrogen ion (H^+) gas, which is accelerated to 50 MeV by a linear accelerator (LINAC) and stripped of its electrons. The protons then travel through a series of accelerators that gradually increases their energy: a Booster, Proton Synchrotron

(PS), and Super Proton Synchrotron (SPS) sequentially accelerate the protons to 1.4 GeV, 25 GeV, and 450 GeV, respectively. The beams from the SPS are injected into the LHC ring, where the final energy ramp-up occurs. A schematic of these accelerator systems appears in Figure 3.1.

The primary components of the LHC are the radio frequency (RF) cavities, which accelerate the beams using oscillating electric fields, and the superconducting magnets, which steer and focus the beams. In the LHC, the 400 MHz RF cavity oscillations generate 2.5 ns "buckets," or points of stable equilibrium, where the protons reside. The protons are arranged such that one out of every ten buckets is filled; this constitutes a proton "bunch," separated from its neighbors by 25 ns.

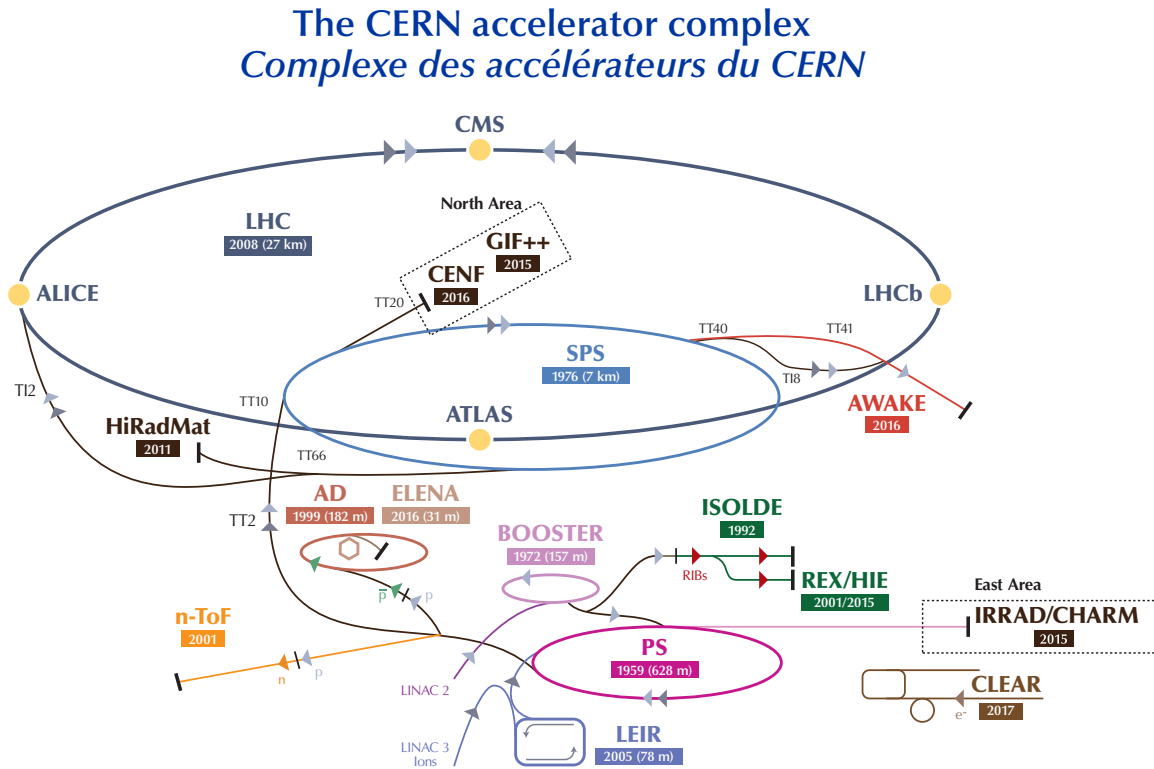


Figure 3.1: The accelerator complex at CERN, including the LINAC, Booster, PS, SPS, and LHC [89].

The LHC superconducting magnets comprise superconducting Niobium-Titanium coils cooled by superfluid helium at 1.4 K. The magnets can be divided into two main groups: dipole magnets and multipole magnets. Dipole magnets produce vertical fields, which provide a centripetal force that bends the proton beams around the collider's arcs. Given the spatial constraints of the LHC tunnel, originally designed for LEP, the dipole magnets adopted a novel "twin-bore" design. This construction delivers a uniform magnetic field in opposite directions to each distinct beam, and together, the two beams share a single cryostat. As the beams approach a collision point, a series of focusing quadrupole magnets squeeze them for optimal collision conditions. Several higher-order multipole magnet systems also correct and fine-tune the optical properties of the beams.

The roughly circular LHC consists of eight 500 m long straight sections connected by eight arcs. Four straight sections contain beam cleaning, beam injection, and beam dump sites; at the center of each of the remaining four, the beams cross and collide at interaction points (IPs). Each IP is surrounded by one of four independent LHC experiments: ATLAS, CMS, LHCb, or ALICE.

3.3 RUN 2 BEAM CONDITIONS

Throughout Run 2, the LHC operated with a center-of-mass energy of 13 TeV, a nominal bunch crossing rate of 40 MHz, and a peak instantaneous luminosity of $2.1 \times 10^{34} \text{ cm}^{-2} \text{ s}^{-1}$. LHC data-taking periods are organized into "runs," constituting a single LHC fill, run, and dump cycle. A typical run, not to be confused with the four-year-long *Run 2*, lasts approximately 24 hours and contains roughly 3000 proton bunches per beam with 10^{11} protons per bunch at the beginning of a fill.

Operating at such a high instantaneous luminosity generally prompts multiple pp collisions per bunch crossing. The distribution of pileup, defined as the mean number of interactions per bunch crossing, is shown for Run 2 in Figure 3.2. Pileup levels vary year-

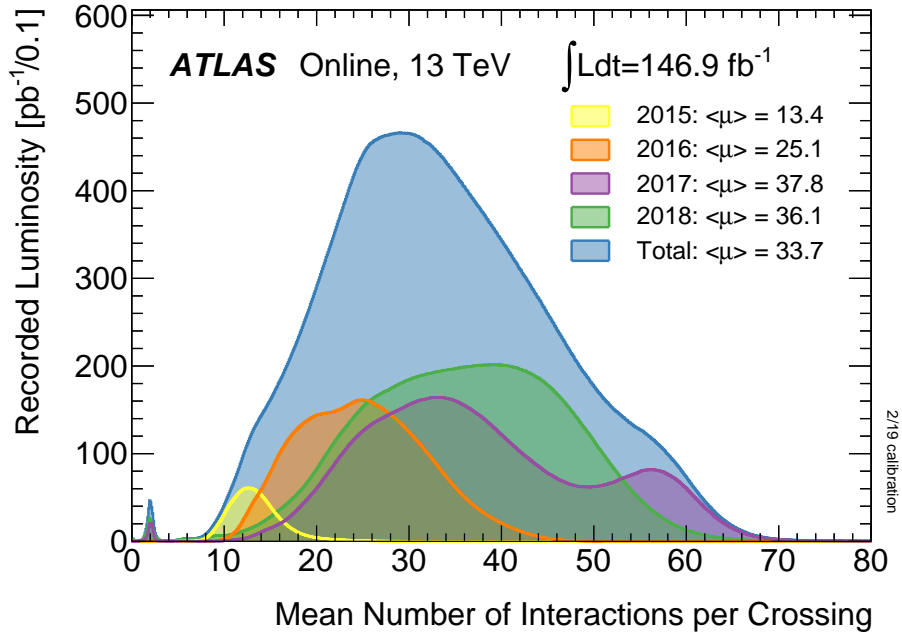


Figure 3.2: Mean number of pp collisions per bunch crossing, weighted by integrated luminosity, during LHC Run 2 [90].

to-year, run-to-run, and even within a single fill, as the number of protons per bunch tapers throughout a run. High-pileup conditions, like those throughout Run 2, precipitate extensive data reconstruction and analysis challenges, which are discussed in various contexts throughout this thesis.

The size of the beams also influences observable features in the data. The collision *beamspot* – the position parallel to the beams where pp collisions occur – has a length² on the order of 100 mm. The location of a particular pp collision within the beamspot can subtly, though measurably, impact the reconstruction of the event (a relevant example is given in Section 6.1.1).

The structure of the beams – proton bunches separated by 25 ns – is actually more complex than previously conveyed, since spillover from nominal RF buckets into neighboring buckets can produce so-called "satellite" bunches [91]. This phenomenon is illustrated in Figure 3.3. After the nominal bunch (at $t = 0$), satellite bunches occurring at ± 5 ns contain

² The standard deviation of pp collision positions in the direction parallel to the beams is typically closer to 40 mm, and the total length of the beamspot along that same direction is around 300 mm.

the most protons, followed by those at ± 10 ns (this pattern is related to the fact that SPS RF cavities operate at 200 MHz, producing buckets with 5 ns spacing). Although suppressed by a factor of $\geq 10^5$ with respect to the nominal bunch, collisions between satellite bunches produce striking and often irreducible signatures at the LHC [92, 93].

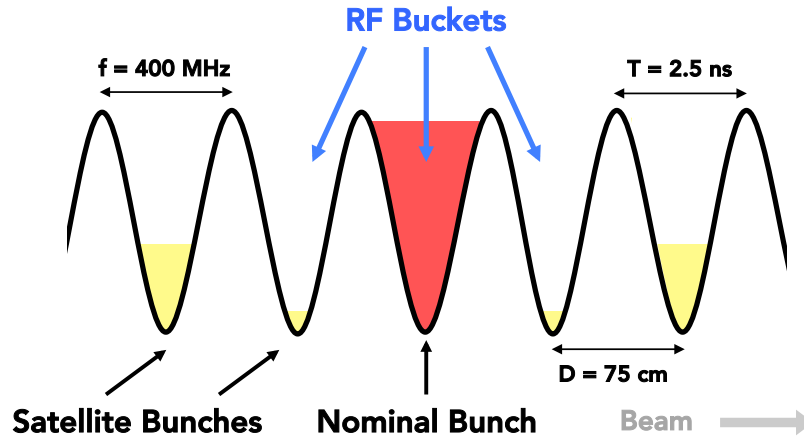


Figure 3.3: Diagram of LHC proton bunch structure, including the RF cavity buckets, the nominal bunch, and satellite bunches.

CHAPTER 4:

THE ATLAS DETECTOR

Art is I; science is we.

— Claude Bernard

The ATLAS detector [94], located at one of the four IPs on the LHC, employs a wealth of strategies and technologies to precisely measure the products of pp collisions. The design of the detector was informed by several factors, including the generations of particle detectors that came before it, the unprecedented energy scale and high-radiation environment of the LHC, and the overarching physics goals of the high-energy particle physics community. The three primary physics objectives used to tailor and optimize the detector were the discovery of the Higgs boson, high precision tests of the SM, and searches for BSM physics. In this sense, ATLAS is adaptable, flexible, and for general-purpose use, capable of performing a variety of measurements across a broad range of energy scales and collision topologies.

The cylindrical detector spans 44 m in length and 25 m in diameter – the largest of the LHC experiments – and weighs approximately 7000 metric tons. ATLAS comprises three main detecting subsystems: the Inner Detector (ID) tracks the trajectories of charged particles, the calorimeters measure the energies of particles, and the muon spectrometer

(MS) delivers information critical to the measurement and identification of muons. Auxiliary ATLAS subsystems, including superconducting magnets, forward detectors, and the trigger system, further support and enable ATLAS measurements. Figure 4.1 shows a diagram of the ATLAS detector, and Table 4.1 outlines the overall performance standards and angular coverage of its subsystems.

This chapter summarizes the construction and performance of the ATLAS detector, beginning with an overview of the detector geometry (Section 4.1), followed by a description of the ATLAS subsystems (Sections 4.2-4.8). The Liquid Argon (LAr) calorimeter (Section 4.3), the measurements of which play an integral role in this thesis, is discussed more thoroughly.

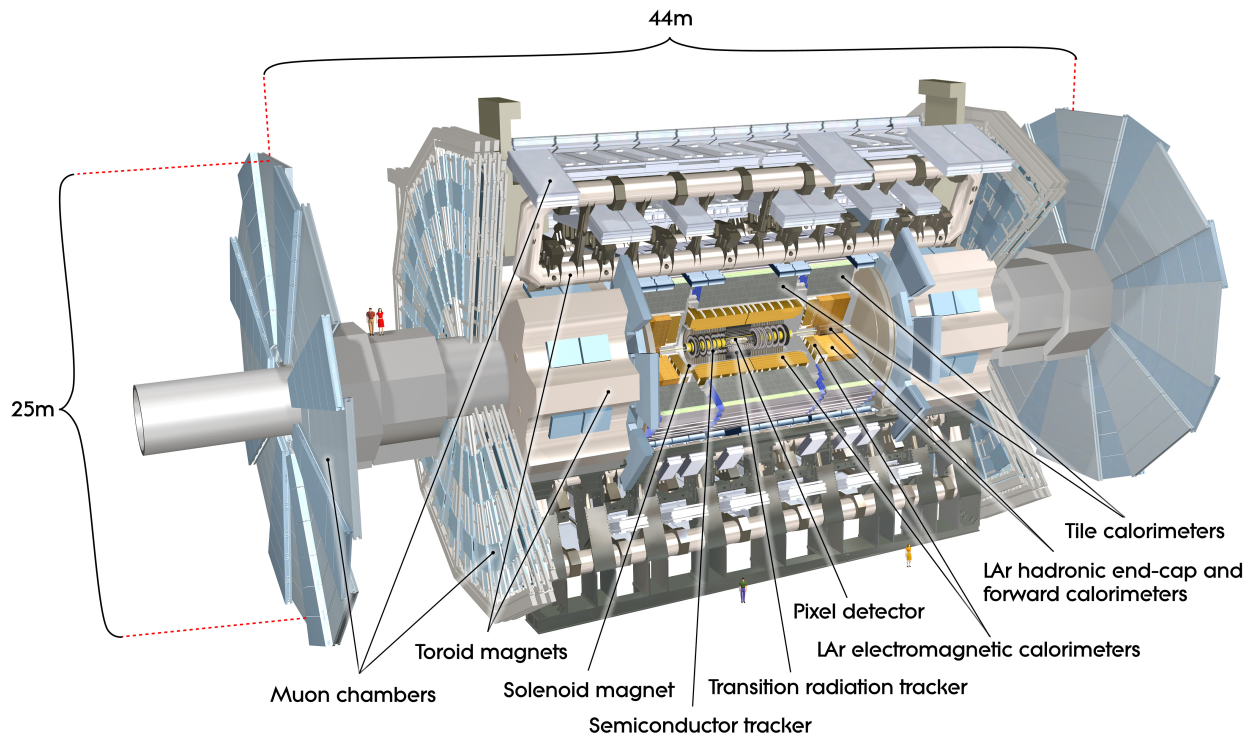


Figure 4.1: Diagram of the ATLAS Detector [94].

| Detector Component | Required Resolution | η Coverage | |
|-----------------------------|---|-----------------|------------|
| | | Measurement | Trigger |
| Tracking | $\frac{\sigma_{p_T}}{p_T} = 0.05\% p_T \oplus 1\%$ | ± 2.5 | - |
| Electromagnetic Calorimetry | $\frac{\sigma_E}{E} = 10\%/\sqrt{E} \oplus 0.7\%$ | ± 3.2 | ± 2.5 |
| Hadronic Calorimetry | | | |
| Barrel and End-Cap | $\frac{\sigma_E}{E} = 50\%/\sqrt{E} \oplus 3\%$ | ± 3.2 | ± 3.2 |
| Forward | $\frac{\sigma_E}{E} = 100\%/\sqrt{E} \oplus 10\%$ | (3.1, 4.9] | (3.1, 4.9] |
| Muon Spectrometry | $\frac{\sigma_{p_T}}{p_T} = 10\% \text{ at } p_T = 1 \text{ TeV}$ | ± 2.7 | ± 2.4 |

Table 4.1: ATLAS subsystem design resolutions and η coverage. The values of transverse momentum (p_T) and energy (E) are given in units of GeV [94].

4.1 COORDINATE SYSTEM AND GEOMETRY

ATLAS employs a right-handed cylindrical coordinate system, where the origin is the nominal IP, the z -axis lies along the beam pipe, and the $x - y$ (transverse) plane lies perpendicular to the beamline (see Figure 4.2a). The transverse components of particle four-vectors, including transverse momentum (p_T) and transverse energy (E_T), play a crucial role in event reconstruction: since the net p_T of the colliding beams is zero, the net p_T of the collision products must also be zero. The quantity of missing transverse energy (E_T^{miss} , verbalized as "MET") corresponds to the magnitude of the net negative transverse momentum of the collision products (see Section 5.7 and Equation 5.2); high values of E_T^{miss} can indicate the presence of a particle or particles invisible to ATLAS, including those from the SM (like neutrinos) and those in BSM physics models.

The angular coordinates of ATLAS include the azimuthal angle, ϕ , and pseudorapidity, η , which can be expressed in terms of the polar angle, θ :

$$\eta \equiv -\ln \left[\tan \left(\frac{\theta}{2} \right) \right]. \quad (4.1)$$

Figure 4.2 illustrates the orientation of the ATLAS coordinate system superimposed on the detector and shows a comparison between η and θ values. There are two key advantages to using η instead of θ : first, unlike θ , η is invariant under Lorentz boosts, making η a highly favorable angular measurement for the relativistic products of pp collisions; second, in the high-energy limit, the products of hadron collisions tend to be distributed roughly uniformly in η . Distances between physics objects are expressed in terms of their angular separation, ΔR :

$$\Delta R \equiv \sqrt{\Delta\phi^2 + \Delta\eta^2}. \quad (4.2)$$

The underlying geometrical structure of the detector varies with $|\eta|$. The following rule is generally true for the structure of most ATLAS subsystems: at low- $|\eta|$, long cylindrical "barrels" surround the beamline and IP; at high- $|\eta|$, "end-caps" lie parallel to the transverse plane, much like the bases of a cylinder. The terms "central" and "forward" refer to detector regions or particles produced with relatively low- and high- $|\eta|$, respectively.

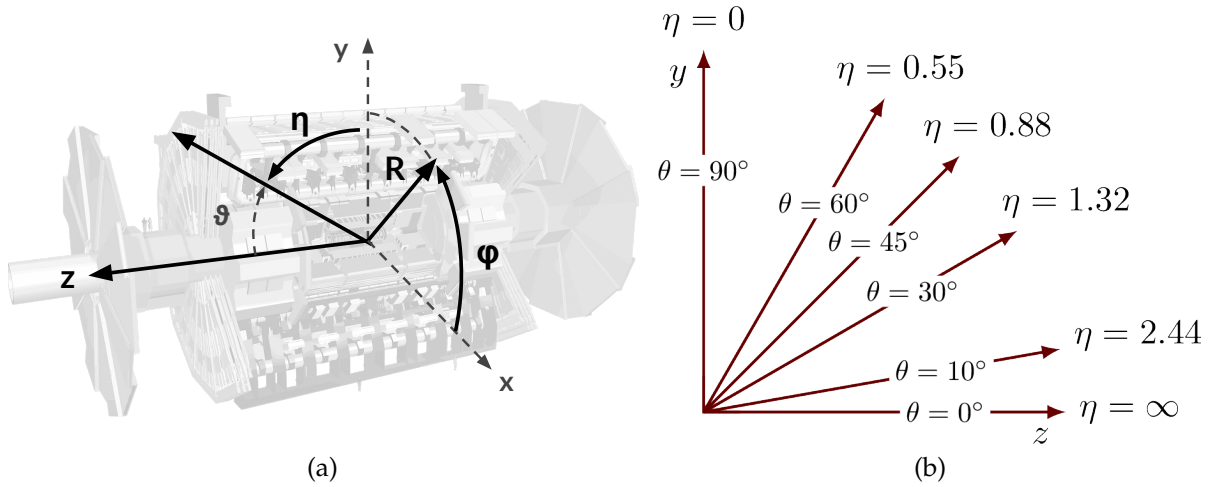


Figure 4.2: The ATLAS coordinate system (a) projected on top of a diagram of the detector and (b) comparing values of θ and η [94].

4.2 INNER DETECTOR

As the subsystem closest to the beamline, the ID [95] provides measurements of charged particle trajectories immediately after they are produced in pp collisions. A roughly 2 T solenoid magnetic field (see Section 4.6) permeates the ID volume, bending the paths of charged particles as they traverse the detector. Complex pattern recognition algorithms reconstruct the detector hits to determine meaningful physical quantities, including the trajectory, momentum, and charge of particles; the positions of collision and decay vertices; and information related to particle identification. The ID is composed of three subdetectors that include, in order of increasing radii, the pixel detector, the semiconductor tracker (SCT), and the transition radiation tracker (TRT). Figure 4.3 shows a diagram of the ID structure, and Table 4.2 outlines the resolutions, number of channels, and pseudo-rapidity coverage of each ID subdetector.

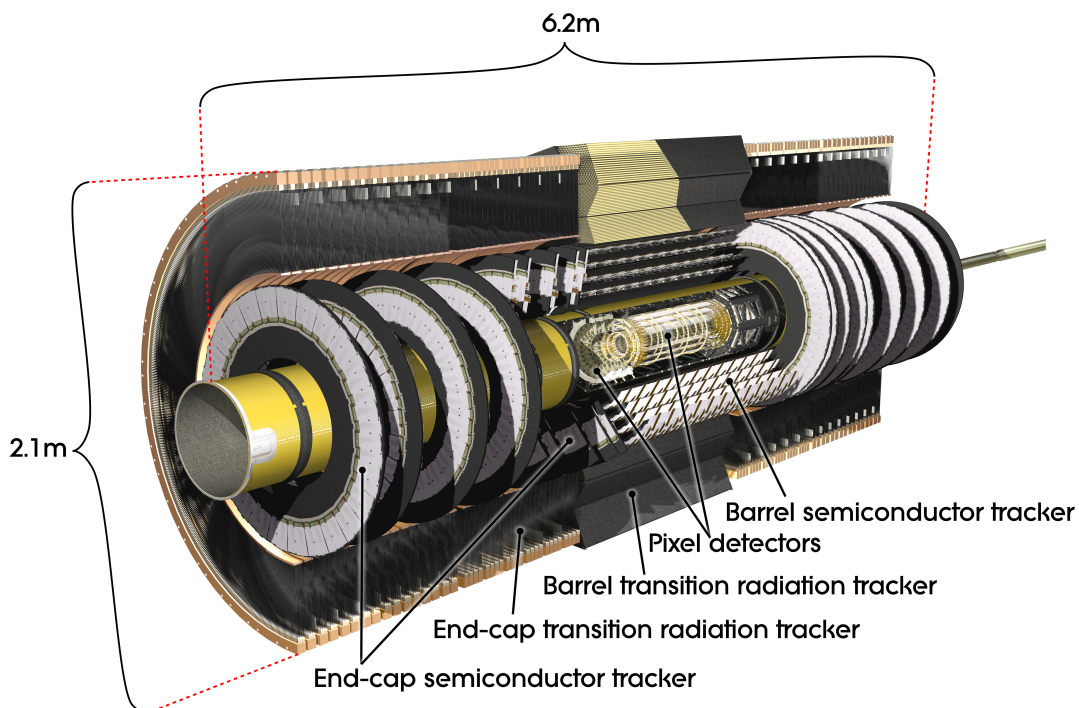


Figure 4.3: Diagram of the ATLAS Inner Detector, including the barrel and end-cap layers of the pixel, SCT, and TRT subdetectors [94].

| System | Description | Resolution (μm) | Channels (10^6) | $ \eta $ coverage |
|--------|-----------------------|------------------------------|---------------------|-------------------|
| Pixel | IBL | $R\phi = 12, z = 66$ | 16 | ± 2.5 |
| | Barrel Layers | $R\phi = 12, z = 66$ | 81 | ± 1.7 |
| | End-cap Disks | $R\phi = 12, R = 77$ | 43 | 1.7-2.5 |
| SCT | Barrel Layers | $R\phi = 16, z = 580$ | 3.2 | ± 1.4 |
| | End-cap Wheels | $R\phi = 16, R = 580$ | 3.0 | 1.4-2.5 |
| TRT | Axial Barrel Straws | 170 (per straw) | 0.1 | ± 0.7 |
| | Radial End-cap Straws | 170 (per straw) | 0.32 | 0.7-2.5 |

Table 4.2: Resolution, number of channels, and pseudorapidity coverage of the various components of the ID. The resolutions quoted are typical values (the precise resolution in each detector depends on $|\eta|$) [95].

The pixel detector consists of 140 million n-type silicon semiconductor sensors that provide four high-precision space-point measurements of charged particle trajectories for tracks with $|\eta| < 2.5$. The initial construction included three concentric cylindrical detectors in the barrel, with radii between 50 and 123 mm, as well as four transverse disks in each of the two end-caps at longitudinal distances between $|z| = 110$ and 200 mm. In 2014, a fourth barrel layer, called the Insertable B-Layer (IBL) [96] – named for its importance in identifying secondary vertices associated with B-hadrons – was added at a radius of roughly 33 mm. This additional layer provides improved vertex identification to compensate for increasing Run 2 pileup levels and mitigates the effects of radiation damage to the other pixel layers. Each sensor is $50 \times 250 \mu\text{m}$ in the IBL and $50 \times 400 \mu\text{m}$ in all other layers.

At intermediate radii, the SCT includes 6.2 million readout channels and provides four precision measurements per particle track. The SCT includes four cylindrical barrels with radii ranging from 299 mm to 514 mm and nine disks in each end-cap at distances between 853 mm and 2721 mm from the IP. Employing the same fundamental silicon technology as the pixel detector, the SCT has larger sensors, which form $126 \text{ mm} \times 80 \mu\text{m}$ strips. Each layer of the SCT contains two sublayers of these strips at a relative stereo angle of 40 mrad, a strategy that allows for sufficient spatial resolution in the z -direction.

The TRT, the outermost layer of the ID, comprises approximately 370,000 gas-filled straw tubes and provides 36 hits per particle track. A gold-plated tungsten wire running through the center of each 4 mm diameter straw collects the products of ionization signals. In the barrel section, 144 cm long tubes are oriented parallel to the beamline, and in the end-cap, 37 cm long tubes are arranged radially into disks. TRT spatial measurements combine the known location of each straw with the drift time of each signal, leading to an overall precision of $170\ \mu\text{m}$ per straw. Each TRT readout channel also provides two independent thresholds to aid particle identification: hits passing only the lower threshold typically correspond to hadrons, while those passing the higher threshold may indicate the presence of an electron.¹

The design of the ID balances precision, radiation hardness, and material budget. Combining precise spatial measurements at small radii with a high multiplicity of hits at larger radii delivers a robust ID subsystem, which can deliver tracking measurements even if one of the three subdetectors fails.

4.3 LIQUID ARGON CALORIMETER

The LAr calorimeter [97] provides electromagnetic (EM) calorimetry for $|\eta| < 3.2$ and hadronic calorimetry for $1.5 < |\eta| < 4.9$. The sampling calorimeter contains cryogenically cooled LAr interspersed between layers of various absorber materials. Key advantages of using LAr as the active material include its linear energy response, high radiation tolerance, and chemical stability when adequately purified. Together, these characteristics ensure reliable and sustainable detector performance. The LAr calorimeter is partitioned into several different sections: the electromagnetic barrel (EMB), two electromagnetic end-caps (EMECs), two hadronic end-caps (HECs), and two forward calorimeters (FCals).

¹ As electrons pass through the TRT, they emit transition radiation in the form of photons, which leads to higher ionization signals than those left by hadrons.

4.3.1 ELECTROMAGNETIC CALORIMETER

The EM calorimeter comprises the EMB and the two EMECs. The EMB (EMECs) covers $|\eta| < 1.475$ ($1.375 < |\eta| < 3.2$) and contains over 110,000 (76,000) readout channels. Residing in a single cryostat, the EMB is divided into two half-barrels, each 3.2 m long with inner and outer radii of approximately 1.4 and 2 m. The EMECs, each of which shares a separate cryostat with one HEC and one FCal module, are 63 cm deep and have inner and outer radii of 0.33 and 2.1 m.

Layers of liquid argon, the lead absorber, and electrode plates are arranged into an accordion shape, as depicted in Figure 4.4. This unique construction provides continuous coverage in azimuth and allows the detector to support itself, without the need for any additional mounting structure that might impede detector measurements. The electrodes

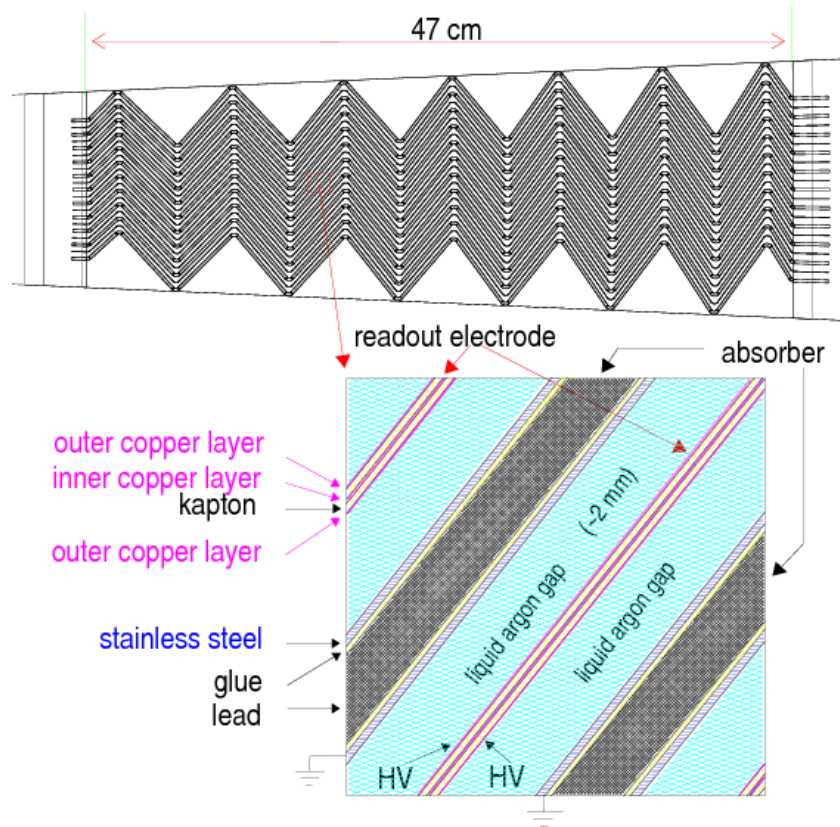


Figure 4.4: Transverse slice of the LAr EM calorimeter, illustrating the accordion geometry (top) and close-up view of liquid argon, lead, and electrode layers (bottom) [97].

consist of multilayer copper-Kapton plates that run through the center of the LAr-filled gap between the absorbers. Each side of the electrode is powered independently – a redundancy feature that ensures that half of the signal may still be recovered even if one side fails. In the EMB, electrodes operate with a voltage of 2000 V and have LAr gaps of 2 mm, leading to typical drift times of around 400 ns. Voltages and gaps in the EMEC vary slightly as a function of radius to maintain a uniform detector response.

The EM calorimeter is segmented in pseudorapidity, azimuth, and depth, enabling the resolution of the shower shapes and the projective angles of incoming particles. In all of the EMB and most of the EMEC, the layers in depth function as follows: the presampler, closest to the beamline, helps account for energy lost upstream of the calorimeter for $|\eta| < 1.8$; the front layer, also called the strip layer, helps determine shower substructure and direction; the middle layer captures most of the energy of a shower; and the back layer collects the tails of high-energy showers to prevent any energy loss. Table 4.3 details the granularity of the detector in $\Delta\eta \times \Delta\phi$ blocks as a function of $|\eta|$ and layer depth, and Figure 4.5 illustrates the cell segmentation in the central region of the LAr calorimeter.

The front EM layer, which is finely segmented in η , plays two critical roles in the performance of EM shower reconstruction. First, particle identification utilizes shower substructure in this layer to discriminate a single EM object from overlapping signatures (like

| $ \eta $ range | 0 to 1.8 | 1.8 to 2.0 | 2.0 to 2.5 | 2.5 to 3.2 |
|----------------------|----------------------|----------------------|----------------------|------------------|
| Presampler | 0.025×0.1 | | | |
| Front Layer (Strips) | 0.003×0.1 | 0.004×0.1 | 0.006×0.1 | 0.1×0.1 |
| Middle Layer | 0.025×0.025 | 0.025×0.025 | 0.025×0.025 | 0.1×0.1 |
| Back Layer | 0.050×0.025 | 0.050×0.025 | 0.050×0.025 | |
| Trigger | 0.1×0.1 | 0.1×0.1 | 0.1×0.1 | 0.1×0.1 |
| No. Channels | 135,808 | 12,288 | 24,064 | 1,792 |

Table 4.3: LAr EM calorimeter cell granularity ($\Delta\eta \times \Delta\phi$) and number of readout channels as a function of $|\eta|$ [97].

4.3.3 FORWARD CALORIMETER

The FCal provides calorimetry for both EM and hadronic objects for $3.1 < |\eta| < 4.9$. Each FCal contains three cylindrical sections: the unit closest to the beamline employs a mainly copper absorber and is optimized for EM particles; the remaining two contain a tungsten-rich absorber designed for hadronic particles. The electrodes of the FCal consist of cylindrical rods that run parallel to the beamline and are embedded in a copper or tungsten matrix (see Figure 4.7). This design, together with the very small LAr gaps ($269\text{-}500\ \mu\text{m}$), enables the FCal to handle very high particle fluxes in the forward region and curtail forward radiation in the MS.

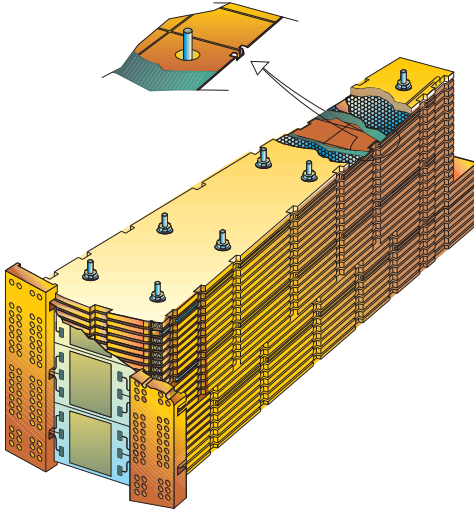


Figure 4.6: Diagram of a LAr HEC module [97].

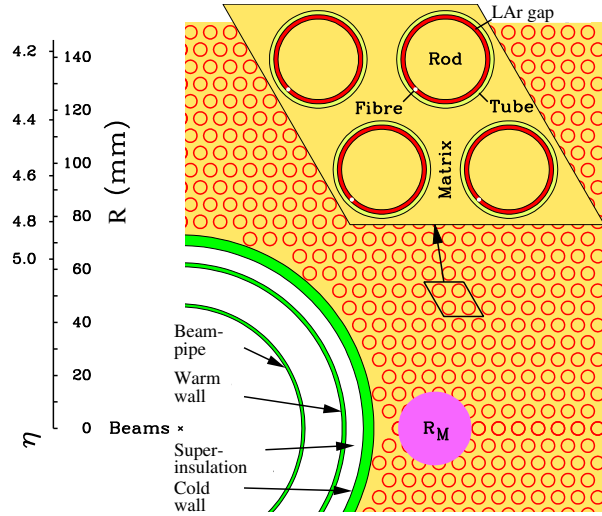


Figure 4.7: Transverse slice of LAr FCal showing the rod and matrix structure [97].

4.4 TILE CALORIMETER

The Tile Calorimeter (TileCal) [98] is a hadronic sampling calorimeter that uses steel as the absorber and approximately 460,000 plastic scintillating tiles as the active material. The calorimeter is partitioned into one central barrel, 5.8 m in length, covering $|\eta| < 1$, and two extended barrels, each 2.6 m in length, covering $0.8 < |\eta| < 1.7$. The three barrels have inner

and outer radii of 2.28 m and 4.25 m, respectively. The 600 mm crack regions between the barrel and extended barrels contain cables, electronics, and services for the ID and LAr calorimeter. Special modules placed in these gaps partially recover energy depositions in these regions.

Figure 4.8 displays one of the 64 TileCal modules, including the scintillator tiles oriented parallel to particle flow. Wavelength-shifting fibers carry signals from the tiles, and photomultiplier tubes (PMT) amplify and convert the scintillation light to electrical signals. The TileCal has three longitudinal layers: cell segmentation in $\Delta\eta \times \Delta\phi$ in the first two layers is 0.1×0.1 , while that in the third layer is 0.2×0.1 . The high granularity in the first two layers helps to inform EM leakage measurements for improved photon and electron identification.

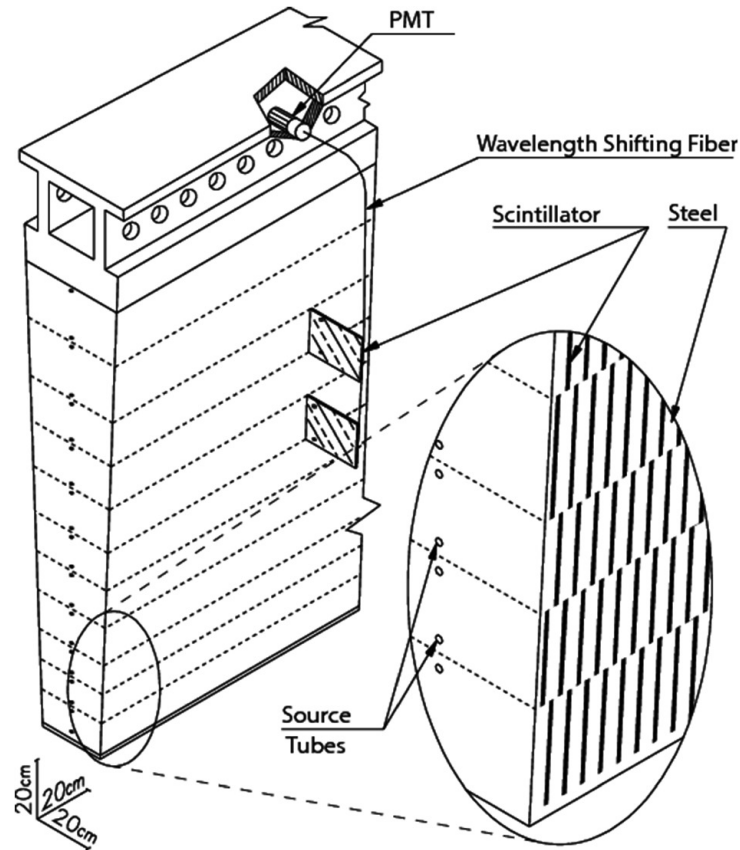


Figure 4.8: ATLAS TileCal module design, including the structure of the steel absorber, scintillator tiles, wavelength-shifting fibers, and PMTs [94].

4.5 MUON SPECTROMETER

Since muons interact minimally with the calorimeters, the MS provides additional tracking hits to improve the momentum measurement, triggering, and identification of muons. Toroid magnets, interspersed throughout the MS, bend muons as they pass through the spectrometer (see Section 4.6). The MS comprises three cylindrical barrel layers with radii of approximately 5 m, 7.5 m, and 10 m, and end-cap wheels at roughly $|z| = 7.4$ m, 10.8 m, 14 m, and 21.5 m. Four different technologies contribute to the MS, each optimized for a specific purpose (triggering vs. precision) and a distinct detector region (central vs. forward). The reconstruction of muon trajectories in the MS utilizes both precision chamber and trigger chamber measurements: precision measurements provide coordinates in the bending plane, while the trigger measurements supply those in the non-bending plane. The MS subdetectors include monitored drift tubes (MDTs), cathode strip chambers (CSCs), resistive plate chambers (RPCs), and thin gap chambers (TGCs). Figure 4.9 illustrates the arrangement of these subdetectors, and Table 4.4 highlights their key specifications.

MDTs and CSCs provide precision MS measurements. MDTs cover $|\eta| < 2.7$, except for the innermost end-cap layer, with covers $|\eta| < 2.0$. CSCs cover the remaining $2.0 < |\eta| < 2.7$ for the innermost layer. The MDT system consists of 30 mm diameter gas-filled tubes with a central anode wire; each tube yields a spatial precision in the bending plane of $35 \mu\text{m}$. The CSC system consists of multi-wire proportional chambers arranged in layers perpendicularly to each other to achieve measurements in both η and ϕ , leading to spatial resolutions of $40 \mu\text{m}$ in the bending plane. To accommodate higher muon flux rates in the forward region, the CSCs have a shorter drift time than the MDTs.

Since the drift times of the precision chambers are much longer than the bunch crossing time (25 ns), the MS trigger requires additional technologies that prioritize fast response times over spatial precision. The MS trigger measurements are available for $|\eta| < 2.4$: RPCs

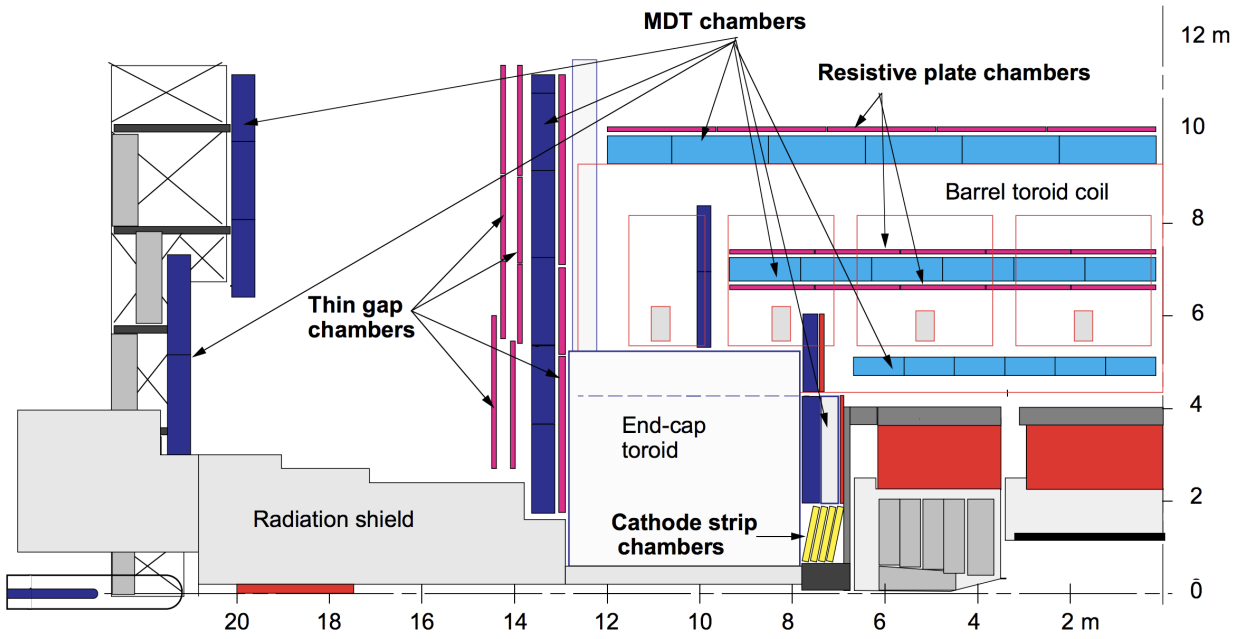


Figure 4.9: Profile view of the muon spectrometer, including the MDT chambers, cathode strip chambers, resistive plate chambers, and thin gap chambers [94]. The positions of toroid magnet components (see Section 4.6) are also shown.

| | MDT | CSC | RPC | TGC |
|----------------|--------------------------|--------------------------|--|---|
| Function | Precision tracking | Precision tracking | Triggering and tracking in non-bending plane | Triggering and tracking in non-bending plane |
| Coverage | $ \eta < 2.0$ | $2.0 < \eta < 2.7$ | $ \eta < 1.05$ | $1.05 < \eta < 2.4$ (2.7 for triggering) |
| No. Channels | 354k | 30.7k | 373k | 318k |
| Resolution | | | | |
| z or R | $35 \mu\text{m}$ (z) | $40 \mu\text{m}$ (R) | 10 mm (z) | $2\text{-}6 \text{ mm}$ (R) |
| ϕ | – | 5 mm | 10 mm | $3\text{-}7 \text{ mm}$ |
| Hits per Track | | | | |
| Barrel | 20 | – | 6 | – |
| End-Cap | 20 | 4 | – | 9 |

Table 4.4: Design specifications of various components of the muon spectrometer [94].

cover $|\eta| < 1.05$, and TGCs cover $1.05 < |\eta| < 2.4$ (TGCs also provide non-trigger measurements up to $|\eta| = 2.7$). The RPCs contain two parallel resistive plates separated by a 2 mm gap filled with a gas mixture. RPC Measurements deliver a spatial resolution of 1 cm in both η and ϕ and a time resolution of 1.5 ns. TGCs are multi-wire proportional chambers designed to handle high muon flux rates in the forward region and maintain a fast response time. The TGC spatial resolution is 2-6 mm and its response time is 4 ns.

4.6 MAGNET SYSTEM

The ATLAS magnet system, depicted in Figure 4.10, contains four sets of superconducting magnets: a barrel solenoid, a barrel toroid, and two end-cap toroids. The solenoid magnetic field bends the trajectories of all charged particles as they pass through the ID, while that of three toroids bends the paths of muons as they traverse the MS.

The solenoid surrounds the ID and provides a 2 T magnetic field parallel to and along the z -axis. The magnet is composed of an Al-stabilized Nb-Ti conductor coil with inner and outer radii of 1.23 and 1.28 m. The LAr barrel cryostat houses and supports the solenoid magnet, while the steel absorber of the TileCal serves as its return yoke and offers additional structural reinforcement. Many elements of the magnet's design – including its material, thickness, and convenient sharing of the cryostat – minimize radiative losses upstream of the calorimeters.

Each of the three air-core toroids contains eight flat racetrack-type coils made of Al-stabilized Nb-Ti-Cu conductor material. The 25.3 m long barrel toroid coils have inner and outer radii of 4.7 and 10.1 m, respectively, and produce a maximum magnetic field strength of roughly 0.5 T. The two smaller end-cap toroids, located at approximately $|z| = 5$ m, provide a magnetic field of approximately 1 T; their coils are 5 m long and have inner and outer radii of 4.7 and 10.1 m.

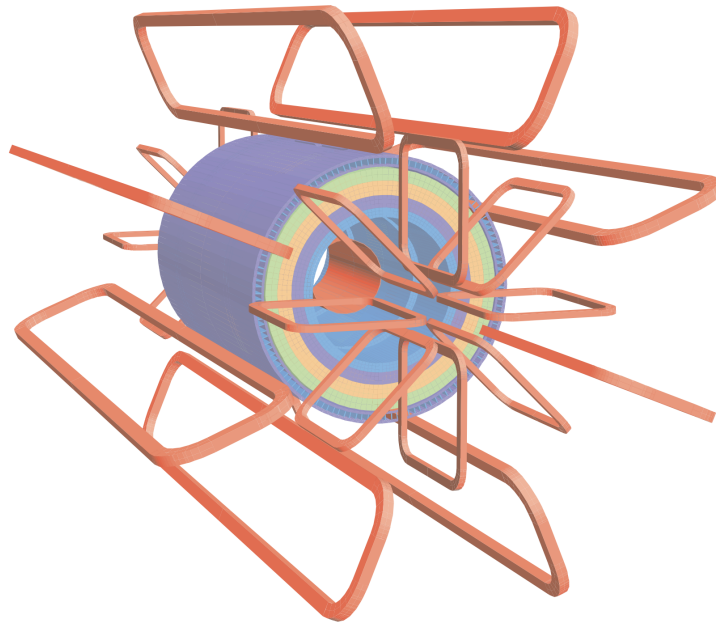


Figure 4.10: A schematic of the ATLAS magnet system, including the solenoid (this innermost structure) and the three toroids (the outermost structures). Magnets are shown in red, and components related to the return yoke of the solenoid are shown in purple, green, orange, and blue [94].

4.7 FORWARD DETECTORS AND LUMINOSITY CALCULATION

A handful of small subdetectors in the forward regions measure the delivered luminosity of the beams. The three principal forward detectors include LUCID (LUMinosity measurement using Cerenkov Integrating Detector) [99], ZDC (Zero Degree Calorimeter), and ALFA (Absolute Luminosity For ATLAS). LUCID measures inelastic pp scattering and provides the main online luminosity measurement within 5% error. The detector uses PMTs to record Cherenkov radiation from particles that pass through its gas-filled aluminum tubes. ZDC, which measures forward neutral particles like photons and neutrons, is primarily responsible for the luminosity calculation for heavy-ion collisions. ALFA provides absolute luminosity measurements from elastic pp scattering at small angles. Table 4.5 gives the position and pseudorapidity of each subdetector.

| Detector | Distance From the IP | Coverage |
|----------|----------------------|------------------------|
| LUCID | 17 m | $5.6 < \eta < 5.9$ |
| ZDC | 140 m | $8.3 < \eta $ |
| ALFA | 240 m | $10.6 < \eta < 13.5$ |

Table 4.5: Forward detector position and pseudorapidity coverage [94].

The forward detectors are calibrated using van der Meer scans [100], which include a set of specialized LHC runs that alter the overlap of the beams. The number of particles observed in the very forward regions is generally proportional to the number of pileup vertices, which is proportional to luminosity. The final offline ATLAS luminosity calculation integrates measurements from the forward detectors and information about particle tracks in the ID, yielding a total uncertainty of 1.7%.

4.8 TRIGGER AND DATA ACQUISITION SYSTEM

The Trigger and Data Acquisition (TDAQ) system, illustrated in Figure 4.11, handles the triggering and readout of data. Since current technologies cannot save all the information at the LHC collision rate of 40 MHz, ATLAS uses a multi-level trigger system to select and save events deemed "interesting" for offline physics analysis. The trigger process includes the Level-1 (L1) trigger, Level-2 (L2) trigger, and event filter stages. The L2 and event filter collectively form the High-Level Trigger (HLT).

The L1 trigger [101] employs hardware-based logic to reduce the event rate from 40 MHz to 100 kHz within a $2.5 \mu\text{s}$ latency time. Such a transient window precludes the reconstruction of ID tracks and the use of precision muon measurements at this stage; therefore, only measurements from the LAr and Tile calorimeters (L1Calo) and those from the RPCs and TPCs (L1Muon) contribute to the L1 trigger decision. Calorimeter measurements do not use their full granularity and instead read out energy information in larger regions ($\Delta\eta \times \Delta\phi = 0.1 \times 0.1$) called trigger towers. The L1Muon system reconstructs high- p_T muon candidates, while L1Calo identifies high- p_T clusters that could correspond to electrons,

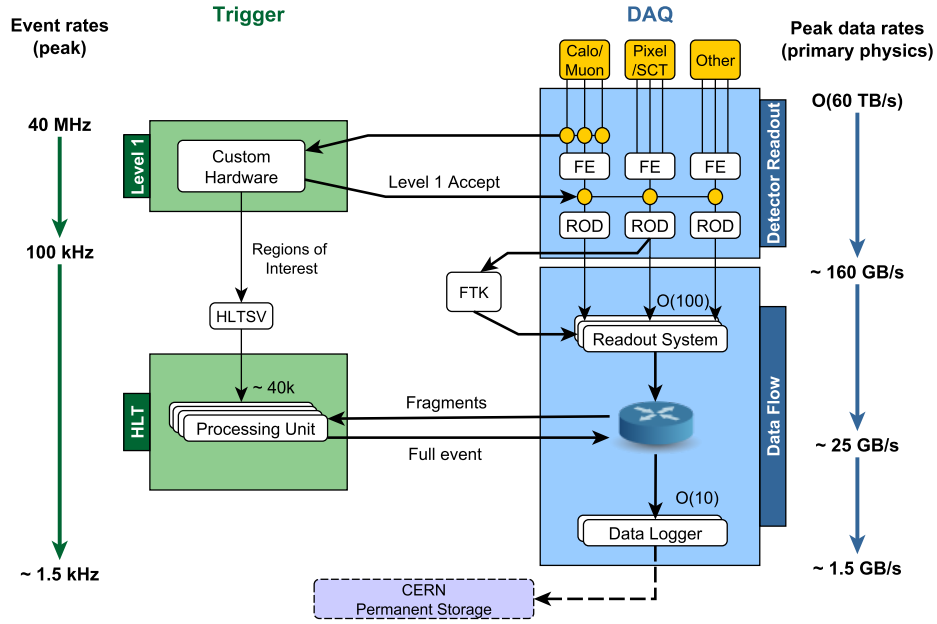


Figure 4.11: Block diagram of the ATLAS TDAQ system [102].

photons, jets, or hadronic τ -leptons. These systems also generate a simplified E_T^{miss} calculation. When an event passes the L1 trigger, the central trigger processor delivers a *Level-1 Accept* to the on-detector electronics, prompting the digitization and readout of the full granularity of the detector. The event is then sent for further processing by the HLT. The L1 trigger also passes along the location of object candidates, called Regions-of-Interest (ROIs).

The HLT [103] implements sophisticated software-based algorithms that run on a high-capacity computer farm using commercially available hardware. Apprized about the ROIs, the L2 trigger reconstructs event fragments with the full detector granularity. Events that pass this step proceed to the event filter, where they undergo full event reconstruction using object definitions and selections similar to those used in offline analysis. This procedure enables the event filter to extract high-level features about the event to inform the final trigger decision. Events passing the HLT are stored permanently at a maximum rate of about 1.5 kHz.

A carefully constructed trigger *menu* contains a set of rules that determine whether the L1 trigger and HLT discard an event or keep it for further processing. Each trigger is generally defined by a set of physics objects, including their identification criteria and E_T (or p_T) thresholds; these object requirements must strike a balance between manageable trigger rates and reasonable efficiencies for physics processes-of-interest. For example, more stringent object requirements may permit lower E_T thresholds, while higher E_T thresholds allow for more relaxed object definitions. Figure 4.12 shows the HLT efficiency for MEDIUM photon objects (see Section 5.3.2) at two distinct E_T thresholds, 25 and 35 GeV. As demonstrated in the figure, triggers are not perfectly efficient at their thresholds; instead, they exhibit a continuous, though sharp, rise in efficiency at their respective threshold points – a behavior referred to as the trigger "turn-on" curve.

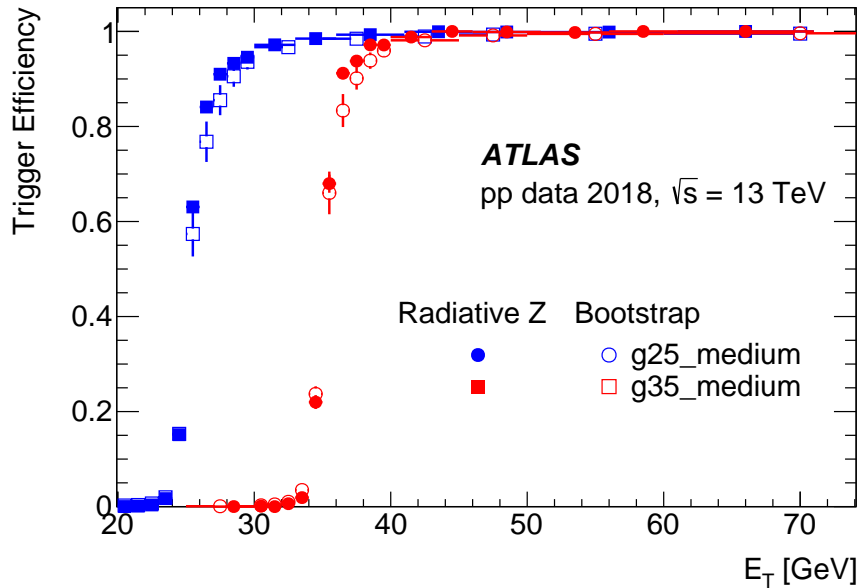


Figure 4.12: Trigger efficiency curves as a function of transverse energy, E_T (here, equivalent to p_T), for the MEDIUM photon objects. Two methods of computing the trigger efficiencies are included: the radiative Z method and the bootstrap method [104].

CHAPTER 5:

OBJECT RECONSTRUCTION AND IDENTIFICATION

They told me computers could only do arithmetic.

— Grace Hopper

Object reconstruction and identification algorithms transform collections of raw and uncalibrated hits across several detector subsystems into precise, accurate, and meaningful physics objects. Since reconstruction methodologies underlie all subsequent physics analysis and interpretation, they play a pivotal role in deciphering pp collision processes.

The reconstruction of objects begins by assembling low-level detector hits into intermediate objects like ID tracks and calorimeter energy clusters (Sections 5.1 and 5.2). The careful matching, combining, and processing of these objects generates collections of analysis-quality physics objects, including photons, electrons, jets, and muons (Sections 5.3-5.5), and crucial high-level variables like E_T^{miss} (Section 5.7). Figure 5.1 illustrates how different idealized physics objects interact with the various subsystems of the ATLAS detector.

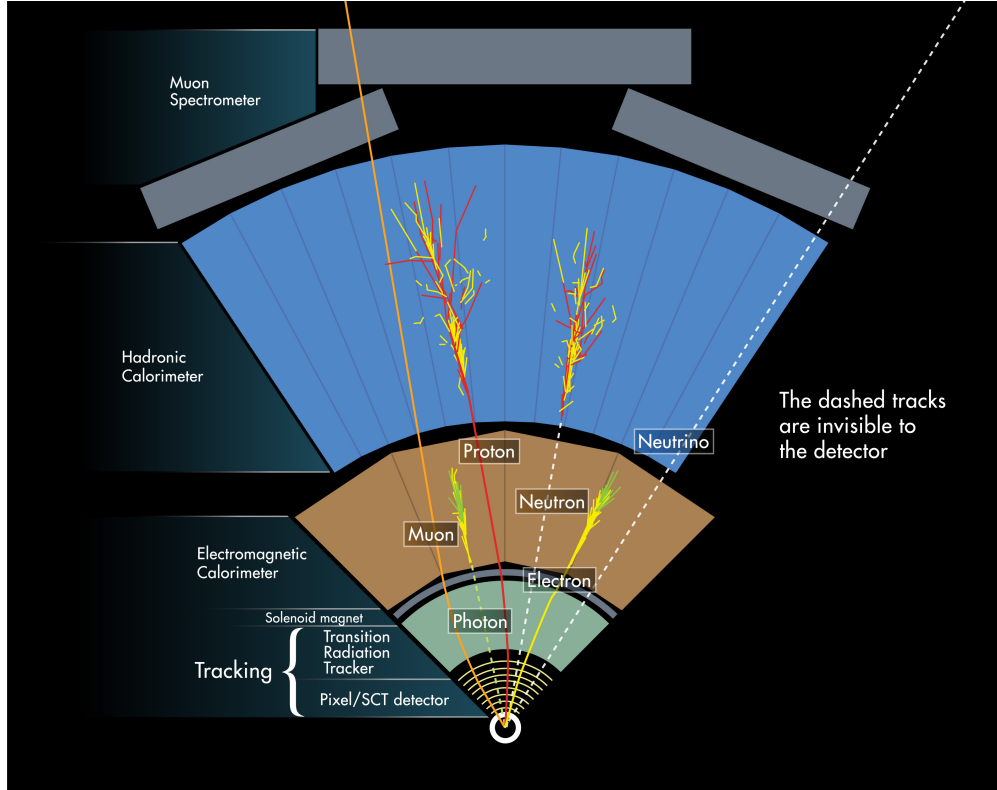


Figure 5.1: Illustration of how different physics objects interact with the various layers of the ATLAS detector [105].

5.1 INNER DETECTOR TRACKS AND VERTICES

Particle hits in the ID are used to reconstruct the trajectories of charged particles, called tracks. ID track reconstruction [106] begins with a preprocessing stage, which creates clusters from pixel and SCT hits and uses TRT drift times to construct drift circles. Next, track-finding algorithms reconstruct tracks in the silicon subdetectors and TRT separately, after which tracks are extended throughout the entire ID and refitted. Since the signatures of physics objects like electrons and jets typically include track and calorimeter measurements, tracks can also be extrapolated to and associated with topological clusters in the calorimeters (see Section 5.2).

The primary vertex (PV) is the vertex associated with the hardest scattering process in a bunch crossing. Due to pileup, there are typically multiple interactions per bunch

crossing and, consequently, multiple PV candidates. PV reconstruction [107] begins with a vertex-finding stage that associates sets of tracks to candidate vertices. A track-fitting stage then reconstructs the precise vertex position and its covariance matrix. The PV is selected as the vertex candidate with the highest $\sum p_T^2$ of constituent tracks. Figure 5.2 demonstrates how increased pileup degrades the PV reconstruction efficiency for various physics processes. Figure 5.3 shows that the PV resolution, which varies as a function of track multiplicity, is typically on the order of 100 μm and sometimes as low as 40 μm .

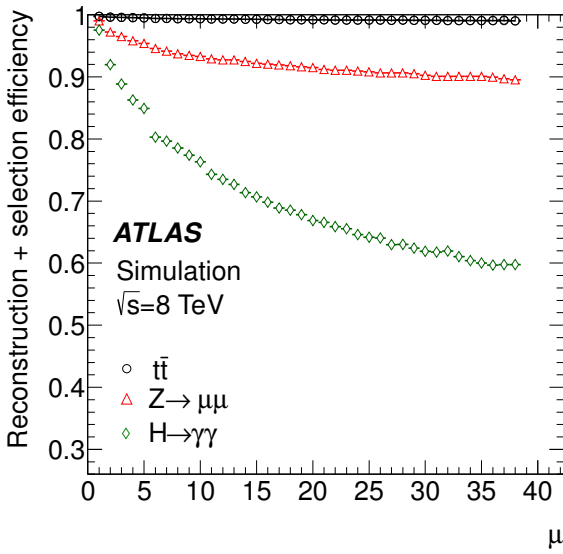


Figure 5.2: Reconstruction and selection efficiency of the hard-scatter pp primary vertex as a function μ for various physics processes [107].

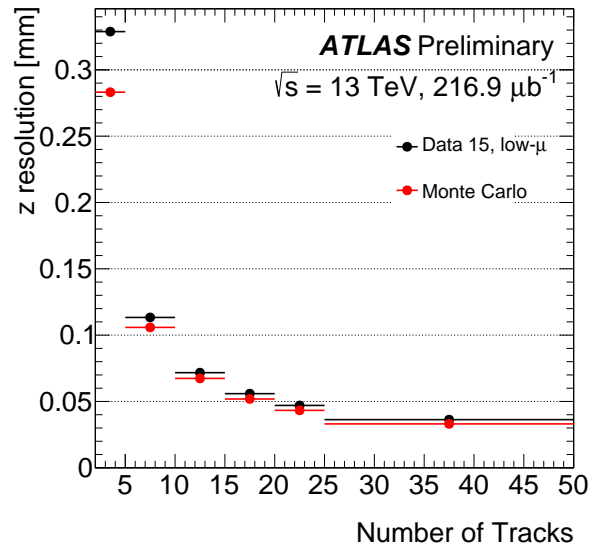


Figure 5.3: Primary vertex resolution in the z -direction as a function of the average number of tracks for low- μ data compared to Monte Carlo simulation [108].

5.2 TOPOLOGICAL CALORIMETER CLUSTERS

Particles that enter the calorimeters produce showers of energy deposited across many calorimeter cells. The reconstruction of EM and hadronic objects begins with the three-dimensional topological clustering of these cells. The resulting object, the topo-cluster, becomes a fundamental building block in reconstructing various physics objects.

The topological clustering algorithm [109] begins by assigning each calorimeter cell with a significance, $\zeta_{cell}^{EM} = \frac{|E_{cell}^{EM}|}{\sigma_{cell}^{EM}}$, where E_{cell}^{EM} is the cell energy, and σ_{cell}^{EM} includes the uncertainties associated with cell noise and pileup. At this stage, cells with negative energies are treated no differently than those with positive energies; this approach improves noise suppression since positive and negative energy contributions can balance each other out.

The clustering algorithm then follows a seed-and-collect process of topo-cluster growth. Cells with $\zeta_{cell}^{EM} > 4$ seed the formation of so-called proto-clusters, which grow by iteratively adding any neighboring cells satisfying $\zeta_{cell}^{EM} > 2$. When no more adjacent cells satisfy this condition, the proto-cluster subsumes the surrounding envelope of cells, and the process is complete. Proto-clusters that overlap at any stage of this process are merged, and those below an energy threshold are removed.

The remaining proto-clusters are checked for substructure since two or more local energy maxima above a certain threshold may indicate the presence of multiple overlapping physics objects. These clusters are divided, and constituent cells are reassigned iteratively. In cases of ambiguity, separated clusters can share the energy from a single cell. After this splitting, the proto-clusters are now defined as topo-clusters and are used as the basic building blocks for further object reconstruction.

5.3 PHOTONS AND ELECTRONS

The reconstruction of photons and electrons is similar since they leave nearly indistinguishable shower signatures in the LAr calorimeter. Their main differentiating feature is that the charged electron leaves a track in the ID while the neutral photon does not. A caveat to this statement is that photons can convert into electron-positron pairs within the ID, leaving tracks pointing to a conversion vertex. The following subsections outline the reconstruction process and identification algorithms of electrons and photons.

5.3.1 ELECTROMAGNETIC SUPERCLUSTERS

As an EM object passes through the ID, electron bremsstrahlung radiation or photon conversion may cause the object to leave multiple energy depositions in the calorimeter. To account for these effects, EM "superclusters" [110] incorporate nearby "satellite" clusters into the EM object energy shower (the satellite *clusters* here should not be confused with the satellite *collisions* introduced in Section 3.3). Superclusters are seeded by topo-clusters that pass a set of requirements. First, more than 50% of topo-cluster energy must be in the EM calorimeter. Additionally, topo-cluster seeds for photon objects must satisfy $E_T^{EM} > 1.5$ GeV; those for electron objects must have $E_T^{EM} > 1$ GeV and have an associated track with at least four hits in the ID. The criteria for incorporating satellite clusters into the supercluster are given in Figure 5.4 and vary across electron, photon, and converted photon candidates. The surviving superclusters continue to the next stage of electron and photon identification.

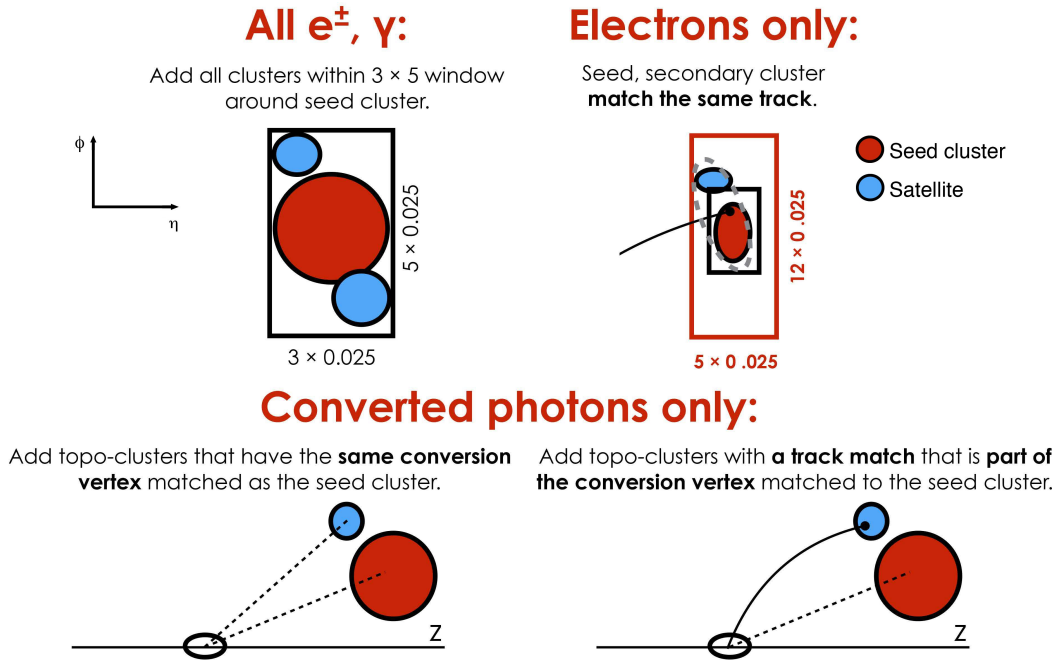


Figure 5.4: Cartoon illustrating the superclustering algorithm for electrons and photons. Seed clusters are shown in red and satellite clusters in blue [110].

5.3.2 PHOTON AND ELECTRON IDENTIFICATION

Until this point, the reconstruction of electron and photon superclusters has proceeded independently, meaning that the same topo-cluster can seed both a photon and an electron supercluster. Since photon and electron showers have similar topologies, the primary way to distinguish them is via their association with a track (or lack thereof). If a supercluster is matched to a high-quality track and not associated with a conversion vertex, then an electron object is created; if a supercluster cannot be matched to a high-quality track, then a photon object is created. Both photon and electron objects are created for all remaining superclusters, with ambiguities resolved at a later stage. Finally, the newly formed photon and electron object candidates undergo an object-dependent energy calibration.

EM particle identification (PID) criteria include selections on supercluster structure, evaluated by EM shower shape variables. For example, hadronic leakage shower shape variables quantify the fraction of particle energy deposited in the hadronic calorimeter, serving as a critical discriminant between EM objects (low hadronic energy fraction) and jets (high hadronic energy fraction). Table 5.1 lists and describes shower shape variables used for photon and electron identification.

ATLAS provides standardized and well-studied identification working points for EM objects. Photon and electron objects each have three primary working points, dubbed LOOSE, MEDIUM, AND TIGHT, that prioritize different balances of reconstruction efficiency versus background rejection: looser working points yield higher efficiencies at the cost of lower background rejection, and vice-versa.

PHOTON IDENTIFICATION

Photon identification relies exclusively on rectangular cuts applied to the shower shape variables. Since photon shower shapes can vary across detector regions, these cut-based selections depend on $|\eta|$. The LOOSE PID includes cuts on hadronic leakage and shower

| Category | Name | Description | Used in Photon PID | | |
|------------------|--------------|--|--------------------|--------|-------|
| | | | LOOSE | MEDIUM | TIGHT |
| Hadronic Leakage | R_{had1} | Ratio of E_T in the first sampling of the hadronic calorimeter to E_T of the EM cluster (for $ \eta < 0.8$ and $ \eta > 1.37$) | ✓ | ✓ | ✓ |
| | R_{had} | Ratio of E_T in all the hadronic calorimeter to E_T of the EM cluster (for $0.8 < \eta < 1.37$) | ✓ | ✓ | ✓ |
| EM Middle layer | R_η | Ratio in η of cell energies in 3×7 and 7×7 | ✓ | ✓ | ✓ |
| | R_ϕ | Ratio in ϕ of cell energies in 3×7 and 7×7 | | | ✓ |
| | $w_{\eta 2}$ | Lateral shower width | ✓ | ✓ | ✓ |
| EM Strip layer | $w_{s,3}$ | Shower width for 3 strips around the maximum energy strip | | | ✓ |
| | $w_{s,tot}$ | Lateral shower width | | | ✓ |
| | f_{side} | Fraction of energy outside the core of 3 central strips but within 7 strips | | | ✓ |
| | f_1 | Ratio of the energy in the first layer to the to the total energy of the EM cluster | | | ✓ |
| | ΔE | Difference between the energy in the second maximum in the strip layer and the energy in the strip with the minimal values found between the first and second maxima | | | ✓ |
| | E_{ratio} | Ratio of the energy in the largest and second-largest energy deposits to the sum of these energies | | ✓ | ✓ |

Table 5.1: Shower shape variables used photon and electron identification. The variables that define the LOOSE, MEDIUM and TIGHT photon PID working points are highlighted [110].

topology in the middle EM layer, contributing to adequate background rejection of jets. The MEDIUM PID utilizes the same cuts as that of LOOSE, with an additional cut on the E_{ratio} variable (see definition in Table 5.1), which serves to reject overlapping photon showers from $\pi^0 \rightarrow \gamma\gamma$ decays (see Figure 5.5). The TIGHT PID imposes stricter cuts on the shower shape, particularly in the strip layer. Table 5.1 details the shower shape variables used to define each of the three photon PID working points.

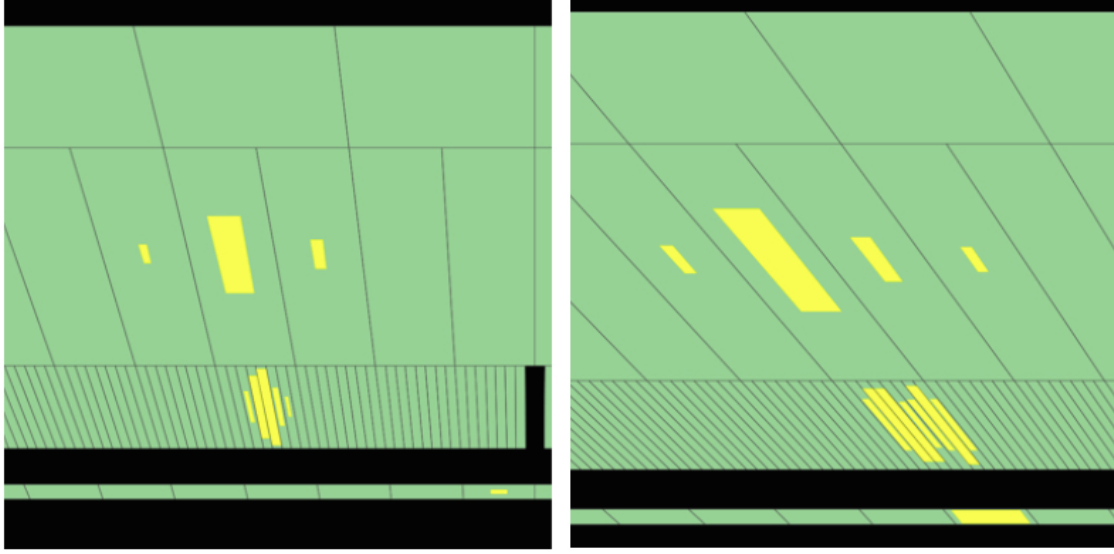


Figure 5.5: Energy depositions across different LAr calorimeter cells of a candidate photon (left) and a candidate π^0 meson decaying to two photons (right) [110].

Photon identification efficiencies depend on numerous factors, including the selected PID working point and the object’s conversion status, p_T , and $|\eta|$; efficiencies typically range from 87% to 98% for photons with $p_T > 25$ GeV [111]. The search presented in this thesis employs the MEDIUM PID – a choice informed by several analysis-specific studies (see Section 8.1.1).

ELECTRON IDENTIFICATION

The electron identification algorithms [112] discriminate prompt electrons from jets, converted photons, and electrons produced in heavy-flavor decays. The discriminants for the three main working points include information from the ID track, calorimeter cluster, and combined track-cluster system. This analysis uses the MEDIUM PID working point, which requires, among other things, hits in the two innermost pixel layers and track compatibility with the PV. It is important to note that these stringent tracking requirements are explicitly designed to identify *prompt* electrons. Sufficiently displaced electrons from either heavy flavor decays or potential BSM LLPs would generally fail these requirements.

5.3.3 ISOLATION REQUIREMENTS

In addition to passing object identification requirements, EM objects used in the analysis must pass specific isolation requirements to ensure reasonable separation from surrounding calorimeter activity. There are two classes of isolation variables: the calorimeter isolation variable, E_T^{cone20} , is equal to the net E_T deposited within a radius of $\Delta R = 0.2$ of the EM object, excluding the deposited energy of the EM object itself; the tracking isolation variable, p_T^{cone20} , is the sum of the p_T of selected tracks within a radius of $\Delta R = 0.2$ of the object, excluding tracks matched to that object. This analysis uses the `FIXEDCUTLOOSE` working point, which requires $E_T^{\text{cone20}} < 0.065 \times E_T$ and $p_T^{\text{cone20}} < 0.05 \times E_T$.

5.4 JETS

When quarks and gluons are produced in the LHC, they fragment and hadronize into conical showers of particles. The resulting hadronic objects, called jets, produce tracks in the ID and energy deposits in both the EM and hadronic calorimeters. While jet objects are not used directly in this analysis, they are used indirectly in the E_T^{miss} calculation. The following description of jet reconstruction is the standard ATLAS approach.

Like EM objects, jets are seeded by topo-clusters that may be matched to ID tracks. A procedure called the particle flow algorithm [113] runs over each track/topo-cluster system to improve jet candidate quality and resolution. The algorithm matches individual tracks from charged hadrons to their respective energy deposits in the calorimeter; it then updates the cluster energy, replacing calorimeter-based measurements with tracking-based ones. This procedure significantly improves the jet energy performance, since tracking offers better energy resolution than calorimetry for low-energy objects.

The resulting modified topo-clusters and their associated tracks are combined into jet objects using the anti- k_T algorithm [114] with radial parameter $R=0.4$. The anti- k_T algorithm is part of a broad class of sequential recombination algorithms, each of which iter-

ates through pairs of clusters and has its own set of rules to distinguish whether the pair gets merged into the same object or separated into distinct objects. The anti- k_T algorithm considers the p_T values and angular separation of the jet pair to decide the cluster grouping. An advantage of this approach is that soft (low p_T) particles tend to combine with hard (high p_T) ones, leading to highly collimated jets around the hardest particles. Another merit of this algorithm is that it is infrared-safe: anti- k_T jet areas can be calculated perturbatively, improving the comparison with theory.

5.5 MUONS

The muon reconstruction algorithm [115] uses ID, MS, and calorimeter measurements. Combining measurements from several subsystems increases the acceptance of muons and allows for sensitivity to a broad spectrum of muon energies, ranging from a few GeV to a few TeV.

MS tracks are reconstructed independently from ID tracks. First, track segments within a single chamber are constructed; segments then seed tracks that may extend throughout the entire MS. Information from the various subsystems converges in one of four ways to reconstruct a muon candidate:

- *Combined* muons are built from independently reconstructed tracks in the MS and ID that pass a global refit procedure.
- *Segment-tagged* muons include ID tracks compatible with at least one MDT or CSC segment.
- *Calorimeter-tagged* muons use ID tracks extrapolated to a calorimeter cluster consistent with minimum-ionizing radiation.

- *Extrapolated* muons employ MS tracks loosely consistent with originating from the PV. These muons help to increase acceptance in the $2.5 < |\eta| < 2.7$ region, which has limited ID coverage.

Muon candidates are required to pass a series of quality cuts. Constraints on the goodness-of-fit χ^2 and consistency requirements between measurements across subsystems help reject hadronic backgrounds, mainly from kaon and pion decays. Muon candidates consistent with cosmic rays, which usually appear as a pair of back-to-back muons, are also used to reject unwanted events.

While this analysis does not directly use muon objects, they contribute to the E_T^{miss} calculation and cosmic ray veto. The analysis uses the default muon selection for ATLAS, designed to minimize systematic uncertainties, retain high reconstruction efficiencies, and achieve high background rejection.

5.6 OVERLAP REMOVAL

The physics objects discussed in this chapter are reconstructed independently using separate algorithms; therefore, a given detector hit or cluster may be associated with multiple physics objects. An overlap removal procedure prevents this unwanted double-counting of objects at the analysis level. The prioritization of how to interpret overlapping objects depends on the needs of the analysis. Since this search focuses on final states with photon objects, photons are given the highest priority in case of any ambiguities in object identification.

The procedure implemented in the analysis goes as follows (overlap distance indicated in parentheses): (1) remove electrons overlapping with photons ($\Delta R < 0.4$); (2) remove jets overlapping ($\Delta R < 0.4$) with photons and those closely overlapping ($\Delta R < 0.2$) with electrons; (3) remove electrons "close to" the remaining jets ($0.2 < \Delta R < 0.4$); and (4) remove muons overlapping with photons or jets ($\Delta R < 0.4$).

5.7 MISSING TRANSVERSE ENERGY

As introduced in Section 4.1, the z -axis is defined as parallel to the colliding proton beams, and the transverse ($x-y$) plane is perpendicular to it. Since the initial state net momentum of the pp collisions in the transverse direction is zero, so must be the final state transverse momentum. As discussed, the missing transverse energy, E_T^{miss} , is defined as the magnitude of the negative vector sum of the final state net transverse momentum:

$$E_T^{miss} = |\mathbf{p}_T^{miss}| = -|\sum \mathbf{p}_T|. \quad (5.1)$$

Several factors might contribute to a non-zero E_T^{miss} . Genuine sources of E_T^{miss} include particles invisible to the detector, including neutrinos and possibly BSM particles. Fake sources of E_T^{miss} are attributed to instrumental errors, including calibration errors, dead channels, and noisy detector regions.

Given the complexities of object overlap and multiple pileup vertices, the calculation of the E_T^{miss} value is non-trivial. This analysis uses the standard ATLAS strategy for E_T^{miss} calculation: the track-based soft term (TST) approach [116]. The TST calculation considers "hard" calorimeter objects surviving the overlap removal procedure (including photons, electrons, muons, and jets) and any remaining "soft" tracking terms consistent with the PV and not assigned to any hard calorimeter object. E_T^{miss} is thus calculated as follows:

$$E_T^{miss} = - \left| \underbrace{\sum_{\text{photons}} \mathbf{p}_T^\gamma + \sum_{\text{electrons}} \mathbf{p}_T^e + \sum_{\text{muons}} \mathbf{p}_T^\mu + \sum_{\text{jets}} \mathbf{p}_T^{jet}}_{\text{hard term}} + \underbrace{\sum_{\text{unused tracks}} \mathbf{p}_T^{trk}}_{\text{soft term}} \right|. \quad (5.2)$$

The E_T^{miss} resolution [116] can be assessed by studying $Z \rightarrow \mu\mu$ events, which are expected to have little to no E_T^{miss} . Figure 5.6 shows that the E_T^{miss} resolution degrades as a function of E_T^{miss} and as a function of the number of pileup vertices.

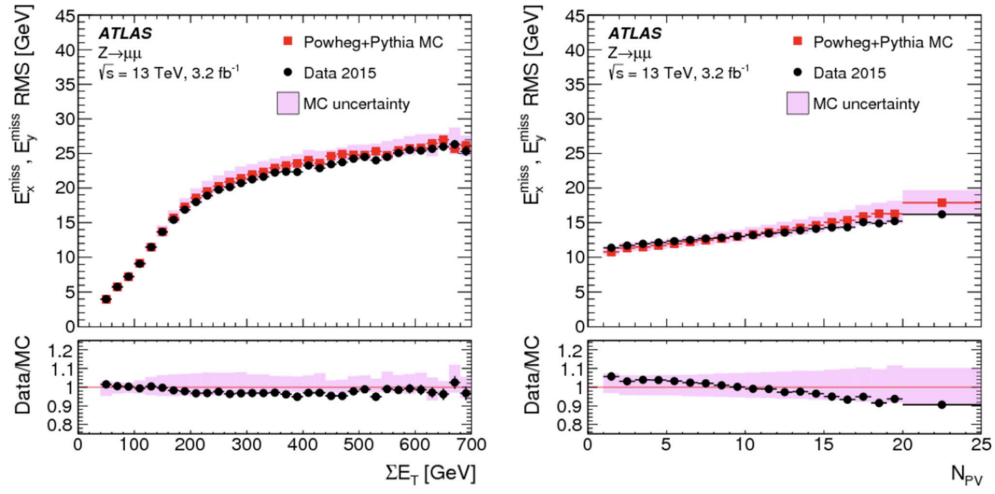


Figure 5.6: The RMS width of $E_{x(y)}^{\text{miss}}$ as a function of ΣE_T (left) and as a function of pileup (right) based on a sample of $Z \rightarrow \mu\mu$ events in data and simulation [116].

CHAPTER 6:

VERTEXING AND TIMING MEASUREMENTS

A day without photons is like a day without sunshine... literally!

— John Parsons

Given the unconventional detector signatures of LLPs, their searches frequently demand creative analysis approaches, dedicated reconstruction algorithms, and fresh perspectives about the capabilities of the ATLAS detector. Incidentally, the specialized strategies developed to attack these unusual signatures often produce the most powerful discriminating variables of an analysis. Such is the case for the search presented in this thesis, which exploits the fine segmentation and excellent timing performance of the LAr calorimeter to isolate the striking signature of displaced and delayed diphoton and dielectron vertices.

This chapter details the transformation of low-level LAr calorimeter information into analysis-quality calorimeter timing and vertexing variables. Section 6.1 introduces a novel method of vertexing EM objects using calorimeter measurements only – the first of its kind not to depend on ID tracking hits. Section 6.2 describes the reconstruction, measurement, and calibration of the LAr timing variable, which constitutes one of the most precise timing measurements at the LHC to date. Each of these approaches is impactful in its own right;

however, the true discriminating power of the analysis transpires from combining these two independent measurements (see Chapter 8).

6.1 TRACKLESS CALO-VERTEXING

A novel algorithm, developed for the analysis and called *Trackless Calo-Vertexing*, employs geometrical shower information to localize the shared production vertex of two EM objects using LAr calorimeter measurements only. This approach represents a significant departure from the traditional paradigm of vertex identification, which, up until this point, has relied on tracking information from charged particles passing through the ID. This section describes the underlying measurement, fundamental strategy, and overall performance of Trackless Calo-Vertexing (dubbed *vertexing* in this thesis).

6.1.1 CALORIMETER POINTING

The segmentation pattern and precise spatial resolution of the LAr calorimeter enable measurements of both the *position* and the *direction* of an EM shower. Calorimeter *pointing* extrapolates the direction of an EM cluster to a position along the beamline – i.e., the position to which a photon (or electron) "points back." ATLAS analyses employ photon pointing measurements in a variety of contexts, from aiding PV identification and thus improving Higgs boson mass measurements in the (prompt) $H \rightarrow \gamma\gamma$ final state [117], to identifying displaced objects in non-pointing photon searches [3, 118, 119].

A cartoon of the LAr calorimeter in Figure 6.1 illustrates the pointing measurement with respect to the origin (z_γ) and with respect to the z -position of the PV (z_{DCA}), where DCA indicates the *distance of closest approach*. The value of z_γ is computed as follows:

$$z_\gamma = \frac{R_1 R_2}{R_2 - R_1} (\sinh \eta_1 - \sinh \eta_2) \quad (6.1)$$

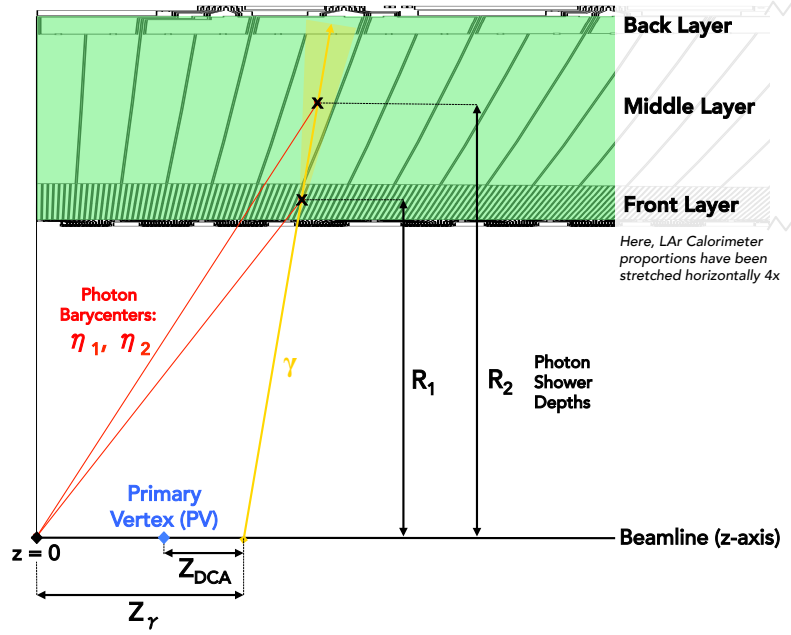


Figure 6.1: Illustration of LAr calorimeter pointing, where z_γ and z_{DCA} correspond to the values of the pointing measurement with respect to the origin and the z -position of the PV, respectively. Three layers of the LAr calorimeter are highlighted, along with the energy deposits of the photon and its barycenters (marked by an "x"). The variables $\eta_{1,2}$ and $R_{1,2}$ represent the η barycenters and photon shower depths of the photon shower in the front and middle layers (front=1, middle=2).

where (η_1, R_1) and (η_2, R_2) correspond to the cylindrical coordinates of the cluster *barycenter* positions in the front and middle layers¹ of the LAr calorimeter. The computation of the η barycenter position accounts for the shower distribution across several cells, yielding more precise resolutions than the width of a single cell. The positions of the barycenters in R , also called *photon shower depths*, are parameterized as a function of photon η and energy. Photon shower depth values are determined a priori using a sample of simulated prompt photons with known production vertex positions; in each LAr layer, the value of R that minimizes the η barycenter resolution is selected.

¹ The pointing calculation does not use measurements in the presampler or back layer of the LAr calorimeter, which have insufficient energy depositions and cell granularities to determine shower barycenter positions reliably.

Successful validation of the pointing measurement helps to verify the accuracy of the underlying particle shower simulation and barycenter computation. This procedure uses a high-purity sample of electrons from prompt $Z \rightarrow ee$ data and EM objects from simulated Monte Carlo (MC) samples. Figure 6.2 shows the pointing resolution as a function of displacement along the z -axis for $Z \rightarrow ee$ data, $Z \rightarrow ee$ simulation, and several simulated long-lived higgsino signal samples (see Chapter 7 for details). For objects produced near the optimal IP ($z = 0$), the pointing measurement achieves resolutions of roughly 10 mm, a value that degrades with increasing displacement. Although the electrons from the prompt $Z \rightarrow ee$ data and MC samples are not technically displaced, the spread of the beamspot provides a sample of EM objects in data with varying production vertices along the z -axis, up to around 150 mm away from the IP. The pointing resolutions of EM objects from the prompt $Z \rightarrow ee$ data and various MC samples exhibit excellent agreement with

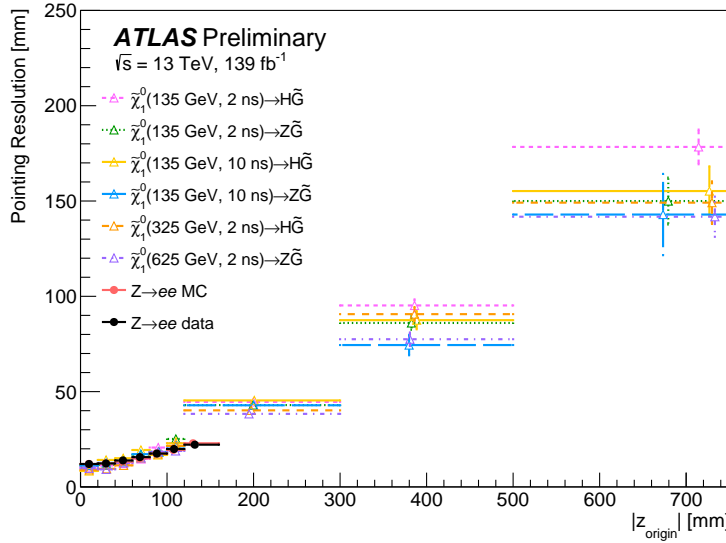


Figure 6.2: Resolution of the pointing variable, z_{DCA} , for photons and electrons as a function of $|z_{\text{origin}}|$, which is equal to the PV position along the z -axis for data and true production vertex position along the z -axis for simulated MC samples. $Z \rightarrow ee$ events in data and simulation are compared to several representative long-lived higgsino MC signal samples. See Section 7.3 for a description of the simulated signal and labeling convention. Signal events shown must satisfy the requirements in Table 8.1.

each other and with the long-lived signal models in the region where there is overlap, providing confidence in the extrapolation to higher displacements.

6.1.2 VERTEXING STRATEGY

The vertexing approach builds on the well-established LAr calorimeter pointing calculation to localize diphoton and dielectron production vertices. While the pointing measurement finds the intersection point of the photon path with the beamline, the vertexing strategy identifies the intersection point of the two photon paths with *each other*. Figure 6.3 illustrates an LLP, produced at the PV, that decays into two photons after traveling some resolvable distance. This procedure determines two "vertexing variables," V_R and V_Z , defined as the positions of the reconstructed secondary vertex (SV) in the R and z direction with respect to the PV of the event.

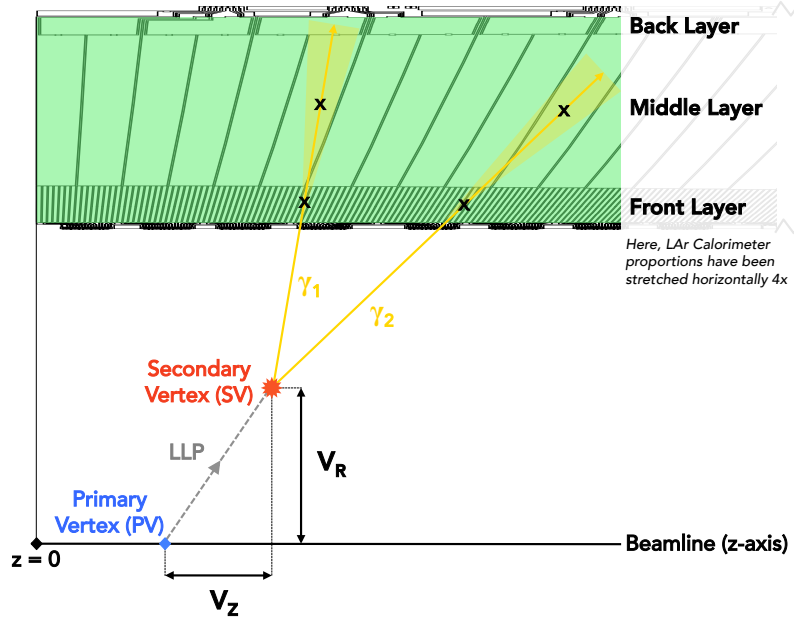


Figure 6.3: Illustration of the two-dimensional Trackless Calo-Vertexing procedure to calculate V_R and V_Z , two of the most powerful discriminating variables used in the analysis. Three layers of the LAr calorimeter are highlighted, along with the energy deposits of the two photons and their barycenters (each marked by an "x"). The secondary vertex, shown in red, corresponds to the decay vertex of a hypothetical LLP.

Since the granularity of the LAr cells in the front layer is very coarse in the ϕ direction ($\Delta\phi = 0.1$, in contrast to $\Delta\eta \approx 0.003$), the inclusion of ϕ measurements in this approach degraded the resolutions of the vertexing variables. Therefore, the algorithm only considers measurements in η and R , effectively rotating all photon measurements onto $\phi = 0$. This geometrical treatment means that V_R is not necessarily equal to the quadrature sum of the vertex positions in the x and y directions; in fact, like V_Z , V_R can have negative values, which corresponds to vertices being reconstructed below the beamline in Figure 6.3.

6.1.3 VERTEXING PERFORMANCE

Extensive studies of the vertexing variables found good agreement in the shapes and resolutions of V_R and V_Z in prompt $Z \rightarrow ee$ data and MC samples (see Appendix A for details), further validating the EM showering process used in simulation. The variable with the most significant impact on the vertexing resolution is the difference in η between the two electrons, $\Delta\eta_{ee}$, shown in Figure 6.4. For very low angular separations – in this case, at very low $\Delta\eta$ values – the photon (or electron) "paths" are nearly parallel; in other words, small uncertainties in the barycenter positions cause the resolutions of V_R and V_Z to blow up for

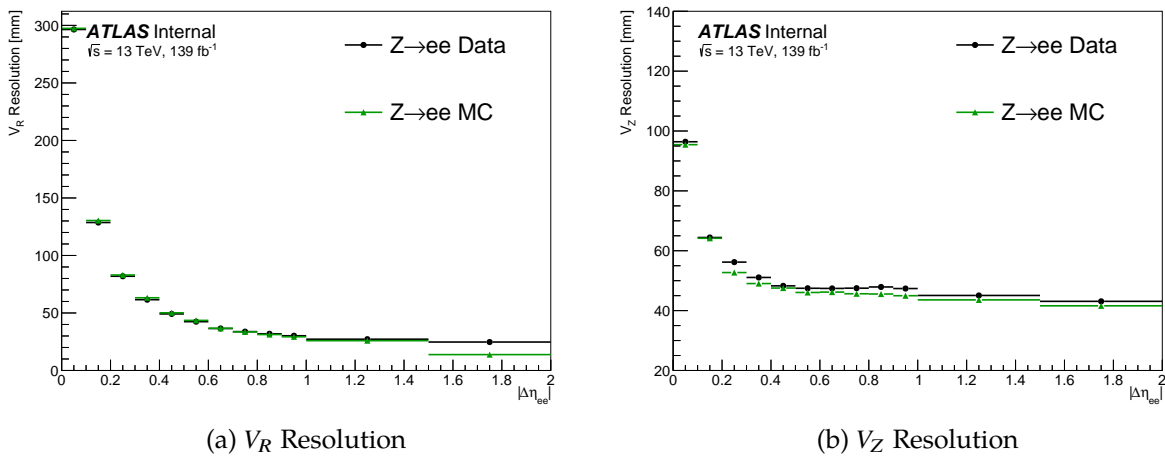
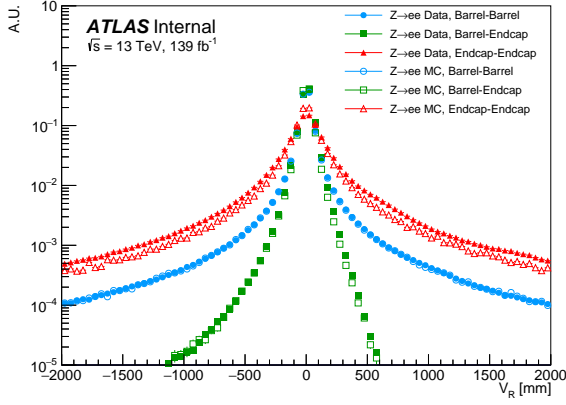


Figure 6.4: Resolution of V_R (left) and V_Z (right) as a function of $\Delta\eta_{ee}$ for $Z \rightarrow ee$ data and MC simulation. Good agreement is observed between these two samples.

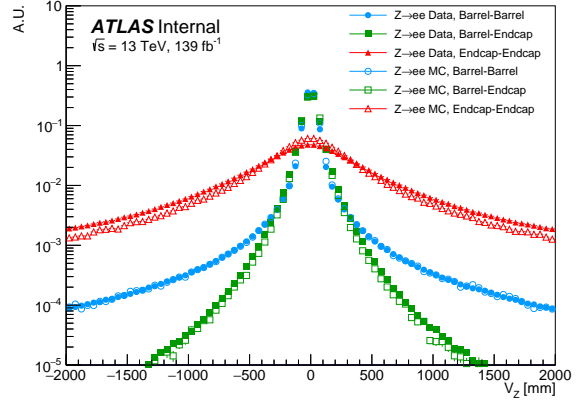
events with small $\Delta\eta$. The rejection of events with low $\Delta\eta$ values significantly improves the resolutions of the vertexing variables.

The distribution of EM objects across the detector – particularly in the LAr calorimeter barrel (B) vs. end-cap (E) – also influences the performance of the vertexing variables, since the pointing resolution varies across detector region. Figure 6.5 shows the vertexing distributions in prompt $Z \rightarrow ee$ data and simulation for two different $\Delta\eta_{ee}$ cuts (no cut and $\Delta\eta_{ee} > 0.1$) in three categories of events: those with both electrons in the barrel (BB), both in the end-cap (EE), and one in each (BE). The distributions illustrate that, in terms of vertexing resolution, BE events perform the best outright, followed by BB and finally EE. When a cut of $\Delta\eta_{ee} > 0.1$ is applied, the performance of BB and BE events more closely agree; however, EE events continue to suffer poor resolution in V_Z . (Note that BE events contain an "implicit" $\Delta\eta_{ee}$ cut of at least 0.15: the pseudorapidity coverage in the barrel extends until 1.37 and begins in the end-cap at 1.52).

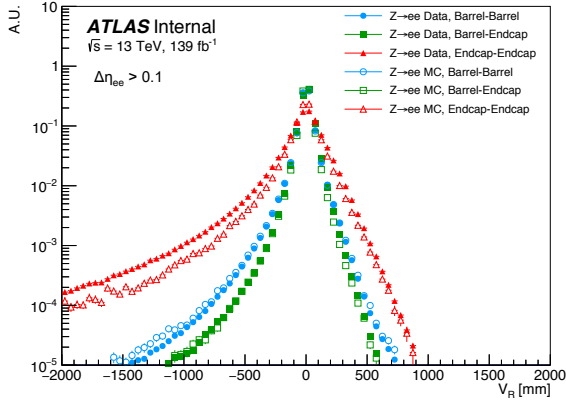
These investigations into the behavior of the vertexing variables directly connect to how the analysis employs them. Chapter 8 provides a more thorough discussion of how the search for displaced di-EM vertices exploits these measurements, including the selections that directly relate to vertexing performance (e.g., a $\Delta\eta$ cut and the rejection of EE events, as discussed in Section 8.1.2) and the combination of V_R and V_Z into a single discriminant, ρ (see Section 8.3).



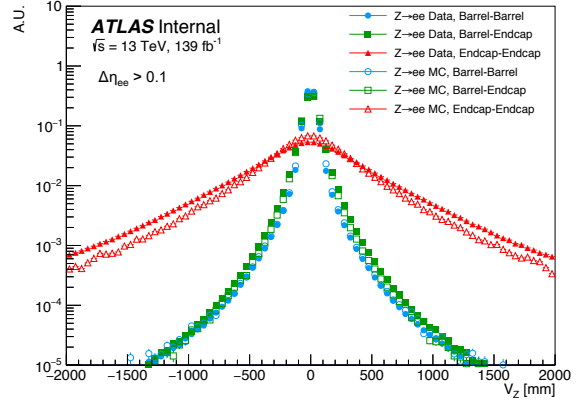
(a) Distribution of V_R , $\Delta\eta_{ee}$ -Inclusive



(b) Distribution of V_Z , $\Delta\eta_{ee}$ -Inclusive



(c) Distribution of V_R , $\Delta\eta_{ee} > 0.1$



(d) Distribution of V_Z , $\Delta\eta_{ee} > 0.1$

Figure 6.5: Comparison of vertexing distributions for different $\Delta\eta_{ee}$ requirements and detector region categories for prompt $Z \rightarrow ee$ data and MC simulation. Good agreement is observed between these two samples, especially for BB and BE events.

6.2 TIMING

In conjunction with their displacement, EM objects from LLP decays arrive at the LAr calorimeter with a time delay compared to those produced directly in the hard-scatter pp process. The delay arises primarily from the time-of-flight of the heavy LLPs, which typically have modest relativistic speeds compared to the speed of light. Additionally, the opening angle of the LLP decay products lengthens the geometrical path to the calorimeter compared to objects coming directly from the PV (see Figure 6.3). This section describes the reconstruction, measurement, calibration, and performance of the LAr timing variable, the most powerful discriminant between delayed signal and prompt background of the analysis.

6.2.1 ELECTRONIC READOUT

When incoming EM particles ionize the LAr calorimeter, the high voltage applied across the LAr-filled gaps causes the newly created ions and electrons to drift to the absorbers and electrodes, respectively [97]. The electrodes send the resulting signal, a triangular pulse, to the on-detector electronics for immediate processing. The signal is split into three overlapping gain scales (HIGH/MEDIUM/LOW), each successively reduced by roughly a factor of ten. For each gain scale, the signal is amplified, shaped by a $CR - (RC)^2$ filter, and sampled at 40 MSPS. Figure 6.6 illustrates the pulse before and after the shaping. The samples are stored in an analog memory, awaiting a Level-1 trigger decision (see Section 4.8); if the event is accepted, four pulse samples from the optimal gain scale are digitized and sent off the detector for further processing.

Since the signal pulse height is directly proportional to the cell energy, the reconstruction of the signal energy relies on two key components: (1) the proportionality factor between the pulse amplitude and deposited energy and (2) the pulse height itself, calculated from the four samples. The calibration and architecture of the on-detector electronics dic-

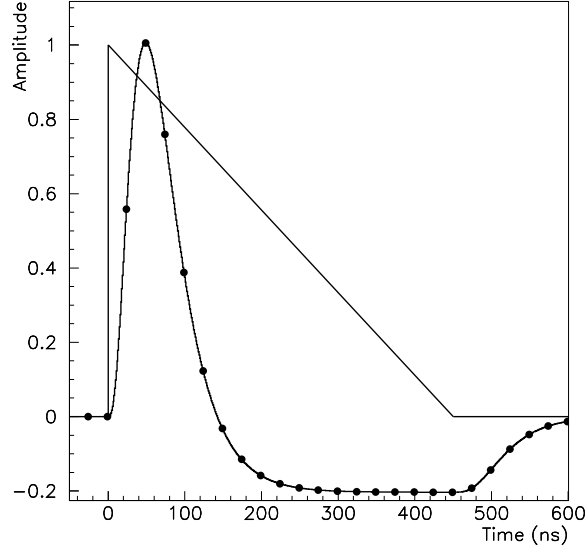


Figure 6.6: LAr calorimeter pulses, including the raw triangular pulse characterizing the detector response and the shaped pulse used in energy and timing computations. The markers on the shaped pulse correspond to the digitized samples, separated by 25 ns [97].

tate the former, and the Optimal Filtering Method [120] determines the latter. This approach derives Optimal Filtering Coefficients (OFCs) using the knowledge of the expected pulse shape and its autocorrelation function. The OFCs (a_i and b_i) are then applied as weights for the samples (S_i) to calculate the pulse amplitude (A) and time (t):

$$A = \sum_{i=0}^{n-1} a_i S_i \quad (6.2)$$

$$t = \frac{1}{A} \sum_{i=0}^{n-1} b_i S_i \quad (6.3)$$

where $n = 4$ for Run 2 measurements.

The advantage of the Optimal Filtering Method lies in its computational simplicity and efficiency: energy and timing information can be computed quickly without needing to read out and fit the entire pulse. OFCs are adjusted periodically (typically a few times per year) to accommodate minor detector fluctuations over time and improve the online

timing performance. An interval of validity (IOV) refers to a data-taking period with a set of constant OFCs.

6.2.2 MEASUREMENT

The raw timing measurement of an EM object is taken from the calorimeter cell in the middle LAr layer with the maximum energy deposit of the cluster ($E_{\text{cell}}^{\text{max}}$, verbalized as "max-E-cell"). This cell generally delivers the measurement with the best timing resolution, which is inversely proportional to cell energy, given that this cell is nearly always the one with the highest energy deposition of the cluster (typically 20-40% of the total energy). Middle layer cells also benefit from lower crosstalk than those in other layers. Studies that investigated incorporating timing measurements from other cells in the cluster found a negligible impact on the timing performance; therefore, only the time corresponding to the $E_{\text{cell}}^{\text{max}}$ is used.

The ATLAS detector's contribution to the LAr cell timing resolution is roughly 100 ps, determined from test beam measurements of individual detector components prior to LHC Run 1. A small portion of this uncertainty arises from the clock jitter of the LAr on-detector electronics, which is less than 20 ps for all channels and is close to 10 ps for most channels [97]; additional sources of uncertainties arise from subtle detector non-uniformities, crosstalk, and noise introduced throughout the TDAQ processing chain.

The longitudinal beams spread of LHC proton bunches introduces a separate, irreducible contribution to the timing resolution for EM objects. Collisions occur at different *positions* along the beamline, with a resolution of about 40 mm, depending on LHC conditions [121]. Similarly, collisions occur at different *times*, with a spread corresponding to a σ of approximately 190 ps.

6.2.3 CALIBRATION

The online timing resolution of EM objects is approximately 1 ns, sufficient for all "standard" ATLAS reconstruction algorithms, including identifying the correct bunch crossing and rejecting out-of-time pileup. However, the online resolution of a single cell is much better than the collective resolution of the 46,000+ middle-layer calorimeter cells, which each have a slightly different, non-zero, online timing mean. The offline timing calibration [93] significantly enhances EM object timing resolution by synchronizing cell times and correcting for various timing dependencies.

The data-driven calibration is performed using prompt electrons from $W \rightarrow e\nu$ and $Z \rightarrow ee$ samples, with selections that provide a relatively high purity of genuine electrons. Since the $W \rightarrow e\nu$ sample has more events than the $Z \rightarrow ee$ sample, the former is used to calculate the timing corrections in the calibration, and the latter serves as a statistically independent validation sample that can guard against over-correction.

The calibration consists of several passes, each correcting for a specific timing dependency. The process is iterative: every new correction is applied to the sample before the next pass proceeds. While this approach does not fully dispel the impacts of correlations between variables involved in the calibration, alternative multidimensional or machine-learning-based approaches were prone to over-correction and suffered from limited statistics. The first calibration pass applies a time-of-flight correction using the spatial positions of the PV and the $E_{\text{cell}}^{\text{max}}$. The remaining corrections are performed separately for each gain (HIGH or MEDIUM) and each IOV. The calibration is not performed for the Low gain, which requires $E_{\text{cell}}^{\text{max}}$ values of at least 250 GeV, due to the insufficient statistics in the $W \rightarrow e\nu$ and $Z \rightarrow ee$ samples.

The second pass introduces a "run number" correction to address variations between LHC fills. Next, corrections for each on-detector electronics board and channel account for hardware-level dependencies; the channel correction constitutes the most impactful

pass of the entire calibration. Subsequently, the calibration applies an energy correction, performed as a function of η , and channel crosstalk corrections which mitigate the impact of crosstalk between cells in the middle layer and across layers. Finally, the channel correction is re-applied to account for minor deviations that re-emerge throughout the calibration due to correlations. Later, at the analysis level, a small analysis-dependent residual timing correction is applied (see Section 8.5.3).

The calibration enacts several safeguards to ensure the validity of each timing measurement. First, since corrections must be calculated for each of the 46,000 channels, some low-luminosity runs and IOVs are removed to combat limited statistics. Additionally, a handful of problematic channels that consistently deliver unreliable timing are flagged as invalid. After applying these performance requirements, the calibration maintains high efficiencies of $> 99\%$ (93%) of HIGH (MEDIUM) gain for most IOVs.

Figure 6.7 illustrates the impact of the Run 2 timing calibration, comparing the pre- and post-calibration electron timing distributions for the $Z \rightarrow ee$ validation sample. Here,

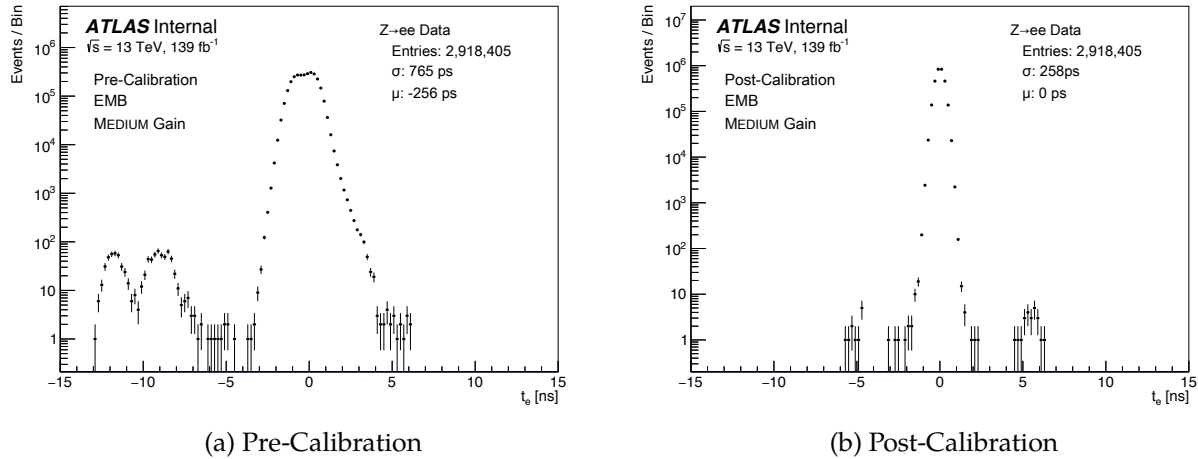


Figure 6.7: Comparison of electron timing distributions (a) before and (b) after the offline timing calibration. Distributions are shown for the MEDIUM gain channels in the EMB for the $Z \rightarrow ee$ validation sample.

representative timing distributions are shown for MEDIUM gain channels in the EMB. The pre-calibration timing distribution is much broader than that of the post-calibration and contains many channels with highly negative timing means around -10 ns. The post-calibration timing distribution features a much narrower core, flanked by smaller peaks at ± 5 ns, which correspond to satellite collisions (see Section 6.2.4). Table 6.1 further showcases the success of the calibration, detailing the pre- and post-calibration timing means and resolutions separately for the HIGH and MEDIUM gain channels, the EMB and EMEC detector regions, and the $W \rightarrow e\nu$ and $Z \rightarrow ee$ data samples. In some cases, the calibration improves timing resolutions by more than a factor of 3.

The uncertainty of each timing measurement is inversely related to cell energy (E_{cell}) and is given by:

$$\sigma_t(E_{cell}) = \frac{p_0}{E_{cell}} \oplus p_1 \quad (6.4)$$

where \oplus represents addition in quadrature and p_0 and p_1 are the coefficients of the noise and constant terms, respectively. Figure 6.8 depicts the falling distribution of the timing resolution as a function of cell energy and illustrates the degree to which the data match the functional form in Equation 6.4. The noise and constant terms vary slightly across

| Detector Region | EMB | | | | EMEC | | | |
|---|-------|----------|--------|----------|-------|----------|--------|----------|
| | HIGH | | MEDIUM | | HIGH | | MEDIUM | |
| GAIN | | | | | | | | |
| Mean (μ) and Resolution (σ) [ps] | μ | σ | μ | σ | μ | σ | μ | σ |
| Pre-Calibration, $W \rightarrow e\nu$ | -274 | 476 | -135 | 710 | -833 | 532 | -263 | 754 |
| Pre-Calibration, $Z \rightarrow ee$ | -476 | 493 | -256 | 765 | -966 | 565 | -235 | 736 |
| Post-Calibration, $W \rightarrow e\nu$ | 0 | 287 | 1 | 250 | -2 | 248 | 1 | 225 |
| Post-Calibration, $Z \rightarrow ee$ | 9 | 275 | 0 | 258 | 3 | 255 | 5 | 230 |

Table 6.1: Comparison of timing distribution means and resolutions in ps, before and after calibration, for HIGH and MEDIUM gains for electrons in $Z \rightarrow ee$ and $W \rightarrow e\nu$ data.

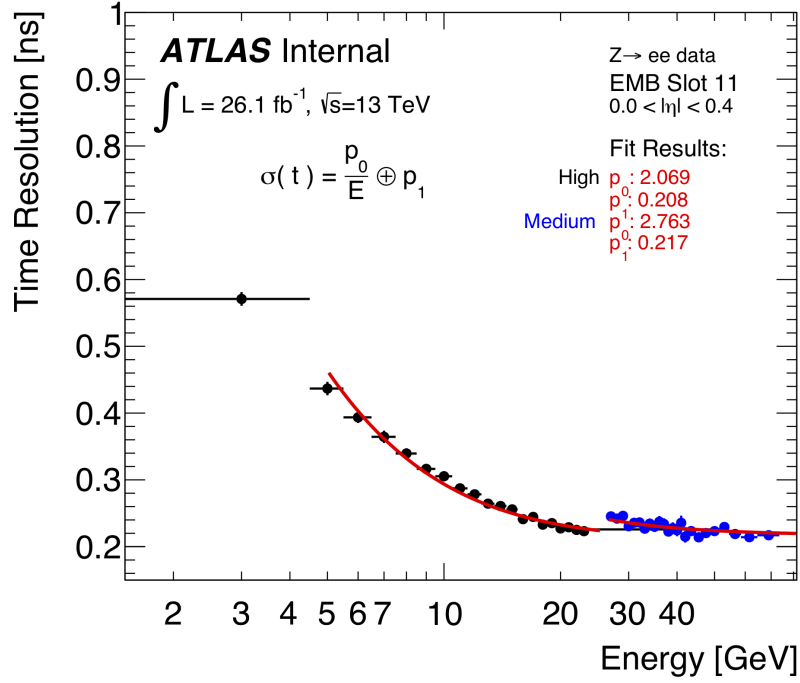


Figure 6.8: Timing resolution as a function of cell energy for HIGH and MEDIUM gain middle-layer cells for a single representative IOV, for $|\eta| < 0.4$. Superimposed are the results of fits using the expression in Equation 6.4, with the values of p_0 and p_1 given in units of GeV·ps and ps, respectively.

different gains and regions of the detector, with p_0 and p_1 each measuring roughly 190-240 GeV·ps and 210-225 ps, respectively.

6.2.4 SATELLITE COLLISIONS

As discussed in Chapter 3, the LHC organizes proton bunches into buckets, with the main bunches separated by 25 ns. However, some overflow into neighboring buckets occurs at multiples of ± 5 ns, producing satellite bunches and, consequently, satellite collisions. Although suppressed relative to the primary collisions by a factor of over 10^5 , satellite collisions introduce a distinct structure into the LAr timing distributions, as exemplified by the peaks at ± 5 ns in LAr timing distributions (see Figure 6.7b). Additionally, Figure 6.9, which shows a two-dimensional distribution of electron times for a $Z \rightarrow ee$ data sample, clearly illustrates the presence of satellite collisions at ± 5 ns and even higher multiples of

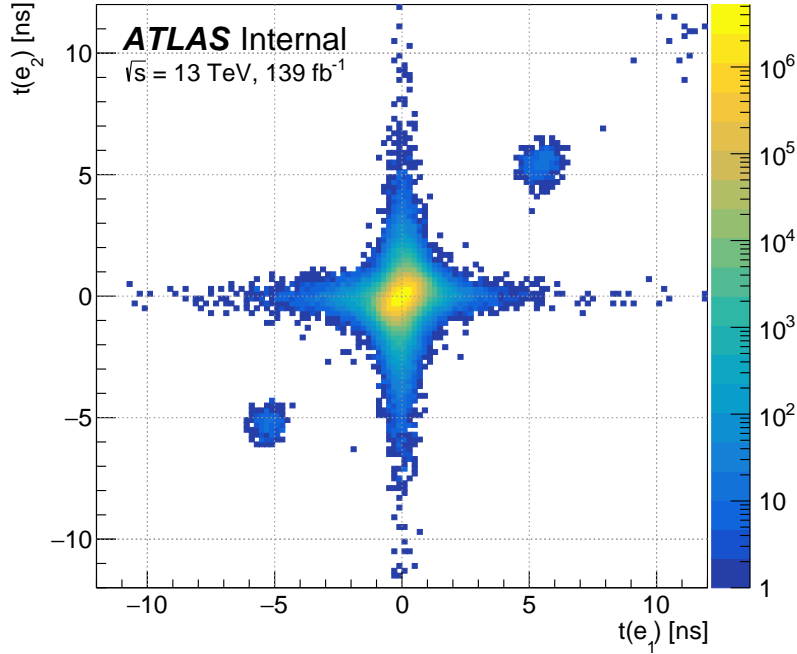


Figure 6.9: Distribution of leading (highest p_T) versus subleading (second-highest p_T) electron time for the $Z \rightarrow ee$ data sample. Populations of electrons from satellite collisions are visible at ± 5 ns and $+10$ ns.

5 ns. Here, the presence of satellite collisions at $+10$ ns and lack of them at -10 ns are artifacts of the asymmetry in the satellite bunch structure. Satellite collisions are discussed in various contexts throughout Part III, and Appendix B.1 discusses the prevalence of satellite collisions in more detail.

6.2.5 MONTE CARLO SMEARING

A timing smearing procedure is applied to simulated samples to ensure that the timing behavior of the MC simulation (see Section 7.2) matches that of the data. The smearing accounts for uncorrelated contributions attributed to the detector and correlated contributions – visible in the core of the distribution in Figure 6.9 – attributed to the beamspread. The electron times in $Z \rightarrow ee$ data can be used to extract the correlated and uncorrelated components of the timing uncertainty. These measurements lead to a correlated compo-

ment of roughly 190 ps, consistent with the expected timing variations due to the beam-spread. This measurement depends slightly on the PV position and the kinematics of the EM objects.

The timing smearing procedure introduces small, randomly generated fluctuations drawn from Gaussian distributions centered at zero with resolutions consistent with the correlated and uncorrelated timing uncertainty components measured in the data. The final smeared time, t_{smeared} , for a given photon is:

$$t_{\text{smeared}} = t_{\text{raw}} + t_{\text{collision}} + t_{\text{uncorr}} \quad (6.5)$$

where t_{raw} is the raw time produced by the simulation, $t_{\text{collision}}$ is the randomly generated collision time, and t_{uncorr} is the randomly generated uncorrelated time component. While $t_{\text{collision}}$ is the same for each object in a single event and represents the correlated uncertainty component, t_{uncorr} is unique to each EM object in order to best match the distributions in data. The resolution of t_{uncorr} varies as a function of $E_{\text{cell}}^{\text{max}}$ and detector region.

Although this smearing procedure accurately models the central Gaussian cores of the timing distributions, it fails to account for higher-order effects present in the data, including non-Gaussian tails and satellite collisions. Therefore, while the timing distributions of photons and electrons in the long-lived simulated signals are generally well-modeled, any background estimation of LAr calorimeter timing measurements must be data-driven.

PART III:

SEARCH

CHAPTER 7:

DATA AND SIMULATED SAMPLES

The edge of the sea is a strange and beautiful place.

— Rachel Carson

ATLAS physics analyses utilize data and simulated samples to expand the understanding of fundamental particles' properties, interactions, and behavior. The careful processing, filtering, and cleaning of data events enhances the quality of observables and thus the potential for precise measurements and novel discoveries. The accurate simulation of various physics processes within and beyond the SM is integral to background modeling, validation of analysis variables, and search optimization.

This chapter discusses the samples used directly in this search. Section 7.1 describes the data sample and various data quality requirements, while Sections 7.2-7.3 focus on simulated samples, including the MC production process and the parameters of the signal models.

7.1 DATA

The analysis uses the full ATLAS Run 2 dataset of pp collisions with center-of-mass energies of 13 TeV. During Run 2, the LHC delivered an integrated luminosity of 156 fb^{-1} , of which the ATLAS detector recorded 147 fb^{-1} . The slight inefficiency arises from disruptions to the data acquisition system and the time delay in starting all detector subsystems after the declaration of stable beams. Most Run 2 ATLAS analyses, including this one, use the 139 fb^{-1} of data considered "good for physics." These events must pass a series of data quality checks that reject corrupted or incomplete events, including those that fail the cosmic muon veto or coincide with any subsystem malfunctioning. Figure 7.1 shows the total integrated luminosity delivered by the LHC, recorded by ATLAS, and considered good for physics as a function of time throughout Run 2, which operated from 2015 through 2018.

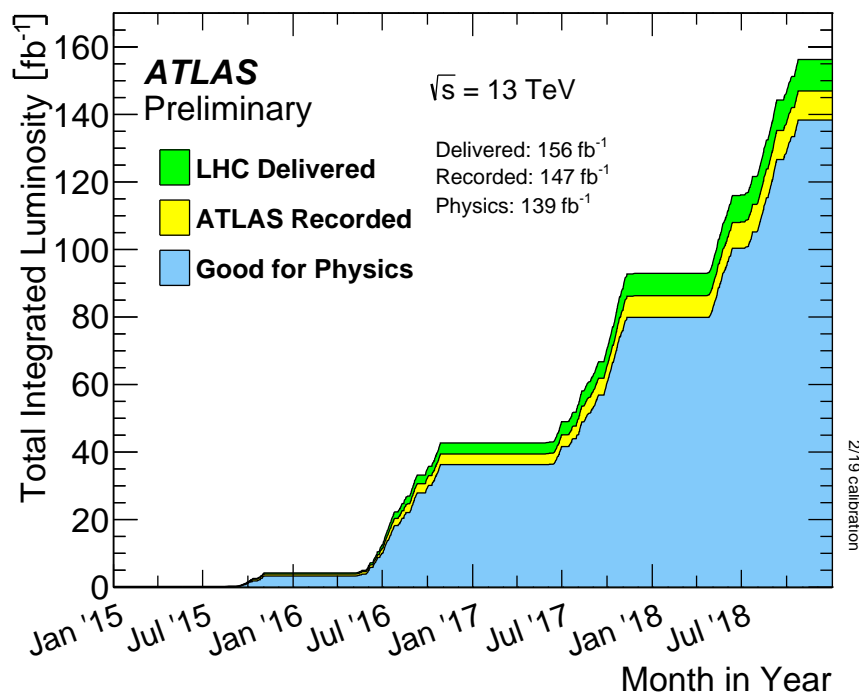


Figure 7.1: Integrated luminosity delivered by the LHC and collected by the ATLAS detector as a function of time during Run 2, the period from 2015 through 2018 [90].

7.2 MONTE CARLO SIMULATION

The simulation of pp collisions utilizes the MC method to capture the wide variety of possible final states produced by a given physics process. Here, the MC production process consists of several steps, from modeling the parton distribution function (PDF), which describes how a proton’s energy is shared amongst its constituent quarks and gluons, to the simulation of detector signatures, reconstructed as if genuinely recorded by the ATLAS detector.

MC production begins with the generation step, which creates all associated Feynman diagrams of a process and models the pp collision by calculating the matrix elements of the $2 \rightarrow n$ scattering. For the long-lived higgsino signal processes described in Section 2.4.2, the matrix elements are generated using MADGRAPH 2.7.3 [122]. MC generation relies on several parameters, including the renormalization factor (μ_R) of the strong force coupling and the factorization scale (μ_F), which sets the spatial scale below which components enter into the PDF and above which they are treated as participants in the hard-scatter process.

The next step in MC production is the showering step, performed by PYTHIA8.2 [123] for the signal, which simulates parton hadronization and introduces pileup effects. The event is then fed through a GEANT4 [124] simulation of the ATLAS detector, producing detector hits and their associated digitized signals. Finally, the event is reconstructed using the same algorithms that are applied to real data, as described in Chapter 5.

7.3 SIMULATED SIGNAL SAMPLES

Chapter 2 introduced the theoretical motivation of the SUSY GMSB model chosen for this analysis, including the general properties of long-lived higgsino NLSPs, whose Feynman diagrams are illustrated in Figure 2.3. This section describes the translation of this simplified model into simulation, including the choices of both fixed and variable parameters.

As discussed, the signal model consists of pair-produced electroweakinos ($\tilde{\chi}_2^0, \tilde{\chi}_1^\pm$) that each decay into a long-lived neutralino NLSP ($\tilde{\chi}_1^0$), which then decays into a Higgs boson or Z boson plus a gravitino LSP (\tilde{G}). At least one of the two¹ Higgs/Z bosons in the event must produce a di-EM decay ($H \rightarrow \gamma\gamma$ or $Z \rightarrow ee$) while the other assumes its SM decay branching ratios ($H \rightarrow \text{SM}$ or $Z \rightarrow \text{SM}$). Table 7.1 summarizes the signal grid, which scans over $\tilde{\chi}_1^0$ mass (m), lifetime (τ), and branching ratio (BR). Specific signal points are typically labeled by these parameters in the following convention: $\tilde{\chi}_1^0(m, \tau) \rightarrow X + \tilde{G}$ with $X = H, Z$.

¹ Here, the "two" Higgs/Z bosons refer to the direct decay products of the two $\tilde{\chi}_1^0$'s in the event and do not include Z boson decay products of the Higgs boson (e.g., $H \rightarrow Z\gamma$ or $H \rightarrow ZZ$).

| Higgsino ($\tilde{\chi}_1^0$) Mass [GeV] | Cross Section [fb] | Run 2 Nominal Yields | | Lifetimes Generated [ns] | |
|--|-------------------------------|--|--------------------------------------|--|--------------------------------------|
| | | $H \rightarrow \gamma\gamma$ | $Z \rightarrow ee$ | $H \rightarrow \gamma\gamma$ | $Z \rightarrow ee$ |
| 100 | $16,797 \pm 603$ | - | 156,897 | - | 2, 10, 20 |
| 135 | $5,996 \pm 241$ | 3,784 | 56,003 | 2, 10, 20, 50 | 2, 10, 20, 50 |
| 175 | $2,268 \pm 100$ | 1431 | 21,184 | 2, 10, 20 | 2, 10, 20 |
| 225 | 861 ± 43 | 543 | 8,039 | 2, 10, 20, 50 | 2, 10, 20 |
| 275 | 400 ± 22 | 252 | 3,737 | 2, 10, 20 | - |
| 325 | 207 ± 13 | 131 | 1,937 | 2, 10, 20 | 2, 10, 20, 50 |
| 375 | 116 ± 7 | 73.2 | 1,084 | 2, 10 | - |
| 425 | 68.7 ± 5.0 | 43.4 | 642 | 2, 10 | 2, 10, 20 |
| 475 | 42.5 ± 3.3 | 26.8 | 397 | 2, 10 | - |
| 525 | 27.2 ± 2.2 | 17.2 | 254 | 2, 10 | 2, 10, 20, 50 |
| 625 | 12.1 ± 1.1 | 7.61 | 113 | - | 2, 10, 20 |
| 725 | 5.78 ± 0.58 | 3.65 | 54.0 | - | 2, 10 |
| 825 | 2.93 ± 0.32 | 1.85 | 27.4 | - | 2, 10 |
| 925 | 1.55 ± 0.18 | 0.98 | 14.5 | - | 2, 10 |

Table 7.1: The grid of long-lived higgsino signal models, including $\tilde{\chi}_1^0$ masses, cross sections, and Run 2 yields, corresponding to an integrated luminosity of 139 fb^{-1} , for various signal points. At least one Higgs boson or Z boson must decay into photons or electrons, with $\text{BR}(H \rightarrow \gamma\gamma) = 2.27 \times 10^{-3}$ and $\text{BR}(Z \rightarrow ee) = 3.36 \times 10^{-2}$. Here, all samples labeled by $H \rightarrow \gamma\gamma$ assume $\text{BR}(\tilde{\chi}_1^0 \rightarrow H + \tilde{G}) = 1$, and those labeled by $Z \rightarrow ee$ assume $\text{BR}(\tilde{\chi}_1^0 \rightarrow Z + \tilde{G}) = 1$. The lifetimes generated for each signal mass and final state are also shown.

Signal points are generated with one of four possible final states: (1) $H \rightarrow \gamma\gamma + H \rightarrow \text{SM}$, (2) $H \rightarrow \gamma\gamma + Z \rightarrow \text{SM}$, (3) $Z \rightarrow ee + H \rightarrow \text{SM}$, and (4) $Z \rightarrow ee + Z \rightarrow \text{SM}$. It is possible to produce signal points along a continuum of $\text{BR}(\tilde{\chi}_1^0)$ values by combining the four different final states and tuning their relative weights. However, for most of this thesis, only signal models with $\text{BR}(\tilde{\chi}_1^0 \rightarrow H + \tilde{G}) = 1$ or $\text{BR}(\tilde{\chi}_1^0 \rightarrow Z + \tilde{G}) = 1$ are explicitly discussed. Unless otherwise specified, signals are often referred to by their final state: $H \rightarrow \gamma\gamma$ for models with $\text{BR}(\tilde{\chi}_1^0 \rightarrow H + \tilde{G}) = 1$, and $Z \rightarrow ee$ for models with $\text{BR}(\tilde{\chi}_1^0 \rightarrow Z + \tilde{G}) = 1$.

A higgsino-like $\tilde{\chi}_1^0$ leads to a nearly mass-degenerate triplet of the lightest three electroweakinos. In this simplified model, these three particles have fixed mass differences, $m(\tilde{\chi}_1^\pm) = m(\tilde{\chi}_2^0) = m(\tilde{\chi}_1^0) + 1 \text{ GeV}$, with the values of $m(\tilde{\chi}_1^0)$ ranging from 100 to 925 GeV. The value of $m(\tilde{G})$ is fixed at 1 MeV, rendering it virtually massless compared to the mass scale of the electroweakinos, a property consistent with GMSB SUSY phenomenology. The lowest values of $m(\tilde{\chi}_1^0)$ are 10 GeV above the final state Higgs/Z boson masses and extend to 525 GeV (925 GeV) for signals with $H \rightarrow \gamma\gamma$ ($Z \rightarrow ee$). The difference in the $m(\tilde{\chi}_1^0)$ coverage emerges from the fact that the branching ratio of $Z \rightarrow ee$ (3.36×10^{-2}) is far greater than that of $H \rightarrow \gamma\gamma$ (2.27×10^{-3}), leading to relatively higher event yields for and higher expected sensitivity to signal models with $Z \rightarrow ee$ in the final state. The spacing between mass points is smaller at lower masses to accommodate the rapid kinematic changes of this region.

The signal grid includes $\tilde{\chi}_1^0$ lifetime values ranging from 2 to 50 ns, which covers lifetimes long enough to be resolved from prompt events but short enough to have a high enough fraction of events still decay inside the detector. A lifetime reweighting procedure allows for the interpolation between and the extension above and below the simulated signal lifetimes. For this procedure, a new weight is calculated for each event in a sample by:

$$w_{\tau_{\text{source}} \rightarrow \tau_{\text{target}}} = \frac{\tau_{\text{source}}}{\tau_{\text{target}}} \exp \left[-t_{\text{event}} \left(\frac{1}{\tau_{\text{target}}} - \frac{1}{\tau_{\text{source}}} \right) \right] \quad (7.1)$$

where τ_{source} (τ_{target}) is the $\tilde{\chi}_1^0$ lifetime of the source (target) signal model, and t_{event} is the decay time of the particular event in question. This strategy provides coverage over a continuum of lifetimes without the considerable computational overhead of simulating distinct signal grid points. Validation studies of the lifetime reweighting procedure are documented in Appendix C.1. These studies demonstrate that the approach delivers reliable reweighting values for signal lifetimes ranging from 0.25 ns to 1 μ s.

CHAPTER 8:

ANALYSIS STRATEGY

You sometimes have to make more of a mess with a Rubik's cube before you can get it to go right.

— Dame Jocelyn Bell Burnell

This search targets the displaced and delayed production of Higgs bosons and Z bosons in the $H \rightarrow \gamma\gamma$ and $Z \rightarrow ee$ final states, as discussed. The analysis draws inspiration from previous singly-produced non-pointing photon searches [3,118,119]; however, at the same time, it explores novel approaches to contend with a unique set of analysis variables and a largely unexplored detector signature. This chapter discusses the strategy of the analysis, from overarching priorities to specific, quantifiable decisions.

The analysis capitalizes on the precise timing and vertexing capabilities of the LAr calorimeter described in Chapter 6. Section 8.1 outlines the event selection criteria, which uses photon objects to reconstruct photons and electrons from displaced $H \rightarrow \gamma\gamma$ and displaced $Z \rightarrow ee$ decays. The analysis strategy relies on a data-driven background estimation derived from a signal-depleted Control Region (CR) to predict the background shape in a signal-enriched Signal Region (SR) (see Section 8.2).

Results are obtained using a simultaneous likelihood fit of the background prediction and SR data across the average photon timing distribution categorized by secondary ver-

tex displacement. Section 8.3 describes and motivates the implementation of the observables in the fit, and Section 8.4 gives an overview of the optimization procedure of the analysis. Finally, Section 8.5 presents the background estimation strategy, including the construction of the background template used in the fit. Appendix D documents additional analysis-related studies not included in this chapter.

8.1 EVENT SELECTION

The event selection strategy aims to maximize signal acceptance, reject background, and enhance the performance of key analysis variables, including timing and vertexing. Also called the analysis *preselection*, the event selection includes requirements on photon objects (Section 8.1.1) and at the event-level (Section 8.1.2). Table 8.1 summarizes these selections and can be found at the end of this section.

8.1.1 PHOTON OBJECT SELECTION

The analysis uses *photon objects* to reconstruct both displaced *photons* and displaced *electrons*. These object requirements are applied to all signals, regardless of the final state ($H \rightarrow \gamma\gamma/Z \rightarrow ee$). This practice is possible because a displaced electron produced in or beyond the pixel detector generally lacks the necessary ID hits to definitively identify the object as an electron (see Section 5.3.2). In the case of any electron-photon ambiguity, the overlap removal procedure described in Section 5.6 prioritizes photon reconstruction. Note that electrons with low displacements (produced within 50 mm of the PV) are frequently reconstructed as electron objects; however, these events constitute only a small fraction of signal events. While previous displaced lepton searches have employed photon triggers for displaced electrons [125], the intentional offline reconstruction of displaced electrons as photon objects is relatively unique to this analysis.

Like most ATLAS standard reconstruction algorithms, photon reconstruction, identification, and isolation algorithms focus on prompt, pointing objects. Photons and electrons that originate from a displaced vertex can be highly *non*-pointing since they enter the detector at non-projective angles with respect to the PV. Therefore, the nature of non-pointing EM objects demands a careful choice of photon identification and isolation working points.

TRIGGER AND IDENTIFICATION

A fundamental challenge in any hadron collider physics analysis is the choice of the trigger. Since the search targets EM objects produced by a heavy resonance (Higgs/Z boson), which has some boost from a heavier parent ($\tilde{\chi}_1^0$), the final state objects are energetic enough to use directly in the trigger. The ability to trigger directly on the signal’s final state of interest – as opposed to associated objects – also enhances the model independence of the analysis.

The ATLAS Run 2 trigger menu provides several diphoton trigger options, each with a distinct PID working point (LOOSE/MEDIUM/TIGHT) and a set of p_T thresholds for the leading and subleading photons (those with the highest and second-highest p_T , respectively). As introduced in Section 4.8, the choice of PID that maximizes signal acceptance is inextricably linked with the p_T requirements on the photons to ensure manageable trigger rates: a more lenient PID algorithm requires higher p_T thresholds and vice-versa.

Figure 8.1 shows photon PID efficiency as a function of pointing for $H \rightarrow \gamma\gamma$ and $Z \rightarrow ee$ signals. The TIGHT PID imposes the most stringent requirements on the photon object shower shape, degrading the overall reconstruction efficiency and introducing a significant bias against displaced objects that becomes particularly pronounced for pointing values beyond 200 mm. Previous ATLAS displaced photon analyses have also observed this behavior and have cited it as a reason against using the TIGHT PID [118,119].

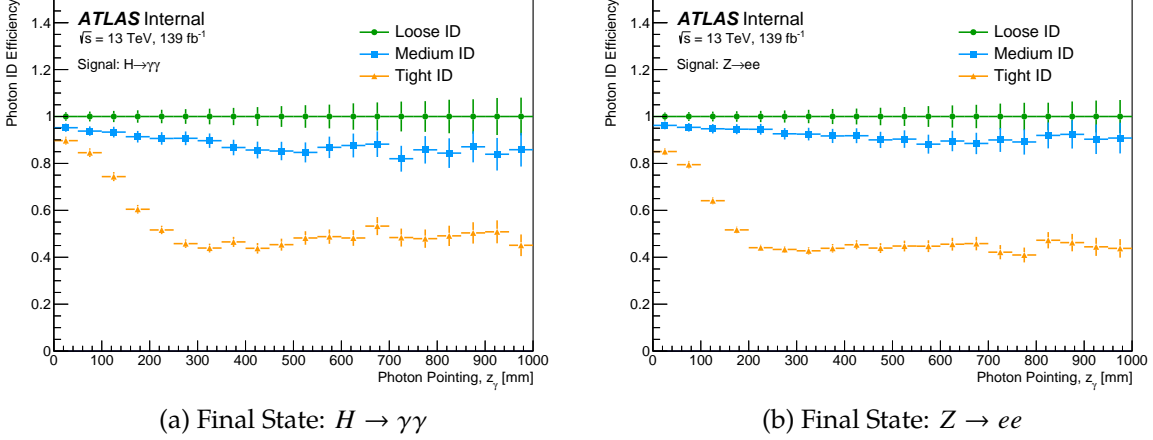


Figure 8.1: Photon identification efficiency as a function of pointing, z_γ (see Equation 6.1). Efficiencies are computed with respect to the LOOSE photon PID working point. Signals shown have $m(\tilde{\chi}_1^0) = 135$ GeV and $\tau(\tilde{\chi}_1^0) = 2$ ns, with final states (a) $H \rightarrow \gamma\gamma$ and (b) $Z \rightarrow ee$.

The LOOSE and MEDIUM PID apply much less strict object requirements and therefore have higher identification efficiencies for displaced objects.

Since the MEDIUM and LOOSE photon PIDs deliver comparable signal identification efficiencies, the set of p_T thresholds of the available triggers becomes the deciding factor of the PID working point. Figure 8.2 demonstrates that the MEDIUM diphoton trigger significantly outperforms the LOOSE in terms of signal efficiency across various signal models. This behavior emerges because the MEDIUM diphoton trigger requires the leading (sub-leading) photon to satisfy $p_T > 35$ (25) GeV, while the LOOSE diphoton trigger requires both photons to pass $p_T > 50$ GeV. The LOOSE diphoton trigger's higher p_T thresholds – especially for the subleading photon – significantly degrades signal acceptance. Another feature evident in Figure 8.2 is that signals with $Z \rightarrow ee$ in the final state have lower trigger efficiencies than those with $H \rightarrow \gamma\gamma$. This phenomenon arises from a combination of two factors: first, electrons have a slightly lower photon PID efficiency than photons do; and second, electrons from $Z \rightarrow ee$ have a slightly softer p_T spectra than photons from $H \rightarrow \gamma\gamma$ do (since $m_Z < m_H$).

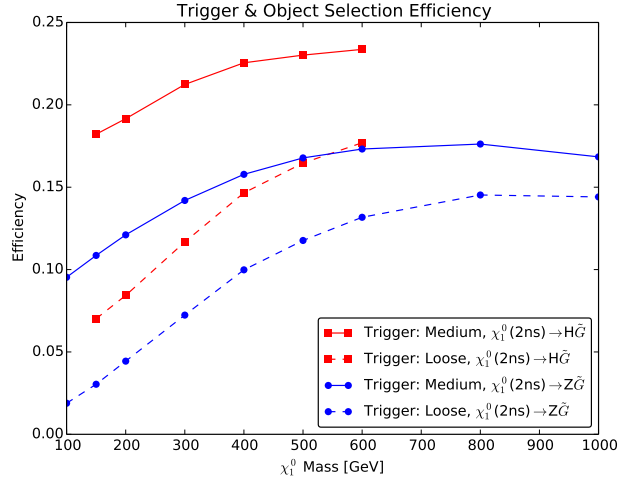


Figure 8.2: Comparison of signal efficiencies for two different trigger scenarios – MEDIUM and LOOSE diphoton triggers – across candidate signal mass, lifetime, and decay mode. Here, the object selection efficiency refers to PID, p_T , and η requirements only.

The analysis, therefore, employs the MEDIUM diphoton trigger and PID (further studies contributing to this decision can be found in Appendix D.1). The leading (subleading) photon must have $p_T > 40$ GeV (30 GeV) – 5 GeV higher than the trigger thresholds to ensure all events are on the trigger efficiency plateau (see Figure 4.12). Additionally, to ensure that the LAr calorimeter captures the entire photon shower, the photon object must be either in the EM barrel ($|\eta| < 1.37$) or EM end-cap ($1.52 < |\eta| < 2.37$).

ISOLATION

Isolation requirements, introduced in Section 5.3.3, eliminate photon candidates with a high amount of surrounding calorimeter activity, a property typically associated with jets. As demonstrated in Figure 8.3, the FIXEDCUTLOOSE working point’s high signal acceptance compared to the other two working points and its lack of significant bias against displaced objects make it the optimal choice for photon isolation.

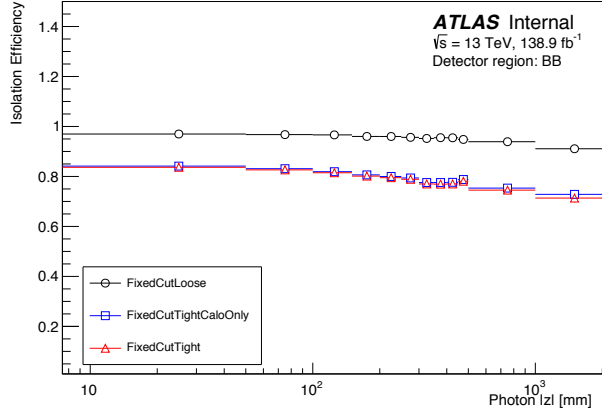


Figure 8.3: Comparison of signal efficiencies for the three ATLAS photon isolation working points as a function of photon pointing. Here, the signal is represented by adding many different signal models together to enhance statistics.

TIMING-RELATED SELECTIONS

The use of photon timing demands several dedicated selections that reject corrupted, invalid, and low-quality measurements. The photon objects must successfully pass the LAr timing calibration described in Section 6.2, which, among other conditions, requires the readout gain of the $E_{\text{cell}}^{\text{max}}$ to be either HIGH or MEDIUM. The rejection of Low gain timing measurements, which are not part of the calibration, has a minimal impact on the signal efficiency.

A selection on the absolute value of the photon time, $|t| < 12$ ns, is also applied. In the data, this requirement rejects objects that might have originated from neighboring bunch crossings at ± 25 ns. Simulation modeling issues distort photon times with $|t| > 12.5$ ns, so this selection also discards problematic MC events. This selection has a negligible impact on signal acceptance for two reasons: (1) the proper decay time of LLPs in the signal follows an exponential decay curve, so only a small fraction of signal events decay beyond 12 ns, and (2) events with higher decay times tend to escape the detector regardless.

Finally, photons must have $E_{\text{cell}}^{\text{max}} > 5$ GeV. This selection reduces the background and rejects very low-energy EM objects with poor timing measurements since the LAr timing

| Category | Variable | Selection |
|---------------|--------------------------------|---|
| Photon Object | Multiplicity | ≥ 2 |
| | Leading (subleading) p_T | $> 40 \text{ GeV}$ ($> 30 \text{ GeV}$) |
| | $ \eta $ | < 1.37 or $\in [1.52, 2.37]$ |
| | Identification | MEDIUM |
| | Isolation | FIXEDCUTLOOSE |
| | Gain | HIGH or MEDIUM |
| | Timing | Valid timing, with $ t < 12 \text{ ns}$ |
| Event-Level | $E_{\text{cell}}^{\text{max}}$ | $> 5 \text{ GeV}$ |
| | Diphoton Mass | $m_{\gamma\gamma} > 60 \text{ GeV}$ |
| | $ \Delta\eta_{\gamma\gamma} $ | > 0.1 |
| | Diphoton Vertex | $0 < V_R < 1500 \text{ mm}$, $ V_Z < 3740 \text{ mm}$ |
| | Detector Region | ≥ 1 photon with $ \eta < 1.37$ (BB or BE events) |

Table 8.1: Summary of the event selection, including photon object and event-level requirements.

resolution is inversely related to $E_{\text{cell}}^{\text{max}}$ (see Figure 6.8). The specific choice of 5 GeV was determined through an optimization procedure (see Section 8.4).

8.1.2 EVENT-LEVEL REQUIREMENTS

Events must have at least two photon objects that satisfy the requirements in Section 8.1.1 and are matched to those selected by the trigger. The diphoton system, defined by the leading and subleading photon, must have $m_{\gamma\gamma} > 60 \text{ GeV}$, a requirement that suppresses residual trigger turn-on effects (see Appendix D.1).

The remaining event-level requirements enhance the resolution and reliability of the diphoton vertexing variables. Events with two end-cap photons (EE) have poor vertex resolution and are rejected (see Section 6.1.3). Eliminating events with photons in the very forward region has the added benefit of improving the signal-to-background ratio. The vertex resolution is inversely related to the absolute difference in η between the two photons, $\Delta\eta_{\gamma\gamma}$ (see Figure 6.4). Therefore, an optimized selection of $\Delta\eta_{\gamma\gamma} > 0.1$ is applied to reject background events with poorly reconstructed vertices. Figure 8.4 shows the dis-

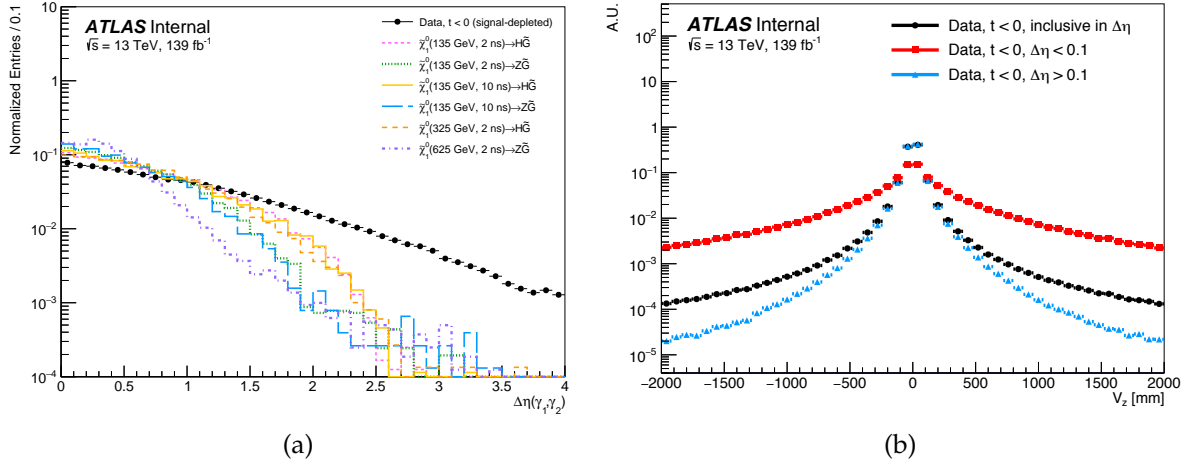


Figure 8.4: Distribution of (a) $\Delta\eta_{\gamma\gamma}$ for data and representative signal points and the (b) impact of the $\Delta\eta_{\gamma\gamma} > 0.1$ selection on the V_R distribution. All samples shown pass the photon object selections. The data samples shown are depleted in signal by requiring both photons to have negative photon times (see Section 8.2.1).

tribution of $\Delta\eta_{\gamma\gamma}$ in data and signal and the impact of the $\Delta\eta_{\gamma\gamma}$ selection on the background vertex distributions. Although imposing this $\Delta\eta_{\gamma\gamma}$ requirement does not improve the signal-to-background ratio, it significantly improves the performance of the vertexing variables used later in the analysis. Events must also satisfy $0 < V_R < 1500 \text{ mm}$ and $V_Z < 3740 \text{ mm}$ to veto pathological vertices, including those reconstructed far beyond the detector.

8.2 ANALYSIS REGION DEFINITIONS

Events passing the event selection are organized into statistically independent analysis regions. The CR, used to derive the background estimation, is designed to have a large sample size while maintaining negligible signal contamination. The Validation Regions (VRs), also depleted in signal, help to validate the background estimation and statistical analysis. Finally, the SR defines the analysis region of interest for the search. To minimize bias, the timing and vertexing distributions in the SR were blinded throughout the development and finalization of the background estimation strategy.

Several event-level variables – photon timing, E_T^{miss} , $m_{\gamma\gamma}$, diphoton transverse momentum ($p_T^{\gamma\gamma}$), and diphoton azimuthal separation ($\Delta\phi_{\gamma\gamma}$) – demarcate the boundaries of the CR, VRs, and SR. These variables, their roles in the analysis region definition, and the analysis regions are discussed throughout this section.

8.2.1 TIMING

The prompt background timing distribution is symmetric about and centered at $t = 0$. In contrast, most signal events include leading and subleading photon times (t_{γ_1} and t_{γ_2}) with positive values; consequently, regions with $t_{\gamma_1}, t_{\gamma_2} < 0$ have very low levels of signal contamination. Therefore, regions separated only by a selection at $t = 0$ share a practically identical kinematic regime but contain very different levels of signal yields. A selection on photon timing – in particular, a selection on the *sign* of the times – provides a critical handle on region definition.

The signs of the two photon times define four timing "quadrants," visualized in Figure 8.5. The quadrants are: pospos ($t_{\gamma_1}, t_{\gamma_2} > 0$), negneg ($t_{\gamma_1}, t_{\gamma_2} < 0$), posneg ($t_{\gamma_1} > 0, t_{\gamma_2} < 0$), and negpos ($t_{\gamma_1} < 0, t_{\gamma_2} > 0$). Since the background timing distributions are sym-

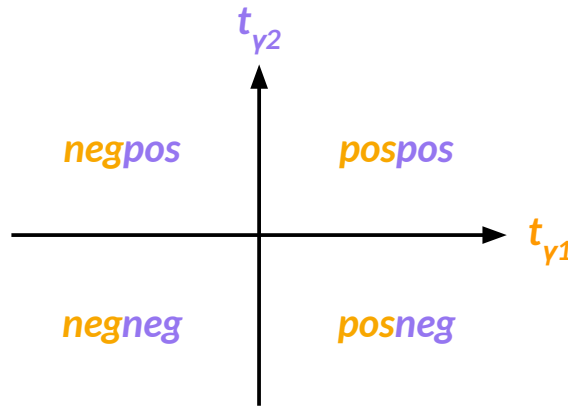


Figure 8.5: Schematic of timing region quadrants for leading photon time (t_{γ_1}) and sub-leading photon time (t_{γ_2}). The four timing quadrants include pospos ($t_{\gamma_1}, t_{\gamma_2} > 0$), negneg ($t_{\gamma_1}, t_{\gamma_2} < 0$), posneg ($t_{\gamma_1} > 0, t_{\gamma_2} < 0$), and negpos ($t_{\gamma_1} < 0, t_{\gamma_2} > 0$).

metric about $t = 0$, it is possible, for example, to use signal-depleted negneg timing distributions to predict and validate the timing distributions of the background in a pospos region (see Appendix C.2).

8.2.2 MISSING TRANSVERSE ENERGY

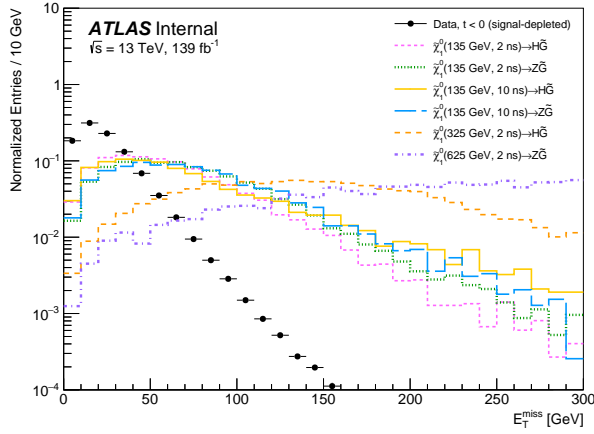
The signal contains several sources of E_T^{miss} , including the stable gravitino LSPs, any $\tilde{\chi}_1^0$'s that escape the detector, and SM decays to neutrinos (e.g., $Z \rightarrow \nu\nu$). This complex pattern of E_T^{miss} sources impacts various signal models differently. For example, signal models with a higher $m(\tilde{\chi}_1^0)$ produce harder detector decay products, including invisible ones; additionally, longer-lived signals contain a higher fraction of $\tilde{\chi}_1^0$'s that decay beyond the detector.

Figure 8.6a shows the E_T^{miss} distribution in data and for several representative signal models. Here, the trends discussed in the previous paragraph hold: signal models with higher $\tilde{\chi}_1^0$ masses and higher $\tilde{\chi}_1^0$ lifetimes tend to have harder E_T^{miss} spectra. Overall, since the data have a much softer E_T^{miss} spectrum than the signal, regions with high (low) E_T^{miss} are relatively enriched (depleted) in signal. Previous analyses targeting SUSY GMSB models with displaced photons have also used E_T^{miss} to define analysis regions [3,118,119].

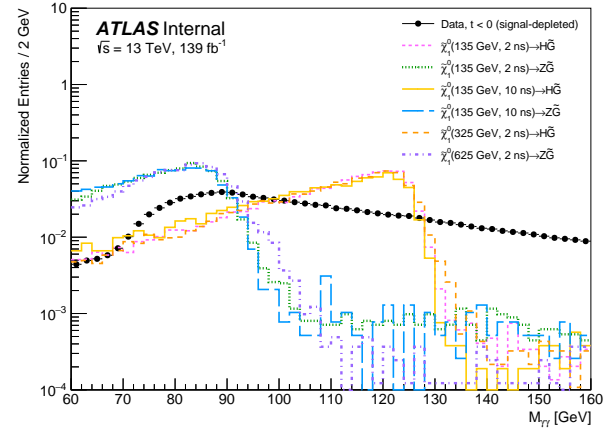
8.2.3 DIPHOTON MASS, MOMENTUM, AND ANGULAR SEPARATION

The kinematic properties of the signal's di-EM system also determine the analysis regions. Figure 8.6b shows the diphoton mass distribution for the background and several representative signal models. As expected, $m_{\gamma\gamma}$ distributions in the signal peak at 125 GeV (91 GeV) for models with $H \rightarrow \gamma\gamma$ ($Z \rightarrow ee$) in the final state. These $m_{\gamma\gamma}$ distributions exhibit slowly falling low-mass tails rather than crisp peaks; this behavior is an artifact of the diphoton mass calculation, which assumes the decay occurs at the PV and therefore underestimates the diphoton opening angle. Consequently, $m_{\gamma\gamma}$ is increasingly underestimated with increasing displacement.

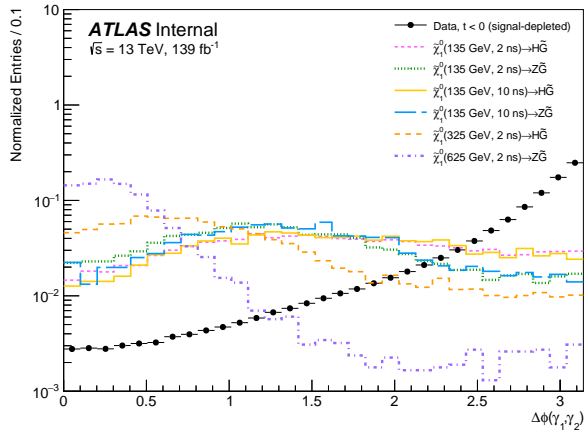
Figures 8.6c and 8.6d show the $p_T^{\gamma\gamma}$ and $\Delta\phi_{\gamma\gamma}$ distributions for signal and background. In the signal, the Higgs boson and Z boson inherit some boost from their heavy parent ($\tilde{\chi}_1^0$), contributing to the final state's high $p_T^{\gamma\gamma}$ and producing somewhat collimated (vs. back-to-back) final state EM objects. Given these variables' modest separation between signal and background, selecting for high- $p_T^{\gamma\gamma}$ and low- $\Delta\phi_{\gamma\gamma}$ in the SR further enhances its signal-to-background ratio.



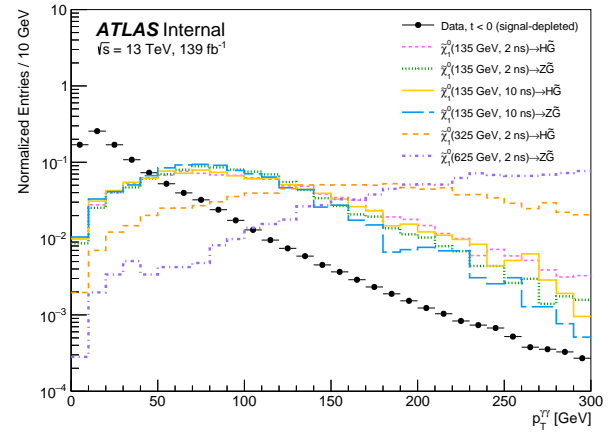
(a) Distribution of E_T^{miss}



(b) Distribution of $m_{\gamma\gamma}$



(c) Distribution of $\Delta\phi_{\gamma\gamma}$



(d) Distribution of $p_T^{\gamma\gamma}$

Figure 8.6: Distributions of the event-level variables, E_T^{miss} , $m_{\gamma\gamma}$, $p_T^{\gamma\gamma}$, and $\Delta\phi_{\gamma\gamma}$, which define the analysis regions. All events must pass the analysis preselection summarized in Table 8.1. The data are shown for $t_{\gamma_1}, t_{\gamma_2} < 0$ (also the negneg selection) and the signal models are shown for $t_{\gamma_1}, t_{\gamma_2} > 0$ (also the pospos selection).

8.2.4 SUMMARY OF ANALYSIS REGIONS

Figure 8.7 shows a visualization of the exclusive regions in the three dimensional phase space defined by photon object timing, E_T^{miss} , and $m_{\gamma\gamma}$; Table 8.2 summarizes the analysis region definitions. The SR is optimized for signal sensitivity (see Section 8.4), and is defined by: $E_T^{miss} > 30$ GeV, $60 < m_{\gamma\gamma} < 135$ GeV, $p_T^{\gamma\gamma} > 70$ GeV, and $\Delta\phi_{\gamma\gamma} < 2.4$. The SR includes only pospos events.

The CR inverts the diphoton mass requirement of the SR ($m_{\gamma\gamma} > 135$ GeV) and occupies the low- E_T^{miss} regime ($E_T^{miss} < 20$ GeV). Both pospos and negneg are included in the CR to enhance the statistical power of the background estimation. Due to correlations between the photon times in the data, the timing shapes in the posneg and negpos regions are

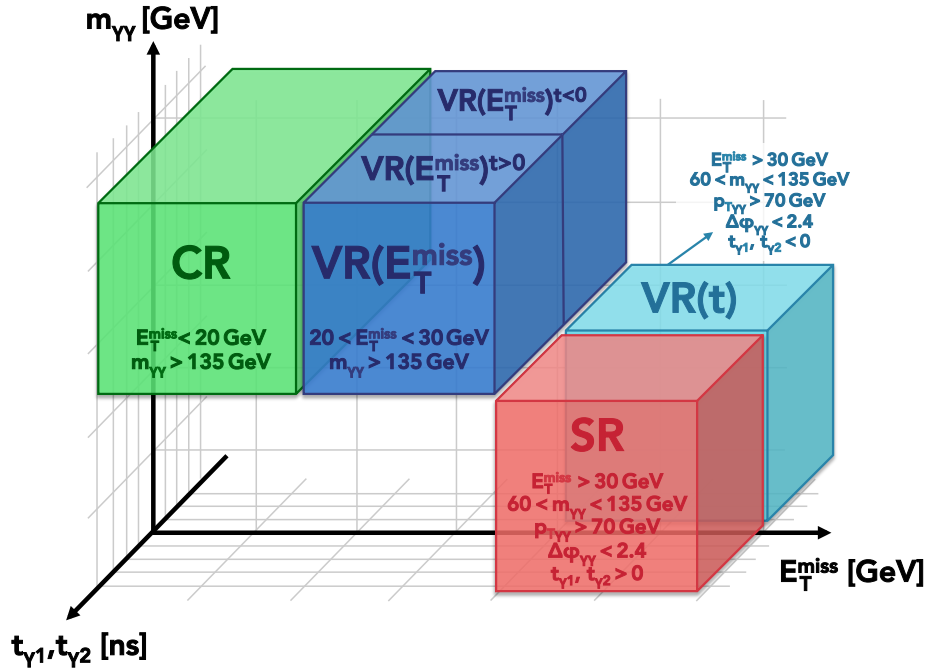


Figure 8.7: Visualization of analysis region selections as a function of E_T^{miss} , $m_{\gamma\gamma}$, and photon timing. Here, only pospos and negneg events are included; posneg and negpos events are not.

| Parameter | CR | VR($E_T^{miss})^{t<0}$ | VR($E_T^{miss})^{t>0}$ | VR(t) | SR |
|--------------------------------------|--|-------------------------|-------------------------|-----------|--------|
| E_T^{miss} [GeV] | < 20 | 20-30 | 20-30 | > 30 | > 30 |
| $m_{\gamma\gamma}$ [GeV] | > 135 | > 135 | > 135 | < 135 | < 135 |
| Sign of $t_{\gamma_1}, t_{\gamma_2}$ | $t_{\gamma_1} \times t_{\gamma_2} > 0$ | < 0 | > 0 | < 0 | > 0 |
| $p_T^{\gamma\gamma}$ [GeV] | - | - | - | > 70 | > 70 |
| $\Delta\phi_{\gamma\gamma}$ | - | - | - | < 2.4 | < 2.4 |
| Data Yields | 221,547 | 54,359 | 54,763 | 18,260 | 18,276 |

Table 8.2: Summary of control, validation, and signal region selections, and the corresponding Run 2 data yields.

slightly narrower than those in the pospos and negneg regions (see Appendix C.2). Therefore, events with opposite-sign photon times are not included in the estimation of the background timing shape. The percentage of signal contamination in the CR is $\ll 0.001\%$ for most signals and $< 0.1\%$ for all signals considered (see Appendix D.2).

There are three VRs. Two VRs span the high- $m_{\gamma\gamma}$ and mid- E_T^{miss} region ($m_{\gamma\gamma} > 135$ GeV, $20 < E_T^{miss} < 30$ GeV): the VR($E_T^{miss})^{t>0}$ and VR($E_T^{miss})^{t<0}$ contain only pospos and negneg events, respectively. These regions help validate the background estimation extrapolation across E_T^{miss} and verify the symmetry between positive and negative photon timing distributions. A third region, VR(t), is defined by the exact same kinematic selections as the SR, but contains negneg events instead of pospos ones. The VR(t) validates the background estimation's extrapolation across the kinematic variables that define the analysis regions (E_T^{miss} , $m_{\gamma\gamma}$, $p_T^{\gamma\gamma}$, and $\Delta\phi_{\gamma\gamma}$). The signal contamination in all VRs is less than 0.2% for all signal models (see Appendix D.2).

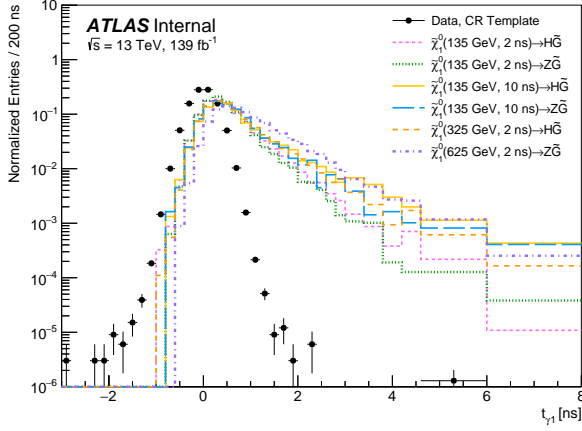
Two regions in Figure 8.7 are notably excluded from the analysis: (1) the low- E_T^{miss} , low- $m_{\gamma\gamma}$ region and (2) the high- E_T^{miss} , high- $m_{\gamma\gamma}$ region. These regions are blinded for possible future searches (e.g., those targeting displaced Higgs bosons or Z bosons without E_T^{miss} or higher-mass di-EM resonances with E_T^{miss}).

A model-independent signal region called the discovery region (SR_{disc}) is defined in the high-timing regime ($0.9 < t_{\text{avg}} < 12$ ns) of the SR (the average time, t_{avg} , is defined in the next section). This timing region represents the highest timing bin of the likelihood fit (see Section 8.4). The region contains no selections on the vertexing variables (except those used in the preselection), allowing for improved model independence.

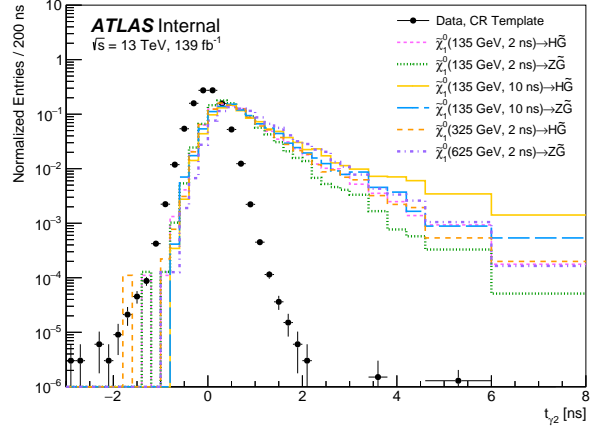
8.3 SENSITIVE VARIABLE SELECTION

As discussed, parameters with the highest sensitivity to a displaced and delayed diphoton resonance are the timing and vertexing variables. To reduce the parameter space of the fit procedure and exploit correlations between these variables, the analysis consolidates these variables into a single timing parameter and sole displacement metric.

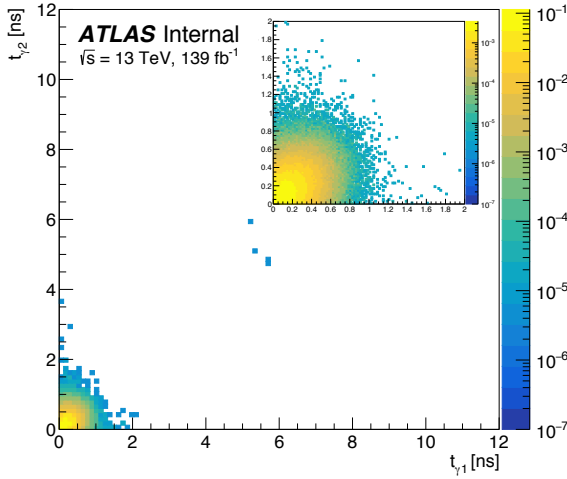
Figure 8.8 shows the distributions of the leading and subleading photon times for the background comprising CR data and several representative signal models. These distributions highlight the discriminating power of the LAr calorimeter timing variables, which is particularly evident in Figures 8.8a and 8.8b. The six signal models highlighted here assume parameters across the three-dimensional signal grid: four models are shown for $m(\tilde{\chi}_1^0) = 135$ GeV, with varying $\tau(\tilde{\chi}_1^0)$ (2 and 10 ns) and final states ($H \rightarrow \gamma\gamma$ and $Z \rightarrow ee$); two higher-mass models, with $m(\tilde{\chi}_1^0) = 325$ GeV and $m(\tilde{\chi}_1^0) = 625$ GeV, represent a pair of samples that lie at the edge of the analysis' sensitivity in the high-mass regime for final states $H \rightarrow \gamma\gamma$ and $Z \rightarrow ee$, respectively. These exact signal models are consistently portrayed in many figures throughout this thesis. These distributions also showcase the correlations between photon times in both background and signal (Figures 8.8c and 8.8d). Photons in the background generally share a collision time (recall that a large portion of the timing uncertainty is due to the beamspread), while a common long-lived parent produces those in the signal. Finally, several satellite collision events in the CR data, occurring near $t_{\gamma_1} \simeq t_{\gamma_2} \simeq 5$ ns, also appear.



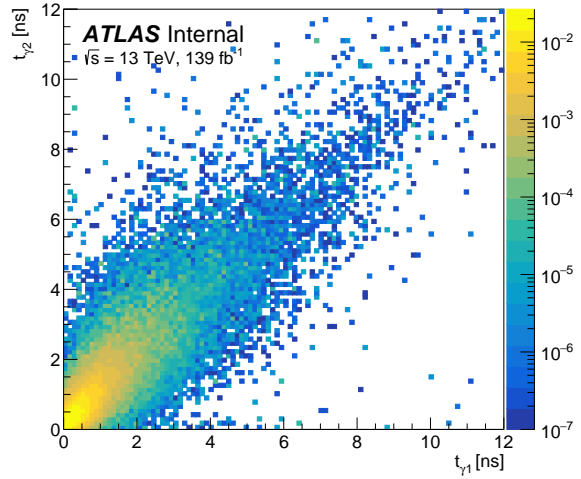
(a) Leading Photon Time



(b) Subleading Photon Time



(c) Timing Correlations in Background (CR Data)



(d) Timing Correlations in Signal

Figure 8.8: Distributions of the photon timing variables, (a) t_{γ_1} and (b) t_{γ_2} , of the background and representative signal points. Two-dimensional distributions of these variables are also shown for (c) the background and (d) the signal, with many different signal models added together to enhance statistics. The background shown is derived from from CR data, with the background estimation processing procedure applied (see Section 8.5); the signal is shown in the SR.

The fitted observable exploits the correlations between these two variables – it is the absolute value of the average of the two photon times, t_{γ_1} and t_{γ_2} :

$$t_{\text{avg}} \equiv \frac{1}{2} |t_{\gamma_1} + t_{\gamma_2}| \quad (8.1)$$

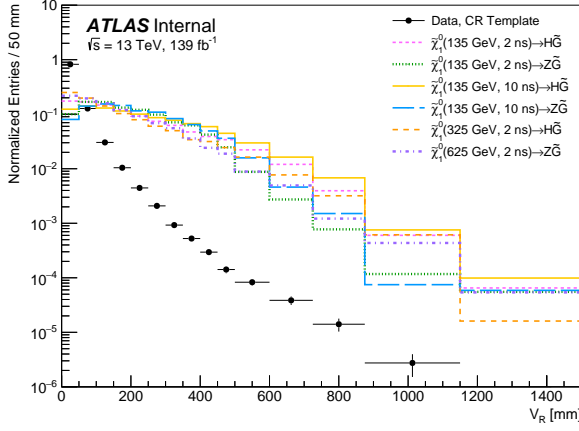
In the fit, the use of the absolute value accommodates negneg events, i.e., photons with negative times in the CR, $\text{VR}(E_T^{\text{miss}})^{t < 0}$, and $\text{VR}(t)$.

Figure 8.9 illustrates the distributions of the vertexing variables in the background derived from CR data and several representative signal models. These distributions underscore the power of these novel variables in distinguishing between long-lived signal and prompt background. A subtle and interesting phenomenon is that signal models with $Z \rightarrow ee$ in the final state are not as highly displaced as those with $H \rightarrow \gamma\gamma$ in the final state. This behavior is attributed to the diphoton mass selection ($m_{\gamma\gamma} > 60$ GeV) required to maintain acceptable trigger performance. Highly displaced events tend to be associated with lower reconstructed $m_{\gamma\gamma}$ values, a correlation that impacts displaced $Z \rightarrow ee$ decays more than displaced $H \rightarrow \gamma\gamma$ decays since $m_Z < m_H$.

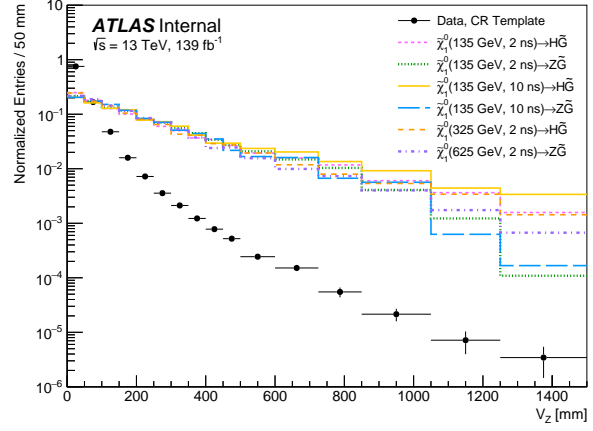
Like the timing variables, V_R and V_Z are also correlated in both background and signal (Figures 8.9c and 8.9d): prompt background events that are mis-reconstructed in one direction are more likely to be mis-reconstructed in the other; and signals with longer lifetimes tend to produce displaced signatures in both the R and z directions. The fit uses the sum of the vertexing variables in quadrature, denoted ρ , to categorize events into exclusive subsamples of varying signal-to-background ratios:

$$\rho \equiv \sqrt{V_R^2 + V_Z^2} \quad (8.2)$$

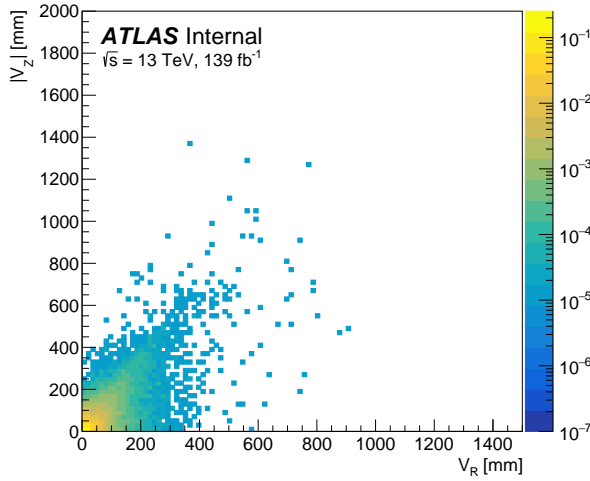
Various candidate variables were considered before deciding on t_{avg} and ρ , which are depicted in Figure 8.10 (see Appendix C.4 for other timing variable candidates considered). For example, alternative weighting schemes, including those that accounted for



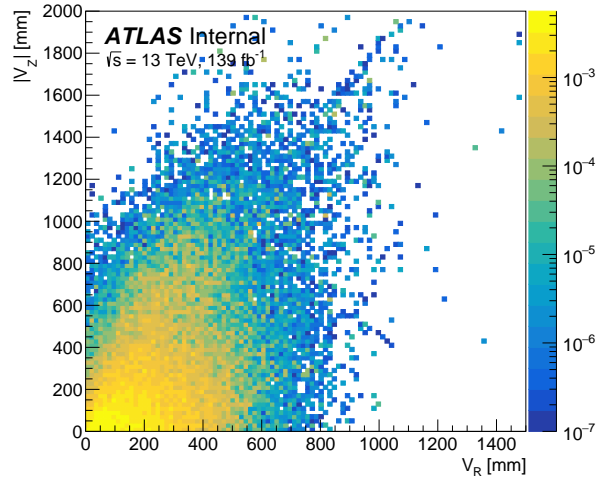
(a) Vertexing Variable V_R



(b) Vertexing Variable V_Z



(c) Vertexing Correlations in Background (CR Data)



(d) Vertexing Correlations in Signal

Figure 8.9: Distributions of the vertexing variables, (a) V_R and (b) V_Z , of the background and representative signal points. Two-dimensional distributions of these variables are also shown for (c) the background and (d) the signal, with many different signal models added together to enhance statistics. The background shown is derived from from CR data, with the background estimation processing procedure applied (see Section 8.5); the signal is shown in the SR.

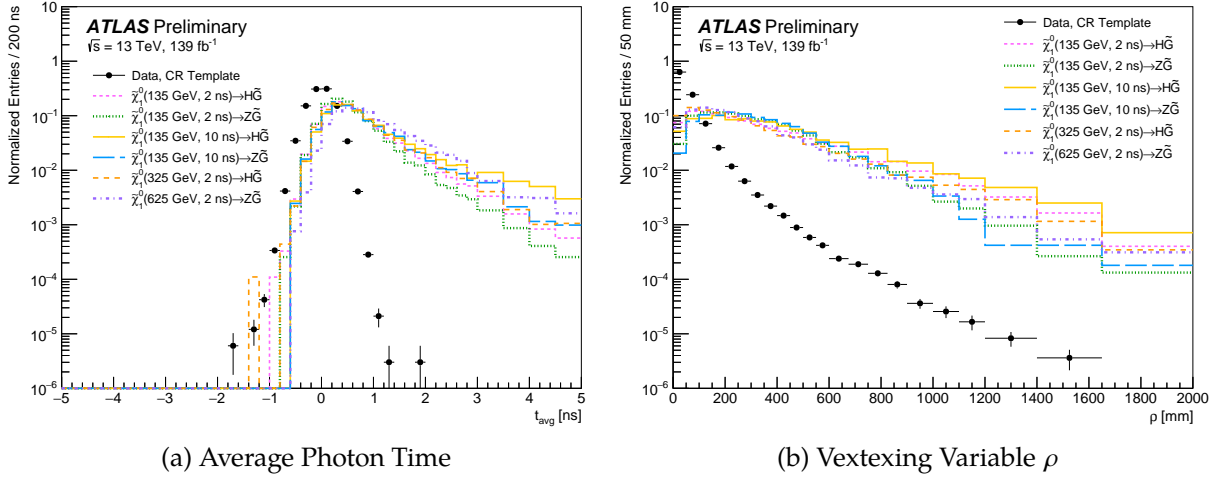


Figure 8.10: Distributions of (a) the average of the two leading photon times, $t_{\gamma 1}$ and $t_{\gamma 2}$, and (b) displacement, ρ , for the background and several representative signal points. Here, the average time is shown with no absolute value sign to capture the symmetry in the data and asymmetry in the signal. The background shown is derived from CR data, with the background estimation processing procedure applied (see Section 8.5); the signal is shown in the SR.

each measurement's resolution, exhibited negligible differences in performance. The variables t_{avg} and ρ were ultimately chosen as the fit observables because of their optimal discriminating power and mathematical simplicity.

8.4 ANALYSIS OPTIMIZATION AND BINNING

A dedicated optimization procedure determines the combination of analysis requirements that maximizes the exclusion reach of the search. Here, rectangular selections on individual variables – as opposed to a highly model-dependent machine learning technique¹ – are performed to facilitate a more robust model-independent interpretation that is easier for theorists to recast. Parameters considered include the requirements on the values of the $E_{\text{cell}}^{\text{max}}$ of the photon objects, $\Delta\eta_{\gamma\gamma}$, the selections that define the SR, and the positions

¹ A machine learning approach using a boosted decision tree was also explored but was found to deliver negligible improvements.

of the t_{avg} and ρ bin edges used in the statistical analysis. These values are optimized simultaneously.

For a given signal point, the optimizer performs a "brute force" scan of a grid of the parameter space (excluding the bin edges). The SR selections of the grid point are applied to the relevant signal model. A simplified "pseudo-background" estimation² is performed by reweighting the $E_{\text{cell}}^{\text{max}}$ distributions of CR data to those in the $\text{VR}(t)$. Note that this procedure differs from the formal analysis $E_{\text{cell}}^{\text{max}}$ reweighting procedure described in the following section (Section 8.5.2): here, the reweighting is performed entirely inclusively (i.e., not exclusively in ρ or any other category). Finally, the CR data is scaled to match the number of events in $\text{VR}(t)$. The optimization does not consider the systematic uncertainties described in Chapter 9. This simplified approach approximates the formal background estimation, and its minimal computational overhead contributes to the efficiency of the optimization procedure.

Next, for each point in the parameter space grid, a minimizer algorithm simultaneously optimizes bin edges in the two-dimensional $t_{\text{avg}}\text{-}\rho$ phase space to deliver the maximum exclusion significance. The exclusion significance is calculated using a modified version of the standard asymptotic formula that accounts for non-negligible signal and background shape uncertainties arising from sparsely populated high timing and vertexing bins [126]. For each bin, the modified exclusion significance is given by:

$$Z'_{ij} = \left(\frac{-1}{2 \left(B_{ij} \log \left(1 + \frac{S_{ij}}{B_{ij}} \right) - S_{ij} \right)} + \frac{B_{ij}}{S_{ij}^2} + \frac{1}{S_{ij}} \right)^{-1/2} \quad (8.3)$$

where B_{ij} and S_{ij} represent the pseudo-background and signal yield, respectively, in timing bin i and vertexing bin j . The total significance, Z' , is equal to the quadrature sum of Z'_{ij} across all bins. This procedure is repeated for the entire grid of the parameter space. For

² Here, the prefix, "pseudo-," is included to limit confusion between the simplified background estimation used in the optimization and the proper background estimation used for the statistical analysis, described in Section 8.5.

each signal, the optimizer identifies the point in parameter space and binning scheme that maximizes Z' . A valid binning scheme must satisfy the following conditions: (1) there are no empty bins in the background; (2) all bin widths increase monotonically; and (3) bins in both dimensions have widths similar to or larger than the resolution of that variable, minimizing bin migration effects (e.g., timing bins must have a width of at least 200 ps).

Figure 8.11 shows the two-dimensional distributions of t_{avg} and ρ for CR data and SR signal, which demonstrate excellent discrimination between the prompt background and the displaced and delayed signal. The *analysis binning* scheme chosen for the likelihood fit is:

- t_{avg} bins: [0, 0.2, 0.4, 0.6, 0.9, 12] ns
- ρ bins: [0, 80, 160, 300, 520, 2000] mm

Various distributions in the analysis binning are shown in Figure 8.12, including (a) the number of events in the CR data that go into the pseudo-background estimation, (b) the

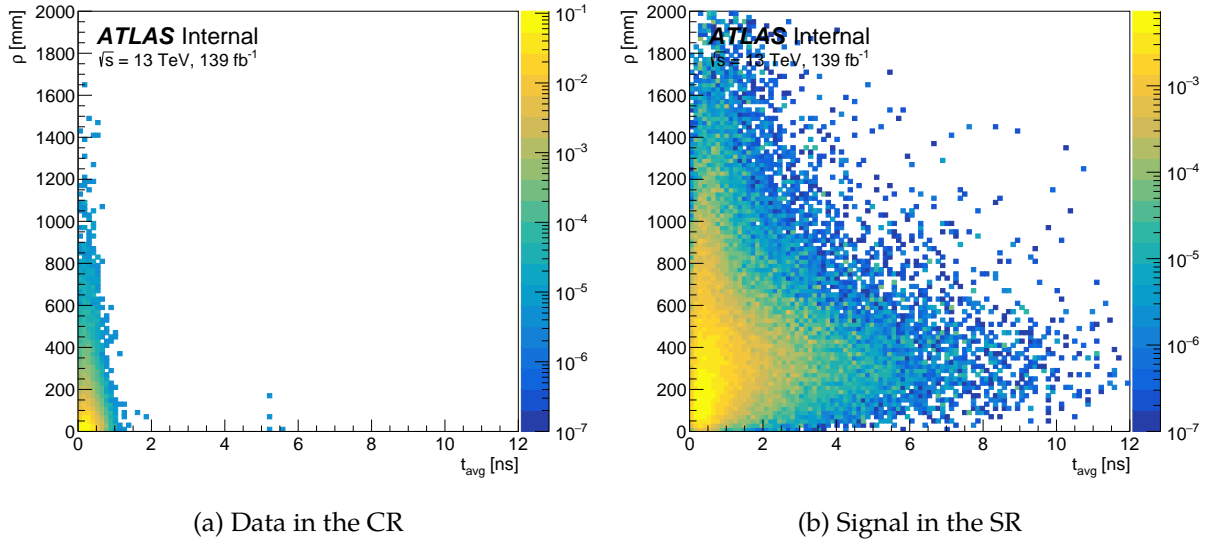


Figure 8.11: Distribution ρ vs. t_{avg} for (a) data in the CR and (b) signal in the SR. In the signal, several different models have been added together to enhance statistics and illustrate the collective behavior of the sensitive analysis variables.

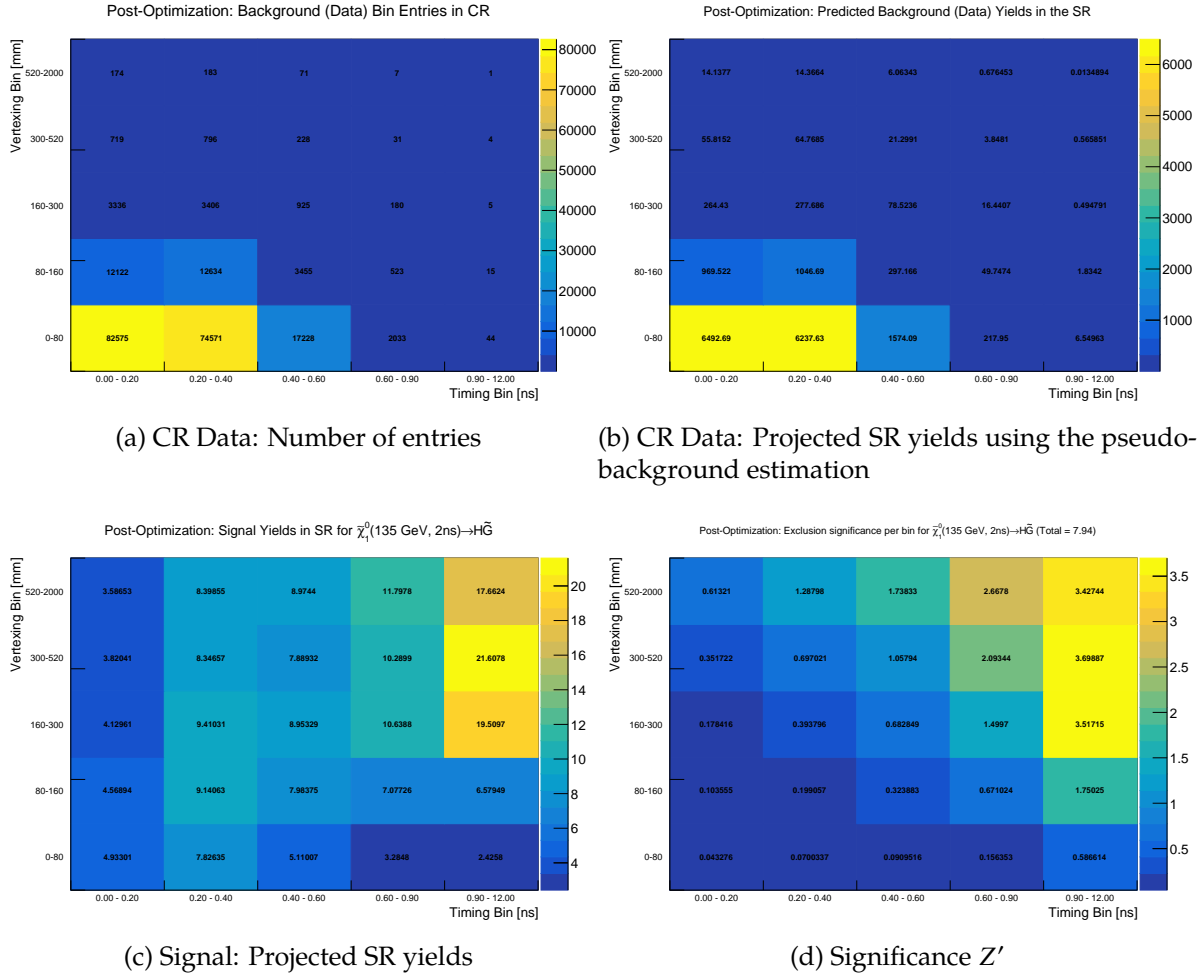


Figure 8.12: Distribution of (a) CR data yields, (b) pseudo-background estimation of the SR using CR data, (c) SR signal yields, and (d) signal significances with the selected analysis binning scheme applied. The distributions in (c) and (d) correspond to the signal model with $\tilde{\chi}_1^0(135 \text{ GeV}, 2 \text{ ns}) \rightarrow H + \tilde{G}$.

projected pseudo-background yields in the SR, (c) the SR yields of a particular signal model, and (d) the exclusion significance per bin corresponding to that signal model. These figures demonstrate the power of the multi-bin fit since several of the highest timing and vertexing contribute considerably to the total exclusion significance.

While calculating the optimal analysis selections for a given signal point is relatively straightforward, harmonizing these requirements across the entire signal grid is not as well-defined. One way to systematically attack this problem is to prioritize signal models

at the edge of sensitivity – those that benefit most from a more customized optimization. However, since the signal grid spans three dimensions ($\tilde{\chi}_1^0$ mass, lifetime, and branching ratio), points along the edge of sensitivity occupy disparate kinematic regimes: sensitivities to the highest $\tilde{\chi}_1^0$ lifetimes occur for the lowest masses, and sensitivities for the highest $\tilde{\chi}_1^0$ masses occur at intermediate lifetimes (near 2 ns).

Fortunately, despite the kinematic differences of these signals, the sensitivity reach of the analysis is not extremely sensitive to modest variations in analysis selections or binning schemes. For models near the sensitivity boundary, the chosen parameters deliver significances within 10% (25%) of the optimal value for $H \rightarrow \gamma\gamma$ ($Z \rightarrow ee$) signals (the only exception are the 100 GeV points with high lifetimes, which experience a roughly 40% drop in significance). Therefore, a single SR definition is chosen since these discrepancies across the signal grid do not warrant multiple optimized signal regions.

8.5 BACKGROUND ESTIMATION

No SM process produces a displaced and delayed diphoton (or dielectron) resonance with resolved, non-overlapping objects. This signature’s primary background originates from mismeasurements of genuine and fake photons (like jets). A sub-dominant background source arises from satellite collisions: these produce delayed objects with times near ± 5 ns but are suppressed by roughly 10^5 with respect to the nominal bunch, as described in Sections 3.3 and 6.2.4.

The MC simulation does not accurately model the non-Gaussian tails and satellite collisions in the timing distributions, as previously mentioned. Therefore, an entirely data-driven background estimation, derived from data events in the CR, is employed to predict the shape of the average photon time in the SR. Additional processing, including purity scaling, $E_{\text{cell}}^{\text{max}}$ reweighting, and residual time-shifting, is applied to the CR data to account for known dependencies and deliver improved background modeling in the SR.

8.5.1 PURITY SCALING

The timing resolution of fake photons is somewhat worse than that of genuine EM objects, as shown in Figure 8.13a. Therefore, to account for this shape difference, two categories of events are defined – one enriched in real photons and another enriched in fake photons. The real-enhanced photon category (called TIGHTTIGHT) requires both photons to satisfy the TIGHT PID criteria; conversely, the fake-enhanced photon category (called ANTI-TIGHTTIGHT) requires at least one photon to fail the TIGHT PID.

The purity fraction, f_{TT} , is defined as the fraction of TIGHTTIGHT events in a given region (note that $f_{anti-TT} = 1 - f_{TT}$). Since the composition of photon purity evolves across the analysis regions, as illustrated in Figure 8.13b, a reweighting procedure is applied to CR data so that the predicted f_{TT} matches that of the SR. The value of f_{TT} also varies across vertexing bins, so this purity scaling procedure is performed exclusively in bins of ρ . Typical values for f_{TT} range from 0.4 to 0.8. For a given analysis region and ρ bin, the TIGHTTIGHT and ANTI-TIGHTTIGHT categories have a roughly similar number of events, never differing by more than a factor of four.

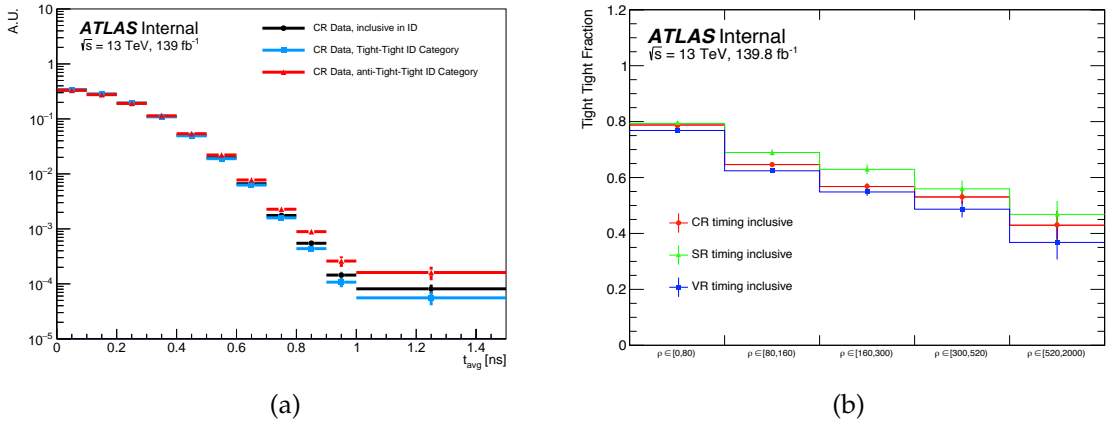


Figure 8.13: (a) The ρ -inclusive t_{avg} distribution of the real-enhanced(TIGHTTIGHT) and fake-enhanced (ANTI-TIGHTTIGHT) photon purity categories, as well as their sum in black, for CR data. (b) Photon purity fraction, f_{TT} , as a function of ρ for different timing-inclusive analysis regions.

8.5.2 $E_{\text{CELL}}^{\text{max}}$ REWEIGHTING

The timing resolution measurement is inversely related to $E_{\text{cell}}^{\text{max}}$ plus a constant (see Figure 6.8 and Equation 6.4). Therefore, the $E_{\text{cell}}^{\text{max}}$ distributions of the leading and subleading photon in the CR are reweighted to match those of the SR. The $E_{\text{cell}}^{\text{max}}$ reweighting procedure is performed exclusively in ρ and separately for the TIGHTTIGHT and ANTI-TIGHTTIGHT categories. A two-dimensional reweighting procedure is implemented to account for correlations between the $E_{\text{cell}}^{\text{max}}$ of the two photons. The $E_{\text{cell}}^{\text{max}}$ energy spectra of photons in the CR and SR are relatively similar, and most of the reweight values fall between 0.5 and 2.

8.5.3 RESIDUAL TIME-SHIFTING

The timing calibration in Section 6.2 delivers excellent performance; however, it does not perfectly center the timing distributions at $t = 0$ throughout every region of phase space due to limited statistics of and imperfections in the calibration. Therefore, two additional analysis-dependent timing corrections are applied. The first is a $E_{\text{cell}}^{\text{max}}$ -dependent correction, which shifts the photon times in bins of $E_{\text{cell}}^{\text{max}}$ for each analysis region; the second shifts the timing distributions in each ρ and purity category in each region. Together, these additional analysis-dependent time corrections apply shifts of no more than 10 ps, with most less than 5 ps. Although these residual shifts are relatively small, they significantly improve the agreement in average timing shape across regions.

8.5.4 TREATMENT OF THE CONTROL REGION

In summary, the background estimation comprises three key processing steps: (1) purity scaling, (2) $E_{\text{cell}}^{\text{max}}$ reweighting, and (3) residual time-shifting. To increase the statistical power of these processes, all three are performed inclusively in timing (i.e., inclusively in pospos, posneg, negpos, negneg). In other words, the region in data with the same kinematic selections as the CR undergoes these three processing steps. The target distribution

for the purity scaling and $E_{\text{cell}}^{\text{max}}$ -reweighting is the region in data with the same kinematic requirements as the SR, which includes both the SR and the VR(t). For validation purposes, in fits with the VR($E_T^{\text{miss}})^{t>0}$ and VR($E_T^{\text{miss}})^{t<0}$ regions, the scaling and reweighting target is the timing-inclusive region with the same kinematic selections as VR($E_T^{\text{miss}})^{t>0}$ and VR($E_T^{\text{miss}})^{t<0}$.

Applying these three processing steps to data in the CR generates the background template used in the statistical fit. The template includes five distributions of t_{avg} – one for each exclusive ρ category. The following chapters discuss the systematic uncertainties on the background and signal templates (Chapter 9) and the validation of the background estimation (Chapter 10).

CHAPTER 9:

SYSTEMATIC UNCERTAINTIES

Nothing in life is to be feared; it is only to be understood.

— Marie Curie

The concept of uncertainty underpins one of the most fundamental notions in science: measurement. Systematic uncertainties quantify consistent differences between measured and true values to contextualize the degree of confidence in a given measurement. For ATLAS analyses, systematic uncertainties arise from a variety of sources, including calibration errors and limitations, simulation mismodeling, and limited information about the behavior and dependencies of a given variable.

This chapter describes several sources of systematic uncertainty and how they impact the signal and background templates. These sources of uncertainty only minimally impact the sensitivity of the final result since the statistical uncertainty dominates the total uncertainty. Section 9.1 details the shape uncertainties of the background timing distributions, while Section 9.2 describes the normalization and shape uncertainties of the signal templates.

9.1 BACKGROUND UNCERTAINTIES

No normalization uncertainties on the background templates are included since these parameters are unconstrained in the fit and allowed to float freely. However, the analysis considers three modeling uncertainties that affect the shape of the background timing distributions, including those related to the purity scaling, $E_{\text{cell}}^{\text{max}}$ reweighting, and the pileup distribution. Given the unique nature of the analysis variables in the fit, all timing shape uncertainties are custom developed and validated via assessments on the VRs. Table 9.1 provides a summary of the background shape uncertainties and their relative impacts.

| Source of Uncertainty | Type | Avg. Bin Deviation | Max. Bin Deviation |
|--|-------|--------------------|--------------------|
| Photon Purity Fraction (f_{TT} , $f_{\text{anti-}TT}$) | Shape | 1.9% | 5.6% |
| $E_{\text{cell}}^{\text{max}}$ Reweighting | Shape | 1.1% | 8.7% |
| Pileup Distribution | Shape | 3.1% | 19.8% |

Table 9.1: Summary of systematic uncertainties on the background shape, which is derived from CR data. Since all uncertainties shown have different shapes, with evolving behavior across bins, the average and maximum bin deviations are shown to capture the relative impacts of the various uncertainties.

9.1.1 PHOTON PURITY FRACTION

Uncertainties on the values of f_{TT} (and $f_{\text{anti-}TT}$) emerge from statistical limitations in the purity fraction measurement (see Section 8.5.1). Since the calculation of f_{TT} uses two categories of events – high-purity (TIGHTTIGHT) or low-purity (ANTI-TIGHTTIGHT) – its associated uncertainty is the binomial error on the number of events in each of these categories. Thus, the systematic variations associated with f_{TT} constitute relatively lower- and higher-purity templates with respect to the nominal template. The values of f_{TT} and their uncertainties are calculated independently for each vertexing category in every region and are uncorrelated across vertexing categories in the fit. The reason for this treatment is twofold:

first, f_{TT} varies with ρ and other event-level variables; and second, the number of available background events in the CR decreases rapidly with increasing ρ , leading to vastly different binomial errors across vertexing bins. Figure 9.1 illustrates the impact of this systematic uncertainty on the five different vertexing categories. The uncertainty on f_{TT} is at the percent- or sub-percent-level for most of the lower vertexing categories and is as high as nearly 6% for the higher timing and vertexing bins.

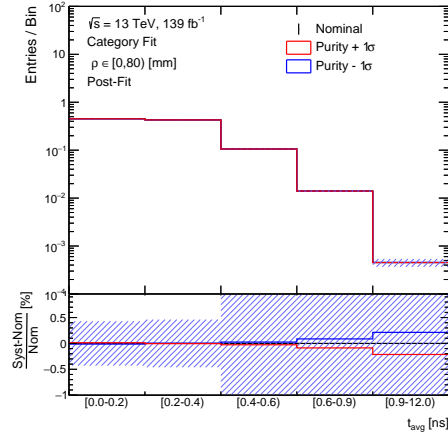
9.1.2 $E_{\text{CELL}}^{\text{max}}$ REWEIGHTING

Uncertainties on the $E_{\text{cell}}^{\text{max}}$ reweighting procedure (see Section 8.5.2) account for the statistical limitation in measuring the $E_{\text{cell}}^{\text{max}}$ distributions. Templates for the $E_{\text{cell}}^{\text{max}}$ systematic variations use the statistical uncertainty on the reweight value assigned to each event. The $E_{\text{cell}}^{\text{max}}$ reweighting is uncorrelated across vertexing categories since the timing templates are reweighted separately for each ρ bin. Figure 9.2 shows the $E_{\text{cell}}^{\text{max}}$ reweighting systematic uncertainties on the timing distributions across vertexing categories; maximum variations are on the order of 10%, with variations across all bins less than or equal to the statistical uncertainty.

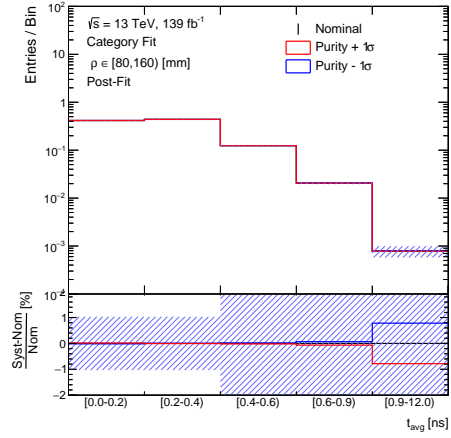
9.1.3 PILEUP DISTRIBUTION

High pileup reduces the PV identification efficiency and exacerbates jet contributions in an event, both of which degrade the timing resolution. Pileup levels also impact the observed E_T^{miss} values (see Figure 5.6) and are correlated with several other analysis variables. The pileup distribution systematic uncertainties accommodate the pileup dependence of background timing shapes.

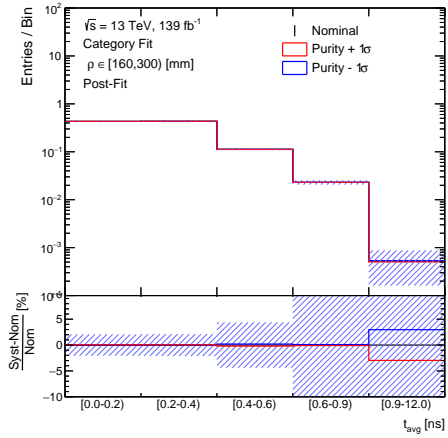
For each vertexing category, events in the CR data are split into low-pileup ($\mu < \langle \mu \rangle$) and high-pileup ($\mu \geq \langle \mu \rangle$) categories, where $\langle \mu \rangle$ is the average number of pileup vertices, which falls in the range of 32-34. These distinct shapes envelop the inclusive nominal template and determine the systematic uncertainty contribution from categories of events



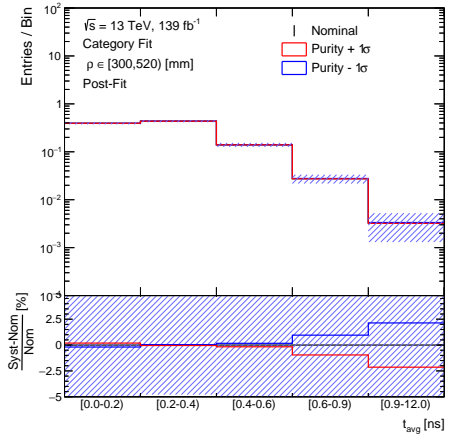
(a) $\rho \in [0, 80)$ mm



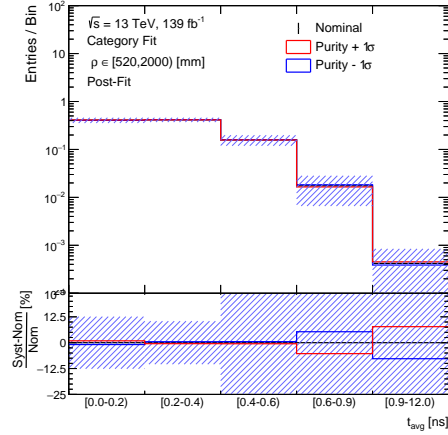
(b) $\rho \in [80, 160)$ mm



(c) $\rho \in [160, 300)$ mm

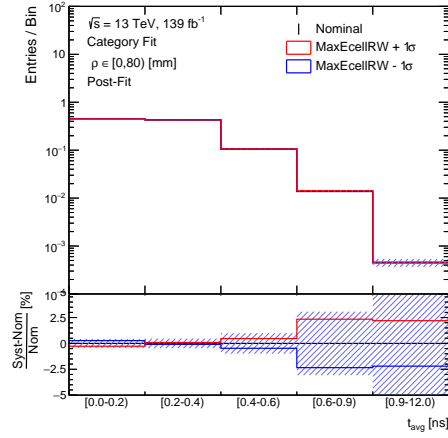


(d) $\rho \in [300, 520)$ mm

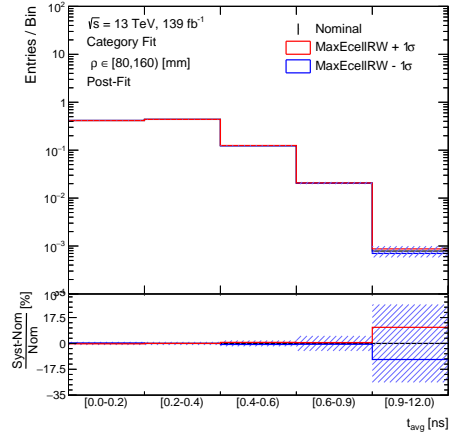


(e) $\rho \in [520, 2000)$ mm

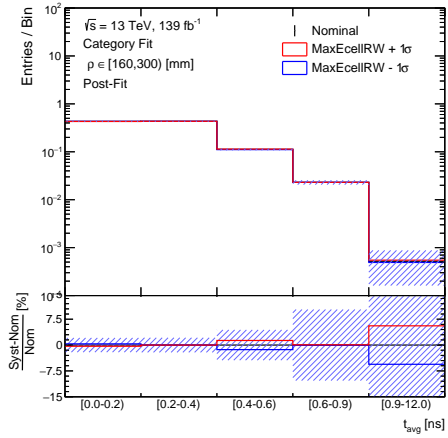
Figure 9.1: The photon purity fraction shape systematic uncertainties constructed using photon purity fraction errors. The variations in red show the timing shapes associated with a slightly higher balance of f_{TT} (and corresponding lower contribution of $f_{anti-TT}$); those in blue show the opposite.



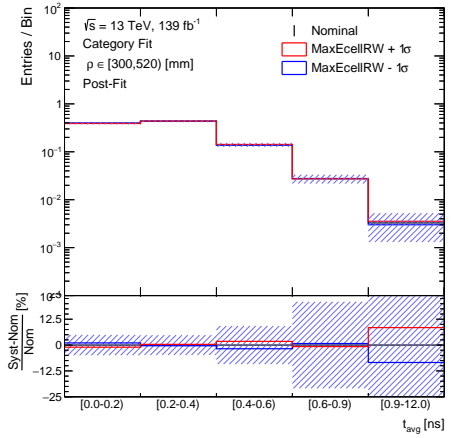
(a) $\rho \in [0, 80)$ mm



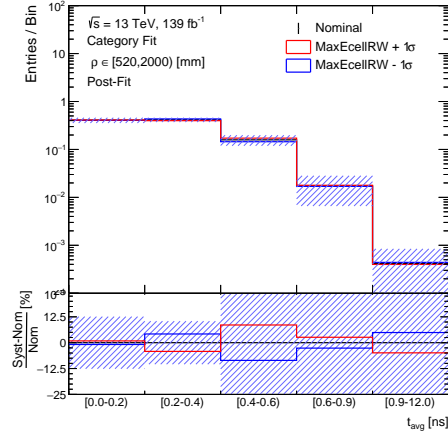
(b) $\rho \in [80, 160)$ mm



(c) $\rho \in [160, 300)$ mm



(d) $\rho \in [300, 520)$ mm



(e) $\rho \in [520, 2000)$ mm

Figure 9.2: The $E_{\text{cell}}^{\text{max}}$ reweighting shape systematic uncertainties constructed using the $E_{\text{cell}}^{\text{max}}$ reweighting errors. The variations in red (blue) illustrate the timing shape differences that emerge by adding (subtracting), event-by-event, the $E_{\text{cell}}^{\text{max}}$ reweight error to the nominal $E_{\text{cell}}^{\text{max}}$ reweight value.

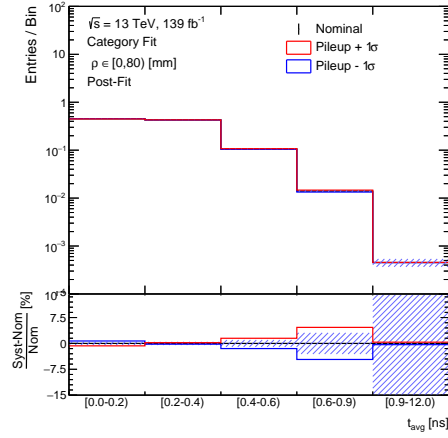
with differing pileup compositions. Like the treatment of the f_{TT} and $E_{\text{cell}}^{\text{max}}$ reweighting systematic uncertainties, the pileup distribution systematic uncertainties are uncorrelated across vertexing categories. Given the limited CR sample size, the low-pileup variation has zero entries in the highest timing bin in the highest vertexing category ($\rho \in [520, 2000)$). A smoothing procedure is applied to the systematic variations in this category to avoid deriving an uncertainty with zero events in one bin. Figure 9.3 displays the pileup systematic uncertainties on the timing distributions across vertexing categories. The systematic uncertainties on the pileup distribution generally dominate the other sources of systematic uncertainty (see Table 9.1), though, in most bins, the variations are still less than the statistical uncertainty.

9.2 SIGNAL UNCERTAINTIES

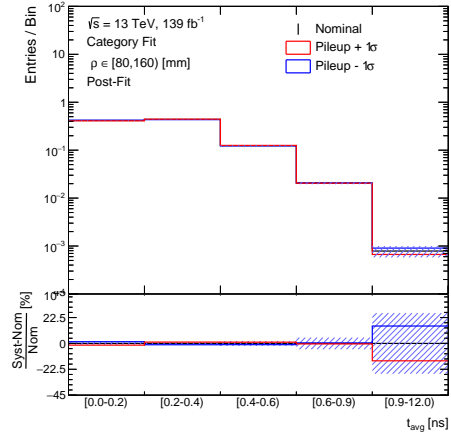
The systematic uncertainties associated with the signal impact the normalization and timing shape of the templates. This section first discusses the "flat" systematic uncertainties that only impact the signal normalization, including those related to the integrated luminosity measurement, detector modeling, and the theoretical assumptions that underlie the signal MC generation; next, it addresses the systematic uncertainties on the signal timing shape. All systematic uncertainties on the signal are treated as correlated across all vertexing categories. Table 9.3 summarizes the sources and impacts of the signal systematic uncertainties and is given towards the end of this section.

9.2.1 INTEGRATED LUMINOSITY UNCERTAINTY

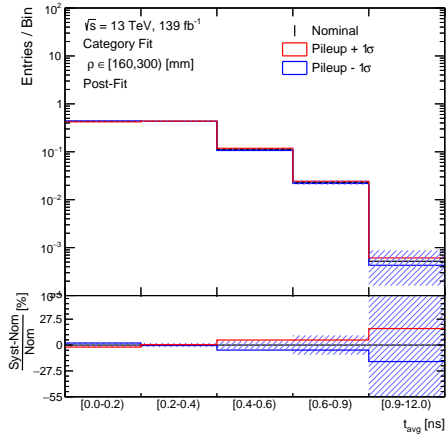
The analysis includes the standard uncertainty on the integrated luminosity of the full ATLAS Run 2 dataset of $\pm 1.7\%$ [127]. The value of this uncertainty is derived from measurements made by the LUCID subdetector [99] and other detector components using the methodology summarized in Section 4.7.



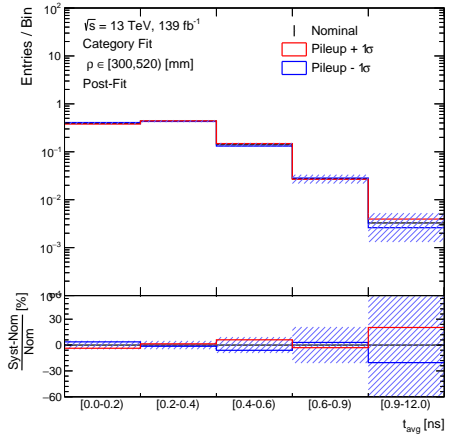
(a) $\rho \in [0, 80)$ mm



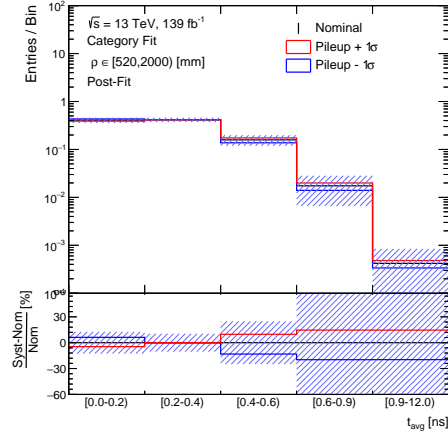
(b) $\rho \in [80, 160)$ mm



(c) $\rho \in [160, 300)$ mm



(d) $\rho \in [300, 520)$ mm



(e) $\rho \in [520, 2000)$ mm

Figure 9.3: The pileup shape systematic uncertainties constructed by dividing events into low- and high- pileup categories, defined by a cut on μ . The variations in red (blue) are created by requiring the analysis events to have $\mu > \langle \mu \rangle$ ($\mu < \langle \mu \rangle$). The value of the $\langle \mu \rangle$ cut is calculated for each ρ category in the CR data.

9.2.2 THEORY UNCERTAINTIES

The analysis considers four sources of systematic uncertainties related to the signal MC generation: the choices of the strong coupling constant (α_S), renormalization scale (μ_R), factorization scale (μ_F), and parton distribution function (PDF) (see Section 7.2). The uncertainties on each of these parameters are determined by varying their respective values – often producing samples with alternative sets of values – and measuring the impact on the signal. The systematic uncertainties are relatively flat across timing and vertexing distributions, so the theory uncertainties generally only impact the signal normalization. Table 9.2 shows the breakdown of the various theoretical uncertainty contributions; the uncertainties of μ_F and μ_R dominate the total signal systematic uncertainty contribution on the signal.

| Source of Uncertainty | $\tilde{\chi}_1^0(225 \text{ GeV}, 2 \text{ ns}) \rightarrow H + \tilde{G}$ | $\tilde{\chi}_1^0(225 \text{ GeV}, 2 \text{ ns}) \rightarrow Z + \tilde{G}$ |
|-----------------------|---|---|
| | $\pm 1\sigma$ [%] | $\pm 1\sigma$ [%] |
| α_S | ± 0.1 | ± 0.1 |
| μ_F, μ_R | ± 12.6 | ± 12.6 |
| PDF Replicas | ± 0.4 | ± 0.6 |
| Total | ± 12.6 | ± 12.6 |

Table 9.2: Breakdown of theory systematic uncertainties for signal models with $m(\tilde{\chi}_1^0) = 225 \text{ GeV}$, $\tau(\tilde{\chi}_1^0) = 2 \text{ ns}$, in the $H \rightarrow \gamma\gamma$ and $Z \rightarrow ee$ final states. These values are incorporated into the systematic uncertainty on the signal normalization.

9.2.3 INSTRUMENTAL UNCERTAINTIES

Instrumental uncertainties emerge from experimental limitations related to the detector and object reconstruction and primarily address disagreement between data and MC simulation. The analysis follows ATLAS standard recommendations for instrumental uncertainties and includes those related to photon objects, E_T^{miss} , and pileup modeling. Since

these uncertainties are uncorrelated with photon timing and vertexing, they are integrated into a single flat systematic uncertainty on the normalization of the signal.

Electromagnetic energy resolution and scale uncertainties [128] account for a variety of phenomena, including pileup effects, non-linearities in cell energy response, simulation of electromagnetic showers, and modeling passive detector material upstream of the LAr calorimeter. The uncertainties are determined through a calibration performed with electrons from prompt $Z \rightarrow ee$ events and validated with electrons from $J/\psi \rightarrow e^+e^-$ events and photons from radiative Z boson decays ($Z \rightarrow ll\gamma$, $l = e, \mu$).

Photon trigger, identification, and isolation efficiency uncertainties correspond to various sources of disagreement between data and simulation reconstruction efficiencies. Photon trigger efficiency uncertainties [104] are calculated using two different approaches: the "bootstrap" method uses photons triggered by a lower-threshold trigger or an unbiased

| Source of Uncertainty | -1 σ (%) | +1 σ (%) |
|-----------------------------------|-----------------|-----------------|
| Luminosity | -1.70 | 1.70 |
| Theory | -12.6 | 12.6 |
| Instrumental Uncertainties | | |
| Electromagnetic Energy Scale | -1.17 | 1.04 |
| Electromagnetic Energy Resolution | -0.03 | 0.14 |
| Photon Trigger Efficiency | -0.49 | 0.49 |
| Photon Identification Efficiency | -1.54 | 1.55 |
| Photon Isolation Efficiency | -1.45 | 1.46 |
| E_T^{miss} Scale | -0.51 | 0.66 |
| E_T^{miss} Resolution | -0.77 | 0.77 |
| Pileup Reweighting | -0.39 | 0.68 |
| Total Flat Systematic Uncertainty | -13.0 | 13.0 |
| Timing Resolution | Shape | |

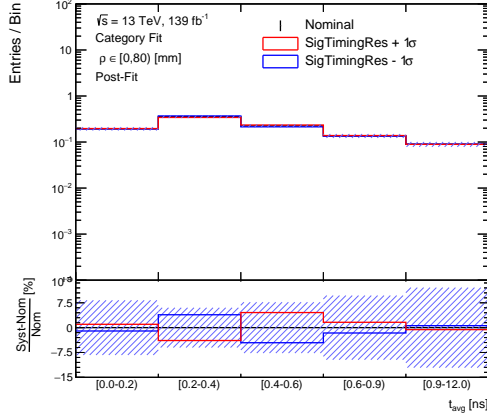
Table 9.3: Summary of flat systematic uncertainties on the signal. The instrumental systematic uncertainties are shown for the signal point with $\tilde{\chi}_1^0(135 \text{ GeV}, 2 \text{ ns}) \rightarrow H + \tilde{G}$ and vary only slightly across signal points.

trigger; the second method uses photons from radiative Z boson decays that pass dilepton triggers. Photon identification and isolation uncertainties [110] use photons from radiative Z boson decays and those from an inclusive photon sample.

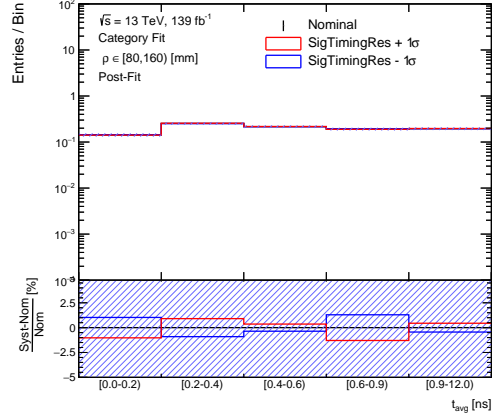
The systematic uncertainties associated with the full event topology include those related to E_T^{miss} and pileup. The E_T^{miss} scale and resolution uncertainties [116] are derived from $Z \rightarrow \mu\mu$ events, which are expected to have little to no E_T^{miss} (see Section 5.7). A pileup reweighting uncertainty is included to account for discrepancies in the pileup distribution between data and MC.

9.2.4 TIMING RESOLUTION UNCERTAINTY

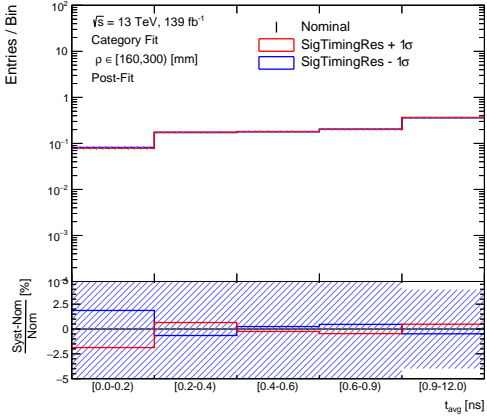
The measurement of the timing resolution in data directly informs the MC timing smearing procedure (Section 6.2.5). Therefore, simulated timing is also smeared according to resolutions of $\pm 1\sigma$ with respect to the nominal value. The resulting systematic variations, shown in Figure 9.4, have a relatively minimal impact on the signal timing shape, with maximum shape deviations of roughly 5%. Notably, the variations in the *average* photon time do not produce consistent "wider" or "narrower" envelopes around the nominal distribution, in contrast to the variations on *single* photon times, which do. This behavior is attributed to correlations and the complex interplay between the leading and subleading photon times in the t_{avg} variable.



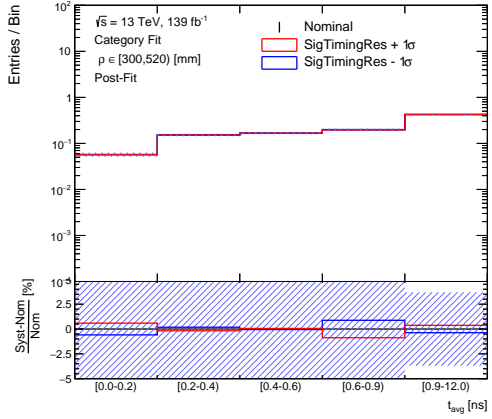
(a) $\rho \in [0, 80)$ mm



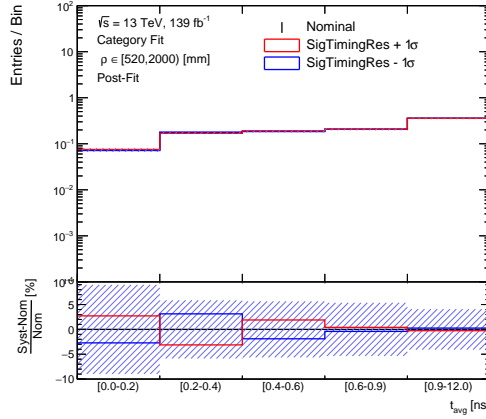
(b) $\rho \in [80, 160)$ mm



(c) $\rho \in [160, 300)$ mm



(d) $\rho \in [300, 520)$ mm



(e) $\rho \in [520, 2000)$ mm

Figure 9.4: The timing resolution shape systematic uncertainty on the signal, constructed via alternative timing smearing procedures. The variation in red (blue) is created via alternative timing smearing procedures, leading measurements to assume a timing resolution $+1$ (-1) σ with respect to the nominal value (see Section 6.2.5). The distributions shown here correspond to the signal point with $\tilde{\chi}_1^0(135 \text{ GeV}, 2 \text{ ns}) \rightarrow \text{H} + \tilde{G}$.

CHAPTER 10:

STATISTICAL ANALYSIS AND FIT VALIDATION

If your experiment needs statistics, you ought to have done a better experiment.

— Ernest Rutherford

Experiments endeavoring to capture the behavior of a handful of events out of billions, unavoidably, need statistics. Statistical tools are indispensable in analyzing, interpreting, and communicating experimental high-energy physics results. When applied to a finite dataset – in this case, 139 fb^{-1} – statistical inference enables conclusions to be drawn about the properties of the universe.

This chapter briefly introduces the underlying statistical principles, metrics, and practices ubiquitous in high-energy physics (Section 10.1). Next, Section 10.2 describes the implementation of the fit in the context of the analysis and highlights several validation studies performed on both the fit implementation and the background modeling strategy.

10.1 HYPOTHESIS TESTING AND INTERPRETATION

Hypothesis testing in particle physics assesses two distinct scenarios: the background hypothesis (H_0), also called the null hypothesis, which encapsulates the behavior of SM processes; and the alternative hypothesis (H_1), which assumes a signal-plus-background scenario. The discovery or exclusion of a process depends on how well the observed data match each of these hypotheses. This section describes the standard statistical approaches employed by most LHC analyses that quantify the (dis)agreement between prediction and observation.

In a simplified, single-bin experiment, the number of predicted background events, n_{pred} , is given by:

$$n_{pred} = \mu s \theta_s + b \theta_b \quad (10.1)$$

where s is the predicted signal yield of a given model and b is the predicted background yield. The signal strength, μ , is equal to the ratio between the observed and expected signal cross section (assuming H_1). The nuisance parameters (NPs), θ_s and θ_b , represent the systematic uncertainties on the signal and background models, respectively. Since the signal strength is the distinguishing factor between H_0 ($\mu = 0$) and H_1 ($\mu = 1$), the parameter of interest (POI) in a fit between predicted background and observed data is μ .

The fit is performed by maximizing the likelihood function, $\mathcal{L}(\mu, \theta)$, which quantifies the probability of the observed data occurring given the predicted background estimation and signal hypothesis. In this analysis, the full expression for $\mathcal{L}(\mu, \theta)$ contains the product of Poisson probabilities (\mathcal{P}) for every timing bin (i) in each ρ category (j) and Gaussian terms (\mathcal{G}) for every systematic uncertainty on the signal (k) and background (l) models:

$$\mathcal{L}(\mu, \theta) = \prod_{ij} \mathcal{P}(n_{obs}^{ij} | n_{pred}^{ij}) \prod_k \mathcal{G}(\tilde{\theta}_s^k | \theta_s^k, \sigma_s^k) \prod_l \mathcal{G}(\tilde{\theta}_b^l | \theta_b^l, \sigma_b^l) \quad (10.2)$$

Here, $\tilde{\theta}_s^k$ and $\tilde{\theta}_b^l$ represent the global observables corresponding to the NPs. The likelihood function can be *globally* maximized, which allows the signal strength and NPs to vary in the fit, assuming fitted values of $\hat{\mu}$ and $\hat{\theta}$; it can also be *conditionally* maximized for a fixed value of μ , returning only values for the NPs, $\hat{\theta}(\mu)$. For example, setting $\mu = 0$ corresponds to a background-only fit.

A powerful tool used to discriminate between H_0 and H_1 is the profile likelihood, $\lambda(\mu)$, which is defined as the ratio between the global and conditional maximum likelihood functions [129]:

$$\lambda(\mu) = \frac{\mathcal{L}(\mu, \hat{\theta}(\mu))}{\mathcal{L}(\hat{\mu}, \hat{\theta})} \quad (10.3)$$

The profile likelihood can be used to calculate a statistical model's p -value [130], which quantitatively summarizes the agreement between prediction and observation. The value of $p_0(p_\mu)$ corresponds to the probability that the data agree with H_0 (H_1). A p_0 -value close to 0.5 signifies that the observation agrees with the background-only hypothesis, while one less than (greater than) 0.5 indicates the presence of a signal excess (deficit). A small degree of model dependence exists in the p_0 -value estimation since a given signal scenario is assumed in the calculation.

In high-energy physics, the p_0 -value is customarily translated into significance, Z . By convention, a measurement of $|Z| < 2$ indicates that observation is consistent with the SM expectations; $Z > 3$ suggests evidence for new physics; and $Z = 5$ represents the threshold for claiming a discovery – corresponding to a 1-in-3.5 million chance that the observation arises only from statistical fluctuations.

Signal model exclusions and limits rely on the CL_s technique [131, 132] to determine whether to reject the signal-plus-background hypothesis. The confidence level (CL) of a given signal hypothesis is given by:

$$\text{CL}_s = \frac{p_\mu}{1 - p_0} \quad (10.4)$$

By convention, processes with signal strength μ that yield $CL_s < 0.05$ are excluded at $\geq 95\%$ CL. The highest value of μ not excluded by this method corresponds to the *upper limit* on the signal strength of a given model.

10.2 FIT IMPLEMENTATION AND VALIDATION

The statistical analysis is performed with TREXFITTER [133], a flexible framework employed by many ATLAS analyses. As discussed, the statistical strategy consists of a simultaneous template fit of the average timing distribution sliced into five vertexing categories. The background normalization in each ρ category is taken as an unconstrained NP, allowed to float freely in the fit. The NPs associated with the systematic uncertainties on the signal and background templates are assigned Gaussian constraints in the fit. To limit bias, the SR timing and vertexing distributions were blinded throughout the entire development of the background estimation and fit framework. The remainder of this section discusses a rigorous set of studies that validate both the fit procedure itself (Section 10.2.1) and the background estimation strategy (Section 10.2.2).

10.2.1 VALIDATION OF FIT PROCEDURE

The validation of the fit procedure requires its decoupling from the problem of background modeling. Therefore, the fit is tested against *pseudo-datasets*, which are drawn from the shape of the predicted background template. Each pseudo-dataset is generated with random fluctuations according to the statistical and systematic uncertainties implemented in the fit. Fits with pseudo-datasets are therefore immune to any artifacts or background modeling issues that might appear in the VRs.

Spurious signal tests using these pseudo-datasets confirm that the fit does not find a signal when none is present in the data. Figure 10.1 shows the extracted signal strength for signal-plus-background fits to 1000 different background-only pseudo-datasets. Note

that the distribution is cut off around $\mu = -0.05$ since highly negative values of the signal strength cause the yields in the highest timing and vertexing bin to be negative, preventing the fit from converging. This issue does not indicate a problem with the statistical model; instead, it illustrates a high degree of sensitivity to the signal. Overall, the distribution of fitted spurious signal values is centered around $\mu = 0$ and contains no outliers, demonstrating sound and reliable fit performance.

A series of signal injection tests verify that the fit correctly identifies a signal when one is present. To estimate the background, these studies use a so-called *Asimov* dataset, which provides the median experimental result of background-only pseudo-datasets in the asymptotic ($N \rightarrow \infty$) limit, as well as fluctuations about this expectation [130, 134, 135]. A signal of known strength is then injected into the background, and a signal-plus-background fit is performed. Figure 10.2 shows the fitted μ as a function of injected μ for a representative signal point, $\tilde{\chi}_1^0(135 \text{ GeV}, 2 \text{ ns}) \rightarrow H + \tilde{G}$. All signal injection tests reflect excellent agreement – always well within uncertainty – between the injected and measured values of μ . The signal injection study demonstrates a linear fit response and showcases the fit’s accuracy and sensitivity to a broad range of signal strengths.

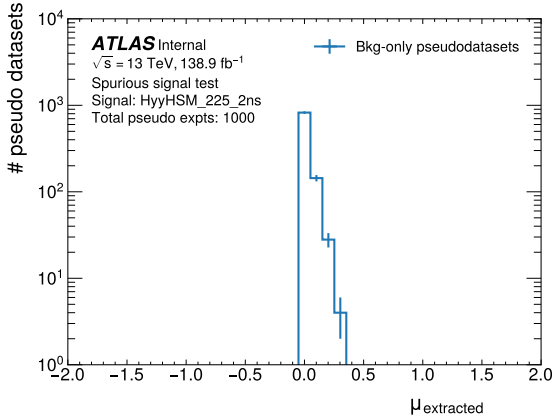


Figure 10.1: Fitted signal strength, μ , for 1000 pseudo-datasets generated under the background-only hypothesis. No signal is injected.

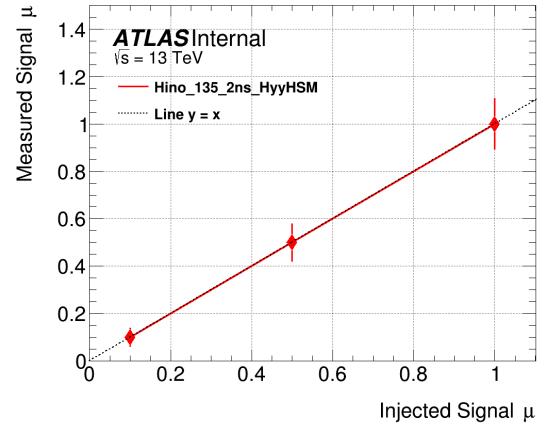


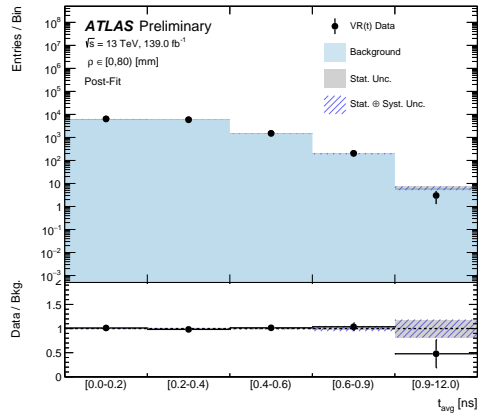
Figure 10.2: Fitted signal strength as a function of injected signal strength for $\mu = 0.1$, 0.5 , and 1 , performed with Asimov data.

10.2.2 VALIDATION OF BACKGROUND MODELING

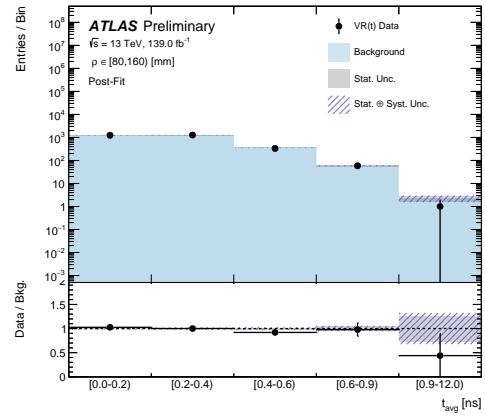
Armed with a robust fit framework, the next fit performance check is to validate the background modeling. Background-only fits to data in the VRs, shown in Figure 10.3 for $\text{VR}(t)$ and in Appendix E.1 for $\text{VR}(E_T^{\text{miss}})^{t>0}$ and $\text{VR}(E_T^{\text{miss}})^{t<0}$, test both the performance of the background estimation and its systematic uncertainties. Good agreement is observed between the predicted background and data in the various VRs, with VR data falling within uncertainty for nearly all timing and vertexing bins. Furthermore, no systematic deviations in timing shapes are observed, reinforcing the reliability of the background estimation strategy.

The systematic uncertainty pulls for background only fits to data in the VRs are shown in Figure 10.4. While there are some minor trends in the pulls within the $\text{VR}(t)$ and $\text{VR}(E_T^{\text{miss}})^{t>0}$ regions, the collective behavior of the pull distributions across the three VRs displays no strong bias associated with any of the background systematic uncertainties. The systematic uncertainties on the background shape, therefore, exhibit good behavior.

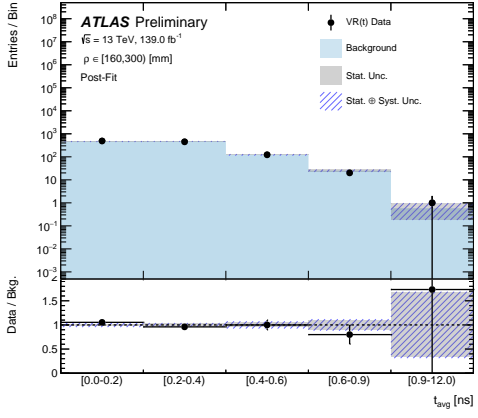
Table 10.1 shows the p_0 -values and corresponding significances of fits to the VRs for two representative signal points. All values are consistent with the background-only hypothesis. Additionally, spurious signal tests to data in the VRs confirm that no significant spurious signal was observed across all signal points. The maximum spurious signal value, defined as the extracted signal strength divided by its uncertainty, is roughly 1. These validation checks confirm that the VRs contain no unexpected features that might mimic a signal, further attesting to the soundness of the background estimation.



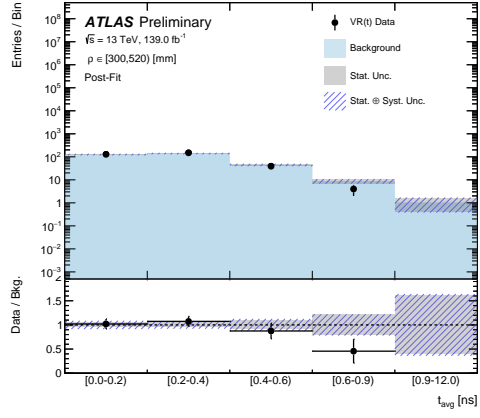
(a) $\rho \in [0, 80)$ mm



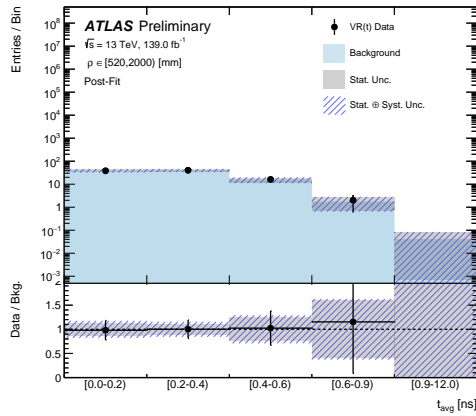
(b) $\rho \in [80, 160)$ mm



(c) $\rho \in [160, 300)$ mm



(d) $\rho \in [300, 520)$ mm



(e) $\rho \in [520, 2000)$ mm

Figure 10.3: Average timing distributions, $|t_{\text{avg}}|$, in each of the five exclusive ρ categories for $\text{VR}(t)$ data and the estimated background as determined by a background-only fit.

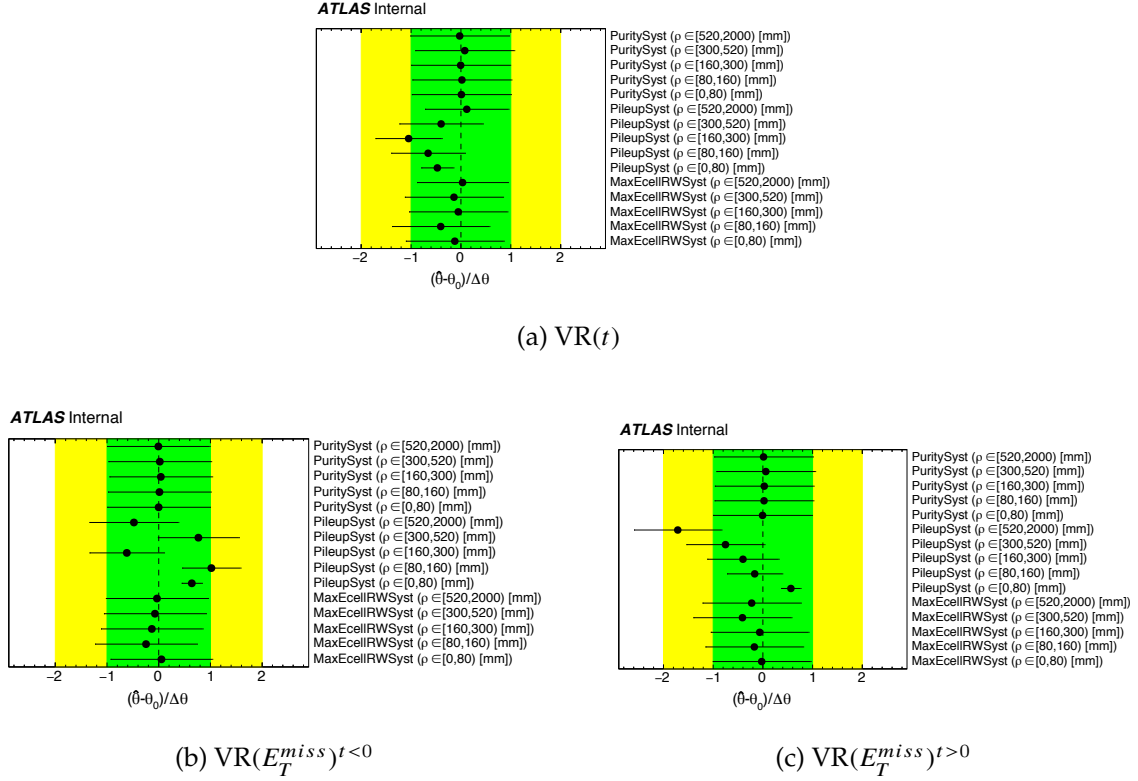


Figure 10.4: Pull distributions of a background-only fit to data in $VR(t)$, $VR(E_T^{miss})^{t<0}$, and $VR(E_T^{miss})^{t>0}$.

| | $BR(\tilde{\chi}_1^0 \rightarrow H + \tilde{G}) = 1$ | | $BR(\tilde{\chi}_1^0 \rightarrow Z + \tilde{G}) = 1$ | |
|------------------------|--|--------------|--|--------------|
| | p_0 -value | Significance | p_0 -value | Significance |
| $VR(t)$ | 0.65 | -0.41 | 0.71 | -0.55 |
| $VR(E_T^{miss})^{t<0}$ | 0.37 | 0.34 | 0.19 | 0.87 |
| $VR(E_T^{miss})^{t>0}$ | 0.14 | 1.09 | 0.22 | 0.76 |

Table 10.1: Fitted p_0 -values and significances for the three VRs. The signal models selected have $m(\tilde{\chi}_1^0) = 135$ GeV and $\tau(\tilde{\chi}_1^0) = 2$ ns, with two different $\tilde{\chi}_1^0$ decay modes shown.

10.2.3 VALIDATION OF DISCOVERY REGION

The number of events in highest timing bin of the background estimation serves as the prediction for SR_{disc} , defined in Section 8.2.4. Table 10.2 shows the predicted and observed number of events in each of the VRs with $0.9 < |t_{\text{avg}}| < 12$ ns. All predicted and observed values agree within 2σ , indicating a reasonable background prediction for the SR_{disc} , which is used for the model-independent interpretation.

| | $\text{VR}(E_T^{\text{miss}})^{t<0}$ | $\text{VR}(E_T^{\text{miss}})^{t>0}$ | $\text{VR}(t)$ |
|--------------|--------------------------------------|--------------------------------------|----------------|
| N. Predicted | 18.8 ± 4.4 | 17.2 ± 4.3 | 10.2 ± 3.0 |
| N. Observed | 14 | 18 | 5 |
| σ | -1.1 | 0.2 | -1.7 |

Table 10.2: Predicted and observed number of events in the highest timing bin, $0.9 < |t_{\text{avg}}| < 12$ ns, of each VR. The predicted values are determined using the background estimation drawn from the CR. The agreement between these values help validate the discovery region (SR_{disc}) strategy.

CHAPTER 11:

RESULTS AND INTERPRETATION

Science progresses best when observations force us to alter our preconceptions.

— Vera Rubin

The translation of quantitative, statistically-driven results into meaningful and digestible descriptions of and limits on reality represents a critical component of the scientific process. Just as promising theories galvanized much of the work in this thesis, these findings and their generalized constraints may inform the pursuits of theorists (and the symbiotic cycle continues). This chapter presents and discusses the unblinded SR results in Section 11.1. Section 11.2 provides the 95% CL exclusion limits on the cross section for $\tilde{\chi}_1^0$ pair-production in the context of the simplified GMSB SUSY model introduced in Section 2.4.2. Model-independent results are given in Section 11.3.

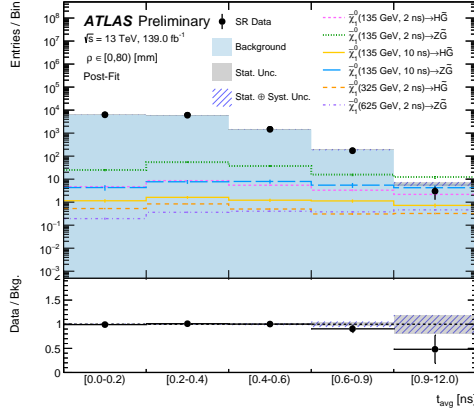
11.1 UNBLINDED SIGNAL REGION RESULTS

Once the background estimation strategy is solidified and validated, the SR timing and vertexing distributions are unblinded. The first step in the unblinding process is to perform a background-only fit to assess the compatibility of the observed SR data with the background-only hypothesis.

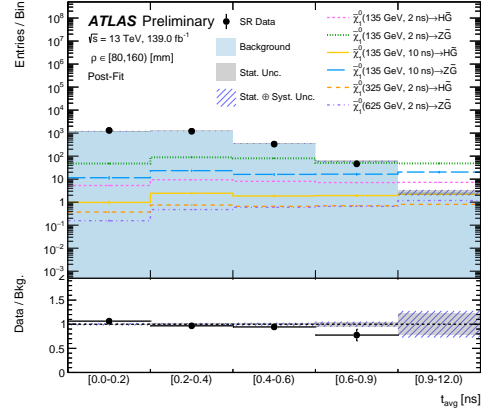
Figure 11.1 shows the unblinded post-fit t_{avg} distributions of the SR data and background estimation. Although the timing distributions in the SR are slightly narrower than those predicted by the nominal background template, the systematic uncertainties on the background estimation help account for this slight shape difference, leading to an acceptable overall agreement between the SR data and predicted background. The resulting pull distributions, shown in Figure 11.2, reveal that the fit pulls the pileup systematic uncertainty the most since it introduces the largest shape uncertainties on the background prediction (see Table 9.1). The origin of the slight shape disagreement is not completely clear since the timing resolutions do not exhibit large variations across the variables that define the SR (see Appendix C.3). However, one possible explanation is that the purity scaling procedure – i.e., the scaling of just two categories – does not fully capture the evolution of the photon purity composition across the analysis regions and its impact on the timing shapes.

The most significant single-bin deviation in the fitted results occurs in the highest ρ category and highest timing bin, where a single event is observed with $\rho = 560$ mm, $t_{\gamma_1} = 5.82$ ns, and $t_{\gamma_2} = 0.45$ ns. Other LAr calorimeter cells in the leading photon cluster (not only corresponding to the $E_{\text{cell}}^{\text{max}}$) also have times close to 5 ns, so this value is unlikely a mismeasurement. This event is highly incompatible with the signal hypothesis, which features correlated photon times with similar time delays (see Figure 8.8). Instead, this event is consistent with a satellite collision producing the leading photon and an overlaid in-time collision producing the subleading photon. Detailed information on this event can be found in Appendix B.2.

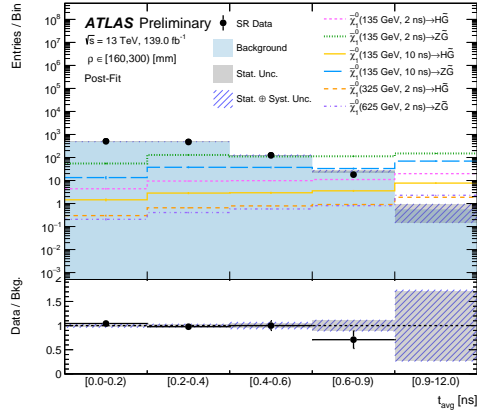
The background estimation derived from the CR contains several satellite collisions (albeit all at lower displacements – see Figure 8.11). An estimated number of satellite collisions is obtained by calculating the fraction of candidate satellite collision events in the CR and multiplying that fraction by the number of events in the SR. This process relies on the fact that the prevalence of satellite collisions is not found to be correlated with photon



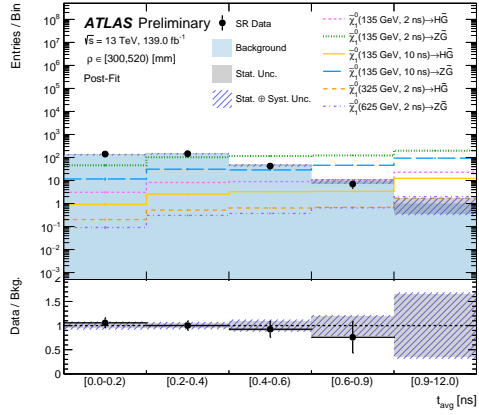
(a) $\rho \in [0, 80)$ mm



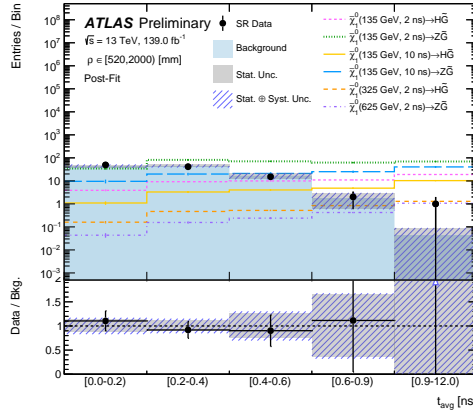
(b) $\rho \in [80, 160)$ mm



(c) $\rho \in [160, 300)$ mm

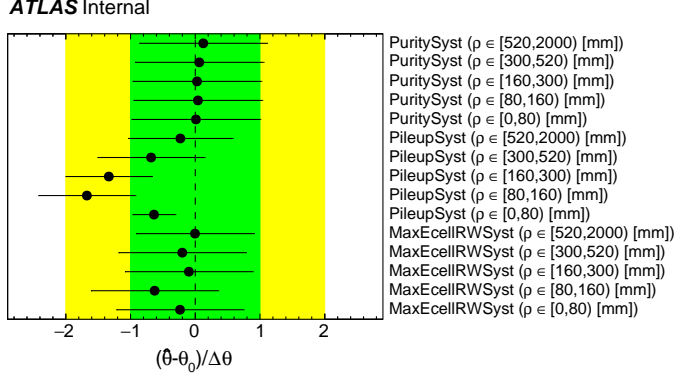


(d) $\rho \in [300, 520)$ mm



(e) $\rho \in [520, 2000)$ mm

Figure 11.1: Average timing distributions, $|t_{\text{avg}}|$, in each of the five exclusive ρ categories for SR data and the estimated background as determined by a background-only fit. For comparison, the expected timing shapes for several representative signal models normalized to their expected yields for the ATLAS Run 2 dataset, corresponding to an integrated luminosity of 139 fb^{-1} , are superimposed.



(a) VR(t)

Figure 11.2: Pull distributions of a background-only fit to the SR data.

kinematics (see Appendix B.1). Here, a candidate satellite collision must have at least one photon with a time between 4 and 6.5 ns. This procedure predicts 0.5 ± 0.3 satellite events in the SR; 1 such event is observed. While this simplified, statistics-only estimation omits sources of systematic uncertainty, it demonstrates that the number of satellite collisions observed in the SR is relatively compatible with the predicted value.

The next step in the unblinding process is to perform signal-plus-background fits to calculate the relevant p_0 -values and significances of the fit for the various signal hypotheses. The measured p_0 -values across all signal points range between 0.09 and 0.17, which correspond to a range of significances between 0.95 and 1.35σ . Since the timing and vertexing templates across signal models have relatively similar shapes, as shown in the overlaid distributions in Figure 11.1, the p_0 -values and significances across signal points are expected to have comparable values. Indeed, the distribution of these values across signal points is relatively flat and contains no local spikes or significant deviations from the background (see Appendix E.2). The fact that no significant excess is observed, despite the presence of one event in the highest timing and vertexing bin, showcases the robustness of the fit strategy and its immunity to insignificant statistical fluctuations.

11.2 LIMITS AND EXCLUSIONS ON SUPERSYMMETRIC MODELS

Since no significant signal excess is observed in the SR data, the results are used to set 95% CL exclusion limits on the signal production cross section, $\sigma(pp \rightarrow \tilde{\chi}_1^0 \tilde{\chi}_1^0)$, via the CL_s technique [131, 132] under the asymptotic approximation [130]. The exclusion limits are set as a function of the mass, lifetime, and branching ratio of the lightest neutralino, $\tilde{\chi}_1^0$, in the context of the simplified GMSB SUSY model discussed in Sections 2.4.2 and 7.3. The model assumes a higgsino-like $\tilde{\chi}_1^0$, corresponding to a nearly degenerate electroweakino triplet ($\tilde{\chi}_1^\pm$, $\tilde{\chi}_2^0$, and $\tilde{\chi}_1^0$), with $\text{BR}(\tilde{\chi}_1^0 \rightarrow H + \tilde{G}) + \text{BR}(\tilde{\chi}_1^0 \rightarrow Z + \tilde{G}) = 1$.

Figure 11.3 shows 95% CL limits on $\sigma(pp \rightarrow \tilde{\chi}_1^0 \tilde{\chi}_1^0)$ as a function of $m(\tilde{\chi}_1^0)$ for signals with (a) $\text{BR}(\tilde{\chi}_1^0 \rightarrow H + \tilde{G}) = 1$ and (b) $\text{BR}(\tilde{\chi}_1^0 \rightarrow Z + \tilde{G}) = 1$. For models with insufficient statistics, the asymptotic approximation breaks down, and no limit is provided. The results are presented in the different colored distributions, including curves corresponding to the

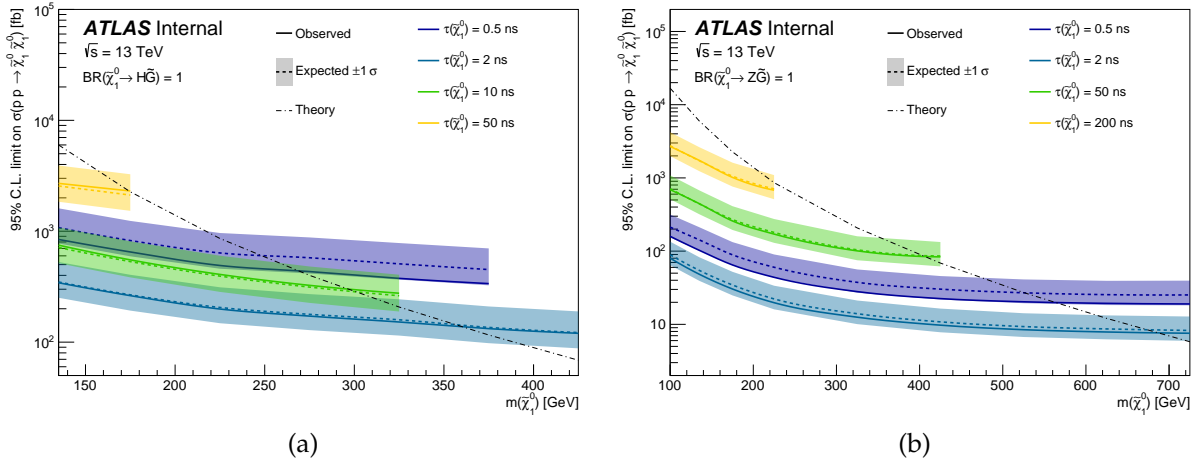


Figure 11.3: The 95% CL limits on $\sigma(pp \rightarrow \tilde{\chi}_1^0 \tilde{\chi}_1^0)$ as a function of $\tilde{\chi}_1^0$ mass for the different decay modes of (a) $\text{BR}(\tilde{\chi}_1^0 \rightarrow H + \tilde{G}) = 1$ and (b) $\text{BR}(\tilde{\chi}_1^0 \rightarrow Z + \tilde{G}) = 1$. Several signal models with varying lifetimes are overlaid for comparison. Included are the theoretical expectations for each signal hypothesis, calculated from a GMSB SUSY model that assumes nearly degenerate $\tilde{\chi}_1^0$, $\tilde{\chi}_1^\pm$, and $\tilde{\chi}_2^0$ masses.

observed, expected, and expected $\pm 1\sigma$ cross section upper limits. An additional curve represents the theoretical cross section of the selected models, which varies as a function of $\tilde{\chi}_1^0$ mass. As expected, signal models with more energetic decay products – those with higher $\tilde{\chi}_1^0$ masses – tend to be associated with lower cross section limits. However, only signal models corresponding to those where the observed limit curve lies below the theoretical cross section curve – occurring at lower $\tilde{\chi}_1^0$ masses – are considered *excluded*.

Figure 11.4 shows 95% CL limits on $\sigma(pp \rightarrow \tilde{\chi}_1^0 \tilde{\chi}_1^0)$ as a function of $\tau(\tilde{\chi}_1^0)$ for signals with (a) $\text{BR}(\tilde{\chi}_1^0 \rightarrow \text{H} + \tilde{G}) = 1$ and (b) $\text{BR}(\tilde{\chi}_1^0 \rightarrow \text{Z} + \tilde{G}) = 1$. These figures follow the same formatting convention as those described in the previous paragraph. Here, signals with lower lifetimes suffer from diminished discrimination between the prompt background and the signal, while those with higher lifetimes lose a higher fraction of events decaying beyond the detector. These counteracting effects generate the strongest limits at intermediate lifetimes near 2 ns.

Figure 11.5 shows 95% CL limits on $\sigma(pp \rightarrow \tilde{\chi}_1^0 \tilde{\chi}_1^0)$ as a function of the $\tilde{\chi}_1^0$ branching ratio for signals with varying $m(\tilde{\chi}_1^0)$ and with $\tau(\tilde{\chi}_1^0) = 2$ ns – near the lifetime value

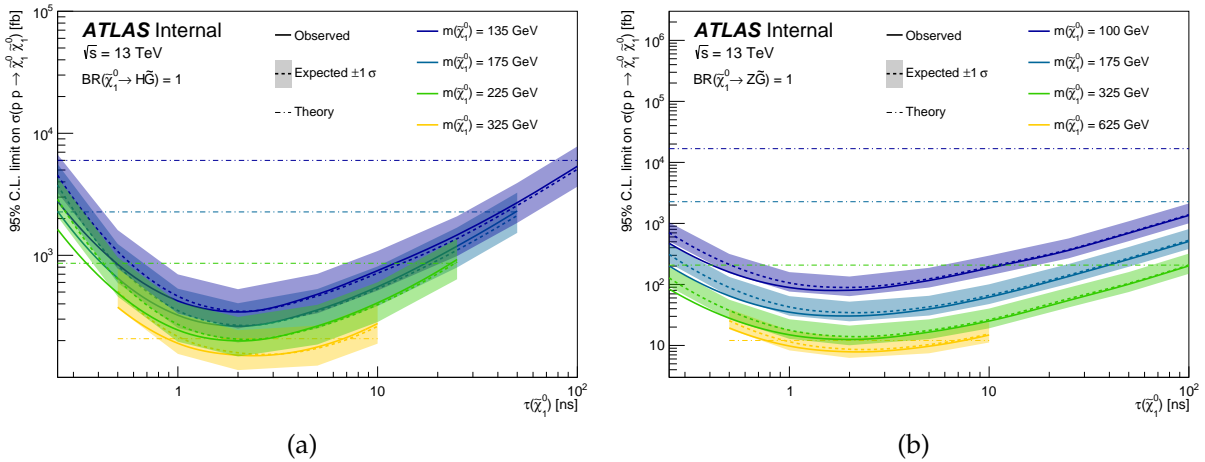


Figure 11.4: The 95% CL limits on $\sigma(pp \rightarrow \tilde{\chi}_1^0 \tilde{\chi}_1^0)$ as a function of $\tilde{\chi}_1^0$ lifetime for the different decay modes of (a) $\text{BR}(\tilde{\chi}_1^0 \rightarrow \text{H} + \tilde{G}) = 1$ and (b) $\text{BR}(\tilde{\chi}_1^0 \rightarrow \text{Z} + \tilde{G}) = 1$. Several signal models with varying masses are overlaid for comparison. Included are the theoretical expectations for each signal hypothesis, calculated from a GMSB SUSY model that assumes nearly degenerate $\tilde{\chi}_1^0$, $\tilde{\chi}_1^\pm$, and $\tilde{\chi}_2^0$ masses.

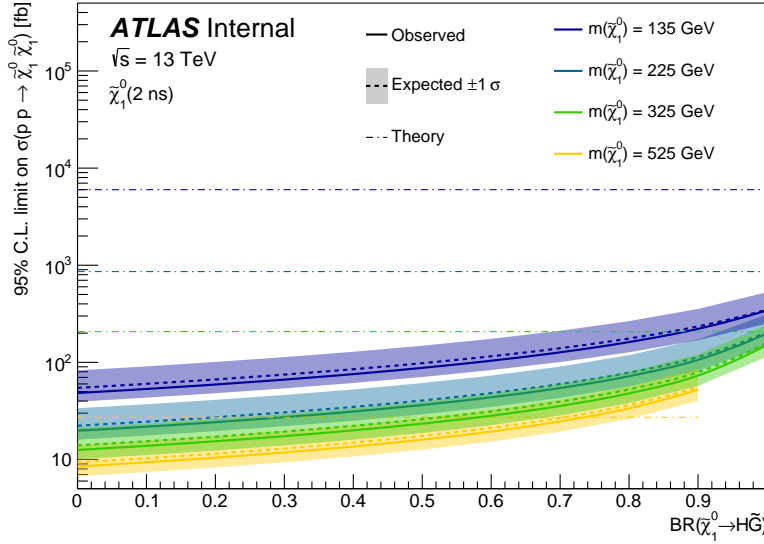


Figure 11.5: The 95% CL limits on $\sigma(pp \rightarrow \tilde{\chi}_1^0 \tilde{\chi}_1^0)$ as a function of $\text{BR}(\tilde{\chi}_1^0 \rightarrow H + \tilde{G})$, with $\text{BR}(\tilde{\chi}_1^0 \rightarrow H + \tilde{G}) + \text{BR}(\tilde{\chi}_1^0 \rightarrow Z + \tilde{G}) = 1$. Several signal hypotheses are overlaid that are labeled by the $\tilde{\chi}_1^0$ mass, all with a fixed $\tilde{\chi}_1^0$ lifetime of 2 ns. Included are the theoretical expectations for each mass hypothesis, calculated from a GMSB SUSY model that assumes nearly degenerate $\tilde{\chi}_1^0$, $\tilde{\chi}_1^\pm$, and $\tilde{\chi}_2^0$ masses.

with optimal sensitivity. The trends in this figure are compatible with those shown previously: stronger exclusions are achieved for signals with higher masses and larger values of $\text{BR}(\tilde{\chi}_1^0 \rightarrow Z + \tilde{G})$. The latter feature occurs because the branching ratio of $Z \rightarrow ee$ is higher than that of $H \rightarrow \gamma\gamma$, leading to significantly higher signal yields and, thus, enhanced sensitivity.

As discussed, signal models whose observed cross section limit is lower than that of the theoretical prediction are considered excluded. The distributions shown in Figure 11.6 portray the 95% CL exclusions as a function of $m(\tilde{\chi}_1^0)$ and $\tau(\tilde{\chi}_1^0)$ for several different $\text{BR}(\tilde{\chi}_1^0)$ scenarios. Here, signal models whose parameters lie to the left of the various curves are excluded. This rich figure reveals that for signals with $\text{BR}(\tilde{\chi}_1^0 \rightarrow H + \tilde{G}) = 1$, exclusions on $m(\tilde{\chi}_1^0)$ reach nearly 370 GeV and those on $\tau(\tilde{\chi}_1^0)$ range from 0.25 to 100 ns; for signals with $\text{BR}(\tilde{\chi}_1^0 \rightarrow Z + \tilde{G}) = 1$, exclusions extend past $m(\tilde{\chi}_1^0) = 700$ GeV and span nearly four orders of magnitude in $\tau(\tilde{\chi}_1^0)$, from 0.25 ns to 1 μs .

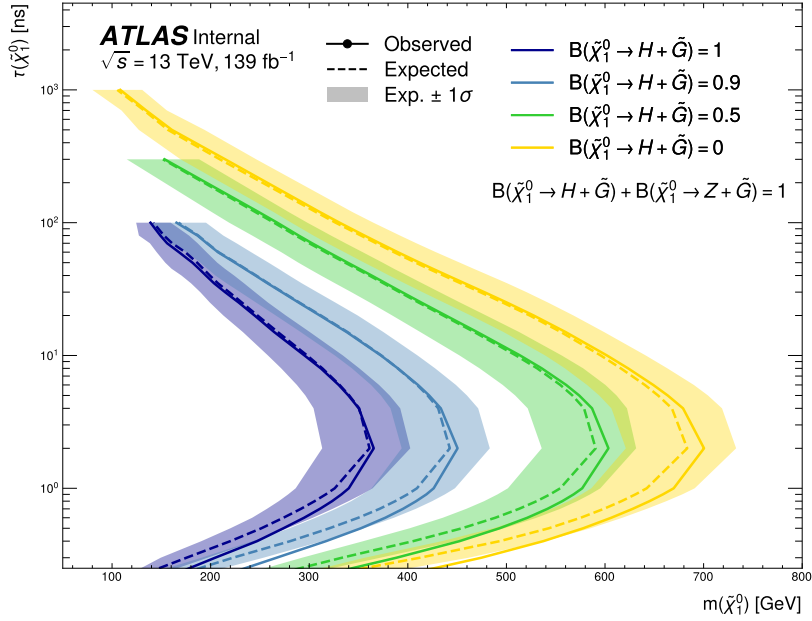


Figure 11.6: The 95% CL exclusion limits on the pair-production of $\tilde{\chi}_1^0$ in the context of the simplified SUSY GMSB model described in the text. The model assumes $\text{BR}(\tilde{\chi}_1^0 \rightarrow H + \tilde{G}) + \text{BR}(\tilde{\chi}_1^0 \rightarrow Z + \tilde{G}) = 1$. Exclusions are shown for various $\tilde{\chi}_1^0$ branching ratio hypothesis as a function of $\tilde{\chi}_1^0$ mass and lifetime.

Finally, Figure 11.7 shows excluded values of $m(\tilde{\chi}_1^0)$ as a function of $\text{BR}(\tilde{\chi}_1^0 \rightarrow H + \tilde{G})$ and $\tau(\tilde{\chi}_1^0)$. Models with parameters enclosed by the contours of constant $m(\tilde{\chi}_1^0)$ are considered excluded at 95% CL. This distribution further illustrates how the exclusion limits evolve throughout the three-dimensional signal grid.

11.3 MODEL-INDEPENDENT LIMITS

Model-independent limits are determined by examining the number of expected and observed events in the discovery region, SR_{disc} , which occupies the highest timing bin in the SR ($0.9 < t_{\text{avg}} < 12$ ns). As discussed in Section 10.2.3, the CR predicts 10.18 ± 3.02 events in the SR_{disc} ; 4 events are observed. This result corresponds to a deficit with a significance

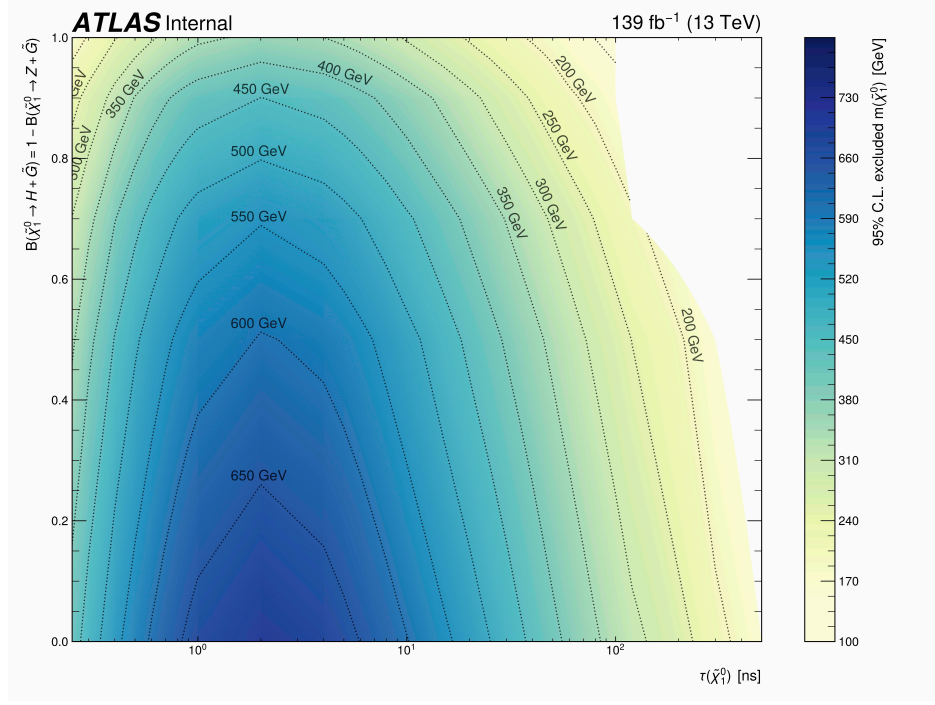


Figure 11.7: The 95% CL exclusion limits on the pair-production of $\tilde{\chi}_1^0$ in the context of the simplified SUSY GMSB model described in the text, which assumes $\text{BR}(\tilde{\chi}_1^0 \rightarrow H + \tilde{G}) + \text{BR}(\tilde{\chi}_1^0 \rightarrow Z + \tilde{G}) = 1$. Exclusions are shown as a function of $\tilde{\chi}_1^0$ mass, lifetime, and branching ratio, where signal models with parameters enclosed by the mass contour lines are considered excluded.

of -2σ and is consistent with observing slightly narrower timing distributions in the SR than in the background prediction.

CHAPTER 12:

CONCLUSIONS AND OUTLOOK

There were no textbooks, so we had to write them.

— Katherine Johnson

Long-lived particles constitute some of the most promising, yet weakly constrained, classes of signatures explored at the LHC. Recent years have witnessed a steady, persistent expansion of coverage of LLP signatures, and the results presented in this thesis represent a small slice of this collective effort. The search establishes the first dedicated sensitivity to displaced and delayed diphoton vertices and extends phase space coverage for displaced and delayed dielectron vertices.

The analysis utilizes the full Run 2 dataset recorded by the ATLAS detector at the LHC, corresponding to an integrated luminosity of 139 fb^{-1} of pp collisions at a center-of-mass energy of $\sqrt{s} = 13 \text{ TeV}$. The sensitivity of the search is driven by the capabilities of the LAr calorimeter measurements, which provide excellent discriminating power between the prompt background and the displaced and delayed signal models. These measurements include the timing variables, with resolutions as low as 200 ps, and the novel Trackless Calo-Vertexing strategy, delivering spatial resolutions approaching 20 mm. Each of these approaches provides an independent handle on critical features of the signal.

The background estimation follows a data-driven approach since MC simulation does not fully capture the shape of the non-Gaussian tails of the LAr calorimeter timing distributions. The background estimation is extracted from data in the control region, defined as a low- E_T^{miss} , high- $m_{\gamma\gamma}$ region, which contains negligible levels of signal contamination. A statistical analysis framework executes a simultaneous fit of the average photon timing distribution in categories of secondary vertex displacement. This fit is performed using the predicted background model from the control region and data and simulated signal in the signal region, which occupies a high- E_T^{miss} region with a broad $m_{\gamma\gamma}$ mass window surrounding the mass peaks of the Higgs boson and Z boson.

No significant deviations in the data with respect to the predicted background are observed. One event, measured in the highest timing bin and highest vertexing category, has features compatible with a satellite collision – a source of expected background. Results are interpreted in a GMSB SUSY model as 95% CL upper limits on the cross section of di- $\tilde{\chi}_1^0$ production, scanning the $\tilde{\chi}_1^0$ mass, lifetime, and branching ratio to the Higgs boson or Z boson; the model assumes a nearly degenerate electroweakino triplet ($\tilde{\chi}_1^0$, $\tilde{\chi}_2^0$, $\tilde{\chi}_1^\pm$) with $\text{BR}(\tilde{\chi}_1^0 \rightarrow \text{H} + \tilde{G}) + \text{BR}(\tilde{\chi}_1^0 \rightarrow \text{Z} + \tilde{G}) = 1$. For signal models with $\text{BR}(\tilde{\chi}_1^0 \rightarrow \text{H} + \tilde{G}) = 1$, the highest excluded $\tilde{\chi}_1^0$ mass is nearly 370 GeV, and excluded lifetimes at lower $\tilde{\chi}_1^0$ masses range from 0.25 to 100 ns. For signal models with $\text{BR}(\tilde{\chi}_1^0 \rightarrow \text{Z} + \tilde{G}) = 1$, $\tilde{\chi}_1^0$ masses as high as 700 GeV are excluded, and lifetime exclusions for lower $\tilde{\chi}_1^0$ masses span several orders of magnitude, from 0.25 ns to 1 μs .

These results mark the first foray into the sphere of displaced diphoton vertices; however, they by no means cover the entire phase space of this elusive and challenging final state. The analysis intentionally blinded two critical regions of phase space that have low signal yields for this particular SUSY GMSB model but could serve as promising signal regions for other signal models with displaced di-EM vertices. These regions include: a low- E_T^{miss} , low- $m_{\gamma\gamma}$ region, for possible displaced production of Higgs bosons and Z

bosons without E_T^{miss} ; and a high- E_T^{miss} , high- $m_{\gamma\gamma}$ region, for possible displaced production of new, exotic di-EM resonances at higher masses produced in association with E_T^{miss} .

Expanded applications of dedicated LAr calorimeter measurements and methodologies may broaden sensitivity to a wealth of other long-lived BSM physics signatures. The capabilities of the LAr timing measurement are already being explored by other delayed electron analyses, and one could even imagine applying this specialized variable to delayed jets with sufficient electromagnetic activity. As demonstrated by the success of the Trackless Calo-Vertexing tool, the power of calorimeter pointing-based measurements can be far-reaching; further adaptations could include extensions to many-body decays or integration with displaced track measurements.

As LHC Run 3 ramps up this year, the prospect of discovering new physics in the long-lived regime has never been so auspicious. The Phase I installation and commissioning process has equipped LHC detectors with upgraded hardware components and data processing systems, improving and expanding the triggering capabilities of these machines. In particular, freshly minted trigger menus include novel LLP triggers that explicitly target displaced or delayed objects. Looking further ahead, preparation for the much-anticipated HL-LHC upgrade, which promises to increase the delivered instantaneous luminosity of the LHC, is already underway. Runs 4 and beyond are slated to record up to 3000 fb^{-1} of data – over 20 times the size of the current dataset. Particle physics is in for quite a ride, and, as a field defined by pushing boundaries, it is exciting to think about what the coming years of innovation may bring.

REFERENCES

- [1] T. Andeen, J. Ban, G. Brooijmans, A. Emerman, P. Kinget, J. Kuppambatti, D. Mahon, I. Ochoa, W. Sippach, and Q. Wang, *Journal of Instrumentation* **15** no. 04, (2020) P04012–P04012.
<https://doi.org/10.1088/1748-0221/15/04/p04012>.
- [2] K. E. Kennedy, Oct. 2019. <https://cds.cern.ch/record/2696186>.
- [3] ATLAS Collaboration, tech. rep., CERN, Geneva, Apr. 2022.
<https://cds.cern.ch/record/2805799>.
- [4] ATLAS Collaboration, tech. rep., CERN, Geneva, Jul. 2022.
<https://atlas.web.cern.ch/Atlas/GROUPS/PHYSICS/CONFNOTES/ATLAS-CONF-2022-051/ATLAS-CONF-2022-051.pdf>.
- [5] E. Noether, *Nachrichten von der Gesellschaft der Wissenschaften zu Göttingen, Mathematisch-Physikalische Klasse* **1918** (1918) 235–257.
<http://eudml.org/doc/59024>.
- [6] M. Gell-Mann, *Phys. Lett.* **8** (1964) 214–215.
- [7] G. Zweig, An SU(3) model for strong interaction symmetry and its breaking. Version 2. Feb. 1964.
- [8] D. J. Gross and F. Wilczek, *Phys. Rev. Lett.* **30** (1973) 1343–1346.
<https://link.aps.org/doi/10.1103/PhysRevLett.30.1343>.
- [9] H. D. Politzer, *Phys. Rev. Lett.* **30** (1973) 1346–1349.
<https://link.aps.org/doi/10.1103/PhysRevLett.30.1346>.
- [10] F. Englert and R. Brout, *Phys. Rev. Lett.* **13** (1964) 321–323.
- [11] P. W. Higgs, *Phys. Lett.* **12** (1964) 132–133.
- [12] P. W. Higgs, *Phys. Rev. Lett.* **13** (1964) 508–509.
- [13] G. Guralnik, C. Hagen, and T. Kibble, *Phys. Rev. Lett.* **13** (1964) 585–587.
- [14] P. W. Higgs, *Phys. Rev.* **145** (1966) 1156–1163.
- [15] T. Kibble, *Phys. Rev.* **155** (1967) 1554–1561.
- [16] G. Costa and G. Fogli, Symmetries and group theory in particle physics. An introduction to space-time and internal symmetries, vol. 823. 2012.

- [17] Y. Nambu, Phys. Rev. Lett. **4** (1960) 380–382.
<https://link.aps.org/doi/10.1103/PhysRevLett.4.380>.
- [18] J. Goldstone, Il Nuovo Cimento **19** (1961) 154–164.
- [19] M. Drewes, International Journal of Modern Physics E **22** no. 08, (2013) 1330019.
<https://doi.org/10.1142%2Fs0218301313300191>.
- [20] Super-Kamiokande Collaboration, Y. Ashie et al., Phys. Rev. Lett. **93** (2004) 101801.
<https://link.aps.org/doi/10.1103/PhysRevLett.93.101801>.
- [21] S. L. Glashow, J. Iliopoulos, and L. Maiani, Phys. Rev. D **2** (1970) 1285–1292.
<https://link.aps.org/doi/10.1103/PhysRevD.2.1285>.
- [22] SLAC-SP-017 Collaboration, J. E. Augustin et al., Phys. Rev. Lett. **33** (1974) 1406–1408.
- [23] E598 Collaboration, J. J. Aubert et al., Phys. Rev. Lett. **33** (1974) 1404–1406.
- [24] M. L. Perl et al., Phys. Rev. Lett. **35** (1975) 1489–1492.
<https://link.aps.org/doi/10.1103/PhysRevLett.35.1489>.
- [25] S. W. Herb et al., Phys. Rev. Lett. **39** (1977) 252–255.
<https://link.aps.org/doi/10.1103/PhysRevLett.39.252>.
- [26] M. Kobayashi and T. Maskawa, Prog. Theor. Phys. **49** (1973) 652–657.
- [27] Aachen-Annecy-Birmingham-CERN-Helsinki-London(QMC)-Paris(CdF)-Riverside-Rome-Rutherford-Saclay(CEN)-Vienna Collaboration, UA1 Collaboration, G. T. J. Arnison et al., Phys. Lett. B **122** (1983) 103–116. 31 p.
<https://cds.cern.ch/record/142059>.
- [28] G. Arnison et al., Phys. Lett. B **126** no. 5, (1983) 398–410.
<https://www.sciencedirect.com/science/article/pii/0370269383901880>.
- [29] F. J. Hasert, W. Krenz, J. Krogh, D. Lanske, J. Morfin, K. Schultze, H. Weerts, G. Bertrand-Coremans, J. Lemonne, J. Sacton, W. Doninck, P. Vilain, C. Baltay, D. Cundy, D. Haidt, M. Jaffre, P. Musset, A. Pullia, S. Natali, and W. Scott, Phys. Lett. B **46** (1973) 121–124.
- [30] D0 Collaboration, S. Abachi et al., Phys. Rev. Lett. **74** (1995) 2632–2637.
<https://link.aps.org/doi/10.1103/PhysRevLett.74.2632>.
- [31] CDF Collaboration, F. Abe et al., Phys. Rev. Lett. **74** (1995) 2626–2631.
<https://link.aps.org/doi/10.1103/PhysRevLett.74.2626>.
- [32] K. Kodama et al., Phys. Lett. B **504** no. 3, (2001) 218–224.
<https://doi.org/10.1016%2Fs0370-2693%2801%2900307-0>.

- [33] ATLAS Collaboration, Phys. Lett. B **716** no. 1, (2012) 1 – 29.
<http://www.sciencedirect.com/science/article/pii/S037026931200857X>.
- [34] CMS Collaboration, Phys. Lett. B **716** (2012) 30–61, arXiv:1207.7235 [hep-ex].
- [35] CDF Collaboration, Science **376** no. 6589, (2022) 170–176,
<https://www.science.org/doi/pdf/10.1126/science.abk1781>.
<https://www.science.org/doi/abs/10.1126/science.abk1781>.
- [36] ATLAS Collaboration, “Standard model summary plots.” <https://atlas.web.cern.ch/Atlas/GROUPS/PHYSICS/PUBNOTES/ATL-PHYS-PUB-2022-009>.
- [37] K. G. Begeman, A. H. Broeils, and R. H. Sanders, Mon. Notices Royal Astron. Soc. **249** no. 3, (1991) 523–537. <https://doi.org/10.1093/mnras/249.3.523>.
- [38] J. A. Tyson, G. P. Kochanski, and I. P. Dell’Antonio, The Astrophysical Journal **498** no. 2, (1998) L107–L110. <http://dx.doi.org/10.1086/311314>.
- [39] C. Abel et al., Phys. Rev. Lett. **124** (2020) 081803.
<https://link.aps.org/doi/10.1103/PhysRevLett.124.081803>.
- [40] Y. Golfand and E. Likhtman, JETP Lett. **13** (1971) 323. [Pisma Zh. Eksp. Teor. Fiz. **13** (1971) 452].
- [41] D. Volkov and V. Akulov, Phys. Lett. B **46** (1973) 109.
- [42] J. Wess and B. Zumino, Nucl. Phys. B **70** (1974) 39.
- [43] J. Wess and B. Zumino, Nucl. Phys. B **78** (1974) 1.
- [44] S. Ferrara and B. Zumino, Nucl. Phys. B **79** (1974) 413.
- [45] A. Salam and J. Strathdee, Phys. Lett. B **51** (1974) 353.
- [46] S. P. Martin, Adv. Ser. Direct. High Energy Phys. **18** (1998) 1,
arXiv:hep-ph/9709356.
- [47] N. Sakai, Z. Phys. C **11** (1981) 153.
- [48] S. Dimopoulos, S. Raby, and F. Wilczek, Phys. Rev. D **24** (1981) 1681.
- [49] L. E. Ibáñez and G. G. Ross, Phys. Lett. B **105** (1981) 439.
- [50] P. Langacker, arXiv: High Energy Physics - Phenomenology (1993).
- [51] J. R. Ellis, S. Kelley, and D. V. Nanopoulos, Phys. Lett. B **260** (1991) 131–137.
- [52] U. Amaldi, W. de Boer, and H. Furstenau, Phys. Lett. B **260** (1991) 447–455.
- [53] P. Langacker and M. Luo, Phys. Rev. D **44** (1991) 817–822.
<https://link.aps.org/doi/10.1103/PhysRevD.44.817>.

- [54] C. GIUNTI, C. W. KIM, and U. W. LEE, *Mod. Phys. Lett. A* **06** no. 19, (1991) 1745–1755, <https://doi.org/10.1142/S0217732391001883>.
<https://doi.org/10.1142/S0217732391001883>.
- [55] R. Haag, J. T. Lopuszanski, and M. Sohnius, *Nucl. Phys. B* **88** (1975) 257.
- [56] S. Coleman and J. Mandula, *Phys. Rev.* **159** (1967) 1251–1256.
<https://link.aps.org/doi/10.1103/PhysRev.159.1251>.
- [57] G. 't Hooft, C. Itzykson, A. Jaffe, H. Lehmann, P. K. Mitter, I. M. Singer, and R. Stora, eds., Recent Developments in Gauge Theories. Proceedings, Nato Advanced Study Institute, Cargese, France, August 26 - September 8, 1979, vol. 59. 1980.
- [58] S. Weinberg, *Phys. Rev. D* **13** (1976) 974–996.
<https://link.aps.org/doi/10.1103/PhysRevD.13.974>.
- [59] S. Weinberg, *Phys. Rev. D* **19** (1979) 1277–1280.
<https://link.aps.org/doi/10.1103/PhysRevD.19.1277>.
- [60] E. Gildener, *Phys. Rev. D* **14** (1976) 1667–1672.
<https://link.aps.org/doi/10.1103/PhysRevD.14.1667>.
- [61] S. P. Martin, *Adv. Ser. Direct. High Energy Phys.* **21** (2010) 1–153,
[arXiv:hep-ph/9709356](https://arxiv.org/abs/hep-ph/9709356).
- [62] P. Fayet, *Phys. Lett. B* **64** (1976) 159.
- [63] P. Fayet, *Phys. Lett. B* **69** (1977) 489.
- [64] Particle Data Group, *Progress of Theoretical and Experimental Physics* **2020** no. 8, (2020). <https://doi.org/10.1093/ptep/ptaa104.083C01>.
- [65] G. R. Farrar and P. Fayet, *Phys. Lett. B* **76** (1978) 575.
- [66] L. Girardello and M. T. Grisaru, *Nucl. Phys. B* **194** (1982) 65.
- [67] D. Z. Freedman, P. van Nieuwenhuizen, and S. Ferrara, *Phys. Rev. D* **13** (1976) 3214.
- [68] M. Dine and W. Fischler, *Phys. Lett. B* **110** (1982) 227.
- [69] S. Ferrara, L. Girardello, and F. Palumbo, *Phys. Rev. D* **20** (1979) 403–408.
<https://link.aps.org/doi/10.1103/PhysRevD.20.403>.
- [70] G. Giudice and R. Rattazzi, *Phys. Rep.* **322** (1998) 419–99. 102 p.
<https://cds.cern.ch/record/342670>. Submitted to None.
- [71] L. Alvarez-Gaume, M. Claudson, and M. B. Wise, *Nucl. Phys. B* **207** (1982) 96.
- [72] C. R. Nappi and B. A. Ovrut, *Phys. Lett. B* **113** (1982) 175.

- [73] M. Dine and A. E. Nelson, Phys. Rev. D **48** (1993) 1277–1287.
<https://link.aps.org/doi/10.1103/PhysRevD.48.1277>.
- [74] M. Dine, A. E. Nelson, and Y. Shirman, Phys. Rev. D **51** (1995) 1362–1370.
<https://link.aps.org/doi/10.1103/PhysRevD.51.1362>.
- [75] M. Dine, A. E. Nelson, Y. Nir, and Y. Shirman, Phys. Rev. D **53** (1996) 2658–2669.
<https://link.aps.org/doi/10.1103/PhysRevD.53.2658>.
- [76] P. Meade, M. Reece, and D. Shih, JHEP **10** (2010) 067, arXiv:1006.4575 [hep-ph].
- [77] L. Lee, C. Ohm, A. Soffer, and T.-T. Yu, Progress in Particle and Nuclear Physics **106** (2019) 210–255. <https://doi.org/10.1016%2Fj.ppnp.2019.02.006>.
- [78] S. Bobrovskiy, J. Hajer, and S. Rydbeck, Journal of High Energy Physics **2013** no. 2, (2013). <https://doi.org/10.1007%2Fjhep02%282013%29133>.
- [79] J. Fan, M. Reece, and J. T. Ruderman, Journal of High Energy Physics **2011** no. 11, (2011). <https://doi.org/10.1007%2Fjhep11%282011%29012>.
- [80] M. Guchait and J. Kumar, Phys. Rev. D **95** no. 3, (2017).
<https://doi.org/10.1103%2Fphysrevd.95.035036>.
- [81] D. Curtin, R. Essig, S. Gori, P. Jaiswal, A. Katz, T. Liu, Z. Liu, D. McKeen, J. Shelton, M. Strassler, Z. Surujon, B. Tweedie, and Y.-M. Zhong, Phys. Rev. D **90** no. 7, (2014).
<https://doi.org/10.1103%2Fphysrevd.90.075004>.
- [82] M. Bauer, M. Heiles, M. Neubert, and A. Thamm, The European Physical Journal C **79** no. 1, (2019). <https://doi.org/10.1140%2Fepjc%2Fs10052-019-6587-9>.
- [83] K. S. Agashe, J. H. Collins, P. Du, S. Hong, D. Kim, and R. K. Mishra, Journal of High Energy Physics **2017** no. 5, (2017).
<https://doi.org/10.1007%2Fjhep05%282017%29078>.
- [84] G. F. Giudice, Y. Kats, M. McCullough, R. Torre, and A. Urbano, Journal of High Energy Physics **2018** no. 6, (2018).
<https://doi.org/10.1007%2Fjhep06%282018%29009>.
- [85] P. Meade, N. Seiberg, and D. Shih, Prog. Theor. Phys. Suppl. **177** (2009) 143, arXiv:0801.3278 [hep-ph].
- [86] M. Buican, P. Meade, N. Seiberg, and D. Shih, Journal of High Energy Physics **2009** no. 03, (2009) 016–016. <https://doi.org/10.1088/1126-6708/2009/03/016>.
- [87] C. Cheung, A. L. Fitzpatrick, and D. Shih, JHEP **07** (2008) 054, arXiv:0710.3585 [hep-ph].
- [88] L. Evans and P. Bryant, JINST **3** (2008) S08001.
- [89] E. Mobs,, <https://cds.cern.ch/record/2636343>.

- [90] ATLAS Collaboration, “Luminosity public results run 2.” <https://twiki.cern.ch/twiki/bin/view/AtlasPublic/LuminosityPublicResultsRun2>.
- [91] A. Jeff, M. Andersen, A. Boccardi, S. Bozyigit, E. Bravin, T. Lefevre, A. Rabiller, F. Roncarolo, C. P. Welsch, and A. S. Fisher, Conf. Proc. **C1205201** (2012) MOEPPB010. 3 p. <https://cds.cern.ch/record/1459107>.
- [92] B. Cleland, N. Nikiforou, and J. Parsons, tech. rep., CERN, Geneva, Apr. 2014. <https://cds.cern.ch/record/1697773>.
- [93] J. Chen, D. J. Mahon, and J. Parsons, tech. rep., CERN, Geneva, Jan. 2020. <https://cds.cern.ch/record/2707701>.
- [94] ATLAS Collaboration, JINST **3** (2008) S08003. <http://stacks.iop.org/1748-0221/3/i=08/a=S08003>.
- [95] ATLAS Collaboration, tech. rep., Geneva, 1997. <https://cds.cern.ch/record/331063>.
- [96] ATLAS Collaboration, tech. rep., Sep. 2010. <https://cds.cern.ch/record/1291633>.
- [97] ATLAS Collaboration, tech. rep. CERN-LHCC-96-041, CERN, Geneva, 1996. <https://cds.cern.ch/record/331061>.
- [98] ATLAS Collaboration, tech. rep., Geneva, 1996. <https://cds.cern.ch/record/331062>.
- [99] G. Avoni et al., Journal of Instrumentation **13** no. 07, (2018) P07017–P07017. <https://doi.org/10.1088/1748-0221/13/07/P07017>.
- [100] S. van der Meer, tech. rep. CERN-ISR-PO-68-31. ISR-PO-68-31, CERN, Geneva, 1968. <https://cds.cern.ch/record/296752>.
- [101] ATLAS Collaboration Collaboration, tech. rep., Geneva, 1998. <https://cds.cern.ch/record/381429>.
- [102] ATLAS Collaboration, “Approved plots DAQ.” <https://twiki.cern.ch/twiki/bin/view/AtlasPublic/ApprovedPlotsDAQ>.
- [103] ATLAS Collaboration, tech. rep., Geneva, 2003. <https://cds.cern.ch/record/616089>.
- [104] ATLAS Collaboration, The European Physical Journal C **80** no. 1, (2020) 47. <https://doi.org/10.1140/epjc/s10052-019-7500-2>.
- [105] J. Pequeno, Mar. 2008. <https://cds.cern.ch/record/1096081>.
- [106] T. Cornelissen, M. Elsing, S. Fleischmann, W. Liebig, E. Moyse, and A. Salzburger, tech. rep. ATL-SOFT-PUB-2007-007. ATL-COM-SOFT-2007-002, CERN, Geneva, Mar. 2007. <https://cds.cern.ch/record/1020106>.

- [107] ATLAS Collaboration, The European Physical Journal C **77** no. 5, (2017).
<https://doi.org/10.1140%2Fepjc%2Fs10052-017-4887-5>.
- [108] ATLAS Collaboration, tech. rep., CERN, Geneva, Jul. 2015.
<https://cds.cern.ch/record/2037717>.
- [109] ATLAS Collaboration, Eur. Phys. J. C **77** (2016) 490. 87 p, arXiv:1603.02934.
<https://cds.cern.ch/record/2138166>.
- [110] ATLAS, JINST **14** (2019) P12006, arXiv:1908.00005 [hep-ex].
- [111] ATLAS Collaboration, Eur. Phys. J. C **79** (2018) 205. 55 p, arXiv:1810.05087.
<https://cds.cern.ch/record/2643391>.
- [112] ATLAS Collaboration, The European Physical Journal C **79** no. 8, (2019).
<https://doi.org/10.1140%2Fepjc%2Fs10052-019-7140-6>.
- [113] ATLAS Collaboration, Eur. Phys. J. C **77** (2017) 466, arXiv:1703.10485 [hep-ex].
- [114] M. Cacciari, G. Salam, and G. Soyez, JHEP **04** (2008) 063, arXiv:0802.1189 [hep-ph].
- [115] ATLAS Collaboration, Eur. Phys. J. C **76** (2016) 292, arXiv:1603.05598 [hep-ex].
- [116] ATLAS Collaboration, Eur. Phys. J. C **78** no. arXiv:1802.08168. 11, (2018) 903. 66 p.
<https://cds.cern.ch/record/2305380>.
- [117] ATLAS Collaboration, Phys. Rev. D **90** no. 11, (2014).
<https://doi.org/10.1103%2Fphysrevd.90.112015>.
- [118] ATLAS Collaboration, Phys. Rev. D **88** (2013) 012001.
<https://link.aps.org/doi/10.1103/PhysRevD.88.012001>.
- [119] ATLAS Collaboration, Phys. Rev. D **90** (2014) 112005.
<https://link.aps.org/doi/10.1103/PhysRevD.90.112005>.
- [120] W. Cleland and E. Stern, NIM A **338** no. 2, (1994) 467 – 497.
<http://www.sciencedirect.com/science/article/pii/0168900294913323>.
- [121] ATLAS Collaboration, “Beampspot public results.”
<https://twiki.cern.ch/twiki/bin/view/AtlasPublic/BeamSpotPublicResults>.
- [122] J. Alwall, M. Herquet, F. Maltoni, O. Mattelaer, and T. Stelzer, Journal of High Energy Physics **2011** no. 6, (2011).
<https://doi.org/10.1007%2Fjhep06%282011%29128>.
- [123] T. Sjostrand, S. Ask, J. R. Christiansen, R. Corke, N. Desai, P. Ilten, S. Mrenna, S. Prestel, C. O. Rasmussen, and P. Z. Skands, Computer Physics Communications **191** (2015) 159–177. <https://doi.org/10.1016%2Fj.cpc.2015.01.024>.

- [124] S. Agostinelli et al., Nuclear Instruments and Methods in Physics Research Section A: Accelerators, Spectrometers, Detectors and Associated Equipment **506** no. 3, (2003) 250–303.
<https://www.sciencedirect.com/science/article/pii/S0168900203013688>.
- [125] Phys. Rev. Lett. **127** no. 5, (2021).
<https://doi.org/10.1103/PhysRevLett.127.051802>.
- [126] E. Gross, CERN Yellow Rep. School Proc. **3** (2018) 199–221.
- [127] ATLAS Collaboration, The European Physical Journal C **76** no. 12, (2016) 653.
<https://doi.org/10.1140/epjc/s10052-016-4466-1>.
- [128] ATLAS Collaboration, JINST **14** no. 03, (2019) P03017, arXiv:1812.03848 [hep-ex].
- [129] J. Neyman and E. S. Pearson, On the Problem of the Most Efficient Tests of Statistical Hypotheses. Springer New York, New York, NY, 1992.
https://doi.org/10.1007/978-1-4612-0919-5_6.
- [130] G. Cowan, K. Cranmer, E. Gross, and O. Vitells, The European Physical Journal C **71** no. 2, (2011). <https://doi.org/10.1140/epjc/s10052-011-1554-0>.
- [131] A. L. Read, J. Phys. G **28** (2002) 2693–2704.
- [132] T. Junk, Nuclear Instruments and Methods in Physics Research Section A: Accelerators, Spectrometers, Detectors and Associated Equipment **434** no. 2, (1999) 435–443.
<https://www.sciencedirect.com/science/article/pii/S0168900299004982>.
- [133] “TRExFitter documentation.”
<https://trexfitter-docs.web.cern.ch/trexfitter-docs/>.
- [134] S. S. Wilks, Annals Math. Statist. **9** no. 1, (1938) 60–62.
- [135] A. Wald, Transactions of the American Mathematical Society **54** no. 3, (1943) 426–482. <http://www.jstor.org/stable/1990256>.

APPENDICES

APPENDIX A:

TRACKLESS CALO-VERTEXING

PERFORMANCE

This appendix showcases the resolutions of the vertexing variables, V_R and V_Z , as a function of various kinematic variables. Here, $Z \rightarrow ee$ data and MC samples are used to characterize and validate vertexing variable performance. In data, this sample delivers a very pure sample of real electrons, through which it is possible to reliably compare the behavior of the vertexing variables for a similar profile of events in data and MC simulation. Although these studies focus on electron objects, they utilize only electron shower measurements in the LAr calorimeter. Since electron and photon showers in the LAr calorimeter are very similar, these results can be extrapolated to photons.

Figure A.1 shows the V_R , V_Z , and ρ variables for $Z \rightarrow ee$ data and MC simulation. Here, the data from 2017 is used, and the $Z \rightarrow ee$ simulation corresponds to that data-taking period. The electrons' $E_{\text{cell}}^{\text{max}}$ distributions in the $Z \rightarrow ee$ MC sample have been reweighted to match those of the data. The ratio panel shows that these vertexing shapes exhibit good agreement both in their high-statistics cores and sparsely populated tails. The similarities in these distributions indicate that the simulation accurately models the collision process, decay, and electron showering.

Figures A.2 and A.3 show the resolutions of V_R and V_Z as a function of various electron kinematic parameters, including p_T , $|\eta|$, $E_{\text{cell}}^{\text{max}}$, m_{ee} , p_T^{ee} , and $\Delta\phi_{ee}$. No $E_{\text{cell}}^{\text{max}}$ reweighting

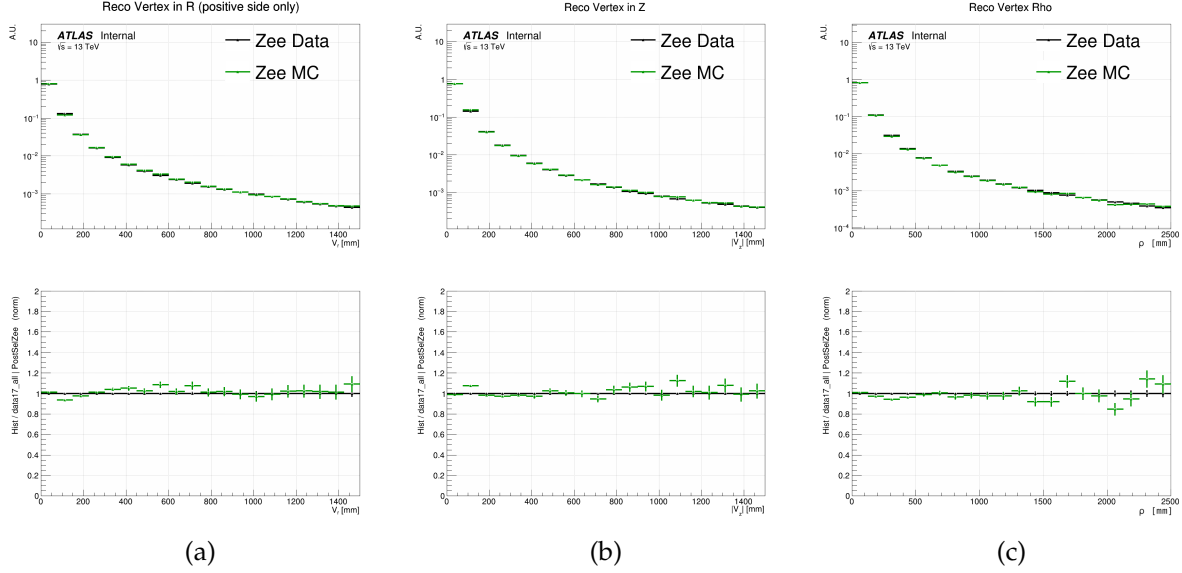
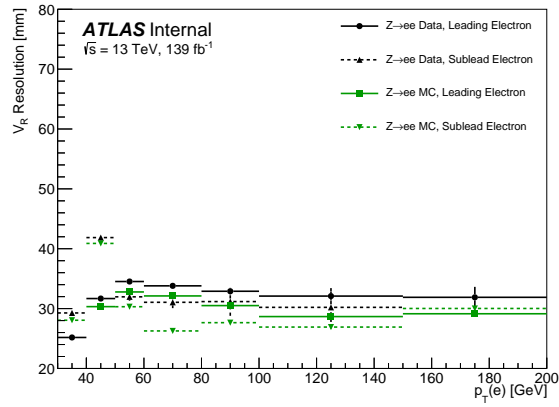
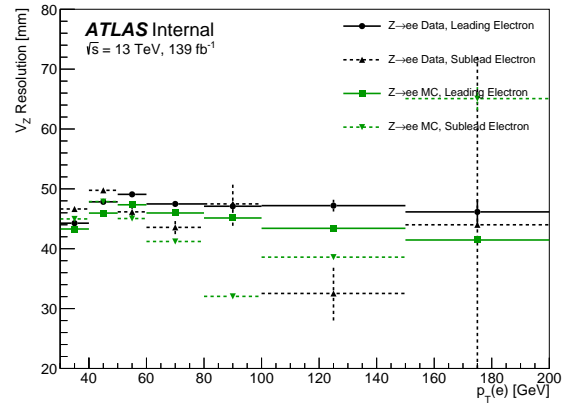


Figure A.1: Comparison of vertexing distributions in $Z \rightarrow ee$ samples illustrate good agreement between data and MC simulation.

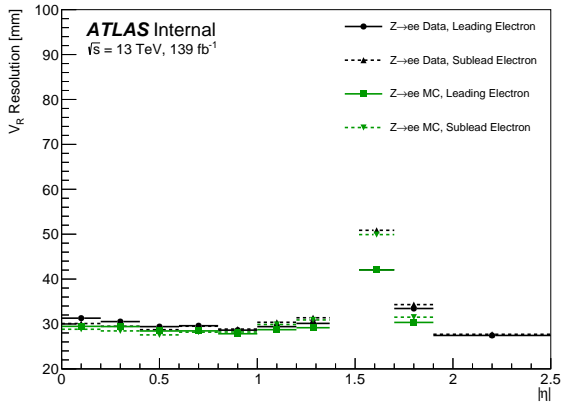
procedure has been applied. Trends between $Z \rightarrow ee$ data and MC simulation largely agree, with only slight deviations. Note that relationships between variables likely influence these distributions and that overall, the geometric variables ($|\eta|$, $\Delta\eta$, $\Delta\phi$) play the most significant role in determining vertexing performance. The vertexing resolutions as a function of $\Delta\eta_{ee}$, which plays the largest role in determining vertex resolution, are shown in the main body of this thesis (see Figure 6.4). The $\Delta\phi$ dependence comes from the fact that the vertexing procedure is performed in two dimensions (in the $R - z$ plane) and is agnostic to ϕ measurements; therefore, the procedure is more "physically accurate" for events with small $\Delta\phi$ than for those with large $\Delta\phi$.



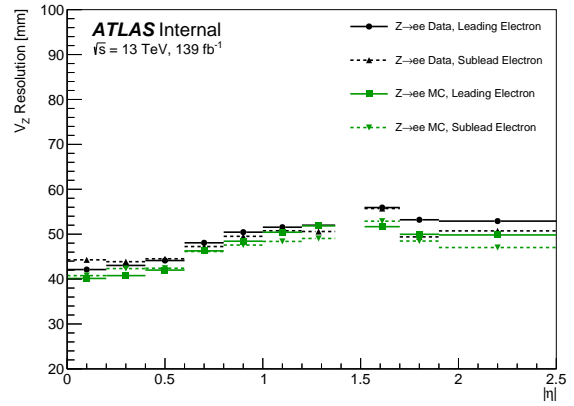
(a)



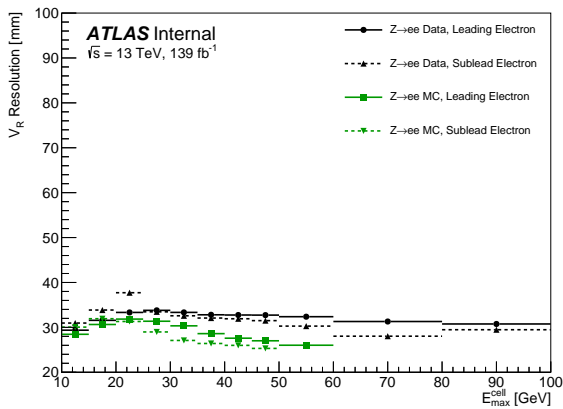
(b)



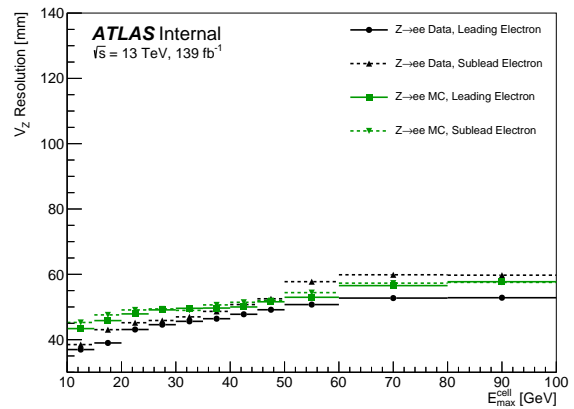
(c)



(d)

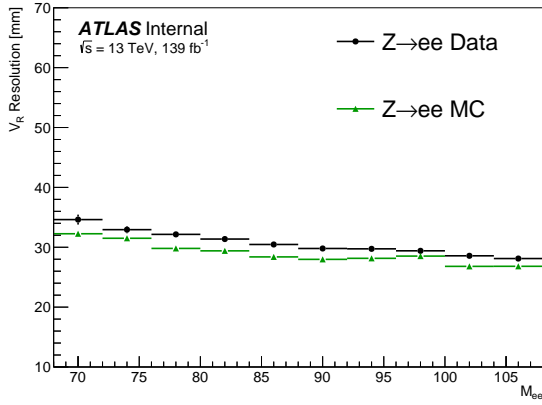


(e)

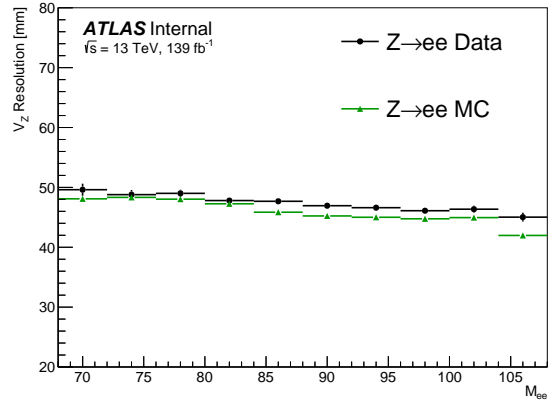


(f)

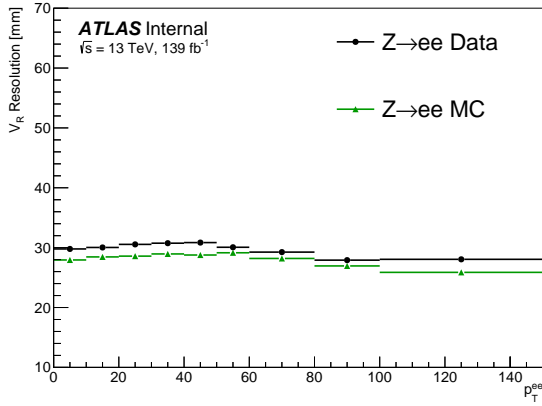
Figure A.2: Vertexing variable resolution as a function of electron kinematics, including p_T (top), $|\eta|$ (middle), and $E_{\text{cell}}^{\text{max}}$ (bottom) for V_R (left) and V_Z (right).



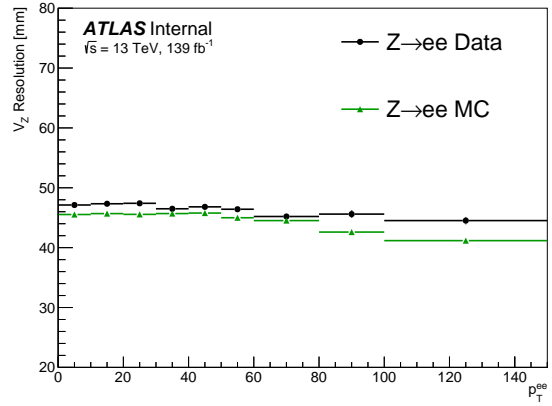
(a)



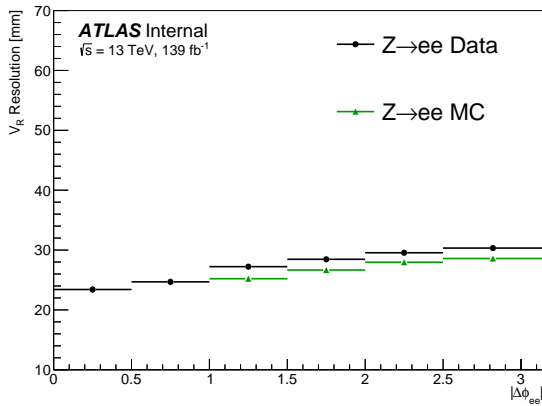
(b)



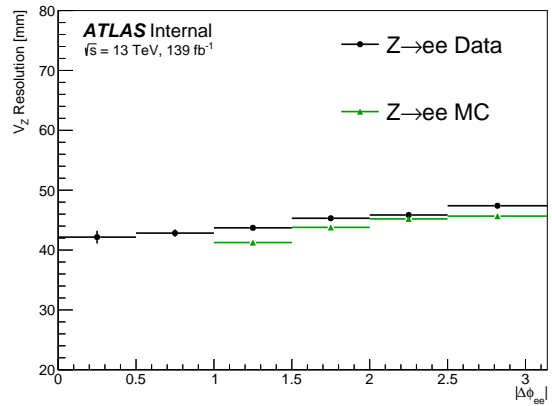
(c)



(d)



(e)



(f)

Figure A.3: Vertexing variable resolution as a function of electron kinematics, including m_{ee} (top), p_T^{ee} (middle), and $\Delta\phi_{ee}$ (bottom) for V_R (left) and V_Z (right).

APPENDIX B:

SATELLITE COLLISION STUDIES

This appendix discusses both the general dependencies and prevalence of satellite collisions across various analysis regions (Section B.1), as well as the candidate satellite collision event identified in the SR (Section B.2).

B.1 SATELLITE COLLISIONS ACROSS ANALYSIS REGIONS

This section discusses the observation of satellite collisions across regions and explores possible mechanisms that might increase or reduce the likelihood of a satellite collision occurring. Figure B.1 shows the leading and subleading photon timing distributions for all events passing the photon object selection described in Section 8.1.1. Candidate satellite collision events are defined as those that contain at least one photon with $4 < |t| < 6.5$ ns. Note that this selection requires only one photon to pass this criterion and not both, allowing for a higher-statistics sample and the inclusion of candidate satellite events like the one in the SR that has only one photon with a significantly delayed time.

Table B.1 shows the predicted and measured number of satellite collisions across various event selection scenarios and analysis regions. The table divides events into pospos and negneg events since the size of the preceding and trailing satellite bunches with respect to the nominal bunch can be slightly asymmetric. The table includes the measured number of satellites for events that pass the photon object selection, for those that pass

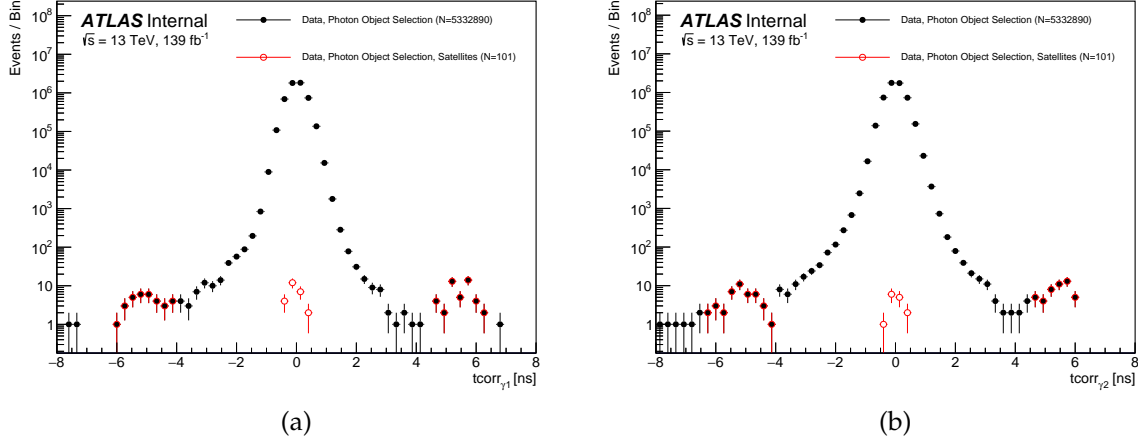


Figure B.1: Timing distributions in data for events passing the photon object selection for the analysis (in black), and those that additionally contain at least one photon object with $4 < |t| < 6.5$ ns (in red). Events that contain photons with times in that window are considered satellite collision candidates.

| Timing Category | γ Object Sel. | Analysis Presel. | CR | $VR(E_T^{miss})$ | $VR(t)$ | SR |
|-------------------------|----------------------|------------------|---------|------------------|---------------|---------------|
| negneg | 1,769,870 | 701,841 | 107,859 | 53,424 | 18,260 | - |
| - Satellites (CR pred.) | - | - | - | 0.5 ± 0.5 | 0.2 ± 0.2 | - |
| - Satellites (Meas.) | 35 | 13 | 1 | 2 | 0 | - |
| pospos | 1,820,405 | 727,357 | 112,868 | 55,405 | - | 18.276 |
| - Satellites (CR pred.) | - | - | - | 1.4 ± 0.9 | - | 0.5 ± 0.3 |
| - Satellites (Meas.) | 44 | 20 | 3 | 0 | - | 1 |

Table B.1: Predicted and measured number of satellite collisions across regions.

the full analysis preselection (see Section 8.1), and for each of the analysis regions (see Section 8.2). The CR is used to predict the number of satellite collisions in each of the validation regions and the SR and follows the procedure described in Section 11.1: the number of satellite collisions in each region is determined by scaling the number observed in the CR to the target region yields. This statistics-only estimation omits sources of systematic uncertainty; however, it is intended to show the number of satellite collisions across regions is relatively compatible with prediction.

Figures B.2 and B.3 show the prevalence of satellite collisions in data as a function of the analysis variables that define the SR, including E_T^{miss} , $m_{\gamma\gamma}$, $\Delta\phi_{\gamma\gamma}$, and $p_T^{\gamma\gamma}$, as well as photon p_T , E_{cell}^{max} , and $|\eta|$. These figures compare the distributions of data events passing the photon object selection with those that are also satellite collision candidates. These distributions reveal no statistically significant trend, correlation, or dependencies associated with the occurrence of satellite collisions.

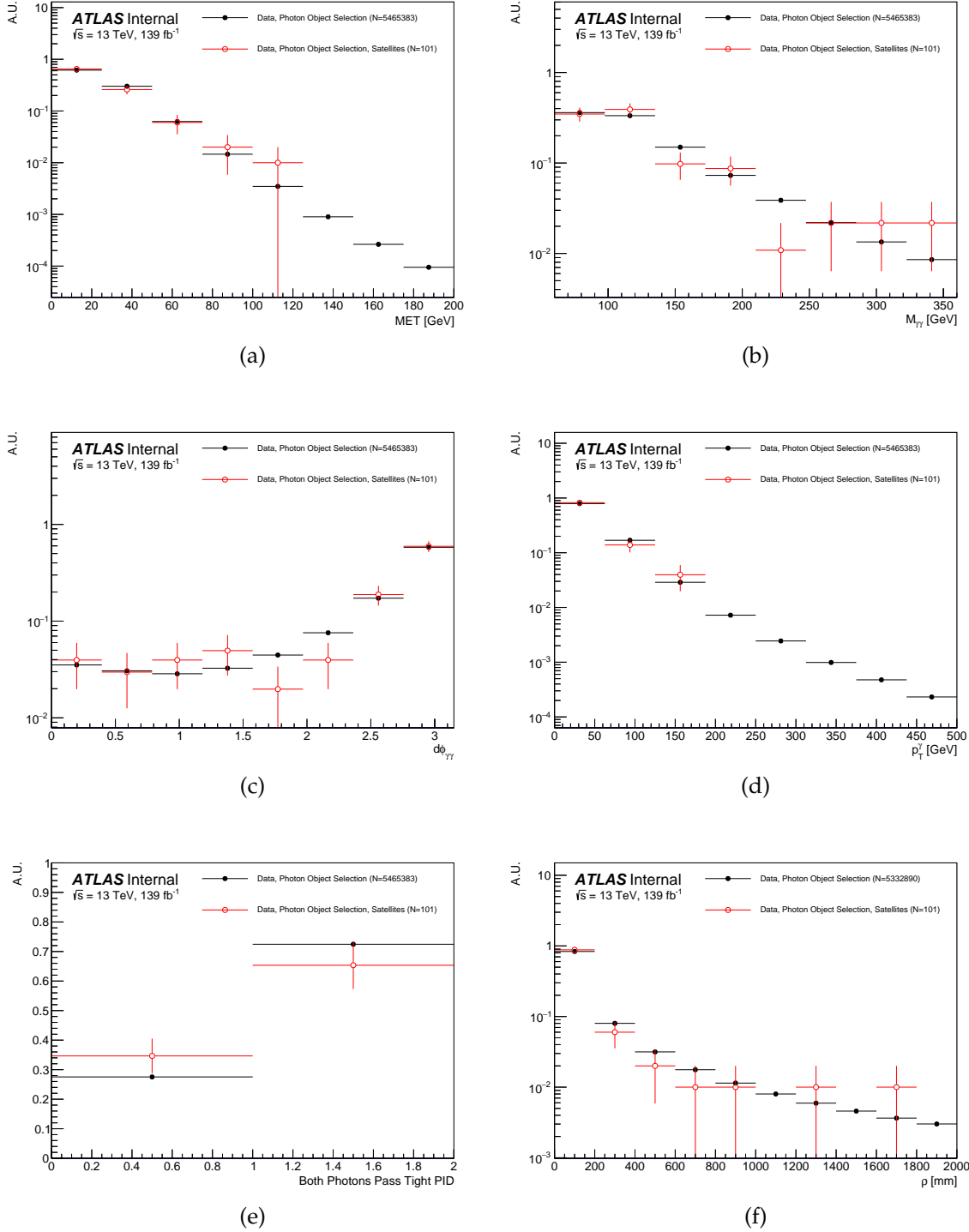


Figure B.2: Prevalence of satellite collisions as a function of critical analysis variables, including (a) E_T^{miss} , (b) $m_{\gamma\gamma}$, (c) $\Delta\phi_{\gamma\gamma}$, (d) $p_T^{\gamma\gamma}$, (e) photon purity category (pass TIGHTTIGHT), and (f) ρ . The histograms in black show the distributions for all data events passing the photon object selection described in Section 8.1.1; those in red show events that additionally contain at least one candidate satellite photon, with $4 < |t| < 6.5$ ns.

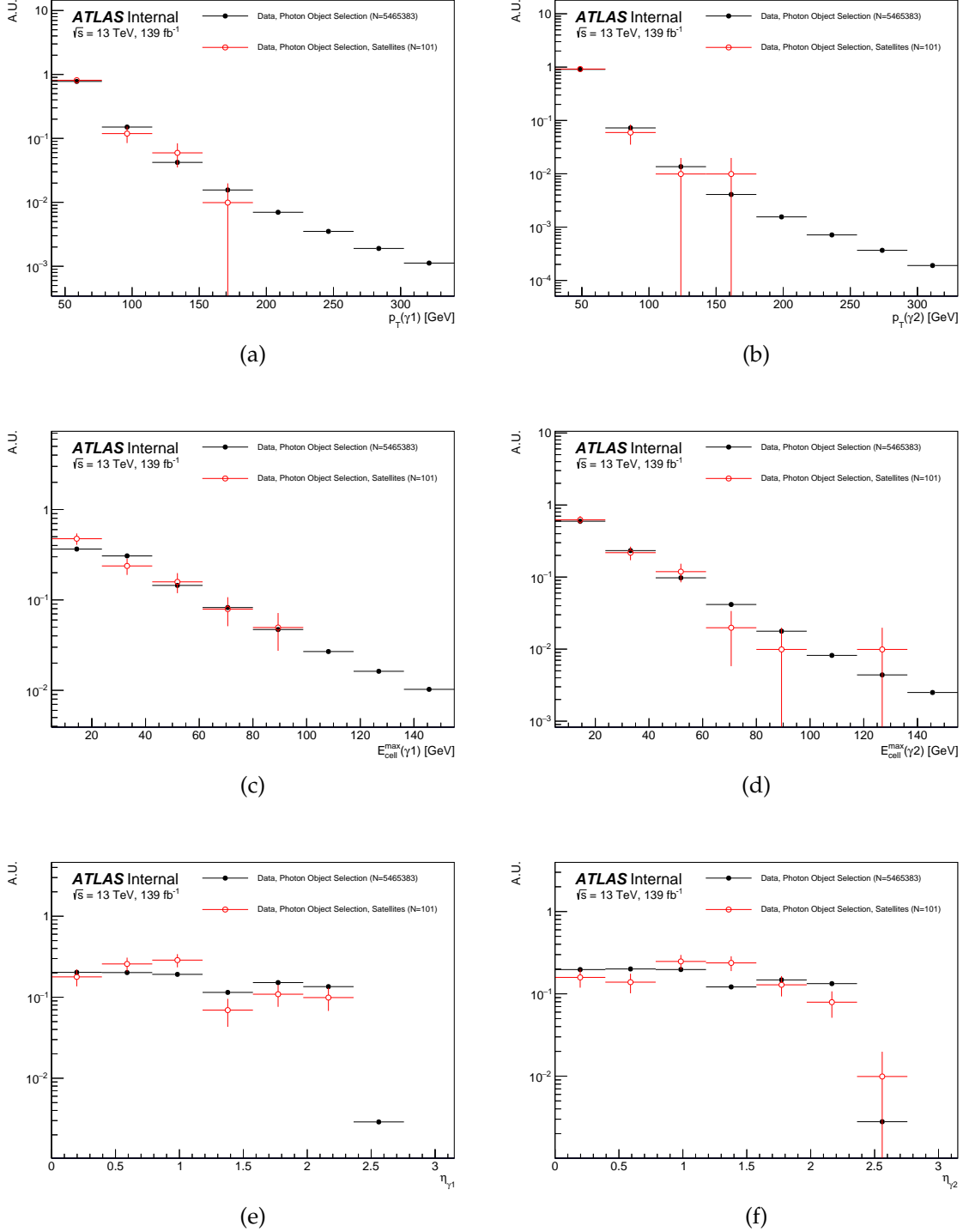


Figure B.3: Prevalence of satellite collisions as a function of photon object variables, including photon p_T (top), $E_{\text{cell}}^{\text{max}}$ (middle), and $|\eta|$ (bottom) for the leading (left) and subleading (right) photon. The histograms in black show the distributions for all data events passing the photon object selection described in Section 8.1.1; those in red show events that additionally contain at least one candidate satellite photon, with $4 < |t| < 6.5$ ns.

B.2 SATELLITE COLLISION EVENT IN THE SIGNAL REGION

All ATLAS events come with a unique identifier in the form of a run number and the event number in that particular run. The signal region event in the highest vertexing and timing bin has been identified as ATLAS run 359593, event 761048468, and is shown in an event display in Figure B.4. Here, the leading and subleading photons have times of 5.8 and 0.5 ns, respectively. The leading photon can be seen in the ATLAS end-cap in the bottom left of the figure and can be identified by the higher energy deposit in the LAr calorimeter (in green) in the right image.

Table B.2 details relevant event- and object-level variables pertaining to this event. In addition to the high probability that this event contains a satellite collision overlaid with an in-time collision (see Section 11.1), the leading photon is very likely a jet (i.e., a fake photon). The object corresponding to the leading photon was reconstructed as both a photon

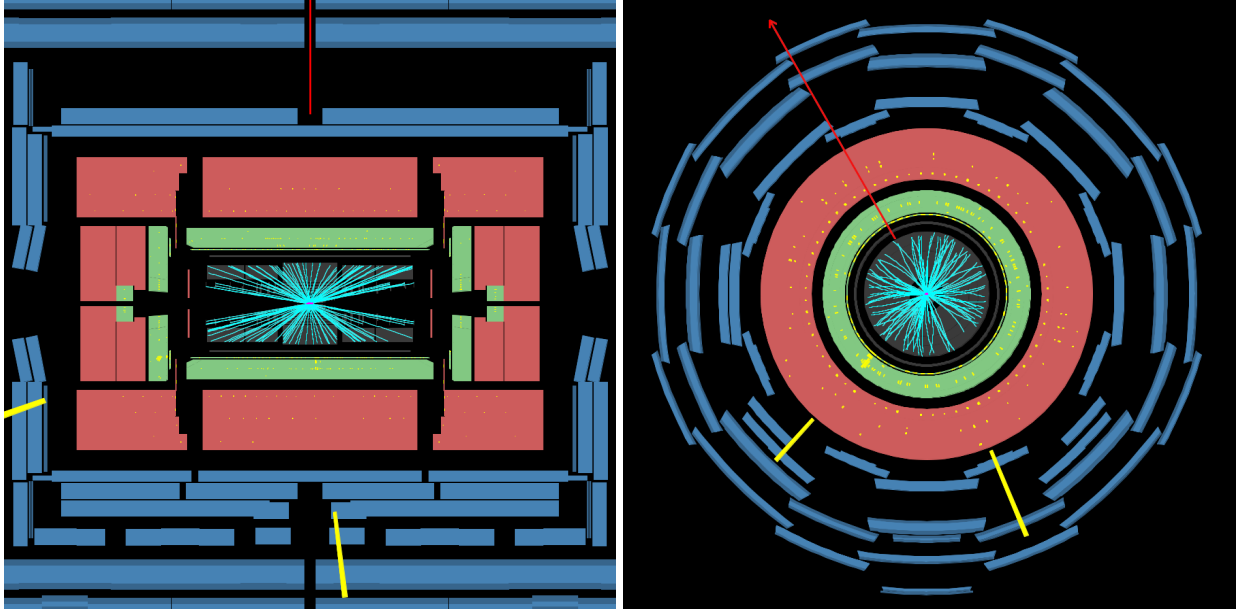


Figure B.4: Event display of ATLAS run 359593, event 761048468, shown as longitudinal (left) and transverse (right) slices. Various light blue charged particle tracks are shown in the center of each image, surrounded by the LAr (green) and Tile (red) calorimeters and energy deposits therein (yellow). Finally, the MS is shown in dark blue and E_T^{miss} is represented by the red arrows.

and a jet; since this analysis prioritizes photons in overlap removal, event reconstruction, and analysis proceeded with the photon object. This object also fails the TIGHT photon object requirement. Therefore, this object is likely not a genuine photon. However, it is important to note that the background estimation strategy specifically accounts for fake photons.

| <u>Event Level Variables</u> | | |
|-------------------------------------|---|------------------|
| Variable Type | Variable | Value |
| Fit | t_{avg} | 3.13 ns |
| | ρ | 560 mm |
| Region | E_T^{miss} | 79 GeV |
| Definition | $m_{\gamma\gamma}$ | 109 GeV |
| | $p_T^{\gamma\gamma}$ | 84 GeV |
| | $\Delta\phi_{\gamma\gamma}$ | 1.13 |
| Event-Level | PV z-position | -30 mm |
| | Pileup μ | 44 |
| | Number of γ 's, jets, e 's, muons: | |
| | - Before overlap removal | 2, 2, 0, 0 |
| | - After overlap removal | 2, 0, 0, 0 |
| | V_R | 554 mm |
| | V_Z | 79 mm |
| | $\Delta\eta_{\gamma\gamma}$ | 1.8 |
| <u>Photon Object Variables</u> | | |
| Variable | Leading Value | Subleading Value |
| Timing | 5.82 ns | 0.45 ns |
| Pointing | 2578 mm | -11.6 mm |
| PID | MEDIUM | TIGHT |
| p_T | 65 GeV | 32 GeV |
| η | -1.71 | 0.12 |
| ϕ | -1.2 | -2.3 |
| Energy | 187 GeV | 33 GeV |
| $E_{\text{cell}}^{\text{max}}$ | 53 GeV | 6.3 GeV |
| $E_{\text{cell}}^{\text{max}}$ gain | MEDIUM | HIGH |

Table B.2: Key event variables for ATLAS run 359593, event 761048468, including event-level variables (top) and photon object-level variables (bottom).

APPENDIX C:

TIMING STUDIES

This appendix summarizes several key timing-related studies, including the validation of the lifetime reweighting procedure (Section C.1), the timing shapes across the four timing quadrants (Section C.2), the timing resolutions as a function of the four kinematic variables that define the SR (Section C.3), and a brief comparison of different timing fit variable candidates (Section C.4).

C.1 LIFETIME REWEIGHTING

The lifetime reweighting procedure introduced in Section 7.3 allows for the interpretation of results for signal models with lifetimes above, below, and between the points generated. This section discusses the performance of this process and establishes the range of lifetimes over which it is considered valid. The main factor constraining the extrapolation range is the limited statistics, especially for events that contain a $\tilde{\chi}_1^0$ with a very high decay time, which can cause their reweight values to blow up or become disproportionally small. The reweighting procedure uses the so-called *truth* information from the simulated signal to determine the proper decay time of the $\tilde{\chi}_1^0$ for each signal event. Since there are two $\tilde{\chi}_1^0$'s in each event, only the one producing a displaced $Z \rightarrow ee$ or $H \rightarrow \gamma\gamma$ decay is considered; in the rare cases where a signal event contains two displaced di-EM resonances, one $\tilde{\chi}_1^0$ is chosen at random, with the requirement that it decays within the ID volume (i.e.,

before it passes through the LAr calorimeter). The impact of this vertex misidentification is negligible since signal events with two di-EM resonances are extremely rare given the small branching ratios of $H \rightarrow \gamma\gamma$ and $Z \rightarrow ee$.

The validation strategy of the lifetime reweighting procedure compares signals generated at different lifetimes that are reweighted to the same lifetime. Figure C.1 shows the distributions of the average photon time in the SR, for various signal lifetime sources and targets, for signals with $m(\tilde{\chi}_1^0) = 135$ GeV and $\text{BR}(\tilde{\chi}_1^0 \rightarrow Z + \tilde{G}) = 1$. Source lifetimes include 2, 10, 20, and 50 ns, while the target lifetimes shown span nearly four orders of magnitude, from 0.1 to 500 ns. These distributions illustrate the extent to which the lifetime reweighting procedure holds. For target lifetimes between 0.25 ns and 1 μs , the timing distributions of the four different source lifetimes generally agree within statistical uncertainty; however, for target lifetimes less than 0.25 ns and greater than 1 μs , the timing distributions of the four different target begin to diverge. Therefore, the lifetime reweighting extrapolation range is determined to be [0.25 ns, 1 μs].

C.2 TIMING SHAPES ACROSS QUADRANTS

As introduced in Section 8.2.1, the shapes of the average timing distributions vary across timing categories. Figure C.2 shows the average of the absolute value of photon times for data with CR kinematic cuts applied in the four different timing quadrants (see Section 8.2.1): pospos ($t_{\gamma_1}, t_{\gamma_2} > 0$), negneg ($t_{\gamma_1}, t_{\gamma_2} < 0$), posneg ($t_{\gamma_1} > 0, t_{\gamma_2} < 0$), and negpos ($t_{\gamma_1} < 0, t_{\gamma_2} > 0$). Here, the absolute value of the times is taken prior to their average. This figure highlights the similarity in timing shape between the pospos and negneg quadrants, as well as between the posneg and negpos quadrants; additionally, it showcases the disagreement in timing shape between the same-sign and opposite-sign categories. The disparity between the two groups of categories emerges from photon correlations in data,

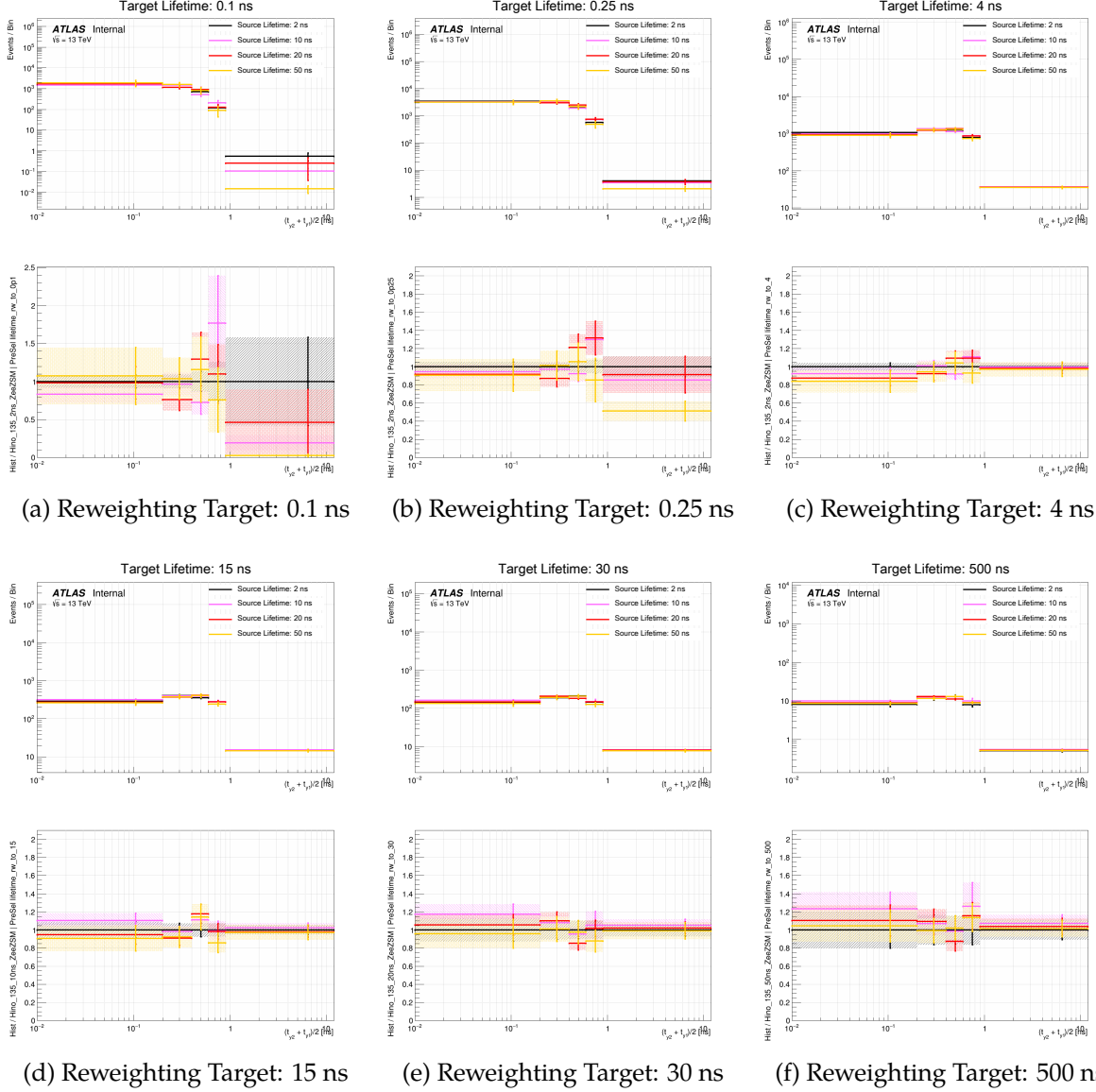


Figure C.1: Comparison of various lifetime reweighting sources and targets for signals with $m(\tilde{\chi}_1^0) = 135$ GeV and $\text{BR}(\tilde{\chi}_1^0 \rightarrow Z + \tilde{G}) = 1$. Source lifetimes include 2, 10, 20, and 50 ns, while target lifetimes are (a) 0.1 ns, (b) 0.25 ns, (c) 4 ns, (d) 15 ns, (e) 30 ns, and (f) 500 ns. Each timing distribution is accompanied by a ratio panel, which shows the timing distributions with respect to the 2 ns source signal.

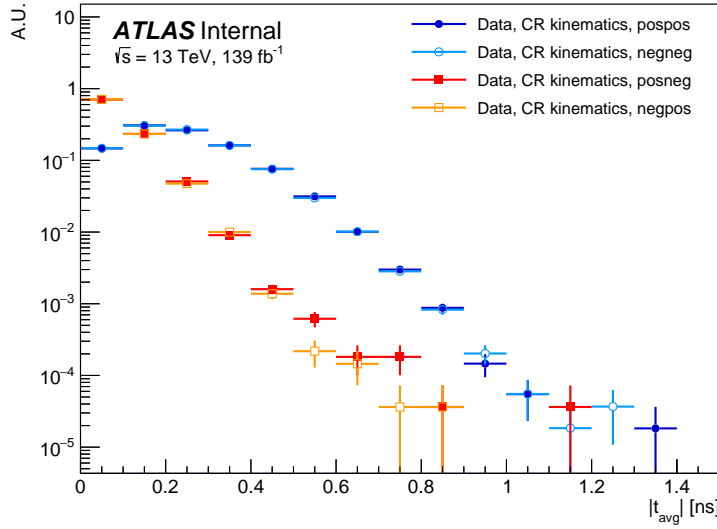


Figure C.2: Comparison of the average of the absolute value of photon times for data with CR kinematic cuts applied in the four different timing quadrants. The absolute value of each photon time is taken prior to their average.

where an event that has one positive-time and one negative-time photon is more likely to have photon times closer to zero than events that have same-sign photon times.

C.3 TIMING RESOLUTIONS ACROSS CRITICAL VARIABLES

As discussed throughout this thesis, several factors influence the resolution of the timing measurement, including $E_{\text{cell}}^{\text{max}}$, the photon purity composition, and the amount of pileup. However, the background estimation strategy did not fully capture all of the dependencies of the timing shape since the average timing distributions in the SR are slightly narrower than the predicted background. Figure C.3 shows the resolution of leading and subleading photon times, as well as their average and difference, as a function of the four kinematic variables that define the SR: E_T^{miss} , $m_{\gamma\gamma}$, $\Delta\phi_{\gamma\gamma}$, and $p_T^{\gamma\gamma}$. Only the analysis pre-selections have been applied (note that these plots were created after unblinding), and no form of $E_{\text{cell}}^{\text{max}}$ reweighting, purity scaling, or residual time shifting procedure (as described in Section 8.5) has been performed. While the timing resolution trends are distinguishable,

they are subtle – certainly much more so than the timing resolution as a function of $E_{\text{cell}}^{\text{max}}$, shown Figure 6.8. The relative flatness of the timing resolutions in Figure C.3 indicates that the analysis strategy did not fail to capture some striking correlation; instead, the slight narrowness of the SR timing distributions compared to the predicted background likely emerges from a more subtle correlation or mechanism. Additionally, the fact that the timing average and difference exhibit fluctuations similar to those in the single photon timing distributions suggest that the degree of *correlation* between the photon times is not an obvious culprit either.

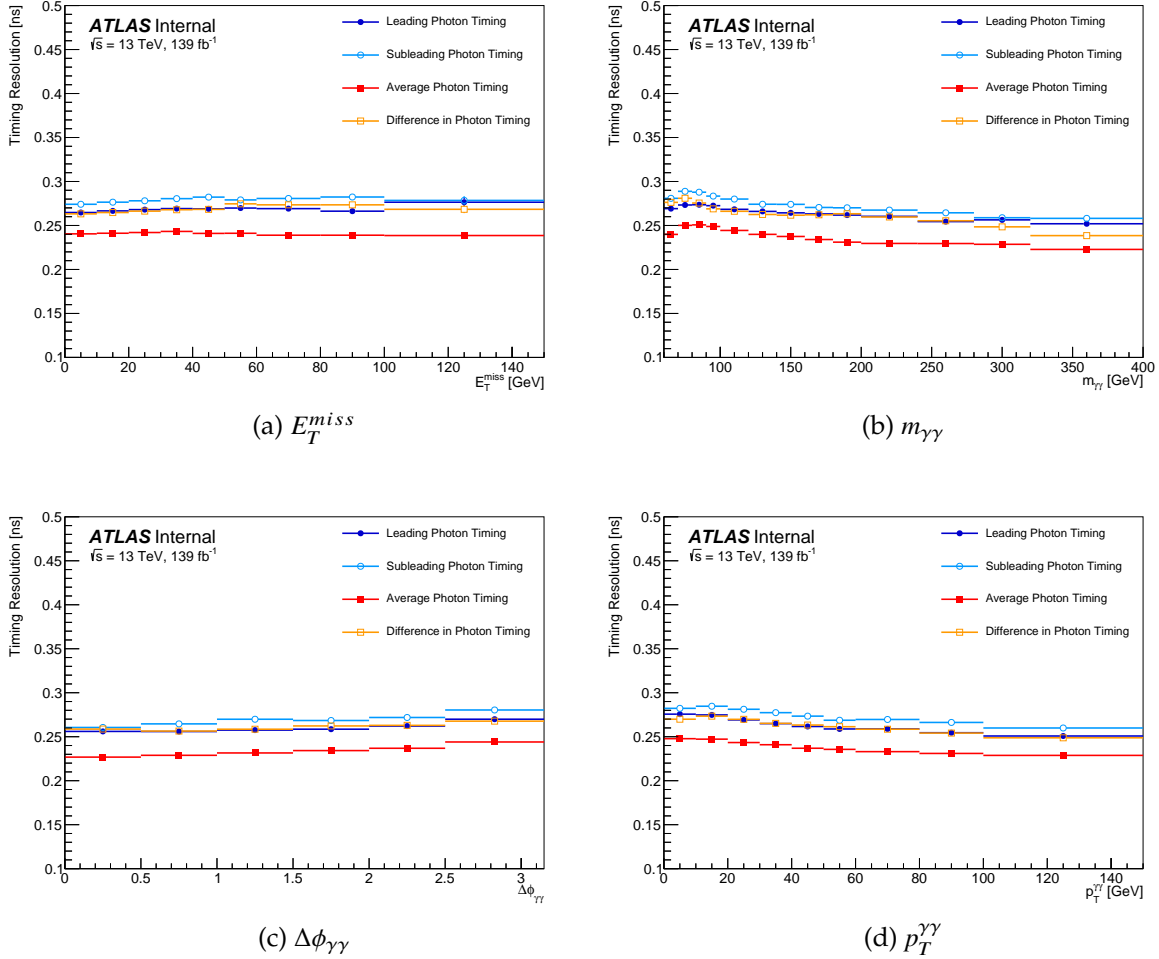
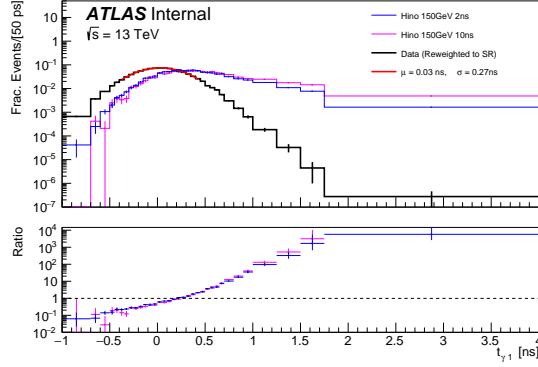


Figure C.3: Timing resolution as a function of (a) E_T^{miss} , (b) $m_{\gamma\gamma}$, (c) $\Delta\phi_{\gamma\gamma}$, and (d) $p_T^{\gamma\gamma}$, for the leading and subleading photon times, as well as their average and difference.

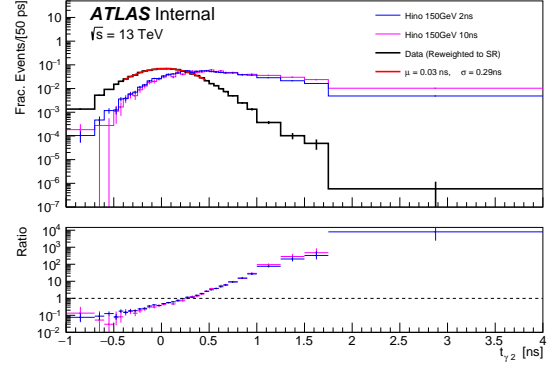
C.4 COMPARISON OF TIMING VARIABLE CANDIDATES

In selecting the optimal timing analysis variable from the photon times, four candidate variables were considered: the individual times measured for each photon ($t_{\gamma_1}, t_{\gamma_2}$), the average time of the two photons (t_{avg}), and the difference between the photon times, defined as $\frac{1}{2}(t_{\gamma_1} - t_{\gamma_2})$. Figure C.4 shows the performance of each of these choices in discriminating CR data from selected signal points. Based on these comparisons, the average photon time t_{avg} was chosen as the most powerful discriminator. This variable provides better time resolution on CR data as compared to individual photon times and removes many CR events from the most sensitive high-timing bins. In contrast, the difference between photon times in the signal MC samples is comparable to the difference between CR data times.

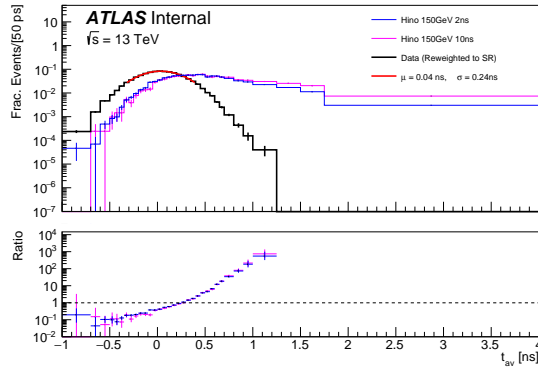
Further studies considered the *weighted* average of photon times: one examined weighting the photon times by the overall resolution of the leading and subleading photon timing distributions in a particular category or region; while a second explored weighting the leading and subleading photon times in each event according to their $E_{\text{cell}}^{\text{max}}$, which is inversely related to timing resolution. Both of these approaches found negligible differences in performance with respect to the average of the two photons times, so t_{avg} was chosen as the fit variable.



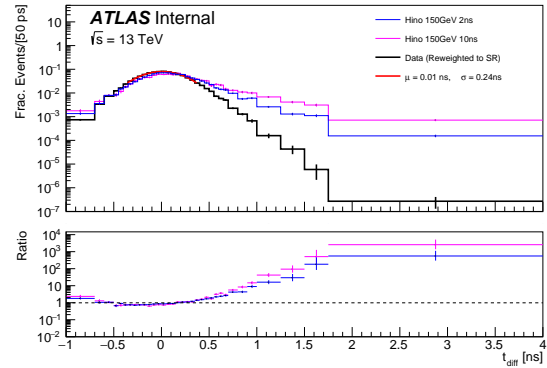
(a)



(b)



(c)



(d)

Figure C.4: CR data is compared to selected signal MC for the candidate timing variables ($t_{\gamma 1}$, $t_{\gamma 2}$, t_{av} , t_{diff}). The most powerful discriminant of the candidates is t_{ave} (c), which shows no CR events in the high timing region.

APPENDIX D:

ANALYSIS DEVELOPMENT:

ADDITIONAL MATERIAL

This appendix documents several key studies that informed the development of the analysis, including various trigger efficiency optimization studies (Section D.1), assessments of signal contamination (Section D.2), and additional distributions related to the topology of signal and background events (Section D.3).

D.1 TRIGGER STUDIES

The analysis originally considered several trigger candidates, including photon and E_T^{miss} triggers, since the final state of the long-lived $\tilde{\chi}_1^0$ decay contains two photons and missing energy from the gravitinos. Figure D.1 shows various trigger efficiencies and projected Run 2 event yields for signals with $\text{BR}(\tilde{\chi}_1^0 \rightarrow \text{H} + \tilde{G}) = 1$ and $\tau(\tilde{\chi}_1^0) = 2 \text{ ns}$ as a function of $m(\tilde{\chi}_1^0)$ for the following triggers: MEDIUM diphoton (g35_medium_g25_medium), LOOSE diphoton (2g50_loose), LOOSE single photon (g140_loose), LOOSE photon plus E_T^{miss} (g80_loose_xe80), and E_T^{miss} (xe110). Events must contain at least two LOOSE photons with $p_T > 20 \text{ GeV}$, with at least one photon in the barrel. It is evident that, for lower $\tilde{\chi}_1^0$ masses ($M < 450 \text{ GeV}$), which are those that the analysis is most sensitive to, the MEDIUM diphoton trigger delivers the highest trigger efficiency over those considered. At higher masses, the E_T^{miss} trigger

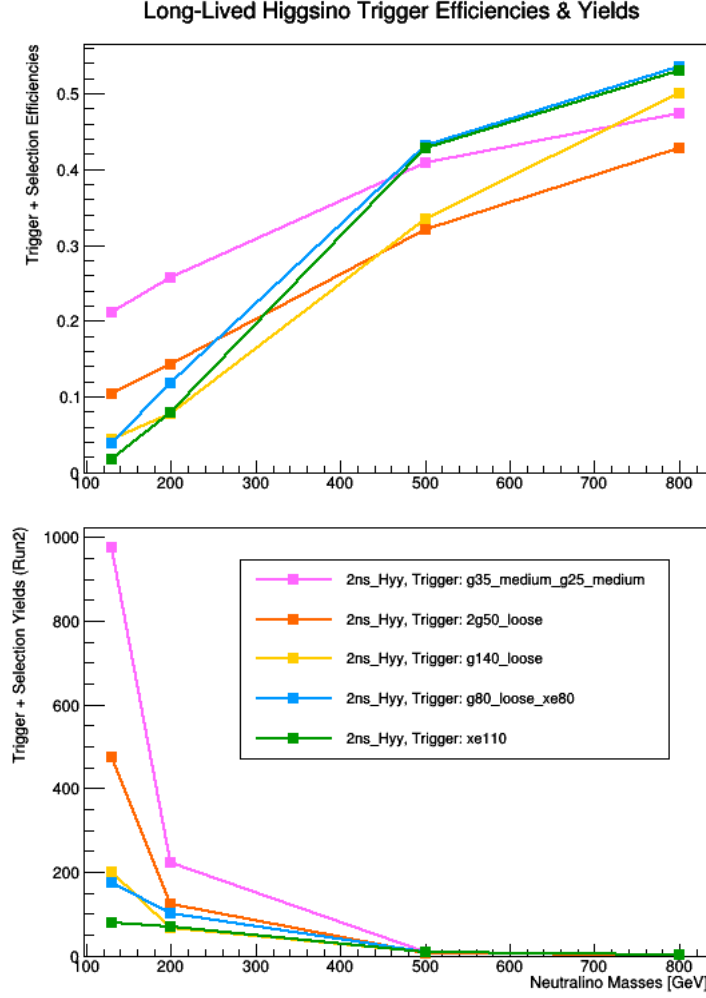
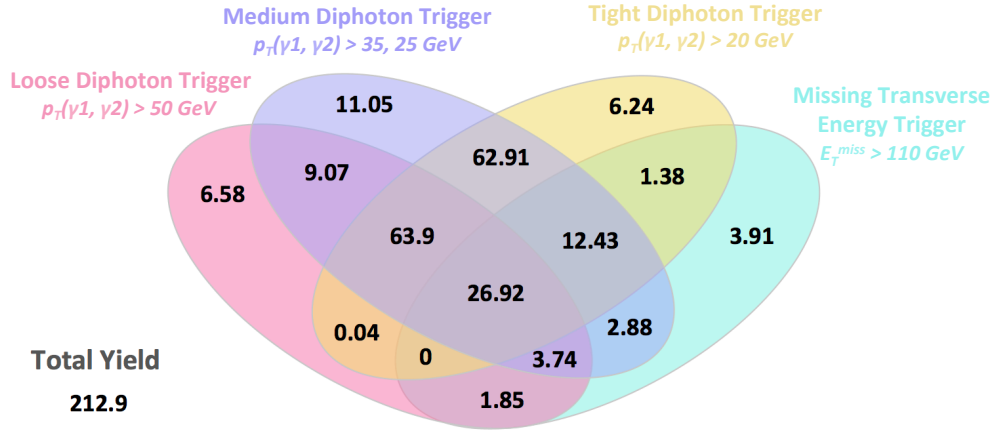


Figure D.1: Trigger and object selection efficiencies and yields as a function of $\tilde{\chi}_1^0$ (here, neutralino) mass for signals with $\text{BR}(\tilde{\chi}_1^0 \rightarrow H + \tilde{G}) = 1$ and $\tau(\tilde{\chi}_1^0) = 2$ ns. The yields shown are those corresponding to the ATLAS Run 2 integrated luminosity. The object selection requires at least two LOOSE photons with $p_T > 20$ GeV, with at least one photon in the barrel.

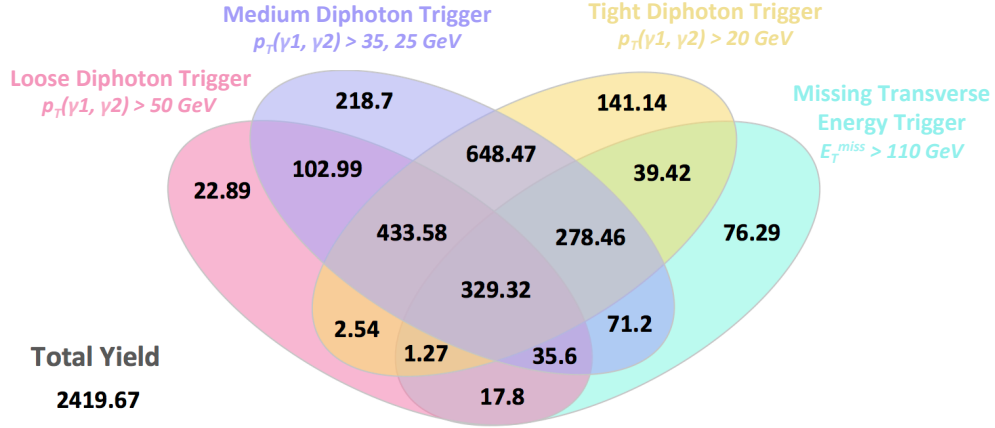
and photon plus E_T^{miss} trigger dominate; however, these efficiencies are only slightly higher than those of the MEDIUM diphoton trigger.

Figure D.2 shows a four-way Venn diagram of the projected Run 2 yields passing various triggers for two different signal models (one with $\text{BR}(\tilde{\chi}_1^0 \rightarrow H + \tilde{G}) = 1$, and one with $\text{BR}(\tilde{\chi}_1^0 \rightarrow Z + \tilde{G}) = 1$). Events passing the E_T^{miss} trigger must contain at least two LOOSE photons with $p_T > 20$ GeV. These Venn diagrams showcase the degree to which various signal events may pass all, a few, one, or even no trigger(s). Here, again, the MEDIUM diphoton

trigger is consistently highly appealing: it captures the highest total signal yields and the most events that otherwise fail all other triggers considered. These distributions helped inform the decision to utilize the MEDIUM diphoton trigger. Given some technical constraints related to difficulties in employing both diphoton triggers and E_T^{miss} triggers, only this trigger is used in the analysis.



(a) $\tilde{\chi}_1^0(200 \text{ GeV}, 2 \text{ ns}) \rightarrow H + \tilde{G}$



(b) $\tilde{\chi}_1^0(200 \text{ GeV}, 2 \text{ ns}) \rightarrow Z + \tilde{G}$

Figure D.2: Venn diagrams of Run 2 signal yields for various trigger candidates, including the LOOSE, MEDIUM, and TIGHT diphoton triggers and the E_T^{miss} trigger. Photon object p_T requirements and the E_T^{miss} requirement are shown in the diagrams.

Once the MEDIUM diphoton trigger was selected for the analysis (see Section 8.1.1), studies were performed to assess the trigger efficiency turn-on (see Section 4.8 for more information). Figure D.3 displays the trigger efficiency as a function of $m_{\gamma\gamma}$. The residual trigger turn-on effects at low $m_{\gamma\gamma}$ inform the choice to require $m_{\gamma\gamma} > 60$ GeV as part of the event selection (see Section 8.1). After the application of this selection, trigger efficiencies were studied as a function of other critical analysis variables, including $p_T^{\gamma\gamma}$ and E_T^{miss} ; all observed efficiencies are essentially flat and at 1.0, with only negligible deviations, indicating that the photon object p_T requirements and $m_{\gamma\gamma}$ selection are sufficient in eliminating all significant trigger-turn effects.

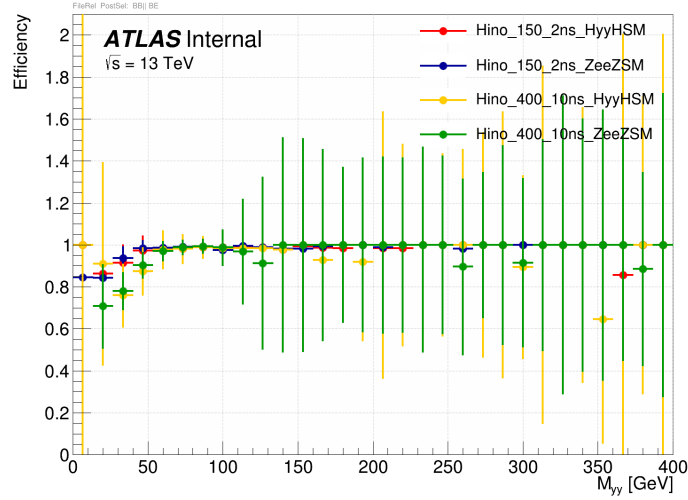


Figure D.3: Trigger efficiency as a function of $m_{\gamma\gamma}$ for events passing the photon object selection for various signal points.

D.2 SIGNAL CONTAMINATION

Figure D.4 shows the signal contamination for various analysis regions, including the prompt $Z \rightarrow ee$ selection, the negneg region, the CR, and the $VR(E_T^{miss})$. These figures confirm negligible signal contamination in critical analysis regions outside the SR. Notably, very low levels of signal contamination are observed in the prompt $Z \rightarrow ee$ selection,

largely because photon objects are prioritized in the overlap removal procedure, and relatively few displaced electrons in the signal pass the MEDIUM electron PID requirements.

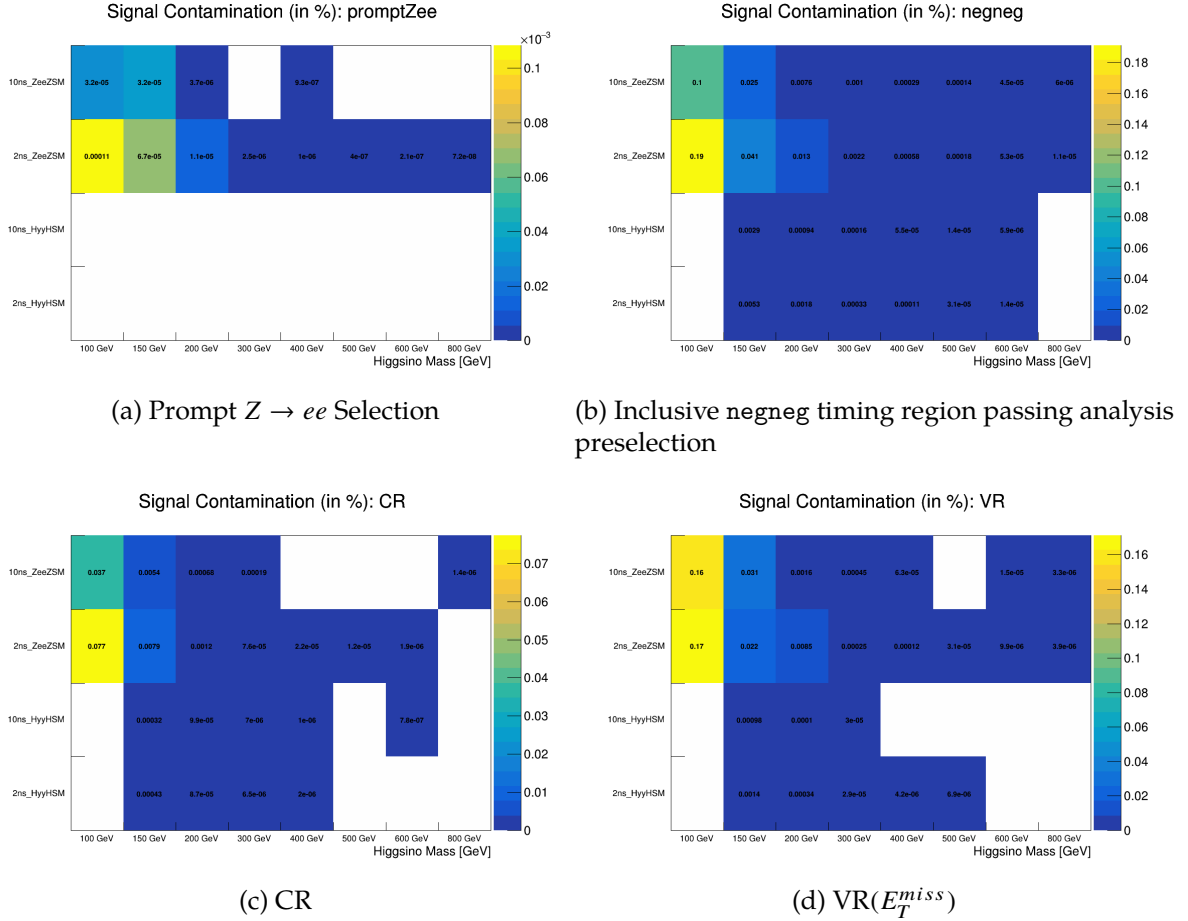
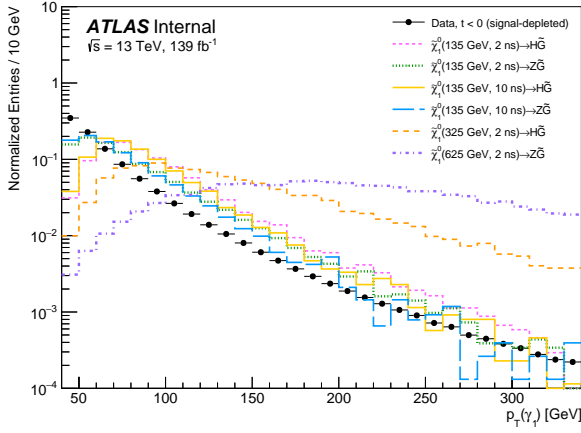


Figure D.4: Signal contamination in various analysis regions, including (a) events passing the prompt $Z \rightarrow ee$ selection, (b) events passing the analysis preselection containing two photons with negative times (negneg), (c) the CR, and (d) the timing-inclusive VR(E_T^{miss}). Signal contamination is shown in %, across various values of $m(\tilde{\chi}_1^0)$ on the x -axis, and across various signal lifetimes (2 and 10 ns) and final states on the y -axis. Here, "HyyHSM" and "ZeeZSM" correspond to events with $\text{BR}(\tilde{\chi}_1^0 \rightarrow H + \tilde{G}) = 1$ and $\text{BR}(\tilde{\chi}_1^0 \rightarrow Z + \tilde{G}) = 1$, respectively. Whitespace indicates zero signal events observed.

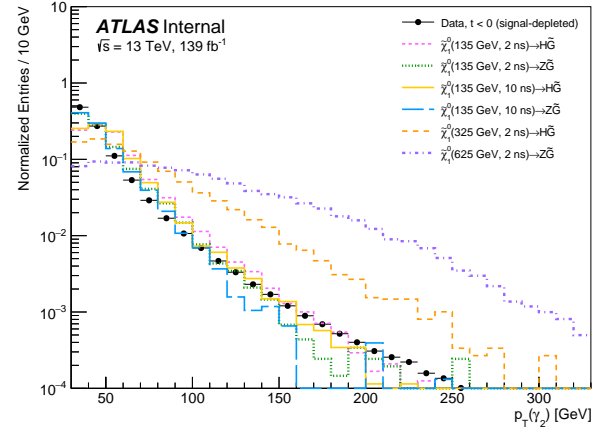
D.3 SIGNAL AND BACKGROUND TOPOLOGY

This section includes additional material illustrating the kinematics and full vertexing distributions of the data and several simulated signal models. All events described in this section must pass the photon object selection in Section 8.1.1; in addition, data events must be in the negneg region, while signal events are shown in the pospos region. Figure D.5 shows photon object p_T , η , and $E_{\text{cell}}^{\text{max}}$ for these samples. For signals with lower values of $m(\tilde{\chi}_1^0)$, the p_T and $E_{\text{cell}}^{\text{max}}$ distributions are relatively similar to those of the data; at higher signal masses, harder p_T and $E_{\text{cell}}^{\text{max}}$ spectra become more evident. The η distributions for the signal show that across various signal models, the signal is produced relatively centrally in the detector, as is the case for many processes produced via hard pp interactions.

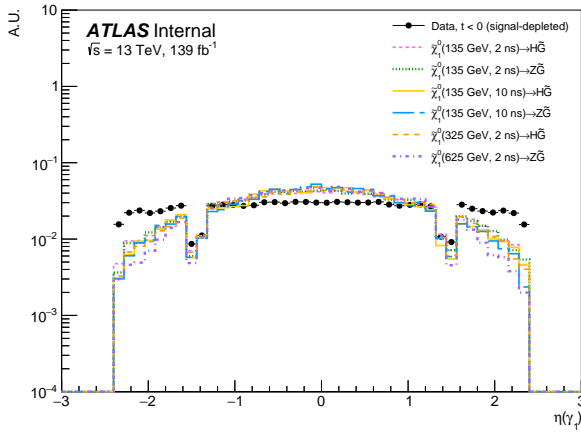
Figure D.6 shows the distributions of the vertexing variables, V_R and V_Z , in signal and data with various $\Delta\eta_{\gamma\gamma}$ requirements: no selection, $\Delta\eta_{\gamma\gamma} < 0.1$, and $\Delta\eta_{\gamma\gamma} > 0.1$, the last of which is used in the analysis. While the $\Delta\eta_{\gamma\gamma}$ sculpts all of the vertexing distributions in various ways, the chosen $\Delta\eta_{\gamma\gamma}$ was determined through optimization (see Section 8.4. The decision to require $V_R > 0$ was also informed by analysis sensitivity studies.



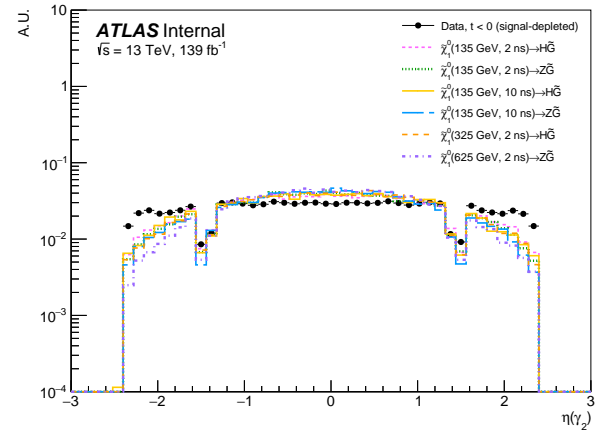
(a)



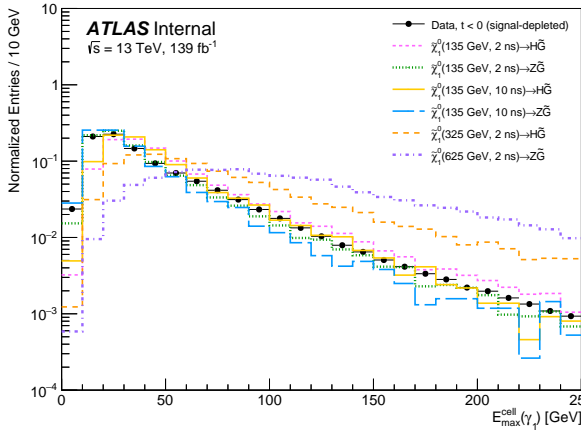
(b)



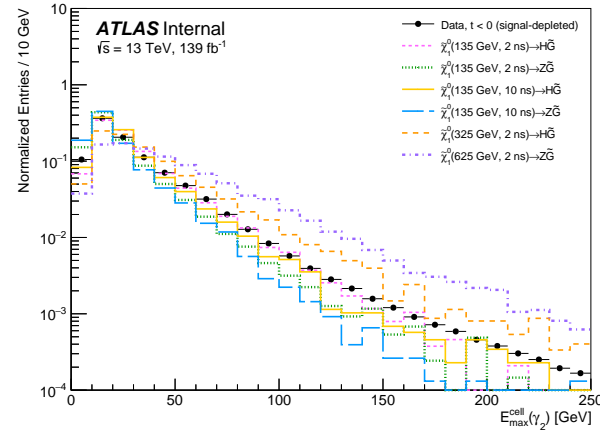
(c)



(d)

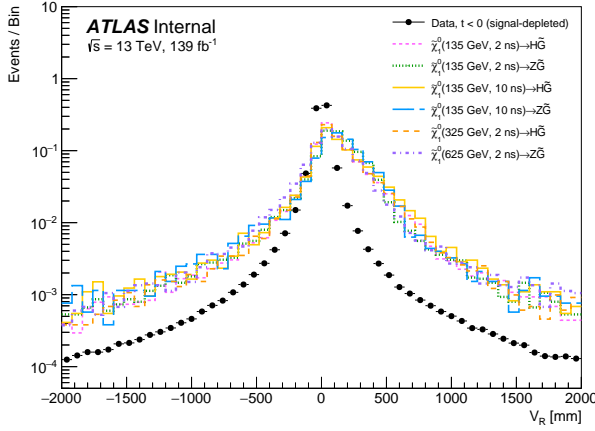


(e)

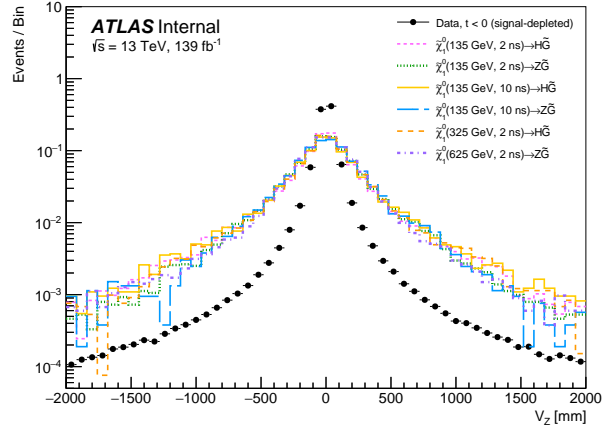


(f)

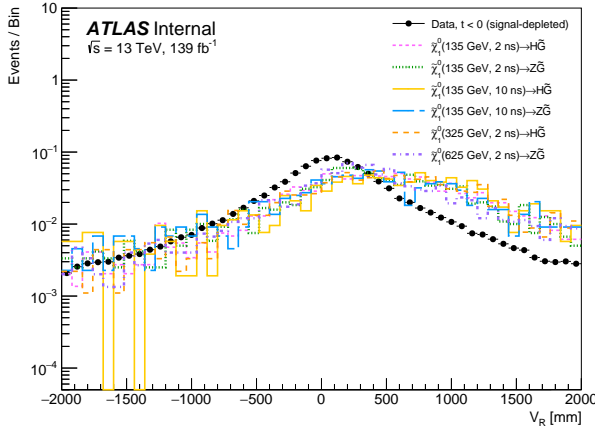
Figure D.5: Photon kinematics in data and simulated signal, including the p_T (top), η (middle), and $E_{\text{cell}}^{\text{max}}$ (bottom) distributions for the leading (left) and subleading (right) photon. All events must pass the photon object selection, and the data is shown for the signal-depleted negneg region, while the simulated signal samples are shown in the pospos region.



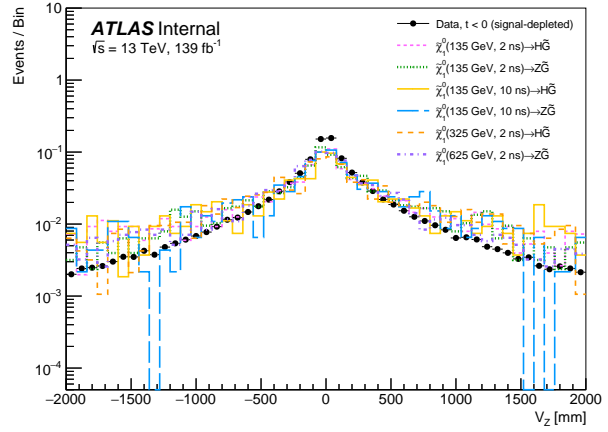
(a) V_R Distribution, No $\Delta\eta_{\gamma\gamma}$ selection



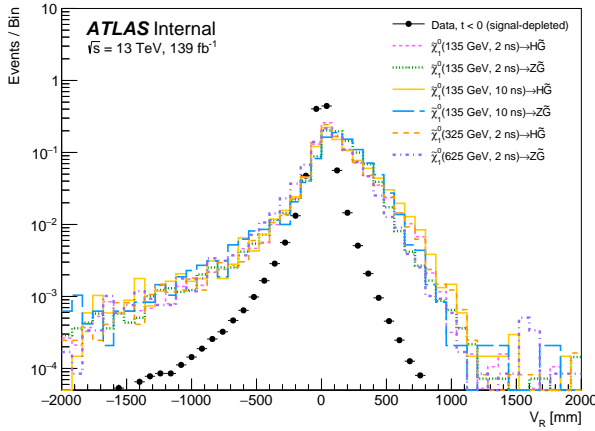
(b) V_Z Distribution, No $\Delta\eta_{\gamma\gamma}$ selection



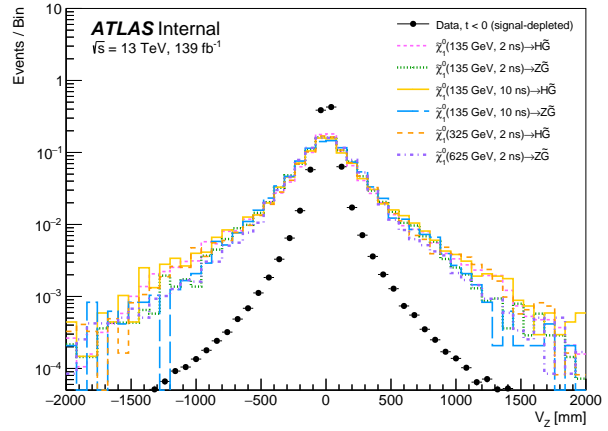
(c) V_R Distribution, $\Delta\eta_{\gamma\gamma} < 0.1$



(d) V_Z Distribution, $\Delta\eta_{\gamma\gamma} < 0.1$



(e) V_R Distribution, $\Delta\eta_{\gamma\gamma} > 0.1$



(f) V_Z Distribution, $\Delta\eta_{\gamma\gamma} > 0.1$

Figure D.6: Vertexing variables, V_R (left) and V_Z (right) in data and simulated signal with no $\Delta\eta_{\gamma\gamma}$ selection (top), $\Delta\eta_{\gamma\gamma} < 0.1$ (middle), and $\Delta\eta_{\gamma\gamma} > 0.1$ (bottom). All events must pass the photon object selection, and the data is shown for the signal-depleted negneg region, while the simulated signal samples are shown in the pospos region.

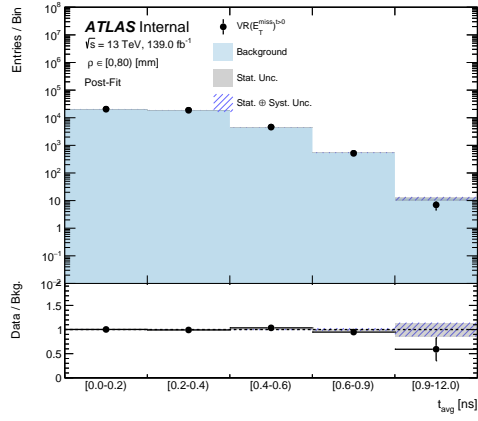
APPENDIX E:

FIT STUDIES

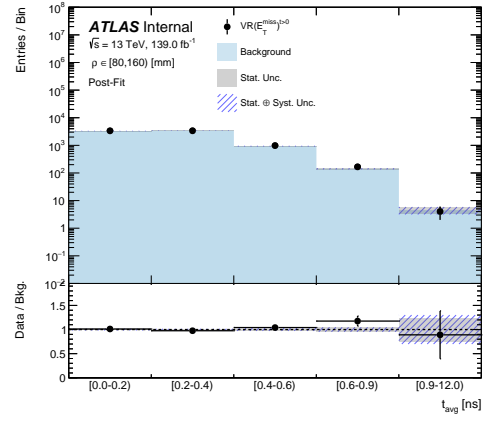
This appendix documents auxiliary studies related to the fit validation and performance, including background-only fits to the $\text{VR}(E_T^{miss})^{t>0}$ and $\text{VR}(E_T^{miss})^{t<0}$ (Section E.1) and p_0 -values and significances of various signal models in the SR (Section E.2).

E.1 FIT VALIDATION

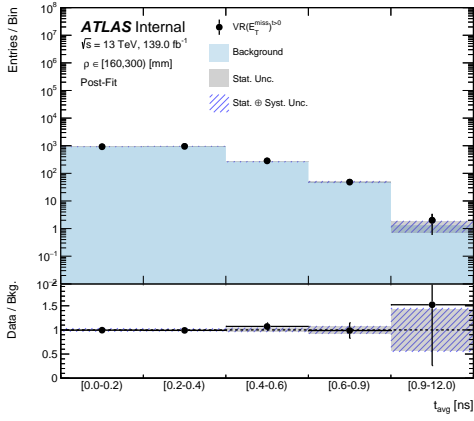
The validation of the fit procedure, discussed in Section 10.2, includes performing background-only fits to all validation regions. Figures E.1 and E.2 show the background-only fit results to $\text{VR}(E_T^{miss})^{t>0}$ and $\text{VR}(E_T^{miss})^{t<0}$ data, respectively, where the average distributions have been sliced into exclusive categories of ρ . Here, the background estimation employs the same procedure described in Section 8.5, with the timing-inclusive $\text{VR}(E_T^{miss})$ (i.e., kinematic selections only) as the E_{cell}^{max} reweighting and purity scaling target. The fits show good agreement between the predicted background and the data in these two VRs.



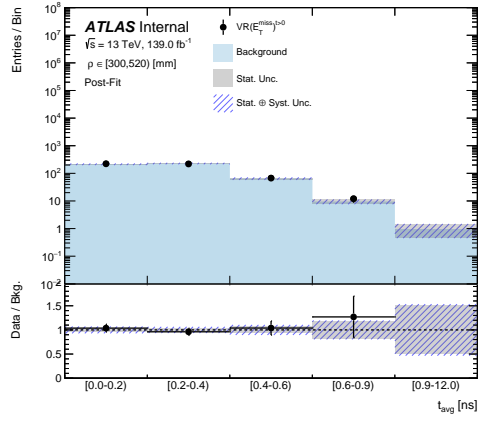
(a) $\rho \in [0, 80)$ mm



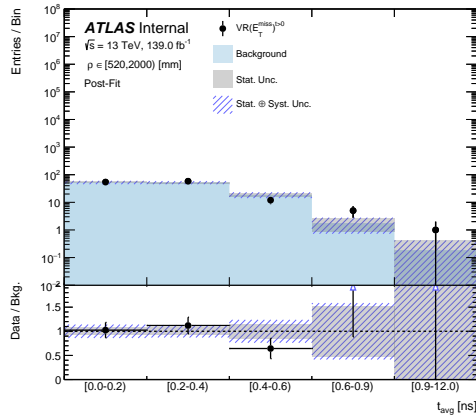
(b) $\rho \in [80, 160)$ mm



(c) $\rho \in [160, 300)$ mm

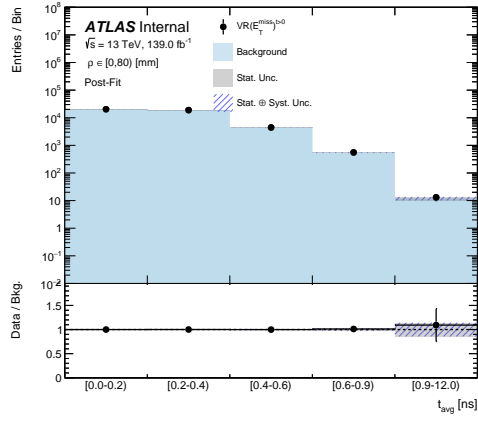


(d) $\rho \in [300, 520)$ mm

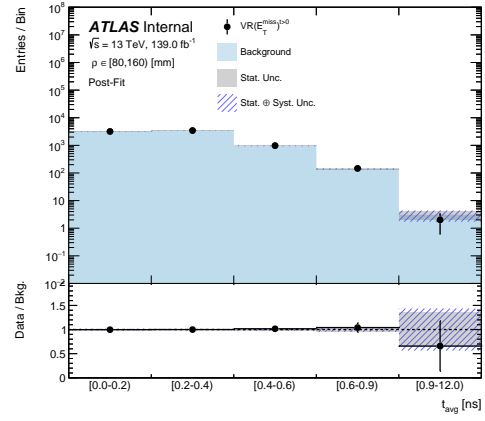


(e) $\rho \in [520, 2000)$ mm

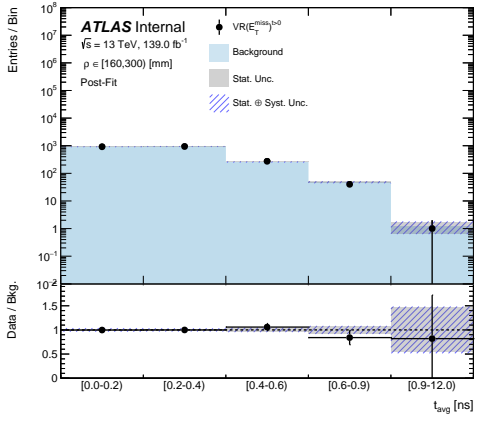
Figure E.1: Average timing distributions for $VR(E_T^{miss})^{t>0}$ data and the estimated background as determined by the background- only fit, in each of the five exclusive ρ categories.



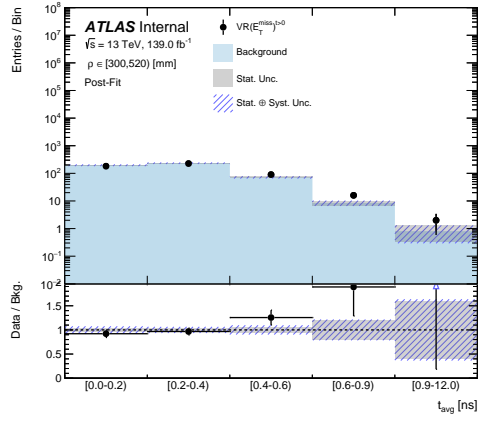
(a) $\rho \in [0, 80)$ mm



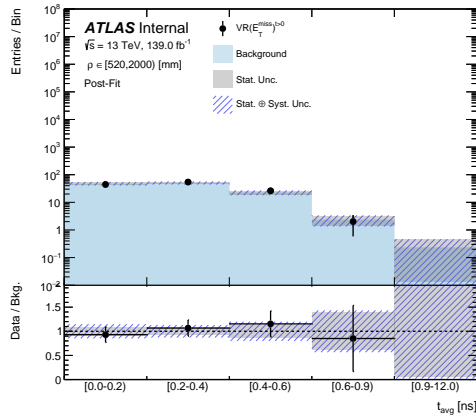
(b) $\rho \in [80, 160)$ mm



(c) $\rho \in [160, 300)$ mm



(d) $\rho \in [300, 520)$ mm



(e) $\rho \in [520, 2000)$ mm

Figure E.2: Average timing distributions for $VR(E_T^{miss})^{t<0}$ data and the estimated background as determined by the background- only fit, in each of the five exclusive ρ categories.

E.2 SIGNAL REGION RESULTS

Figure E.3 shows the observed p_0 -value and significances of signals across a range of $\tilde{\chi}_1^0$ masses, lifetimes, and final states. The observed significances in the solid lines exhibit reasonable behavior and reveal no significant structure across signal points. For comparison, the dashed blue and green lines indicate the measured significance if the signal hypothesis were realized (with $\mu = 1$).

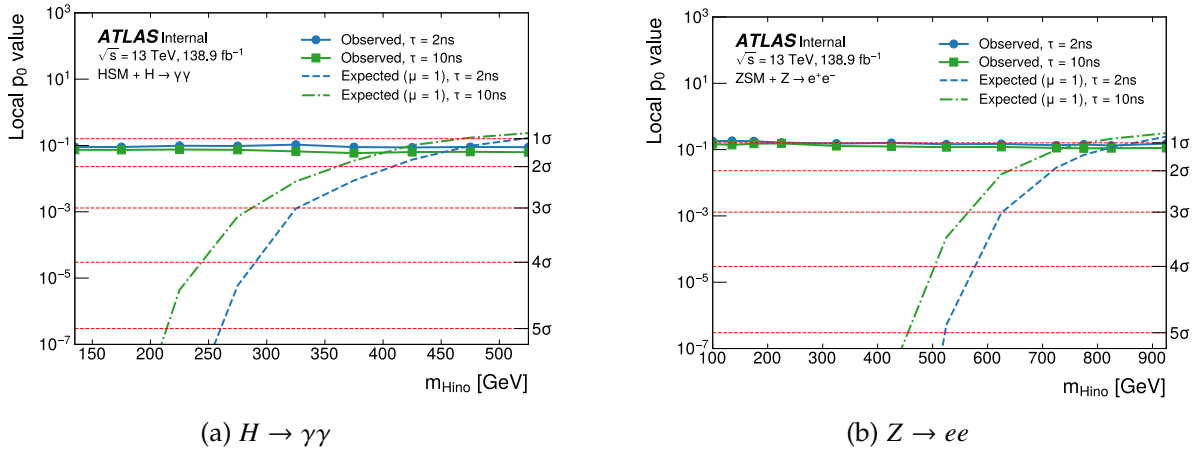


Figure E.3: Observed significances and p_0 -values across signal models (solid lines) compared to the expected measured significance with the signal hypothesis were true with $\mu = 1$ (dotted lines). Results are included for signals with $\text{BR}(\tilde{\chi}_1^0 \rightarrow H + \tilde{G}) = 1$ (left) and with $\text{BR}(\tilde{\chi}_1^0 \rightarrow H + \tilde{G})$ (right).